DOE/NASA/0342-3
NASA CR-182237

Methods for Heat Transfer and Temperature Field Analysis of the Insulated Diesel

Phase III—Final Report

Thomas Morel, Syed Wahiduzzaman, Edward F. Fort,
Rifat Keribar, and Paul N. Blumberg
Ricardo—ITI
Westmont, Illinois 60559

December 1988

Prepared for
National Aeronautics and Space Administration
Lewis Research Center
Cleveland, Ohio 44135
Under Contract DEN3-342

for
U.S. DEPARTMENT OF ENERGY
Conservation and Renewable Energy
Office of Vehicle and Engine R&D
Washington, D.C. 20585
Under Interagency Agreement DE-AI01-86CE50162

TABLE OF CONTENTS

TABLE OF CONTENTS (continued)

SUMMARY

This report presents the results of Phase III of a three-phase program sponsored by DOE and administered by NASA. The program was initiated in June 1983. The objective of the program was to develop a methodology for the thermal analysis of insulated diesel engine design concepts, to validate it with experiments, and to use the methodology to address significant issues related to concept optimization. The progress made on the program in the previous phases has been described in the Phase I Report issued in August 1984 (DOE/NASA/0342-1, NASA CR-174783) and in the Phase II Report issued in September 1985 (DOE/NASA/0342-2, NASA CR-175072).

During the first phase of the program, work concentrated on the development of a new convective heat transfer model based on fluid flow calculations including swirl, squish and turbulence. The objective was to develop a model which would display the correct sensitivity to flow details and piston geometry, and would have sufficient spatial resolution for engine design analysis purposes. Another task that was fully completed was a method for studying surface temperature transients fully coupled with the in-cylinder gas-phase heat transfer and with steady-state conduction through the engine structure. These surface transients can be large (several hundred degrees K) and must be accounted for in application of low conductivity materials. Also, during Phase I, preliminary work was carried out in several other program areas, i.e. analysis of heat radiation insulated diesel engines, single cylinder engine installation and development of experimental techniques for the validation work, and an early parametric study into the anticipated benefits of insulated engines.

During the second phase of the program, progress was made in a number of additional areas. In the area of heat radiation, a comprehensive model was developed that represents the key phenomena and processes which affect radiation heat transfer in diesel engines. The absorption and emission of radiation by soot is treated by a kinetics-based model which calculates the soot formation and burnup. The geometrical description of the process, which is essential to calculation of spatial distribution, uses a zonal

approach capable of treating surface radiation and multiple reflections. A methodology was developed for coupling the multi-dimensional heat conduction calculations to cycle thermodynamics and in-cylinder heat transfer. This methodology can use network-type representations of the structure, as well as detailed finite element models (FEM). Further, a rigorous mathematical procedure was developed for the treatment of the piston-liner interface, accounting for the piston motion and the resulting thermal interactions.

In the latter part of Phase II, after completion of the analytical methodology, studies were carried out of some of the key issues in low heat rejection engines using the newly developed calculation techniques for convective and radiative gas-phase heat transfer, multi-dimensional heat conduction and cyclic heat conduction transients. A wide-ranging design analysis matrix was covered, including seven different heat rejection design configurations, and three different engine operating conditions. These studies identified benefits due to insulation, indicated preferred directions for the application of insulation, and quantified benefits of exhaust heat recovery.

As a critical part of the overall program, the analytical methodology was to be supported and validated by engine experiments carried out at Purdue University on a single-cylinder engine, which was donated to Purdue in conjunction with this project by Cummins Engine Company. The purpose of these experiments was to provide experimental data for calibration and validation of the analytical methods. The single cylinder test engine used in this work is based on a Cummins NH engine. During the second phase of the program this engine was brought to operational status including super-charging and air heating equipment necessary to duplicate the in-cylinder conditions found in turbocharged highway truck diesels under typical operating conditions.

In Phase III, specialized instrumentation was developed at Purdue University capable of measuring heat radiation, total surface heat flux and accurately phased cylinder pressure. Radiation heat flux was determined

from a signal collected by a paired fiber-optic bundle protected from direct gas impingement by a sapphire window. Total heat flux was measured by a fast-response surface thermocouple mounted on a probe installed in the cylinder head. Two different thermocouple types were used. For measurements in the cooled baseline engine, an iron-nickel (iron plug plated with a nickel film) thermocouple was used. In the ceramic-coated, i.e., insulated engine, the probe was also ceramic-coated with overlapping films of platinum and platinum-rhodium. Pressure-crank-angle data was measured by a commercial water-cooled pressure transducer, widely accepted and used throughout the diesel industry, combined with a precision angle encoder rigidly mounted to the engine crankshaft. Top dead center reference was determined by splitting a symmetrical piston-reflected light signal emanating from a specially designed optical proximeter described in the Phase I report.

A considerable effort was expended on the development of the ceramic heat flux probe. Its development was a joint effort of Purdue University and ITI, in which the leading role was played by Purdue, supported through advice and fabrication by NASA Lewis Research Center and the National Bureau of Standards. Plasma Technics and Turbine Components were contracted to plasma spray the zirconia ceramic coatings on the probe bodies. A large number of iterations were necessary in depositing the thin film materials (primarily platinum and platinum-rhodium) onto the ceramic probes and welding the probe lead wires to the films in such a manner as to insure adhesion at the high temperatures of interest (>1000 K) and operation for a long enough period of time to acquire the desired data.

Using the developed instrumentation, experimental heat transfer data were acquired in the single-cylinder diesel engine. Data over a comprehensive matrix of operating conditions were first acquired in a cooled baseline engine. From this data trends were established of heat transfer with engine speed (four settings), load (four settings) and location (two probe positions in the head). The data were compared to predictions obtained using the new gas phase heat transfer methodology over the entire data set. Very good agreement was found in the time resolved heat flux profiles and

in trends with engine speed and load, demonstrating the strong effect of in-cylinder fluid mechanics on the convective heat flux. Most importantly, the large differences in the heat flux between the two locations in the head, seen experimentally, were correctly predicted by simulations containing the flow-driven convective heat flux calculations.

Following that, the engine was converted to an insulated configuration by installing plasma sprayed zirconia components. These included the piston, head and valves. The experiments were then repeated with the modified engine over the same matrix of operating conditions used in the baseline cooled engine. Due to probe problems caused by the high surface temperatures (exceeding 1000 K), the process of data acquisition extended over a period of many months during which issues of building durable probes and of probe calibration were tackled through a scientifically guided, iterative procedure. In the end, the total matrix of data could not be acquired because probes systematically failed at the highest load operating points. Nevertheless, a large set of data was acquired with the different probes. The analysis of the acquired data showed that in all cases, i.e., at all operating points where comparison of insulated vs. baseline cooled heat transfer could be made, the heat flux decreased when the wall temperature was raised by insulation. The decrease of the peak heat flux rate with respect to baseline was on the order of 30-40% for the level of insulation used in the experiments. The heat transfer predictions obtained employing the new methodology were in agreement with the experimental data, showing the same general level of heat transfer decrease due to insulation, as well as agreement in time and spatial resolution of the heat flux.

It was concluded from the comparison of measured and predicted heat flux and radiation, that the program is validated and represents a significant evolution in the state-of-the-art with respect to previous methods for prediction of heat transfer and component temperatures in metallic and diesel engines.

Using the measured pressure data, ISFC values were computed for both the baseline and insulated engine operating points. The decrease in ISFC

corresponding to the 30-40% reduction in heat transfer, determined by computer simulation to be approximately 3% over the entire range of test conditions, was not discernible within the scatter of the data. It is believed that this inconsistency with the heat transfer measurements may be due to changes in the combustion process and/or basic inaccuracies in the measurement of cylinder pressure. Resolution of his paradox requires a careful experimental/analytical program incorporating heat flux measurements, accurate ISFC determination and combustion analysis.

ACKNOWLEDGEMENTS

The work reported herein has benefited from the contributions of many individuals and organizations.

A major part of this work was carried out at Purdue University in the Internal Combustion Engine Laboratory. The principal investigators at Purdue were Profs. Colin Ferguson and David P. DeWitt. Their efforts in directing the group of students who participated in the program and in providing technical input into the entire experimental program were important and are acknowledged. The efforts of Prof. Cecil Warner and his assistance in the installation and operation of the uncoated engine are appreciated. A number of students were involved, taking on tasks of developing experimental probes and techniques as well as participating in data acquisition. Among them Mr. Dale Tree was responsible for the development of the heat flux probes for the insulated engine, Mr. Greg Rodriguez worked with the heat flux probes for the cooled engine, Mr. Curtis Fiene and Mr. Joseph Timar developed the probes and methods for measurement of radiation heat transfer and Mr. Rudolf Gottschlitch was involved in the development of the optical proximeter. In addition, Mr. Gene Risser and Mr. George Urbanus were involved in many facets of the probe development program, and in addition Mr. Urbanus maintained the engine in running condition and participated in much of the data acquisition. Contributions of all of the above are gratefully acknowledged.

Very important contributions were made by Mr. Walter Kim and Mr. Richard Barrows, both of NASA Lewis, in plating and welding of the first generation ceramic heat flux probes used in this work. The second generation probes benefited from the extensive efforts of Dr. Kenneth Kreider at the National Bureau of Standards who investigated a number of alternative methods of thin film deposition and plated all of the probes used in the last year of the program.

Thanks are also due to the Cummins Engine Company for their support, starting with a donation of the single cylinder engine and of contributing to funds needed for its installation. At Cummins, Dr. S. M. Shahed, Mr. Michael Brands, Mr. Kevin Hoag, Mr. Roy Primus and Mr. Gary Hunter all played important roles including technical liaison with Cummins, providing data for model development, consultation with respect to the single cylinder engine, and feedback on the technical direction of the program. U.S. Tank and Automotive Command (TACOM) made available for use in this program several specially designed iron pistons; thanks for this are due to Dr. Walter Bryzik and Mr. Ernest Schwartz.

I. INTRODUCTION

A technological thrust is in progress to develop insulated, low heat rejection diesel engines which exhibit higher thermal efficiency and lower heat rejection than current state-of-the-art diesel engines. Both industrial and government funded programs of significant magnitude are in place to develop the high temperature materials, lubricants and technical know-how required to achieve this potential.

Integral Technologies Incorporated (ITI) has carried out a three phase program, funded by the U.S. Department of Energy and administered by NASA-Lewis Research Center, aimed at developing a comprehensive heat transfer and thermal analysis methodology oriented specifically to the design requirements of insulated diesel engines. The technology developed in this program will make possible a quantitative analysis of the low heat rejection concept, including the determination of the degree of heat transfer reduction and performance improvement that may be realistically achieved, the identification of design strategies that may be adopted toward that end, and a detailed characterization of the thermal environment in which new materials, lubricants and lubricant concepts will have to exist.

The program is comprehensive in that it addresses all of the heat transfer issues that are critical to the successful development of the low heat rejection diesel engine, ie:

1) in-cylinder convective and radiative heat transfer;
2) cyclic transient heat transfer in thin solid layers at component surfaces adjacent to the combustion chamber;
3) heat transfer and heat flux paths to the moving interface between the piston, rings and liner;
4) steady-state heat conduction in the overall engine structure;
5) "slow" transients in the engine structure resulting from warmup or changes in speed and load.

Heat transfer data for development and validation of the methodology were acquired at Purdue University under subcontract. In order that practical considerations would be adequately reflected in the development of the analytical methods, the program was structured around a commercial, state-of-the-art, heavy-duty diesel engine. Early in the program, NASA approved ITI's request to involve a major diesel engine manufacturer in the program on a voluntary, non-funded basis. As a result, the Cummins Engine Company and ITI reached an agreement along these lines and Cummins' extensive design and testing experience in this field were made available to the program.

The ITI program was comprised of a set of integrated analytical and experimental tasks. This report provides a review of the ITI program approach, including the technical issues which underlie it, a summary of the methods that were developed and presents in detail the results which were obtained in the third phase of the contract effort. The methodology developed and results obtained during the first two phases of the program have been presented in the Phase I Report -- NASA CR-174783 and Phase II Report -- NASA CR-175072.

Technical Issues Underlying ITI Program

A controlled amount of heat transfer is incorporated by design in current metal engines to assure adequate cooling of internal surfaces even at the highest thermal loadings, i.e., at the highest fuel flow rates occurring at the rated speed and load. The result is that a substantial amount of fuel energy is carried away from the combustion chamber, reducing the in-cylinder cycle efficiency and the energy availability of the exhaust gases. Based on ITI's calculations, for typical Class 8 highway truck diesel engines the heat transfer from the combustion chamber gases ranges from over 10 to 30 percent of the fuel energy depending on the operating conditions. In order to reduce the rate of in-cylinder heat transfer substantially, it is necessary to increase the temperature of in-cylinder surfaces from current values near 500 K (440°F) to well over 1000 K (1340°F). Since the current levels of heat transfer are near the lowest

values achievable with practical metal components, efforts are concentrated on the design of components using high temperature materials which would require less engine cooling. For a number of reasons, cost being prominent among them, ceramics appear to be the most likely candidates to satisfy the requirements set by practical considerations. However, their use as engine structural materials introduces a large number of materials-oriented, engine design considerations and issues. Some of the more prominent of these are:

1. material strength, toughness and stability at elevated temperatures;
2. thermal conductivity of high temperature, high strength, durable materials;
3. fatigue due to high cyclical thermal loading;
4. thermal expansion matching for ceramic and metallic materials;
5. lubricant stability and performance at high temperatures;
6. friction and wear characteristics with new structural materials and lubricants.

In all these areas it is desired that engines containing ceramic power cylinder materials have a reliability, availability, maintenance and durability (RAM-D) potential at least comparable to today's engines. As a result, sizable programs to evaluate insulated engine materials and designs and exhaust energy recovery methods (e.g., power turbine, organic Rankine cycle) are currently in progress, supported by both the industry and by the government. To be most effective, these efforts should be grounded in a comprehensive system analysis, which combines thermodynamic and heat transfer considerations and is designed to fully assess the implications of the concept as well as its feasibility and benefits in practical terms. The need for such an analysis becomes apparent once one considers some basic facts about the engine heat transfer process:

1. Combustion gas temperatures (spatially averaged) may be expected to reach values of up to 1800-2000 K at the highest thermal loading, which corresponds to a cycle-averaged temperature of 1300-1400 K. Therefore, in order to eliminate or substantially

reduce the convective heat transfer, the average wall temperature must be allowed to rise up to or near these levels.

2. Materials available for combustion chamber application appear to be limited to about 1400°K, which is close to the value estimated above for the desired average wall temperature. However, the materials limitations are accentuated by the fact that the wall temperature is non-uniform spatially as well as temporally.
3. Some of the heat transfer is due to heat radiation, which is cited in the literature to be on the order of 20-30% of the total heat rejected. This radiation emanates from the hottest portions of the flame--on the order of 2500 K--which are well above any envisioned wall temperatures. Consequently, it is likely that in insulated engines with low convective heat transfer, a much higher percentage of the heat transfer will be through the radiation mechanism.
4. There is a complex interaction between the piston, piston rings, lubricants and the cylinder liner surface which determines the amount of energy (approximately three percent of the fuel energy) which is dissipated into heat at these interfaces and the direction of the resulting heat flow. At these interfaces issues related to lubricant cooling, lubricant consumption and life and component wear must be carefully evaluated.

Therefore, due to fundamental physical phenomena (i.e., radiation, piston ring friction and limitations posed by currently envisioned materials), some engine heat transfer to the coolant will have to be permitted. Additional limitations on maximum permissible temperatures may also be imposed by the lubricant properties. Beyond these, there are numerous other considerations, such as the magnitude of wall temperature swings and their impact on thermal stress fatigue, temperature limitations deriving from the large expansions to which the hot components will be subjected, and special cooling that may have to be provided for injectors and exhaust valves.

Overview of the ITI Program

It is apparent that the task of development of the low heat rejection engine is a multifaceted one, and it requires a synergistic approach combining a number of engineering disciplines and technologies. Prominent among these are: heat transfer, thermodynamics, engine design and development, high temperature structural materials, and high temperature lubrication. All of these issues are coupled and need to be assessed and ultimately solved together in a system solution. They are linked together by what might be termed the "engine environment", i.e., gas temperatures and pressures, wall surface temperatures, transient and steady state thermal profiles within the walls, etc. This environment has impact on engine heat transfer and thermodynamic efficiency and at the same time is a key input into the selection of materials and high temperature lubricants. The constraints that derive from the ranges of applicability of practical and forthcoming materials and lubricants must serve to keep specific designs for reduced heat rejection engines within realistic bounds. For cost effective development of this technology one must be able to assess the merits of different approaches in achieving significant reductions in heat rejection without compromising engine durability.

In view of all the technical issues discussed previously, the ITI program was structured around the development of an integrated methodology which can address the special design considerations inherent in the insulated engine concept. The general objectives of the program were:

1. development of a systematic methodology for quantitative assessment of heat transfer and thermal processes in insulated engines which can serve as a tool for design analysis and concept optimization;
2. validation of the methodology with experimental data;
3. application of the resulting methods to a comprehensive analysis of insulated engine design and operation, including evaluation of temperature fields in engine structural materials and temperature profiles of lubricated surfaces.

To achieve these objectives, a number of closely related program elements or task areas were defined:

1. development of spatially and temporally resolved convection and radiation heat transfer submodels;
2. analysis of conductive heat transfer during fast and slow engine transients;
3. analysis of multi-dimensional steady state conduction heat transfer;
4. baseline cooled engine experiments and calibration of heat transfer models;
5. insulated engine experiments and validation of heat transfer methods;
6. comprehensive analysis of the insulated engine concept.

All of these tasks have been completed and are discussed in this report according to the outline which follows immediately.

II. OUTLINE OF REPORT

In Section III of the report a brief overview is given of work carried out and reported during the earlier Phase I and Phase II parts of the program, emphasizing the analytical methodology and the preparation and instrumentation for the experimental measurements. Section IV and following sections describe results obtained in Phase III, which are documented for the first time in a NASA publication. Consequently, significantly more detail is provided in these sections, although reference is made to SAE or other published material where, for reasons of early dissemination of significant program results, it predates this report. Subjects treated in detail in this report include baseline cooled engine heat flux and radiation measurements, methodology for calculating thermal shock in engine components with illustrative examples, probes for heat flux measurements in insulated engines, heat flux measurements in insulated engines, comparison of heat flux measurements with predicted values, and the effects of insulation on ISFC.

III. PRIOR ACCOMPLISHMENTS REPORTED IN PHASE I AND PHASE II REPORTS

A number of the program tasks were completed in the first two phases of the program, namely those dealing with the development of the methodology and the development of the experimental validation setup and techniques. They were reported in detail in the Phase I and Phase II reports. To provide a complete review of the overall program and to put the remaining tasks into the proper perspective, a brief summary of the prior accomplishments is provided in this section.

Analytical Methodology Development

a. Convective Heat Transfer Model

Convective heat transfer from gases to combustion chamber walls, and its spatial and cyclic temporal variations are driven by the instantaneous mean and turbulent gas motions. As such it is inextricably linked to the fluid dynamics of combustion gases, determined in turn by periodic piston motion, valve flows, injection process, combustion, and chamber and piston geometry. Consequently, prediction of heat transfer cannot be accurate unless it includes the consideration of all the important in-cylinder flow velocities and of the effects of the above factors on their evolution in time.

The gas phase heat transfer correlations currently being used in the industry (based on works of Annand, ref. C1, Woschni, ref. C2, and others) are not adequate for detailed studies of heat transfer and temperature distribution needed in insulated engine analyses. This is because these correlations are global and give a single heat transfer coefficient for all gas enclosing surfaces. Thus they cannot differentiate between different surfaces, a capability needed in any study of optimum insulation strategies. Furthermore, these models have no sensitivity to either in-cylinder flows or piston/head geometry.

To overcome these shortcomings, ITI has developed a new convective heat transfer model which includes the effects of actual gas velocities and

turbulence along seven distinct enclosing surface areas in the combustion chamber. The velocities and turbulence are calculated by solving differential equations for swirl and turbulence (k-ϵ model), and an algebraic equation for squish in three combustion chamber flow zones. These velocity components are combined vectorially to produce "effective" velocities adjacent to a corresponding number of combustion chamber surfaces. The heat transfer coefficient for each surface is obtained from Colburn analogy of heat and momentum transfer, and it is directly linked to the effective velocities. One of the main benefits of this approach is that it captures, to a significant degree, the dependence of the heat transfer coefficient on the magnitude of instantaneous in-cylinder flow velocities. Another benefit is the improved ability of the model to represent the spatial nonuniformity of the heat transfer coefficients. For more details of the in-cylinder flow and convective heat transfer model, the reader is referred to the Phase I report and Morel and Keribar (ref. A3).

b. Radiation Heat Transfer Model

Due to soot formation during the diffusion or mixing limited part of the diesel combustion process, thermal radiation from combustion gases to the surrounding combustion chamber surfaces is a significant component of heat transfer for diesel engines, typically on the order of 20% of the total heat transfer. Instantaneous and mean levels of heat radiation are functions of the volume and distribution of burning gas, the amount of soot present in the burning gas, combustion chamber geometry, and also of surface emissivities and temperatures. A comprehensive model was developed to represent all of the above variables that drive heat radiation in diesel engines, described in detail in the Phase II report and in Morel and Keribar (ref. A8).

The soot loading is calculated by a kinetic rate model, which models the kinetics of soot formation and subsequent burnup. The spatial distribution of the radiation heat flux is obtained by using a zonal radiation model. This model also represents the attenuation of radiation from one surface to another, as it passes through the absorbing burned zone, and accounts for

multiple reflections of incident radiation from one surface to another. The burned zone volume is calculated from the cycle thermodynamic simulation, and its shape and location are obtained from an empirically based geometric model. All soot is assumed to be contained within the burned gas.

The effects of instantaneous burned zone and combustion chamber geometry are accounted for by computing, at every time step, gas-to-surface and surface-to-surface view factors for each combustion chamber surface. These view factors (direct exchange areas) are calculated by interpolating within a pre-computed table that stores the values of each view factor for varying piston position, burned zone volume and soot concentration.

Predictions were made of heat radiation as a function of speed and load, and it was found that for a heavy duty highway truck engine, radiation accounts for five to twenty-five percent of the total in-cylinder heat transfer, depending on operating conditions. Under insulated conditions this fraction increases, and ranges from ten to over forty percent. This means that correct representation of radiative heat transfer is essential in insulated engine studies.

c. One-Dimensional Analysis of Fast Temperature Transients

Cyclic (firing frequency) temperature transients arising on combustion chamber surfaces and other engine surfaces exposed to gases are produced by the peaked nature of the gas-wall heat fluxes. Their prediction is needed in studies of component thermal profiles and stresses, and they also impact in-cylinder heat transfer. In this context it should be noted that the convective heat flux predicted (and measured) by the flow-based methodology is considerably more peaked than that predicted by earlier global heat transfer calculations, with an obvious impact on the magnitude of the predicted temperature swing.

An in-depth analysis of wall temperature swings and their effects has been carried out. The wall temperature transients are calculated by a numerical

model representing one-dimensional transient heat conduction through combustion chamber surfaces. The instantaneous temperature profile within the surface layer and the associated heat flux are computed by integrating the heat conduction equations in the surface layers of all gas enclosing combustion chamber sub-surfaces and, additionally, of the exhaust port and piston liner interface surfaces. A two-way coupling is established: the instantaneous wall temperature is used to calculate the heat flux from the gases to the wall (which is proportional to the instantaneous difference between the gas temperature and the wall temperature), and the non-linear feedback effect of the fluctuating wall temperature on the conduction calculation is accounted for to achieve proper closure of the overall engine heat balance. The model and its predictions have been presented in the Phase I report and in Morel et al (A4).

The magnitudes of surface temperature swings depend on engine load, speed and materials. For metallic engines they reach 20-40 degrees K in most surfaces, and are higher yet at bowl edges. However, for engines insulated with ceramics, the swing magnitude can be quite substantial and can have an effect on the cycle-integrated heat transfer level and also on the ceramic durability. For a zirconia coating the swing can reach several hundred degrees K. The predictions of the model have been found to be in an excellent agreement with measured swings in a ceramic coated engine as will be seen below in Section VIII.

d. Steady State Heat Conduction in the Engine Structure

To calculate mean heat loss from combustion chamber gases to the walls requires the knowledge of wall temperatures. Wall temperatures have to be either 1) known from previous measurements obtained at the same engine operating conditions, and specified as input; or 2) calculated using a heat conduction model with appropiate coolant side boundary conditions. Prior to this work, the state-of-the-art approaches to this problem were limited to the first option, i.e., to prescribing the wall temperature. As such, these approaches could not be used to predict the effects of insulation on wall temperatures. Even when a separate finite element calculation is

carried out, the earlier approaches cannot guarantee that the computed temperature field is in a thermal balance, i.e., that the flux of heat from the gases to the walls equals the flux through the structure and, simultaneously is equal to the flux from the structure to the coolant.

In order to overcome these limitations, a separate component of the analytical methodology was developed for coupling the multi-dimensional heat conduction calculations directly to cycle thermodynamics and in-cylinder heat transfer. This methodology can use detailed finite element models (FEM) to represent the structure. Further, a rigorous mathematical procedure was developed for the treatment of the piston-liner interface, accounting for the piston motion and the resulting thermal interactions. This aspect of the methodology has been described in the Phase II report. Using NASTRAN FEM code, finite element representation of the baseline metallic Cummins NH engine was constructed. The model was then employed in a parametric study of the effects of engine load at rated speed. Detailed results for heat flux and temperature distributions as a function of load were obtained including the details on the piston-ring-liner interface for their implications with respect to top ring reversal temperature and lubricant temperatures in general. Using the simpler network representation, parametric studies were carried out to demonstrate the applicability of the integrated heat transfer methodology and to document some important effects of speed, load and insulation level on component temperatures and main heat paths (see Phase I and Phase II reports and Morel et al, ref. A5).

e. Examination of Key Issues in LHR Engines

Using the complete thermal analysis methodology, i.e., the thermodynamic cycle code, heat transfer submodels, one-dimensional heat conduction model for the near-surface layers, the multi-dimensional heat conduction model for the surrounding structure and engine system model including turbocharger, power turbine and Rankine bottoming cycle, studies of heat rejection and engine performance were made. A wide-ranging design analysis matrix was covered, including seven different heat rejection

configurations, and three different engine operating conditions. These studies led to the identification and definition of an important insulation parameter labeled retained-heat-conversion-efficiency (RHCE), which is the efficiency with which in-cylinder heat retained in the gases by insulation is converted directly into work. The higher the RHCE, the larger the improvement in thermal efficiency produced by a given reduction in in-cylinder heat rejection. For a typical turbocharged intercooled highway truck engine at rated conditions RHCE is near 35-40 percent. This RHCE level is higher than that predicted by previous models due to differences in heat transfer models, specifically due to differences in spatial and temporal distribution of the heat transfer. As a result, the predicted thermal efficiency benefits of insulation are greater than previously reported by others, especially for engines with no exhaust heat recovery. Insulation of the cylinder liner was found to bring only marginal thermal efficiency benefits, offset by the negative effects of lower volumetric efficiency, lower power and higher piston-ring-liner temperatures. A practical zirconia-coated engine configuration with a cooled metal liner, turbocharged and intercooled, with combined turbocompounding and Rankine cycle exhaust heat recovery, provided a 26 percent increase in thermal efficiency over a metallic cooled turbocharged, intercooled baseline engine. Non-intercooled diesel engines have an even larger percentage increase in thermal efficiency, but since they start with a lower efficiency in their cooled baseline configuration, this larger increase only serves to close the gap between the non-intercooled and intercooled engines. The results of this study have been described in detail in the Phase II report and in Morel et al (ref. A9).

Experimental Validation Preparation

a. Engine Installation

All of the engine experimental data presented in this report were generated in a single cylinder Cummins diesel engine based on the NH-engine series. It was brought to Purdue during the Phase I, and its installation was started in that phase. It was brought to full operational status during

Phase II, including super-charging and air heating equipment necessary to duplicate the in-cylinder conditions found at typical operating conditions in turbocharged highway truck diesels. A special test cylinder head with access ports for the required instrumentation was fabricated and installed as part of this effort. In order to provide a suitable access port for the gas radiation probe, one intake valve was replaced by a special sleeve. Since the engine breathes quite freely through the remaining valve, the reduction in air flow can be offset by additional boost from the supercharger. Swirl measurements were also carried out on the modified head to insure that no significant difference in in-cylinder air flow was introduced with this modification. Special rocker arm and crosshead components insure normal timing and lift for the one operational intake valve. The engine installation and design details are described in the Phase I and Phase II reports. The changes involved in the installation of the insulated version of the engine are described in Chapter VIII.

b. TDC Determination

In order to use engine pressure data as a means to calculate IMEP and deduce engine heat transfer one must pay close attention to the proper phasing of the data with respect to crank angle. It may be shown that even small errors in phasing can have a significant effect on the IMEP calculations, and therefore it was one of the objectives of the experimental program to develop a method ensuring high degree of phasing accuracy on the order of 0.1°. The standard approach to crank angle phasing is to determine the TDC location by a static calibration technique using a spring-loaded detector inserted through the injector port, or by a similar means. Such a calibration is not adequate as its accuracy is considered to be at best on the order of 0.3-0.5°. Also, it does not take into account the changes in phasing arising from dynamic effects at higher engine speeds. A new technique was developed in the course of this contract which is based on an optical principle. The head-mounted probe consists of two fiber-optic bundles, one of which directs light at the moving piston and the other collects the reflected light. The resulting signal from a photomultiplier is symmetric with respect to TDC, and from it

one can determine the TDC location even under dynamic conditions. Data was acquired up to 2100 rpm (motoring only) to determine the dependence of TDC phasing over the entire engine operating range. The method and its results have been described in the Phase I and Phase II reports, as well as in Ferguson et al (ref. B1).

c. Total Heat Flux Probe for Cooled Metal Engine

The total heat flux from combustion gases to the wall, including both convection and radiation, was measured using a total heat flux probe. In principle, it was a fast response thermocouple designed to measure surface temperature as a function of time. The probe was designed to be compatible and interchangeable with a standard AVL pressure transducer, and it was built for the project by the Medtherm Corporation. The probe contained both a fast-response surface thermocouple and a subsurface thermocouple located 5 mm below the surface. For fast response surface measurements the probe incorporated an electrically insulated thin nickel wire passing through the pure iron cylinder. The nickel wire and the iron cylinder were electrically connected by a thin nickel plating which forms a fast-response thermocouple junction at the probe surface. The subsurface thermocouple was provided by welding a nickel wire onto the iron cylinder 5 mm from the plated end. The above assembly was swaged into a pure iron body. A common iron lead was attached to the iron body to complete the thermocouple lead wire set. The combination of the central nickel wire and the common iron lead attached to the iron body formed the surface thermocouple, whereas the in-depth nickel wire and the common iron lead formed the subsurface thermocouple. The probe was tested for its time response using a pulsed laser as a source of heat, and it was found to have a time constant of 2-3 μsec which is an order to magnitude less than that required to provide crankangle resolved heat flux data. The probe is discussed in Morel et al (ref. A15).

d. Heat Radiation Probe

One of the difficulties in radiation heat transfer measurements in diesel engines is securing good optical access without disturbing the combustion process. For bowl-in-piston geometries, such access can be gained only through the head. Due to the very complex geometry of a typical engine head there are only limited possibilities for optical access. To allow optical access through a complex head casting, a fiber-optic probe was developed which does not require a straight line of sight from the combustion chamber to the photomultiplier. The probe employed a bifurcated fiber optics bundle which provides a simple means of collecting radiation energy transmitted through a sapphire access window. The collected energy was split and directed to two detectors, each sensing a different narrow band of radiation; this approach which senses radiation at two different wavelengths is referred to as the two-color method. The two measured intensities are used to calculate the radiation temperature and apparent soot volume fraction, from which one can then deduce the total radiation intensity. The sapphire window was mounted in a small holder and was recessed from the combustion chamber to reduce the rate of soot deposition on the window. The probe construction, calibration technique and the analytical method used to deduce the radiation intensity from the probe signal are discussed in the Phase I and Phase II reports and in Wahiduzzaman et al (ref. A14).

IV. TOTAL HEAT FLUX MEASUREMENTS IN THE COOLED ENGINE AND VALIDATION OF MODELS BY COMPARISON TO DATA

In Phase III an experimental program was carried out to acquire heat flux data in the single cylinder Cummins engine. The objective was to generate a data base for testing and validating the newly-developed heat transfer methodology. In the first series of experiments, total heat flux measurements were made in the cooled baseline version of the engine.

Bore and stroke of this engine are 140 mm by 152 mm and the compression ratio is 15.7:1. The combustion chamber is quiescent and features centrally located, multi-jet direct injection into a shallow mexican hat piston bowl which forms the principal part of the combustion chamber. The injector is a production eight-orifice Cummins unit injector, cam/pushrod driven, operating on the Cummins P-T system. Injection timing can be adjusted by a special camshaft mechanism and is measured through a strain-gaged injector link rod. Supercharged operation is accomplished by supplying regulated high pressure air from an external compressor and accumulator to an intake plenum. This air also can be heated to reproduce typical levels of intake air temperature. Back pressure is controlled by a valve in the exhaust line. Although the engine normally has two intake and two exhaust valves, one intake valve was removed to accommodate instrumentation. Since the engine breathes very freely, this modification has very little effect on air consumption at low rpm. At higher speeds the inlet restriction resulting from using only one valve is offset by increasing inlet boost slightly until the desired air flow is attained. Through measurements utilizing an impulse torque swirl rig, it was also verified that no swirl was introduced in the combustion chamber as a result of the modification. The engine is supported by external circuits for fuel, lubrication oil and coolant. All fluids can be cooled or heated as required to maintain desired temperatures to the engine. Engine output is absorbed by a Westinghouse DC electric dynamometer rated at 56 kW from 2000 to 5000 rpm. The dynamometer also can supply 45 kW of motoring power over the 1800 to 5000 rpm range.

The engine combustion chamber is accessible to the probes through two locations provided at the cylinder head. The first probe access views the squish region and the other location views the deepest section of the piston bowl. This access was created by removing an inlet valve and replacing it with a mounting insert.

The engine tests were carried out over a broad range of engine operating points representing typical conditions for a turbocharged heavy-duty diesel engine. To make these conditions realistic, engine simulations were made using cycle simulations of the Cummins six-cylinder NH engine on which the single cylinder test engine is based. The specific multi-cylinder engine simulated was the NTC-350 for which Cummins Engine Company supplied detailed engine description, turbocharger maps, and test data. The simulations were carried out using an engine design analysis code incorporating the new thermal analysis methodology. After correlation with the Cummins-supplied test data, the code was used to calculate operating conditions--intake pressure and temperature, exhaust pressure--at four engine speeds and at several loads at each speed to form a test matrix extending from 1000 to 2100 rpm and from full load at any given speed to 25% of full load at that speed. This assured that all of the operating points were realistic steady-state points of an actual heavy-duty highway diesel engine. Due to dynamometer absorption limitations, the peak loads were limited at the lower engine speeds to values below those for full load.

All of the experimental procedures, data reduction techniques, simulation approaches and all of the resulting data have been presented in a detailed form in an SAE publication by Morel et al (ref. A.15, see Appendix A-1). Only the conclusions of that work are summarized below:

1. A comprehensive set of heat transfer data was obtained in a metallic, conventionally cooled, single cylinder D.I. diesel engine. The data is consistent and thus suitable for validation of gas phase heat transfer models.

2. The heat measured heat flux data was characterized by a high degree of spatial and temporal variations, exhibiting a sharp peak in the vicinity of TDC under firing conditions.

3. The peak heat flux measured under firing conditions at the head location facing the piston crown was about two times lower than the peak heat flux measured at a head location facing the piston bowl. Also, the crown location data showed a delay in heat flux peak, caused by the piston shielding and by the finite time of flame propagation into this region of the combustion chamber.

4. The situation was reversed under motoring conditions, and the heat flux at the crown location was slightly higher than in the bowl location.

5. Comparison of Annand's correlation to the data showed its inability to distinguish between the two probe locations or to predict the correct magnitude of the heat flux. This finding was in agreement with findings made by previous investigators.

6. The present flow-based model was found to predict the magnitude and shape of the heat flux at both locations much more accurately, capturing correctly the differences between them under firing conditions. It also reproduced the behavior under motoring conditions. Overall, it gave a very good agreement over all of the operating conditions, motoring and firing, spanning a wide range of peak heat fluxes, exceeding a ratio of 15:1 from the lowest to the highest.

V. HEAT RADIATION MEASUREMENTS IN THE COOLED ENGINE AND VALIDATION OF MODELS BY COMPARISON TO DATA

The second set of experiments carried out in Phase III involved the acquisition of heat radiation data and their comparisons to simulation results obtained at identical operating conditions. The engine setup was the same as for the total heat flux experiments, and the engine operating conditions were nominally the same.

The heat radiation was measured using the fiber-optics probe operating on the two-color principle. The data obtained from the probe was processed to deduce the apparent radiation temperature and soot volume concentration as a function of crank angle. The resultant profiles of radiation temperature and of soot volume concentrations were compared with the predictions of the zonal heat radiation model discussed above in Section III.b. All of the measurements, measurement techniques, calibration methods and comparisons to predictions have been described in detail in Wahiduzzaman et al (ref. A14, see Appendix A-2), and only the main conclusions are given here:

1. The measured radiation temperatures are 200-300 K higher than observed by some of the previous investigators in engine experiments, although it compares well with experiments reported more recently in the literature.

2. The peak values of the product of volumetric soot fraction and soot layer thickness $f_o r$ increase with load at first. However, the peak value tends to saturate at around 0.5-0.6 μm, and the reason for this is not yet apparent.

3. There is evidence of radial and azimuthal stratification of soot, and the integrity of this stratification appears to be maintained long after the beginning of the combustion period.

4. The apparent radiation temperature and $f_v L$ calculated from these measurements compare favorably with the predictions of the heat radiation model developed in Phase II of the program.

5. The spatially resolved zonal model of radiation, complemented by the two-zone combustion/thermodynamics formulation and by a kinetics-based soot submodel, provides a good representation of the radiation process in diesel engines.

VI. THERMAL SHOCK CALCULATIONS

A sudden change in engine speed and load produces a change in the rate of heat flux from in-cylinder gases to the adjacent structural components. As a result, a thermal transient is produced in the components, which is sometimes referred to as thermal shock. This thermal transient generates a moving front of sharp temperature gradients which propagates through the structure and produces high local stresses. An associated effect is the creation of a moving distortion pattern. As a consequence of these effects, severe load/speed transients are considered to be highly adverse engine operating conditions, which can lead to early structural failures. this is particularly true in highly rated engines, with thinner-wall (lighter) components, and in low heat rejection engines employing insulating materials. Methodologies for analyzing the effects of thermal shock must be developed if durability, maintenance and life-cycle cost targets are to be met in these kinds of engine systems.

The issues discussed above can be analyzed effectively only through computer simulations which correctly represent the key processes, i.e.:

a. engine thermodynamics and combustion;
b. engine transient operation during load/speed changes, including the turbocharger and air flow system;
c. fluid motion based convective heat transfer;
d. radiation heat transfer and frictional heat generation; and
e. steady-state and transient structural heat transfer.

The area of those listed above which has been the most advanced is that of steady-state structural heat transfer, generally addressed by finite element codes, but this has been traditionally done in a decoupled manner, and, at best, with only approximate boundary conditions, which has degraded the utility of the calculated results.

The methodology developed in this work represents a step forward in the state-of-the-art in that it allows the investigation of thermal shock in a fully coupled and consistent manner. To demonstrate the use of the

methodology, three studies of component thermomechanical behavior were carried out. The studies involved 1) monolithic metallic and ceramic pistons; 2) ceramic-coated intake and exhaust valves; and 3) an iron piston with press-fit silicon nitride cap. Two types of engine transients were considered, one with rapid engine speed and load increase and one with a rapid load decrease.

The approaches taken and the results generated are described in detail in an SAE publication by Keribar and Morel (ref. A13), included here as Appendix A-3. Only the main conclusions are summarized below:

1. For all studies carried out, the engine response exhibits distinctly separate near-term and long-term behaviors. During the near term (approximately 20-100 engine cycles), the turbocharger responds with a lag and most engine quantities approach the final steady-state levels only to within 10 percent of those values. The subsequent long-term response reflects gradually changing structure temperatures, which affect exhaust temperature and with it the turbocharger. Steady-state is reached within minutes, the exact duration of the response depending on equilibration time for structure temperatures.

2. A thermal wave is shown to propagate through engine component structures during engine speed and load transients. The steepness of the front in the wave depends on component thermal properties and on the turbocharger response to the transient which influences the maximum allowable rate of smoke-limited fueling. In low conductivity ceramics such as monolithic zirconia and plasma-sprayed zirconia this behavior reaches "thermal shock" proportions. A steep wave is formed early on in the transient event with maximum gradients between 30 and 100 engine cycles after the start of the transient. The severity of the thermal shock is not as pronounced in higher conductivity materials due to the higher thermal diffusivity. It is also attenuated by turbocharger lag and differs from component to component.

3. Results of stress analysis of ceramic components under thermal loads prevailing during engine transients indicate that: a) a severe thermal load increase causes surface compressive stresses to increase and overshoot their final steady-state level; b) a thermal load decrease causes relief of surface compressive stress, which temporarily subjects the surface to potentially damaging tensile stresses; c) this is especially pronounced in coatings when there is mismatch between coating and substrate thermal expansion coefficients; d) under the transient conditions of thermal shocks, the structure is briefly exposed to stresses that exceed those encountered under maximum steady state loads.

VII. HEAT FLUX PROBES FOR THE INSULATED ENGINE

The insulated engine experiments required ceramic coated heat flux probes made of the same materials as the surrounding part of the engine structure. Two sets of these probes have been built during this program. The first of these was constructed with the cooperation with NASA Lewis Research Center and these are discussed below as the "NASA probes". After these failed, a second set was constructed jointly by NBS and Purdue University and these are described and discussed below as the "NBS/Purdue probes".

a. NASA Probes

Probe Design and Fabrication. To measure the total heat flux in the insulated engine, a ceramic insulated probe (Figure 1) was developed similar in nature to that used in the metal engine experiments. It was again based on the principle of a thin film thermocouple deposited on the probe surface. The probe had a metal (iron) body of the same diametral dimensions as the previous one to allow use of the same access ports. However, the probe length was shorter by 1.3 mm (0.050") so that when coated with plasma-sprayed yttria-stabilized zirconia by Plasma Technics its thermocouple surface would be flush with the rest of the combustion chamber which was sprayed with the same material to the same coating thickness.

Prior to applying thermocouple films, the zirconia surface was chemically cleaned, ultrasonically, in baths of acetone, isooctane, methylene chloride and ethyl alcohol (10 min. in each bath) followed by oven baking for 2 hr. at 450 K and argon/10% oxygen plasma gas etching for 30 minutes. The thermocouple was formed by sputtering two thin overlapping films (3-5 μm nominal thickness) of platinum and platinum-13% rhodium, composing an R-type junction. Analysis of the platinum-rhodium film after sputtering showed the Rh content to be 13.4%.

The films were deposited onto an electrically insulating aluminum oxide bond coating 1.7 μm thick to improve adhesion of the thin films to the

ceramic. This was found to be necessary to assure success of sputtering and of subsequent welding of lead wires. The aluminum oxide coating was sputtered first using RF magnatron sputtering in an atmosphere of 9.5 x 10^{-3} mm Hg argon plus 1.5 x 10^{-3} mm Hg oxygen. The platinum and platinum-13% rhodium films were then RF diode sputtered in an atmosphere of 5.0 x 10^{-3} mm Hg argon. The platinum was the first thermocouple element sputtered to avoid any reverse sputtering of rhodium during the deposition of the second film.

Thermocouple lead wires 0.18 mm diameter, made of the same materials as the films and clad in an inconel sheath with magnesium oxide insulation, were brought to the surface of the probe along two outside grooves (Figure 1), and each was welded to the corresponding film of like material. Before welding, both wires were flattened to about 25 to 75 μm in order to decrease the thickness of the wires relative to that of the films. The welding was performed with a parallel gap weld head and a constant voltage power supply. The cleaning, sputtering and welding was done by NASA Lewis Research Center laboratories as described in Kim and Barrows (ref. B3). As an initial functional test, the completed thin-film probe and lead wire assembly was installed in a controlled temperature oven and heated up to a temperature of 870 K. Sputtered films and attached lead wires remained intact at the completion of this test. A centered hole drilled from the back of the probe housed the in-depth thermocouple. Silver solder was applied to the back of the probe where the lead wire sheathe entered the body in order to prevent high-pressure combustion gases from leaking through the wiring path in the probe. Extension wires were attached to the lead wires in order to complete the wiring harness. The probes were wired so that surface thermocouple voltages were measured as a difference from the voltage output of the in-depth thermocouple in order to improve the signal-to-noise ratio. The in-depth thermocouple and extension wiring were installed by Purdue University.

Film thickness is an important design parameter. For a fast response time, the films should be as thin as possible to minimize their mass. On the other hand, one is also concerned with their ability to survive in the

engine environment. As a compromise, the three probes that were built had film thicknesses of 10 μm for probe #1 (estimated) and on the order of 5 μm for probes #2 and #3 (measured by profilometers at NASA Lewis). Based on our prior experience with metal probes, these thicknesses were considered thin enough for good response; however later analysis showed that the metal probe experience was not a good guide. Of the three probes, probe #1 was a test specimen which turned out to have a poor response and was discarded. Probe #2 failed during motoring and calibration runs. Thus all of the data presented here were obtained with probe #3.

Probe #3 was successful in measuring heat flux over 40% of the engine test matrix before failing at 1000 rpm and 75% load. Upon inspection after running this load, the platinum thin film appeared wrinkled and had partly bubbled off the aluminum oxide bond coat. The bond coat, however, was intact. The film apparently reached its adhesion temperature limit at time-averaged temperature above 940 K and peak instantaneous temperature above 1040 K. The platinum-13% rhodium film, which was somewhat thinner than the platinum film, did not display the same wrinkling failure. This may indicate that thinner films, in fact, can resist higher temperatures than thick films.

The thermocouple also was calibrated at steady-state temperatures over a range from 293 to 363 K. The in-depth and surface thermocouples were found to produce identical voltage values (within 20 μV), both of which were systematically shifted from the NBS calibration curve for R-type thermocouples by an amount equal to 4 K (Figure 2). The shift was small and was judged of little or no consequence since heat flux depends on the curve slope, which was the same as for the NBS curve. The outputs of the two thermocouples were also checked before each run to monitor the consistency of the thermocouples. The two thermocouples remained in a very good agreement throughout the experiments indicating that the probe remained stable from run to run. This result does not constitute in the strict sense calibration of the surface thermocouple, since in these experiments the overlapping junction and film-wire weld were all at the same temperature and as such steady-state output of the probe represents in

fact the output of the thermocouple formed by the lead wires. However, since the wires were chosen to have the same composition as the thermocouple thin films, the calibration of the thin film thermocouple should be close to that measured in this experiment.

b. NBS/Purdue Probes

Probe Design and Fabrication. Since the sputtering equipment at NASA used in the fabrication of the first set of probes was available only for a limited period, probes used in the latter part of the test program were fabricated through the joint efforts of Dr. K. Kreider at the National Bureau of Standards (NBS) and Purdue University, with Purdue assuming complete responsibility for the availability of functional probes for the test work. Their efforts are described in refs. B4 to B6. The design of the zirconia-coated metal probe body was essentially the same as that used for the NASA probes, with 1.3 mm (0.050") of plasma sprayed yttria-stabilized zirconia applied to the sensing surface. Twenty-seven bodies were machined and zirconia-coated during the course of this work. A list compiling all of these probes is shown in Table I. Of the 27 bodies, 21 were coated by Plasma Technics and the remaining 6 were coated by Turbine Components. Although the quality of the ceramic coatings applied by Turbine Components appeared good, the physical composition was different from that applied by Plasma Technics. Since the thermal properties of the Turbine Components ceramic were not available, these probes were used only in the general probe development effort but not in the test work.

In the initial stage of probe fabrication, both the sputtering of overlapping thin metal thermocouple films on to the ceramic surface and the attachment of thermocouple wires to these films was done at NBS, with Purdue adding the extension wiring harness. Later, Purdue assumed the task of installing and welding the thermocouple wires to films which NBS had sputtered. Of the 21 bodies sprayed by Plasma Technics, 12 had overlapping films of Pt-Pt10%Rh (S-type junction) and 3 had Pt-Au films, all applied by NBS. The remaining 6 probe bodies either had no films applied or a single

Table I. NBS/Purdue Probes*

Group and Probe Number	Plasma Spray Coating	Surface Thermocouple	Place Sputtered	Film Thickness	Bond Coat
A1	Plasma Tech.	Pt Pt10%Rh	NBS	~3μm	Chromium
A2	Plasma Tech.	Pt Pt10%Rh	NBS	~3μm	Chromium
A3	Plasma Tech.	None			
B1	Plasma Tech.	Pt Pt10%Rh	NBS	~3μm	Ion Beam
B1 (reworked)	Plasma Tech.	Pt Pt10%Rh	NBS	~1μm	Ion Beam
B2	Plasma Tech.	Pt Pt10%Rh	NBS	~3μm	Ion Beam
B3	Plasma Tech.	Pt Pt10%Rh	NBS	~3μm	Ion Beam
B4	Plasma Tech.	Pt Pt10%Rh	NBS	~3μm	Chromel
B5	Plasma Tech.	Pt Pt10%Rh	NBS	~3μm	Chromel
B6	Plasma Tech.	Pt Pt10%Rh	NBS	~3μm	Chromel
I1	Plasma Tech.	Pt Pt10%Rh	NBS	~1μm	Ion Beam
I2	Plasma Tech.	Pt Pt10%Rh	NBS	~1μm	Ion Beam
I3	Plasma Tech.	Pt	NBS	~1μm	Chromium
I4	Plasma Tech.	Pt10%Rh	NBS	~3μm	Chromium
I5	Plasma Tech.	Pt10%Rh	NBS	~1μm	Chromium
I6	Plasma Tech.	None			
C1	Plasma Tech.	Pt Gold	NBS	~3μm	Chromel
C2	Plasma Tech.	Pt Gold	NBS	~3μm	Chromel
C3	Plasma Tech.	Pt Gold	NBS	~3μm	Chromel
C4	Plasma Tech.				
C5	Plasma Tech.				
C6	Plasma Tech.				
D1	Turb. Comp.	Pt Pt10%Rh	NBS	~1μm	Ion Beam
D2	Turb. Comp.	Pt Pt10%Rh	NBS	~1μm	Ion Beam
D3	Turb. Comp.	Pt Pt10%Rh	NBS	~1μm	Ion Beam
D4	Turb. Comp.				
D5	Turb. Comp.				
D6	Turb. Comp.				

*Extracted from Tree (1988), Ref. B.4, Table 3.2, p. 37.

metal film applied for use in wire-welding practice. Since reliable calibration data for the Pt-Au film probes was not determined, only those with Pt-Pt10%Rh (S-type) film junctions were used for test work. Thermocouple film thickness for these probes ranged from 1 to 3 μm. In order to increase the adhesion of the films to the ceramic surface, 3 different types of bonding surface treatments were used: a thin chromium layer, a thin chromel layer or an ion-beam treated ceramic surface without a metal layer between the ceramic and the films. The ion beam treatment consisted of bombarding the ceramic surface with an argon ion beam for 5 minutes prior to applying the Pt or Pt-Rh films and leaving it on for an additional 2 minutes after the start of the film sputtering while holding the ceramic substrate at 100°C. This treatment leads to mixing of the films and the ceramic phases at their interface. Prior to either applying a bond coat or to beginning the ion-beam surface treatment, the ceramic substrate was polished to a 1 μm diamond finish, cleaned by vapor degreasing in acetone, ultrasonic cleaning in methyl alcohol followed by a dionized water rinse, immersion in 30% HF for 10 minutes with a deionized water rinse and baking at 200°C to desorb contamination.

Following application of the metal thermocouple films, matching thermocouple lead wires were welded to the films at their edges and brought to the back of the probe body via grooves at the side of the body and mating holes leading to the rear of the body as for the NASA probes. At NBS, the films were cleaned in HF, acetone and ethyl alcohol followed by ultraviolet-ozone cleaning to remove desorbed gases before welding the wires in place.

Most of the probes (B, C, D and I series) differed from the previous NASA probes with respect to the installation of the film lead wires. For these probes, bare thermocouple wires were installed at Purdue, leading from the surface films down through the side grooves to the body holes where they passed through ceramic tubes and continued to the junction with the extension wiring harness. Since the wires were bare they had to be insulated from the metal body inside the grooves. For this purpose, a non-conducting ceramic cement was used which at the same time served to

fill in the grooves. The combustion gases were then sealed by ceramic cement applied around the wire and ceramic tubes at the back of the bodies. This wiring technique was used on the reworked probe B-1 which is discussed in more detail in the following section, as this was the probe used to obtain the major part of the reliable test data. By way of comparison, the electrical insulation in the NASA probes was accomplished by retaining the commercial wire cladding all the way up the grooves, with only a short length of bare wire leading to the point where it was welded to the edges of the metal films. This clad wiring was held in place in the grooves by spot welds. The sealing of combustion gases was accomplished in the NASA probes by silver soldering around the cladding at the back of the probe. Some of the NBS/Purdue probes also used this approach with clad commercial wiring running through the body holes and up through the grooves, but unfortunately all of these probes had a variety of other failures that precluded their use in engine tests. The in-depth thermocouple was located at the bottom of a centered hole drilled from the back of the body to a short distance from the ceramic surface.

Probe Test Experience. During the startup learning process, the first two NBS/Purdue probes fabricated (A1 and A2 in Table I) failed due to mechanical breakage of the wiring or the ceramic before any useful engine data could be obtained.

The second set of probes, B1 through B6, appeared to be more satisfactory than the first and, as stated earlier, a reworked probe of this set (B1) provided the most reliable test data obtained with the NBS/Purdue probes. All 6 of the B-series probes had overlapping films of Pt-Pt10%Rh. One group of 3 (B4-B6) had a metallic bond coat while the other three (B1-B3) had the films applied directly to the ceramic with the assistance of the ion-beam surface cleaning technique. Originally, thermocouple metal film thickness was approximately 3 μm on all B-series probes. However, when probe B1 was reworked, a thinner (1 μm) film thickness was deposited. From this B set, one probe (B2) was permanently damaged during film deposition and two (B3, B4) suffered separation of the ceramic from the metal body, probably as a result of being overheated during a silver soldering

process. Probes B5 and B6 were installed in the engine for test, but the signal quality from B6 was unsatisfactory and the thermocouple films on B5 blistered before any significant data could be obtained.

The initial version of probe B1 was damaged during attachment of the wiring of the metal films due to the separation of the films from the ceramic. Since, except for the separated film, probe B1 appeared to be in good condition, it was returned to NBS for re-application of metal thermocouple films. In the reworked version, probe B1 had overlapping metal films of Pt-Pt10%Rh, approximately 1μm thick, sputtered directly onto the ceramic with the assistance of the ion-beam surface treatment. This probe was wired successfully at Purdue using the ceramic cement/tube technique described earlier and then installed in the test engine for experimental work. Results from probe B1 were the most satisfactory of any obtained with the NBS/Purdue series of probes. This probe was used for over 4 hours of engine operation at the bowl location which is the hotter of the two access ports available and probably representative of the hottest point on the head (excluding the exhaust valves). Data was collected at progressively higher temperatures up to a surface temperature of about 950K, with swings on the order of 140K, before the metal films blistered and peeled sufficiently to cause significant degradation of signal quality.

A similarly-wired probe, I1, also was run for several hours in the engine under test conditions. This probe did not suffer from mechanical failure of the films or ceramic during this period of time. However, after a short exposure to fired operation the thermocouple signal began to exhibit some form of electrical contamination above a surface temperature of about 800K. It appears that this was due to a change in electrical properties of the ceramic cement at high temperature, which shorted the thermocouple to the body. Similar signal contamination was also observed in the B1 probe shortly before it had to be retired.

As a standard practice for probe B1, prior to each fired run and after many of them, total heat flux data were obtained during a motoring operation. The results of these runs were used as a diagnostic tool. The objective

was to determine whether the probe was in an operational state and whether its response was adequate. The reason for choosing this operating condition as the baseline test was that the signal produced under motoring conditions should be well repeatable, and subject to only a small uncertainty. It was observed that the output of probe B1 used to acquire much of the data shown here tended to decrease with time as the experiments progressed. The deduced peak heat flux thus decreased over the period of time by about 16%. Such behavior did not occur with the previously used NASA probes and it is not understood at this time. As a result, our confidence in the results generated by the NBS/Purdue probes was lower than in those generated using the NASA probes.

c. Calibration and Error Analysis

A major potential source of error in heat flux measurement is the uncertainty in the substrate thermophysical properties (here the ceramic coating). An inspection of the data reduction equation (see Morel et al, ref. A15) reveals that for the transient heat flux one needs to determine the uncertainty in square root of the product $k\rho c$, where k is the thermal conductivity, ρ is density and c is specific heat. Simply taking handbook values for the properties, leads to an uncertainty in this quantity which can be as high as $\pm$20% for metal substrate (Wahiduzzaman, ref. C14), which translates into 10% uncertainty in heat flux measurement. In case of a ceramic substrate, property values are either not available or vary widely in reported data. The only recourse is the direct measurement of the thermophysical properties of the specific ceramic used, and estimation of the uncertainty of the product $k\rho c$ from uncertainty of the property measurement method. As in the previous work with iron-nickel transducers, the present investigation followed this route. Thermophysical properties (specific heat, density and thermal diffusivity α) of free standing samples of the coating were measured as a function of temperature (ref. C13). These are given in Table II. In accordance with standard practice (e.g., J. E. Taylor, ref. C13), the uncertainty in unsteady heat flux was calculated to be 7.7% subject to estimated uncertainties in ρ, c and α which were 5%, 3% and 5%, respectively. The uncertainty was obtained using

Table II. Thermal Properties of Plasma Sprayed Partially Stabilized Zirconia*

T(K)	c(J/kg-K)	$\rho c(J/m^3-K)$	k(W/mK)	$\alpha(m^2/sec)$
296	474	2.25×10^6	0.916	0.406×10^{-6}
373	512	2.44	0.923	0.379
473	553	2.63	0.929	0.353
573	575	2.74	0.917	0.335
673	591	2.81	0.903	0.321
773	599	2.85	0.884	0.310
873	606	2.88	0.871	0.302
973	612	2.91	0.865	0.297
1073	618	2.94	0.867	0.295

*From Taylor et al (ref. C.13).

the following equation:

$$\delta q/q = \sqrt{(\delta\rho/\rho)^2 + (\delta c/c)^2 + (\delta\alpha/2\alpha)^2}$$

It is important to note that this uncertainty does not include the effects of temperature dependence of the thermophysical properties. In the present study this dependence is taken into account in a manner described previously (Morel et al, ref. A15), using the actual temperature dependent values of the properties.

Soot deposit on the surface of the heat flux gage is a source of a systematic error, as it reduces the surface temperature swing and thus the peak heat flux. In the current study, light soot deposit was observed after each engine run. To minimize this error, the probe was removed from the engine at frequent intervals, i.e., after 30-45 minutes of engine running, and any soot deposits were removed by a cotton swab. Estimation of the magnitude of this error is difficult because of absence of reliable data on properties of diesel soot deposits. To obtain at least some estimate of the effect, a calculation was made in which the soot was represented by powdered coal data (Eckert and Drake, p. 783, ref. C3), with $\rho c = 0.95$ J/m^{3}K and $k = 0.13$ W/mK, deposited on the zirconia coating with $\rho c = 3.3$ MJ/m^{3}K and $k = 0.9$ W/mK. The values of ρc and k of soot may be expected to be lower than those of powdered coal, and so the calculated error should provide an upper bound on the actual error due to soot. A one-dimensional transient heat conduction model was used, which showed that for a 5 μm layer of "soot," 10% attenuation was produced in the peak heat flux at 1300 rpm. The soot layer in our experiments is estimated to be at most 5 μm thick. Based on this result, we estimate that the error due to soot was less than 10%.

A significant amount of a signal attenuation and phase lag was observed when using the ceramic probe and comparing its output to the metal probe data. A subsequent study revealed that this distortion was due to the finite thicknesses of the films which constitute the thermocouple junction. As discussed in a separate section below, the finite film thickness did not pose a serious problem for metal probes, because for them

the film thickness is a small fraction of the temperature penetration depth into the metal substrate of the probe. On the other hand, in the case of a ceramic probe, the same physical thickness of the film is a much larger fraction of the penetration depth in the ceramic layer beneath the thermocouple. This makes it essential to make the films quite thin (1-3 μm) and to implement a correction in the data reduction procedure in order to account for any residual signal distortion.

Guided by the analysis of the film thickness effects described in ref. A18, an analytical/experimental correction procedure was designed to accomplish the correction. The procedure utilized motored engine heat flux data because these were reliable and easily reproducible from day to day. Motoring runs were made in which heat fluxes were measured by a metal probe (chromel-constantan) as well as by the ceramic probes. The ceramic probe produced heat flux profiles which were lower in amplitude than those produced by the metal probe and they also lagged behind the latter. Suitable corrections were applied to represent an equivalent thickness of a film made of the same material as the substrate, the errors in amplitude and lag were corrected for to large degree. These corrections should be valid for all engine speeds as demonstrated by the model mentioned above. The correction thicknesses for the probe #3 were found to be 3.4 μm and 3 μm for attenuation and lag, respectively. Figures 3 and 4 show corrected and uncorrected heat flux histories measured by the probe for a motored and a fired run respectively. In contrast to probe #1, which required correction thicknesses of 14 μm and 11 μm (Figure 5), and whose performance motivated us to look into the distortion problem, the corrections for probe #3 were relatively small. Since the measured film thicknesses are quite close to those deduced by the correction techniques, it is reasonable to expect that most of the uncertainty has been eliminated by the above procedure. By examining corrected and uncorrected heat flux histories, it is estimated that the residual uncertainty is of the order of 3%.

All of these uncertainties discussed can be combined in a manner which separates the systematic error due to soot from the other errors that are

random, resulting in a range from -8% to +21% with respect to the actual heat flux value.

d. Conclusions and Recommendations. As a result of fabrication and engine test experience with the NASA and NBS/Purdue probes, some conclusions can be formed.

1. Overlapping metal thermocouple films of Pt-Pt10%Rh as thin as about 1 μm can be successfully applied directly to plasma sprayed zirconia coatings through the use of the ion-beam assisted sputtering process practiced at NBS. These films appear to be able to withstand surface temperatures of at least 900 K.

2. Applying these films directly to the ceramic surface (properly cleaned and conditioned) rather than over an intervening bond coat appears to be preferable from a durability standpoint. If a bond coat is applied, an electrically insulating oxide coat is preferable to a metal coat. It could not be established from this study whether a metal bond coat shorts the thin film thermocouple or increases the probability of contamination between the thermocouple material and the bond coat material. It is therefore recommended that a metallic bond coat should be avoided.

3. Clad or ceramic-sleeved wires are less likely to be subject to electrical shorts than bare wires encapsulated in ceramic cements.

4. Differentially heating the metal part of probe bodies near the ceramic-metal interface in processes such as silver soldering increases the risk of separation failures at the ceramic-metal interface. If silver soldering or other heating processes are employed, a heat sink should be used to protect the ceramic bond.

5. The technique for applying durable thin overlapping metal films directly to ceramic surfaces has not yet been reduced to a routine process and thus a significant number of failures from any group of examples is to be expected. Also, the Seebeck coefficient of the thin film thermocouple should be established by calibration.

6. Although the technique of plasma spraying zirconia onto metal substrate is relatively routine compared to the deposition of thin metal films onto zirconia ceramic surfaces, a significant number of failures also should be expected from this process, especially when the spray must be applied to small diameter parts such as probe bodies.

7. To reduce uncertainties, coating samples needed for the determination of thermal and radiation properties of the coating should be produced at the same time the probes are sprayed.

8. Due to the experimental nature of the processes used to apply thin metallic films to ceramic surfaces and to apply plasma-sprayed ceramics to metal bodies, a significant number of infant failures must be expected in fabricating temperature probes of the NASA or NBS/Purdue type. Thus, at present, an experimentalist should plan on fabricating a significant number of probes (at least ten) in order to obtain a sufficient usable set of operational probes.

9. Incidents of failures of probes, especially ones with thinner films (1 μm), were higher if the surface profiles of the ceramic substrate exhibited a higher degree of roughness. Hence, care must be taken to avoid large voids and pits which cannot be removed by surface polishing.

10. Compared at this stage of their development the NBS/Purdue probes gave less consistent performance than the NASA probes. On the

other hand data could be acquired at higher engine loads, indicating a greater high temperature strength and thus there is a long term potential of the NBS/Purdue probes.

VIII. HEAT TRANSFER MEASUREMENTS IN THE INSULATED ENGINE AND VALIDATION OF MODELS BY COMPARISON TO DATA

The heat flux data obtained with the insulated heat flux probes were obtained in two sets, first with the NASA probes, then with the NBS/Purdue probes. These are discussed separately to allow assessment of the results obtained by the different sets of probes. Comparison plots of the results obtained by the two sets of probes are also provided.

a. Data Acquired Using NASA Probes

In this portion of the experimental work, the engine, the instrumentation and the data reduction schemes were to a large degree the same as those used in the study of heat transfer in the conventionally cooled engine as described earlier in Section IV and in Morel et al (ref. A15). Thus, only an abbreviated summary of these items is given here, together with the description of the changes made when converting to the insulated engine configuration.

Engine. The work was performed on a Cummins single cylinder engine based on the turbocharged 14-liter, NH-series. Bore and stroke are 140 mm by 152 mm and the compression ratio is 15.7:1 for the cooled engine and 15.3:1 for the insulated engine. This change in compression ratio is too small to produce any significant changes in heat transfer or fuel consumption. The combustion chamber is quiescent and features centrally located, multi-jet direct injection into a shallow mexican hat piston bowl. Injection pressure in this engine at rated load and speed (2100 rpm) was 11,000 psi (750 bar), and the peak firing pressure was 1850 psi (130 bar). Super-charged operation was accomplished by supplying regulated high pressure air from an external compressor and accumulator to an intake plenum. This air also can be heated to reproduce typical levels of intake air temperature. As described in Section IV, one of the two intake valves was removed to accommodate instrumentation. In these experiments, the small inlet restriction resulting from using only one valve was offset by increasing inlet boost slightly until the desired air flow was attained.

Most of the data was taken in an insulated version of the engine; an exception was a brief experiment carried out just before the changeover from the cooled configuration to the insulated one. This experiment is described below under the heading Hot/Cold Experiments. The insulated engine incorporated a new piston, head, valves, rocker box and liner. These parts, uninsulated, were provided to ITI by the Cummins Engine Company. The original aluminum piston was replaced by an iron piston, developed originally by Cummins Engine Company for U.S. Army TACOM, and made available to this program by TACOM. The piston was remachined to remove the required amount of metal from its bowl and crown surfaces and then was coated with 0.050" of plasma sprayed zirconia (PSZ) by Plasma Technics. The original head was replaced by one which had a much reduced extent of coolant passages, accomplished through the deletion of all lower jacket cores during casting. Again, the head firedeck was remachined and was coated with 0.050" of PSZ. The valves were coated with 0.030" of PSZ and then installed flush with the head. The liner was replaced with a new one which was not coated with zirconia but was coated with chromium oxide for wear resistance.

The engine was cooled by water circulated both to the liner, in the same manner as in the cooled-engine experiments, and also through the remaining upper passages in the head. Cooling was provided to assure durability since the objective was not to develop an optimum LHR engine, but rather to generate heat transfer data for validation and guidance of the analytical effort at adequately high surface temperatures. This objective was accomplished, with very high surface temperatures being produced in the measurement locations.

Instrumentation and Data Reduction. The engine combustion chamber is accessible to the probes through two locations provided at the cylinder head. One probe access views the squish region and the other location views the deepest section of the piston bowl. This bowl section access was created by removing one inlet valve and replacing it with a mounting insert. The locations of the two probes are shown in Figures 6 and 7,

which represent sections through the engine at the cylinder centerline and valve head plane respectively. The probe accesses were designed to be compatible with an AVL (QP505) pressure transducer, and all special probes for the measurement of total heat flux and radiation heat flux were designed to be installed into these probe access ports.

The total heat flux probe was designed to operate on the thin-film principle, where thin films deposited on the probe surface measure the instantaneous fluctuating surface temperature, from which one can calculate the instantaneous heat flux. Two types of total heat flux probes were used: a metallic probe described in Morel et al (ref. A15) and a ceramic probe described in the previous section.

The data reduction techniques used to deduce the heat flux from surface temperature records were the same as those used previously, augmented by corrections for ceramic probes described earlier in this report.

Matrix of Data. The experimental program plan called for the measurements to be made at specific engine operating points described by a matrix identical to that used in the previous metal engine experiments and shown in the table below. These operating points were defined by IRIS simulation of the six-cylinder turbocharged Cummins NTC-350 engine on which the single cylinder test engine is based, as explained in Section III of this report.

The data could not be obtained for the entire matrix due to the failure of the total heat flux probe. As the data were being taken in the order of increasing engine power, they are limited to the lower speed/load region as indicated in the table.

Data Points Acquired with the NASA Probes

Speed/Load	100%	88%	75%	50%	35%	25%
2100	N*	-	N	N	-	Y
1700	-	N	-	N	-	Y
1300	-	-	N	Y	Y	Y
1000	-	-	N	Y	-	Y

*N(o) and Y(es) denote matrix points, dashes denote points not included in the matrix.

Wall Temperatures at Probe Locations. The ceramic coatings installed in the engine and on the heat flux probe produced high surface temperatures, increasing sharply with the engine load (Figure 8a). The temperatures shown in Figure 8a are the time-average values measured at the bowl location. All of the points acquired are shown, including repeats of data points. At the light loads of the test matrix, the temperatures are a little over 600 K, but at mid-load points this rises to 940 K, which is the highest point at which the probe performed reliably. The last point in the upper right corner is the point at which the probe began to fail, as determined from the erratic behavior which appeared in the instantaneous temperature record. The highest cyclic surface temperatures are larger than the time mean, and this is illustrated by the bar labeled "swing," denoting the smallest and highest cyclic temperature at one of the data points.

The average surface temperatures at the crown location are shown in Figure 8b. The average temperatures at the measurement locations in the ceramic-coated engine are substantially larger than those measured previously in the metal engine, as can be seen from the comparison in Figures 9a and 9b.

The measured wall temperature "swings" (maximum-minimum cyclic temperatures) are shown in Figure 10. They show a gradual increase with increasing load, reaching values of 130K at the highest-load point measured. Extrapolating to the maximum load range one can expect swings on

the order of 180K. These magnitudes of surface swings agree well with the theoretical predictions made by Morel et al (ref. A4).

Total Heat Flux Data. The time-resolved heat flux data obtained at the bowl position are presented in Figures 11a-d. As in the cooled engine experiments, the heat flux level is relatively low during the compression stroke, increasing sharply near the TDC when the combustion begins. (Note that the start of combustion advances with increasing load as the Cummins P-T injector advances start of injection with load, keeping the end of injection constant.)

The heat flux in the crown location is shown in Figures 12a-d. It differs significantly from the bowl data. Its values are substantially lower, consistent with the shielding effect of the piston crown. A similar observation was made previously in the cooled engine experiments.

The trends in the peak heat flux values with engine speed and load are summarized in Figure 13. It is plotted with respect to the fueling rate per stroke. The data shows the difference between the peak heat flux levels at the two locations.

Comparison of Predictions to Data. All of the experimental data points were simulated by the IRIS code to generate the heat flux predictions using the flow-based heat transfer model. Their comparison to the data is shown in Figures 14 and 15. The model, by its nature, shows a gradual, consistent increase in the heat flux level with increasing load, and the shape of the curves also evolves in a consistent manner. There is of course more variation in the measured data. The predicted peak heat flux values (Figures 16a and b) are sometimes higher and sometimes lower than the measured ones. Overall the agreement is quite good, and this includes the ability of the model to differentiate between the two spatial locations showing the large differences observed in the data.

Combustion. In addition to the total heat flux measurements, data were also acquired on pressure and on heat radiation. The combustion chamber

pressure was measured using an AVL pressure transducer, and the heat radiation was measured using the same probe employed in a previous metal-engine study by Wahiduzzaman et al (ref. A14).

The pressure data was analyzed by a reverse-cycle procedure to deduce the apparent rate of heat release. Comparing the heat release curve to previously deduced heat release rate in a cooled metal engine at the same operating conditions, it was found that the combustion was affected by the insulation. The ignition delay was shorter and the premixed combustion peak was smaller. However, the bulk of the heat release curve was essentially unchanged, except for a shift by 2-3 CA degrees (Figure 17). Similar effects of insulation on ignition delay and premixed combustion have been observed by others e.g., by Havstad et al (ref. C6). The main conclusion that can be drawn from this figure is that at this load level the engine exhibited no obvious degradation in the combustion process.

A brief test was carried out to assess whether these effects were due to the higher in-cylinder temperatures or due to the increased heating of the fuel prior to injection. (As already mentioned, the insulated configuration used an engine head in which all lower cooling passages had been eliminated, reducing substantially the cooling of the injector). In this test head cooling water was cooled to a lower temperature, and, in addition, a separate jet of water was directed at the injector boss. This proved to be very effective, as indicated by the temperature of fuel returning from the injector bypass. This increased cooling produced a change in the cylinder head temperature: where in the metal baseline the surface temperature at the bowl-facing probe location was 550 K, and in the insulated engine was 780 K, the increased cooling produced a temperature of 745 K. This drop of 35 K due to the cooling is equivalent to 15% of the total difference between the metal and the insulated engine, acting on the head only and not on the piston. The in-cylinder gas temperatures were also lowered, as evidenced by an increase in the volumetric efficiency produced by the increased head cooling. The decrease in gas temperature can be calculated from the change in the volumetric efficiency, and it amounted to 17 K. In response to these changes, the heat release was altered, the heat

release curve pertaining to this enhanced cooling case is shown as a dotted curve in Figure 17. It may be seen that it lies essentially midway between the other two curves, somewhat closer to the insulated case. As for the question of relative importance of the insulation and injector heating on the changes in combustion, one cannot make a clear-cut statement. However, it appears that the relatively small changes in the head temperature and the intake charge produced by the enhanced cooling cannot account for the entire change in the heat release curve, and that changes in injector temperature are partly responsible. Since the injector would become much hotter yet at higher loads, thought must be given to a proper protection of this vital component, as well as to the impact of a hot injector on the spray development and engine combustion process.

Heat Radiation. Heat radiation data were acquired at several operating points, and from these were deduced the apparent radiation temperature and the product of apparent soot volume fraction and soot layer depth. This measurement can be made only during the diffusion burn period, i.e., when the diffusion burn (which forms soot) is taking place, and when the flame is located within the sight of the probe (see Wahiduzzaman et al, ref. A14). The results obtained at 1300 rpm, 25% load are shown in Figure 18a which compares the following three cases: metal engine, insulated engine and insulated engine with enhanced head cooling. The temperatures are seen to be similar for all three cases, being the highest for the insulated engine. The main difference is in the tail region, which shows a much lower temperature for the two insulated cases. A similar result is seen in Figure 18b for 1300 rpm, 35% load. The corresponding soot volume fractions are shown in Figure 19, which indicates a small decrease in the peak soot concentration for the insulated cases. The low tail of the radiation temperature seen in the insulated cases is likely due to contamination by large wavelength emissions emanating from the hot insulated piston top towards the probe. The piston is much hotter than in the metal engine and so its emission is not negligible, yet it is still much cooler than the combustion gases. Thus, when the gases become optically thinner towards the end of combustion, the piston radiant energy

is picked up as a contribution to the total radiation and it skews the result towards lower temperatures.

Hot/Cold Wall Experiments. In addition to the experiments carried out on the ceramic configuration of the engine, a separate special test was carried out on the metal engine, in which the probe surface temperature was altered and heat flux was measured. The objective was to observe the change in heat flux produced by a highly localized change in wall temperature alone, with no other changes in the engine operation present to complicate the result.

To accomplish this objective, it was necessary to find a method to lower the probe surface temperature, which was accomplished by additional cooling provided at the back of the probe (this approach was followed to approximate as best as possible the experiments carried out by Woschni et al, ref. C12, to be discussed in a later section). Of the two probe locations, the one facing the bowl and installed in the intake valve location was hotter and easier to cool, and was selected for these experiments.

Specifically, the additional cooling of the probe was accomplished by blowing cold air at the back surface of the probe holder. The experimental setup used for wall cooling is shown in Figure 20. A small portion of intake air was separated from the rest of the intake stream after passing through the air flow meter. It was compressed and then cooled by a heat exchanger before being blown onto the base of the probe holder. The closed loop heat exchanger was operated at -9°C utilizing a cold bath composed of a mixture of ice, ethylene glycol and dry ice. No separate air metering system was necessary since both the diverted portion of the intake air and the main air originated from the intake plenum and both were ingested by the engine. A thermometer placed in the air stream near the intake valve inside the port measured the temperature of the intake air at that location with and without the cooling jet operating. This difference in intake temperature was then accounted for in the subsequent simulations.

This cooling method reduced the surface temperature at the probe from 667 K to 564 K, i.e., by 103 K. Figure 21 shows the results of the experiments carried out at one engine operating condition, 1300 rpm and 50% load. It is seen that with the higher surface temperature the heat flux is lower, as would be expected from a conventional understanding of convective heat transfer. The simulation of these two operating conditions shows a very good agreement with the data (Figure 22), including the magnitude of the decrease in heat flux obtained with increased wall temperature. The mean heat flux, measured by the difference between the surface thermocouple and an in-depth thermocouple, was seen to decrease by over 20%.

b. Data Acquired Using NBS/Purdue Probes

The experimental work in the insulated engine was interrupted when the last probe of the first set fabricated by NASA blistered and became unusable. When the new probes fabricated by NBS and Purdue University became available, the work was restarted. The instrumentation and data reduction schemes were the same.

Engine. The same Cummins single cylinder engine was used. The engine was torn down during the period when no probes were available, it was inspected and some parts such as bearings were replaced. The engine was then reassembled and brought back into operation. When the first set of matrix data was obtained it was noted that the engine volumetric efficiency had changed. A set of diagnostic measurements determined that the valve timing and injection timing were not correctly set when the engine was rebuilt. Following this determination, the timings were reset and the data retaken. At the same time, corrections were made to a new fuel-return system which was put into operation while the engine was disassembled, and which was suspected of providing inaccurate fuel rate information.

Probes. All of the data were taken with probes B1 and I1. It was reported in the probe section that at high surface temperature both B1 and I1 probes malfunctioned, possibly due to loss of electrical resistance of ceramic putty used to insulate the lead wire from the body. This manifested itself

in the form of unusual but repeatable spikes in the surface thermocouple signal. In addition, there was also evidence of deterioration of the in-depth thermocouple especially after prolonged use. Hence, following analysis of all the data, an inventory of the insulated engine data was made to identify data which were free of surface and in-depth signal distortion, and all of the contaminated data were rejected.

Matrix of Data. The objective of these experiments was to acquire data over the matrix of engine operating conditions described previously. Many of these were successfully acquired, however some of the points were yet to be taken when the last of the operational probes failed. The table below shows the matrix operating conditions indicating the operating conditions at which data was acquired after the engine timing was corrected. As mentioned in the section above, some of the data was taken with incorrect timing of valve and injection events and with the new fuel return system before it was corrected. That data was judged unreliable and was not included in the final analysis. Dashes indicate points which were not parts of the desired matrix. The data were acquired only at the bowl location, while the crown location data could not be obtained because of unavailability of probes. As can be seen, data was obtained successfully at several of the operating points at which data could not be acquired using the NASA probe. In addition, data were acquired at many other points where direct comparison could then be made with the NASA probe results.

Data Points Acquired with the NBS/Purdue Probes

Speed/Load	100%	88%	75%	50%	35%	25%
2100	N*	-	N	Y	-	Y
1700	-	Y	-	N	-	Y
1300	-	-	Y	Y	Y	Y
1000	-	-	N	Y	-	Y

*N(o) and Y(es) denote matrix points, dashes denote points not included in the matrix.

Probe Surface Temperature. The time-averaged surface temperature of the probe at the bowl location showed a strong dependence on the engine fueling rate (Figure 23). The maximum measured value of surface temperature was 940 K, reached at the 75% load at 1300 rpm. This maximum value is equal to the maximum temperature measured in the earlier data set using the NASA probes, even though the later experiments were carried out at higher fueling rates. The temperatures obtained using the two types of probes are shown in Figure 24. It can be seen that at lower loads both probes recorded about the same wall temperatures, but as the fueling rate increased towards the mid-range, the NBS/Purdue probe showed lower temperatures at comparable fueling rates. The solid line in the figure indicates the trend line through the wall temperatures measured in the cooled metal engine.

The surface temperature "swings" increased with increasing fueling rate, reaching a maximum value of 140 K at 1300 rpm/75% load (Figure 25). Comparing these swings with those measured using the NASA probe (Figure 26) produces a picture similar to that seen in the case of surface temperatures: the two probes recorded similar swings at light loads, but in the mid-range the NASA probe swings were higher than with the NBS/Purdue probe.

Because of the small gradual decrease in signal strength recorded by the B1 probe as it aged, some if not all of the differences in surface temperature can be explained in terms of the differences between the two sets of probes. As already mentioned in the section on probes, it was concluded that the data obtained using the NASA probes were probably more reliable. The NBS/Purdue probes appeared to require additional development effort to increase their reliability.

Total Heat Flux Data. The time-resolved heat flux data obtained at the bowl position are shown in Figures 27a-d. They are similar in shape and overall level to those obtained with the NASA probes (Figure 11), increasing in magnitude with increasing engine load. The peak heat flux values at the bowl position are presented in Figure 28. As in the previous

cooled metal engine and insulated engine runs, the peak heat flux increases with the fueling rate. When compared to the NASA probe results (Figure 29) the heat flux follows essentially the same trends with somewhat lower values at higher fueling rates than found with the NASA probe. Comparing to the cooled metal engine data shown as the solid line, the peak heat flux is considerably lower in the metal engine at all engine operating points.

Reviewing the results shown in Figures 28 and 29 it can be seen that, as in metal engine data and insulated engine data obtained in the previous phase, the present data shows good correlation with fuel per stroke and is nearly independent of the engine speed. However, the present data exhibited more scatter than the metal engine data or the data obtained using the NASA probe. Also the temperature data obtained by NBS/Purdue probes has lower slope than found in the previous NASA probe data. As a result, higher average surface temperatures which were expected to be found at high fueling rates did not materialize (Figure 24). Two possible reasons for this difference in trends can be postulated. One of them is that there might be differences between the thermophysical properties of the ceramic substrate of the probes. These differences are not expected to be large since both sets of probes were coated by the same supplier. Another cause for the differences could be related to errors in measuring surface temperature accurately if the Seebeck coefficients of the surface thermocouple formed by Pt and Pt-10% Rh films were significantly different from the assumed standard type-S thermocouple values.

The error in heat flux is roughly proportional to the error in Seebeck coefficient, whereas the error due to thermophysical properties is proportional to the square root of the ratio of the product of thermal conductivity, density and specific heat. Using an estimate of 10% error in the Seebeck coefficient and 20% error in the product of thermal properties, one can compute a potential error in peak heat flux of 10% and 10%, respectively. Since either of these errors would be systematic, and consequently additive, the final error could be as high as 20%. Even with this maximum error estimate, peak heat fluxes are still below those

determined for metal engines especially at high fueling rates and high wall temperatures.

Comparison of Predictions to Data. The experimental data points were simulated by the IRIS code to produce heat flux predictions using the flow-based heat transfer model. The time resolved heat flux profiles, measured and predicted, are compared in Figures 30a-d. The comparison shows a good general agreement in the shape of the heat flux curves. The peak magnitudes of the data tend to be lower than the predictions. This is seen clearly in Figure 31 which compares the peak heat flux values for all the acquired data. It is interesting to note that the measured peak heat flux reduction from the cooled metal engine baseline case is thus somewhat greater than that predicted by the model. This is in contrast to some recent literature, discussed in the next section, which suggests that the opposite is the case.

c. Conclusions

1. A set of heat flux data was obtained in a single cylinder direct injection diesel engine coated with zirconia. Data were acquired at two locations on the head, at several speeds and several load levels. In addition, a study was made of heat flux in a metal engine with variable wall temperature at the heat flux probe location. Great care was given to the probes used, to experimental procedures and to data reduction, in order to minimize all sources of error. At the engine load levels investigated, no gross degradation of the combustion process was observed, and thus the observed heat flux rates can be expected to be representative.

2. The data showed that the peak heat flux was consistently decreased as the wall temperatures rose due to insulation. The average heat flux was also reduced.

3. The results agree well with a previously developed flow-based heat transfer model, indicating that the nature of the heat transfer process was unchanged by the increased wall temperatures.

4. Since the heat flux was reduced, the insulation can be expected to decrease specific fuel consumption and increase exhaust energy recovery potential by transferring energy that would have been lost to coolant into useful piston work and into increased exhaust enthalpy flow.

IX. EFFECT OF WALL TEMPERATURE ON HEAT TRANSFER

Experimental Studies by other Investigators. Recent engine heat transfer literature includes several papers which address the effect of wall temperature on heat flux. Most of the reported data pertains to diesel engines, specifically LHR engines. A significant point about these publications is that several of them report results that appear to be contrary to expectations based on the fundamental understanding of heat transfer phenomena: the data seem to indicate that the peak heat flux occurring near firing TDC increases with increasing wall temperature contrary to the expected decrease which would follow from boundary layer heat transfer theory, as contained in the expression

$$q = h\,(T_{gas} - T_{wall}) \qquad (1)$$

Although there is no uniform agreement at this time that this is indeed so, the possibility that this could be happening is of prime importance and requires resolution. The importance for this issue lies in its relevance to the efficiency benefits that could be derived from LHR engines. These benefits are expected to come in part from increased piston work produced by the combustion gases due to reduced heat rejection. Specifically the heat that would have been rejected near TDC has the most potential to produce useful piston work. Thus, if increased wall temperatures (produced by insulation) would increase the heat flux rather than reduce it, the anticipated direct piston work increase would be lost and even a decreased cycle efficiency could be obtained.

Furuhama and Enomoto (ref. C5), and previous papers of the same authors, (ref. C4), report heat transfer experiments in S.I. and diesel engines. Concentrating on their diesel data, they ran experiments with two kinds of instrumented pistons one of which was a baseline aluminum-alloy piston, and the other a piston which incorporated embedded silicon nitride disks with thin film thermocouples.*

*The design of thermocouples is unconventional and it will be discussed below.

Two disks were installed, one on the bottom of the piston cup and one covering the piston crown. Both had a thin air gap layer in the central region under the insulated thermocouple probes.

2The engine was a D.I. diesel with bore of 104 mm and compression ratio of 17.9. The operating conditions were not given, except that it apparently operated under naturally-aspirated conditions producing a peak pressure of about 70 bar (1000 psi). The data taken at the bottom of the insulated piston cup showed a slightly higher peak heat flux than the baseline case at 1000 rpm, about equal at 2000 rpm and slightly lower peak heat flux at 3000 rpm. The time-mean heat flux was about 30% lower in the insulated case at all engine speeds. At the crown location, the trend of peak heat flux was reversed. It was always higher for the insulated case than the metal case, but while it was only slightly higher at 1000 rpm, it was 1.6 times higher at 2000 rpm and 2.2 times higher at 3000 rpm. This sharp heat flux increase was attributed to an increase in the heat transfer coefficient, by a factor of 2.4. The time average heat flux into the insulated piston was about equal at 1000 rpm, 40% lower at 2000 rpm and 32% lower at 3000 rpm. The mean wall temperatures were not shown, and this is unfortunate, since some of the explanations of the observed trends suggested by the authors link them to the wall temperature. There is a certain degree of inconsistency in the trends of the data, but for most of the reported data there was an increase in the peak heat flux and there always was a decrease in the mean heat flux. Based on these results the authors concluded that "the adiabatic engines have to be considered impossible".

A similar type of experiment was carried out by Huang and Borman (ref. C8), who placed thermocouples on different kinds of inserts in the cylinder head. The engine was a D.I. diesel with a high-swirl combustion system, and a bore of 114 mm. It was operated with intake pressure of 1.0 bar and 1.5 bar, at an equivalence ratio of 0.5. Two sets of experiments were conducted: one compared an uninsulated metal insert with one that was insulated by a layer of an aluminum silicate ceramic placed on the back side of the metal insert, the other compared the uninsulated metal insert

to one faced with a zirconia plate. In the first experiment the wall surface temperature was raised by about 180 K and the peak heat flux was seen to increase. The increase was small at full load, but was almost double at light load. The mean heat flux was reduced. Huang and Borman explain the apparent peak heat flux increase as a result of soot deposits, which could not be removed during the experiments. The second set of experiments gave the opposite peak heat flux results: when the wall temperature was increased by about 200K, the peak heat was found to be reduced by over 50%. The mean heat flux was also substantially lower (33-40%).

Woschni et al (ref. C12) carried out a study using a single cylinder D.I. diesel with 125 mm bore. Two pistons were used, one made of aluminum, the other made of high temperature alloy (a Nimonic), with the cup and crown insulated by air gaps. At full load, naturally aspirated, the piston temperature at the bottom of the cup increased by over 400 K to 870 K and on the crown near the bowl edge by over 550 K to 1040 K. Both the ISFC and BSFC were found to increase despite the temperature increase, and this was ascribed to an increase in heat transfer. Based on data analysis and cycle simulation with an extended version of Woschni's correlation, the authors concluded that the mean heat flux increases with increasing wall temperature. In a separate experiment with a different engine, a thin film thermocouple was installed in an instrument plug replacing one of two exhaust valves. By selectively cooling the instrument plug with a cooling air jet, the surface temperature of the probe could be raised from 650 to 1040 K. It was found that the surface temperature swing magnitude was essentially unaffected by the temperature change, but its slope near TDC became steeper. The heat flux deduced from the instantaneous temperature records were not presented, but a statement was made that the sharper surface temperature rise indicated a much higher heat transfer coefficient -- higher for wall temperature T_W = 1040 K by a factor of 3-5 than for T_W = 550 K. The authors conclude that "heat insulation of the combustion chamber walls is not a practical way to decrease the heat losses and fuel consumption."

Another study that may be mentioned is that of Hoag (ref. C7), who studied the effect of wall cooling in a single cylinder D.I. diesel with a bore of 140 mm. Three thin film thermocouples were installed in the head of the engine and two series of runs were made with different levels of head cooling. This brought about a probe surface temperature change of 70 to 115 K with a maximum wall temperature of 640 K reached at 2000 rpm and A/F = 21. Runs were made at four engine speeds and at several loads at each speed. The peak heat flux was found to be changed only slightly by the wall temperature increase. For most of the data points it was found to decrease, although for several there was a small increase. A parallel unpublished analytical investigation of this data set carried out by the present authors with the assistance of K. Hoag, showed that the observed marginal decrease in the peak heat flux was consistent with the conventional formula given by eq. (1) used in conjunction with the ITI flow-based convective heat transfer model.

Some of the results from previous investigations will be discussed in more detail and compared with results from the present study later in this section.

Discussion of Wall Temperature Effect on Heat Transfer. The two sets of experiments conducted in the present program and described earlier, comprising ceramic-insulated engine experiments and hot/cold metal engine experiments, have shown that the heat flux decreases as the wall temperature increases, as may be seen in Figure 32 which shows the data and trend lines for peak heat flux for the metallic and insulated engine configurations. This is in agreement with equation (1), and with the conventional view of heat transfer in insulated engines. Furthermore, the magnitude of this decrease is also in very good agreement with that equation when employing the ITI flow model to calculate the heat transfer coefficient. This implies that the heat transfer coefficient behaves in a predictable way and that it scales with in-cylinder velocities, and that the thermal boundary layer thickness is not affected to a significant degree by the wall temperatures.

These findings are in contrast to those of Furuhama and Enomoto, and of Woschni et al. To find the source of this discrepancy one needs to analyze both of these experiments and compare them to the present one and search for differences that may be responsible for the disagreements. The task of comparing two experiments is not easy, as the details of all procedures employed are always fully described in a publication; nevertheless, some analysis of differences is possible and is given below.

The experiments of Furuhama and Enomoto were carried out using two different probes, one metal and one incorporating silicon nitride ceramic. The details of the probes were given, showing the construction and location of the thermocouple elements. From these one finds that in neither probe was the thin-film construction done in an ideal fashion. In the metal probe, a constantan wire is brought to the surface of an aluminum alloy body through an insulated hole passing along the centerline of the body. A copper plating on the top of the body completes the circuit. Two thermocouples are formed -- one at the constantan wire/copper film junction, the other at the copper plate/aluminum body junction. In steady state, the temperatures at the two junctions are quite close, as their analysis showed. However, that is not necessarily so in the highly transient case involved in engine heat transfer, and in any case, a small difference of even several degrees will dramatically change the apparent heat flux deduced from the probe. A further critical problem with their probe is that the assumption of one-dimensional heat transfer essential in deducing the heat flux is certainly not satisfied. The two junctions are both located at the edges (or interfaces) of dissimilar materials. This is a highly questionable location for a probe of this type, as one ought to keep the junction as far away from the edges as possible. As a result, the question of which substrate properties to use to reduce the data obtained with these probes is open, and it casts doubt on the measured data. Similar problems exist with the ceramic probe. These two wires, nickel and iron, are brought to the surface, and 10 μm plating of nickel is deposited onto the surface. In this case only one junction was formed, at the iron wire/nickel plating interface. However, here again the question of one-dimensionality exists. Even though the junction is on the edges of the

iron wire, the properties used to deduce the heat flux were those of the silicon nitride which was not even adjoining the junction but was separated from it by a layer of an insulator. Finally, no mention is made of how the material properties were determined and whether temperature corrections were applied. As a result, we believe that the data cannot be considered reliable.

Another indication of the unusual results obtained by Furuhama and Enomoto using this probe is that the authors that heat flux to a wall of a given fixed temperature depends on the wall material. They have reported in (ref. C4) a higher heat flux to a wall made of silicon nitride than to one made of constantan, even though the wall temperatures were very close. There is no plausible physical explanation for the effect of the wall material alone on gas phase heat transfer (unless surface combustion is taking place and the wall materials exert different catalytic effects).

Several observations can also be made about the results of Woschni et al (ref. C12). Their measurements led them to deduce a new form of the Woschni heat transfer correlation in which the coefficient C_2 is temperature dependent:

$$h = 130 d^{-0.2} p^{0.8} T^{-0.53} \left(C_1 C_m + C_2 \frac{V_H T_1}{p_1 V_1} (p - p_o) \right)^{0.8} \qquad (2)$$

$$C_2 = 2.3 \cdot 10^{-5} (T_W - 600) + 0.005 \qquad T_W > 523 \text{ K} \qquad (3)$$

The theoretical foundation of equation (3) is that heat transfer from flames can increase when walls are hot, because the flames can approach the wall closer and the thermal boundary layer becomes thinner. The specific form of the correlation (3) was developed using global pressure data, and calibrating C_2 to satisfy a heat release constraint. This procedure is ambiguous since the temperatures of all surfaces in the combustion chamber are not known. Even more seriously, the procedure goes contrary to the theoretical foundation of the model, equation (3), as it is being used at all surfaces at all times between start of combustion and

EVO. Yet, in reality, the flame adjoins any given surface only a small fraction of that time and thus the presumed heat transfer augmentation cannot take place.

Woschni et al concluded that due to the effects discussed above, the heat transfer coefficient increased by up to a factor of five due to an increase of wall temperature from 650 K to 1020 K. But that has direct implications for the boundary layer thickness, δ. Since the heat transfer coefficient varies with $\delta^{-0.25}$ (Morel and Keribar, ref. A3), this implies that the thermal boundary layer would have to be thinner by a factor of 625 -- at all surfaces and at all crank angles. That is clearly not realistic.

Another observation can be made concerning the fast response thermocouple results presented by Woschni et al (ref. C12). These were taken in a set of measurements similar to those reported by the present investigators in an earlier section of this paper as Hot/Cold Experiments. The data presented showed clearly that as the temperature of the wall went up, the engine surface temperature swing magnitude was essentially unchanged. Woschni et al did not present the heat flux deduced from these temperature records. However, it is a simple matter to digitize this data and calculate the heat flux, and this was done here. The data analyzed were those from Woschni and Spindler (ref. C11), their Figure 5, and the results produced by our analysis of that data (with k = 20 W/mK and ρc = 3.0 MJ/m^3 K) are shown in Figures 33a and b. It can be seen that there is a higher instantaneous heat transfer rate at the measurement point when the wall temperature is high. And that is due to the higher slope of surface temperature rise. However, the period of high heat flux is brief and is immediately followed by a low period. The total heat flux is about the same, and that is consistent with the fact that the magnitude of the surface temperature swing was about the same. The data reduction procedure used by the present investigators to produce Figure 33 was of necessity incomplete in that it did not include the dependence of the product $k\rho c$ on temperature, but used fixed values instead. (This was done because the actual probe materials were not given in the paper.) For example, for iron

this product decreases with increasing temperature, and thus the same magnitude swing is associated with a lower heat flux at a high wall temperature than at a low temperature. Thus, if the product $k\rho c$ for their probe material followed the dependence on temperature of iron, the heat flux integrated near TDC measured by Woschni and Spindler could in fact have been lower at higher temperatures than at low temperatures!

A final comment that can be made is that the authors claim that the mean heat flux decreases with increasing wall temperature up to 500 K, reaches a minimum and then increases to about 1000 K. That goes contrary to the present findings of the Hot/Cold experiments and also contrary to current engine experience with many production engines where surface temperatures are over 600 K. The implied claim that engine heat rejection would be reduced by increasing cooling to keep the wall temperatures down to 500 K (440°F) is not supported by experience.

In conclusion it must be stated that the present results stand in contrast to the two recent studies of heat flux with increased wall temperatures. These studies raised questions about the behavior of heat transfer under elevated wall temperatures and suggested that some unusual phenomena take place. However, the present results do not suggest that kind of behavior and instead indicate that the heat transfer process can be described by the standard theory of convective boundary layer heat transfer.

X. EFFECT OF INSULATION ON SPECIFIC FUEL CONSUMPTION

The ultimate objective of insulating a diesel engine is to decrease its specific fuel consumption. Some of the controversy discussed in the previous section relates to the fact that in a number of engine experiments with the insulated engine no improvement was observed in specific fuel consumption and in some cases an increase was noted. A fuel consumption improvement would be expected to accompany reduced heat transfer, because more of the combustion generated heat would be converted into piston work in accord with the RHCE (retained heat conversion efficiency) discussed earlier (Section III). Since this improvement could be masked by changes in engine friction, one has to address the effects of heat transfer by concentrating first on the indicated specific fuel consumption (ISFC). In other words, one draws a control volume within the combustion chamber and integrates the individual terms of the energy equation, which are: piston work, heat transfer and difference between exhaust and intake enthalpy. Reducing the heat transfer, the remaining two terms will both be increased. Thus, if the heat transfer is reduced by insulation as the present data indicates, the piston work should increase.

In addition to this direct increase in useful work obtained in the cylinder, heat insulation provides increased exhaust gas temperatures (enthalpy) available to energy recovery devices such as turbocharger, power turbine or a Rankine cycle bottomer. These benefits have been discussed in detail in Morel et al (ref. A9). In addition there are benefits associated with the reduced cooling system power requirements, which can be substantial. The discussion below concentrates only on the direct in-cylinder power increase where some controversy exists, leaving aside all the other benefits which have all been understood and accepted.

One of the parameters measured in the present experiments was the in-cylinder pressure. By integration of the piston pressure-volume work one can obtain the mean effective pressure and from it the ISFC. This integration was carried out and comparisons were made of ISFC measured in the cooled metal engine and in the ceramic-coated engine. This is not a

straightforward nor is it a highly accurate process. One problem is related to the setting of intake and exhaust pressures simulating turbocharged engine operation. In order to limit the effect of slight differences in the set intake and exhaust pressures in the single cylinder engine between the cooled and insulated cases, the integration of pressure was limited to the 360°CA of the compression-expansion strokes. Other uncertainties include the measurement of the fuel rate (±2%), TDC location (±0.2°CA), engine speed, compression ratio, and pressure transducer accuracy. These all have to be kept in perspective when analyzing and searching for the moderate improvement in ISFC predicted by ITI's flow-based heat transfer methodology, as discussed below.

The ISFC (360°CA) results are presented in a set of figures which compares the actual data from the cooled metal engine and the insulated engine, and a set which compares the predictions for the two engines at the test points which were run. The experimental data shown in Figures 34a-d exhibit a scatter on the order of ±5%. Within this scatter one cannot discern any consistent differences in ISFC between the two engines.

The predicted simulation results shown in Figure 35 display very little scatter as would be expected. In fact any scatter seen in the figure is most likely due to variations in the pressure differences across the engine which are input to the simulation. These were taken from the experimental data sheets, as was the fuel rate and engine speed, and thus the plotted points each represent a simulation of one experimental data point. The simulations predict a consistent decrease in ISFC, due to the specific ceramic insulation package installed in the engine, on the order of 3% reduction over the entire range of data. This predicted decrease is less than the scatter in the experimental data seen in Figure 34, and this partly explains the fact that no improvements in ISFC could be discerned in the experimental results.

Discussion. Experimental results presented in this report show a consistent and significant decrease in peak heat flux for the insulated engine, on the order of 40%, which is well beyond the uncertainty band of

the measurements. As shown above, analysis of the ISFC of the metallic and insulated engines, based on the measured pressure data, did not confirm the expected reduction in ISFC for the insulated engine. On the whole, the results indicated about equal ISFC although it must pointed out that the effect was difficult to determine because the data scatter was greater than the sought after effect. Nevertheless, this result, as best as can be interpreted, is inconsistent with the reduced heat transfer levels measured in the insulated engine.

The question of heat transfer and thermal efficiency of insulated engines has become very controversial in the last two years due largely to the findings of Woschni and Furuhama (refs. C4, C5, C11 and C12), who maintain that peak heat flux actually increases with increased surface temperature and that, therefore, no ISFC improvement but rather a degradation should be expected. The ITI heat flux results, which we believe are the most comprehensive and detailed heat flux data published to date for metallic and insulated diesel engines, are in clear opposition to the Woschni and Furuhama data, and ITI has in several technical forums as well as in the previous sections of the report offered critiques of the methods and results employed by both Woschni and Furuhama (refs. A17 and A18). Nevertheless, the lack of improvement in ISFC, which should have accompanied the reduced heat transfer levels observed, remains an unresolved technical issue which prevents a complete closure on the validation of the heat transfer methodology developed in the program as well as a complete understanding of LHR engine performance.

The work carried out under this contract was originally undertaken with the belief that insulation would have a significant impact on heat transfer but that combustion would be largely unaffected. Therefore, reductions in heat transfer through insulation would translate, it was believed, into corresponding reductions in indicated specific fuel consumption (ISFC). From the recent literature (refs. C14, C15, C16), it is beginning to be apparent that combustion is in fact modified in insulated engines, impacting the thermal efficiency (ISFC) in a negative manner.

Based on our analysis of the data and experimental procedures employed in our work we believe that the failure to measure improved ISFC in the experimental program which has been carried out to date is due to a number of factors, acting either alone or more likely in combination. Among these factors are included:

(1) changes in the injection process, i.e., spray penetration, atomization and mixing due to the higher temperature cylinder gases;

(2) changes in combustion and heat release due to variation in injection, ignition delay, air entrainment and utilization, and the resulting flame propagation;

(3) basic inaccuracies in the pressure and fuel flow measurements with possible systematic shift in the former occurring under high temperature, insulated conditions.

Since the in-cylinder thermal efficiency improvement of LHR engines is one of the incentives for the extensive government-funded and industrial R&D in this area, further work should be carried out toward resolution of the paradox existing between the heat flux and ISFC data that have been measured during this program. Consequently, it seems essential that a careful experimental/analytical program be carried out in which performance, heat transfer, combustion data would be obtained and analyzed in a baseline metallic and insulated diesel engine. This should be supplemented by computational fluid dynamic analysis of boundary layer heat transfer at surfaces with interacting flame propagation in order to understand whether flame interactions need be included with the physical phenomena incorporated in a detailed thermal analysis methodology for LHR engines.

The objective of this additional work should be to resolve the central questions concerning the effect of insulation on ISFC and related performance parameters. Specifically, the indicated performance (IMEP, ISFC) of an insulated versus a metallic baseline engine should be explored in detail by means of a carefully planned and executed experimental/analytical program which would provide diagnostics on

combustion, heat transfer, and emissions, as well as cylinder pressure versus crank angle and measurement of flows, temperatures and pressures. The test engine should allow for reoptimization of the fuel injection system (timing and pressure) in order to include variation of the combustion system as a means of achieving an understanding of the factors which contribute to ISFC in insulated engines.

XI. CONCLUSIONS AND RECOMMENDATIONS

1. A comprehensive methodology has been developed for the thermal analysis of insulated engine concepts. Its cornerstones are new physically based models for gas-phase heat transfer (convection and radiation), which provide more accurate representation of the heat transfer process and allow evaluation of the effects of altered heat transfer on engine performance. The heat transfer models also supply accurate boundary conditions for finite element structural heat transfer calculations, for both steady-state and transient (thermal shock) analyses of engine structures.

2. The methodology was validated by detailed engine heat transfer experiments carried out in a cooled baseline single cylinder engine as well as in a ceramic-coated version of the same engine. The new heat transfer models predicted correctly the magnitudes and shapes of heat flux data at two different head locations, capturing accurately the differences between them under firing conditions.

3. The analysis has been applied to resolve key low heat rejection engine issues, including efficiency benefits due to insulation and due to exhaust heat recovery systems using several different insulation packages. Also, the adverse effect of liner insulation on thermal efficiency and component temperatures has been elucidated.

4. The insulated engine work showed that the heat flux was consistently decreased as the wall temperatures increased due to insulation. This finding contradicts some previous studies which have claimed that the trend is the opposite. The measured results agree well with the predictions of the present physically-based heat transfer models, indicating that the nature of the heat transfer process is unchanged by the increased wall temperatures.

5. Since the mean and peak heat flux were reduced by insulation, it may be expected that insulation will decrease indicated specific fuel consumption (ISFC).

6. The expected decrease in ISFC was difficult to ascertain due to data scatter, but it appeared that there was no change in ISFC with insulation. This is inconsistent with the observed reduction in heat transfer. Among possible explanations are: changes in the injection process, changes in combustion and heat release and basic inaccuracies in measurements of cylinder pressure and fuel flow rates.

7. The above paradox between heat flux and ISFC calls for further work aimed at its resolution. This will require a careful experimental/ analytical program incorporating heat flux measurements, accurate ISFC determination and combustion analysis.

XII. REFERENCES

A. ITI Publications Reporting Contract Work

A1. Morel, T., Blumberg, P. N., Fort, E. F. and Keribar, R., "Methods for Heat Transfer and Temperature Field Analysis of the Insulated Diesel", Phase I Progress Report, DOE/NASA/0342-1, NASA CR-17483, August 1984.

A2. Morel, T., Keribar, R., Blumberg, P. N. and Fort, E. F., "Methods for the Integrated Analysis of Heat Transfer, Component Temperatures and Performance in Insulated Engines," Proceedings of Contractors Coordination Meeting, Dearborn, Michigan, November, 1984, SAE-P-155.

A3. Morel, T. and Keribar, R., "A Model for Predicting Spatially and Time Resolved Convective Heat Transfer in Bowl-in-Piston Combustion Chambers," SAE Paper 850204, SAE Congress, Detroit, 1985.

A4. Morel, T., Keribar, R. and Blumberg, P. N., "Cyclical Thermal Phenomena in Engine Combustion Chamber Surfaces," SAE Paper 850360, SAE Congress, Detroit, 1985.

A5. Morel, T., Fort, E. F. and Blumberg, P. N., "Effect of Insulation Strategy and Design Parameters on Diesel Engine Heat Rejection and Performance," SAE Paper 850506, SAE Congress, Detroit, 1985.

A6. Morel, T., Keribar, R., Fort, E. F. and Blumberg, P. N., "Methods for Heat Transfer and Temperature Field Analysis of the Insulated Diesel", Phase II Report, DOE/NASA/0342-2, NASA CR-175072, September 1985.

A7. Morel, T., Keribar, R., Blumberg, P. N. and Fort, E. F., "Methods for Thermal Analysis of Insulated Diesel Engines," Proceedings of Contractors Coordination Meeting, Dearborn, Michigan, November, 1985.

A8. Morel, T. and Keribar, R., "Heat Radiation in D.I. Diesel Engines", SAE Paper 860445, SAE Congress, Detroit, 1986.

A9. Morel, T., Keribar, R., Blumberg, P. N. and Fort, E. F., "Examination of Key Issues in Low Heat Rejection Engine Concepts," SAE Paper 860316, SAE Congress, Detroit, 1986.

A10. Keribar, R. and Morel, T., "Methods for Thermo-Mechanical Analysis of Thermal Barrier Coatings in Diesel Engines," Proceedings of 13th International Conference on Metallurgical Coatings, April 1986, San Diego, CA.

A11. Keribar, R., Morel, T. and Blumberg, P. N., "Coupled Methodology for Thermal Shock Calculations in I.C. Engines," Proceedings of XXI FISITA Congress, Belgrade, Yugoslavia, June 1986.

A12. Morel, T., Keribar, R., Wahiduzzaman, S. and Fort, E. F., "Analytical and Experimental Study of Heat Transfer in Diesel Engines," Proceedings of Contractors Coordination Meeting, Dearborn, Michigan, October 1986.

A13. Keribar, R. and Morel, T., "Thermal Shock Calculations in IC Engines," SAE Paper 870162, SAE Congress, Detroit, 1987.

A14. Wahiduzzaman, S., Morel, T., Timar, J. and DeWitt, D. P., "Experimental and Analytical Study of Heat Radiation in a Diesel Engine," SAE Paper 870571, SAE Congress, Detroit, 1987.

A15. Morel, T., Wahiduzzaman, S., Tree, D. L. and DeWitt, D. P., "Effect of Speed, Load and Location on Heat Transfer in a Diesel Engine--Measurements and Predictions," SAE Paper 870154, SAE Congress, Detroit, 1987.

A16. Morel, T., Wahiduzzaman, S. and Fort, E. F., "LHR Engine Design Methodology: Heat Transfer Measurements in an Insulated Diesel," 25th ATD-CCM, Dearborn, Michigan, October, 1987.

A17. Morel, T., Discussion of paper by Woschni and Spindler, Journal of Engineering for Gas Turbines and Power, Vol. 110, Number 3, July 1988, pp. 491-492.

A18. Morel, T., Wahiduzzaman, S. and Fort, E. F., "Heat Transfer Experiments in an Insulated Diesel," SAE Paper 880186, SAE Congress, 1988.

B. Purdue University, NASA and NBS Publications Based on Contract Work

B1. Ferguson, C. R., Warner, C. F., Gottschlitch, R. N. and Wahiduzzaman, S., "Using Optical Proximiter to Phase Cylinder Pressure to Crank Shaft Position", SAE Transactions Vol. 96, Paper No. 870478, 1987.

B2. Ferguson, C. R., Tree, D. R., DeWitt, D. P. and Wahiduzzaman, S., "Design, Calibration and Error Analysis of Instrumentation of Heat Transfer Measurements in Internal Combustion Engine," in Developments in Experimental Techniques in Heat Transfer and Combustion, Ed. R. O. Warrington Jr., M. M. Chen, J. D. Felske and W. L. Groshandler. ASME Publication No. HTD-Vol. 71, 1987.

B3. Kim, W. S. and Barrows, R. F., "Prototype Thin Film Thermocouple/Heat Flux Sensor for a Ceramic-Insulated Diesel Engine", NASA Report No. TM-100798, 1988.

B4. Tree, D. R., DeWitt, D. P., Barrows, R. F. and Kim, W., "Development of a Total Heat Flux Gage for Partially Insulated Internal Combustion Engines", 1988 Central States Meeting of the Combustion Institute, Indianapolis, IN, May 2-3, 1988.

B5. Tree, D. R., "Development of a Heat Flux Gauge for a Partially Insulated Internal Combustion Engine," Purdue University M.S.M.E. Thesis, 1988.

B6. Kreider, K. G. and Yust, M., "Thin Film Thermocouples for Heat Engines," to be published, 1988.

B7. Gottschlitch, R. N., "A Numerical and Experimental Technique for Locating the Top Dead Center Position of an Engine Piston," Purdue University M.S.M.E. Thesis, December, 1984.

B8. Rodriguez, G. P., "Access Port and Heat Flux Sensor Development for Measurement of Total Heat Flux from the Combustion Chamber of a Cummins Single Cylinder Research Engine," M.S.M.E. Project Report, Purdue University, 1986.

B9. Timar, J., "Two Color Pyrometry Applied to Diesel Combustion," M.S.M.E. Thesis, Purdue University, 1987.

C. General References

C1. Annand, W. D., "Heat Transfer in the Cylinders of Reciprocating Internal Combustion Engines," Proc. Instn. Mech. Engnrs., Vol. 177, No. 36, p. 973, 1963.

C2. Woschni, G., "A Universally Applicable Equation for the Instantaneous Heat Transfer Coefficient in the Internal Combustion Engine," SAE Transactions, Vol. 76, p. 3065, 1967.

C3. Eckert, E. R. G. and Drake, R. M., "Analysis of Heat and Mass Transfer," McGraw-Hill, p. 783, 1972.

C4. Enomoto, Y. and Furuhama, S., "Heat Transfer into Ceramic Combustion Chamber Wall of Internal Combustion Engines," SAE Paper 861276, 1986.

C5. Furuhama, S. and Enomoto, Y., "Heat Transfer into Ceramic Combustion Wall of Internal Combustion Engines," SAE Paper 870153, 1987.

C6. Havstad, P. H. Garwin, I. J. and Wade, W. R., "A Ceramic Insert Uncooled Diesel Engine," SAE Paper 860447, SAE Congress, Detroit, 1986.

C7. Hoag, K., "Measurement and Analysis of the Effect of Wall Temperature on Instantaneous Heat Flux," SAE Paper 860312, 1986.

C8. Huang, J. C. and Borman, G. L., "Measurements of Instantaneous Heat Flux to Metal and Ceramic Surfaces in a Diesel Engine," SAE Paper 870155, 1987.

C9. Taylor, J. R., An Introduction to Error Analysis, University Science Book, Oxford University Press, 1982.

C10. Wahiduzzaman, S., "A Study of Heat Transfer Due to a Decaying Swirling Flow in a Cylinder with Closed Ends," PhD Thesis, Purdue University, West Lafayette, Indiana, 1985.

C11. Woschni, G. and Spindler, W., "Heat Transfer with Insulated Combustion Chamber Walls and Its Influence on the Performance of Diesel Engines," ASME Journal of Engineering for Gas Turbines and Power, Vol. 110,No. 3, pp. 482-5-2, July 1988.

C12. Woschni, G., Spindler, W. and Kolesa, K., "Heat Insulation of Combustion Chamber Walls -- A Measure to Decrease the Fuel Consumption of I.C. Engines?," SAE Paper 870339, 1987.

C13. Taylor, R. E., Groot, H. and Larimore, J., "Thermal Properties of a Ceramic," Thermophysical Properties Laboratory, Purdue U., West Lafayette, IN, Report no. TPRL 597, 597A, 1987.

C14. "The Adiabatic Engine: Global Developments," SAE Publication SP-650, Detroit, Michigan, 1986.

C15. "Adiabatic Engines and Systems," SAE Publication SP-700, Detroit, Michigan, 1987.

C16. "Recent Developments in the Adiabatic Engine," SAE Publication SP-738, Detroit, Michigan, 1988.

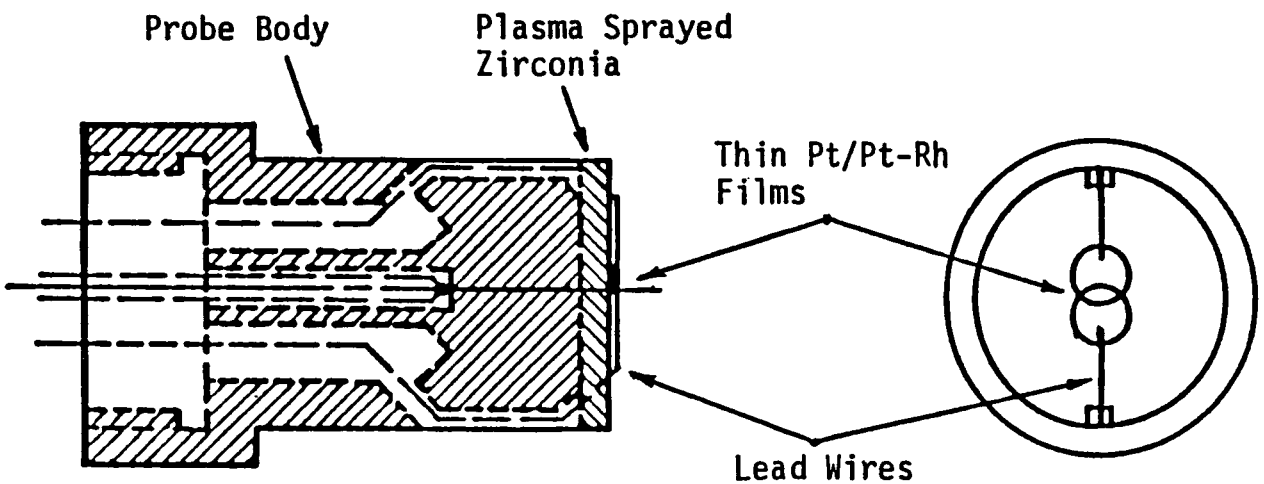

Figure 1. Schematic section of ceramic heat flux probe employing thin Pt-Pt/Rd films deposited on plasma sprayed zirconia.

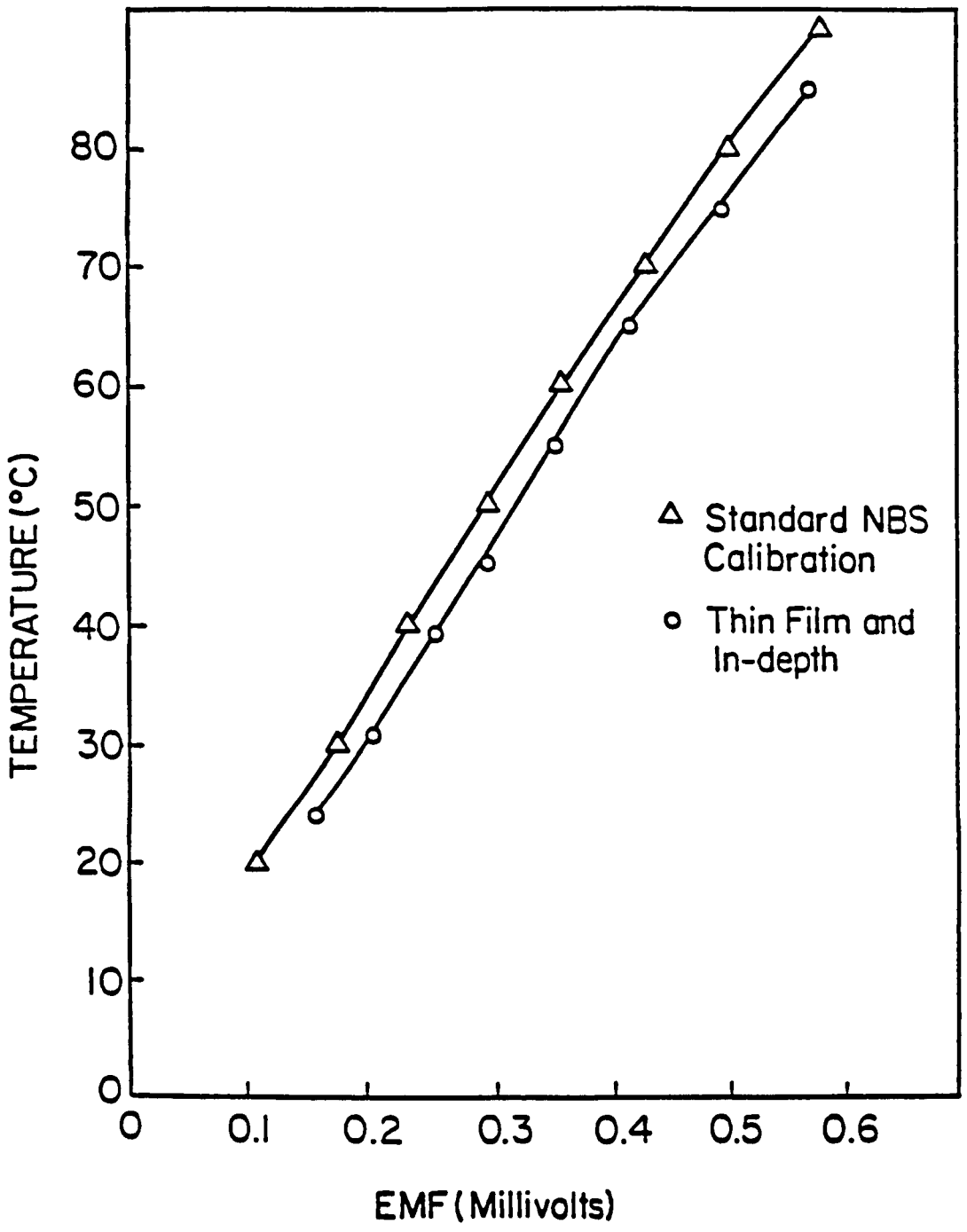

Figure 2. Calibration of thin-film thermocouple and of in-depth thermocouple of the ceramic heat flux probe.

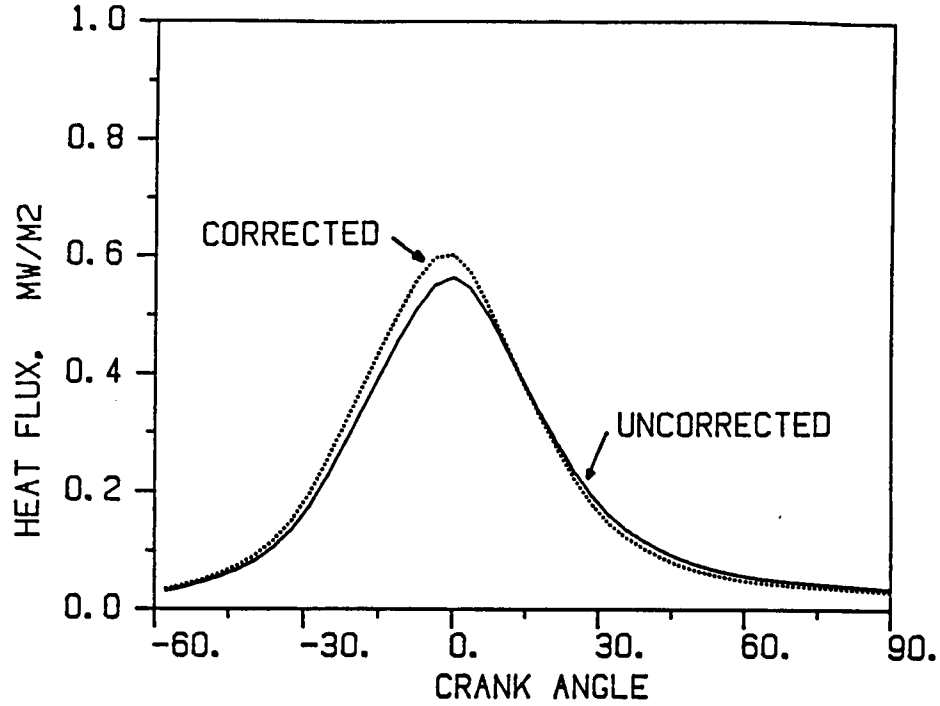

Figure 3. Heat flux in motoring engine, 1300 rpm, bowl location, probe 3. ——— uncorrected, ----- corrected.

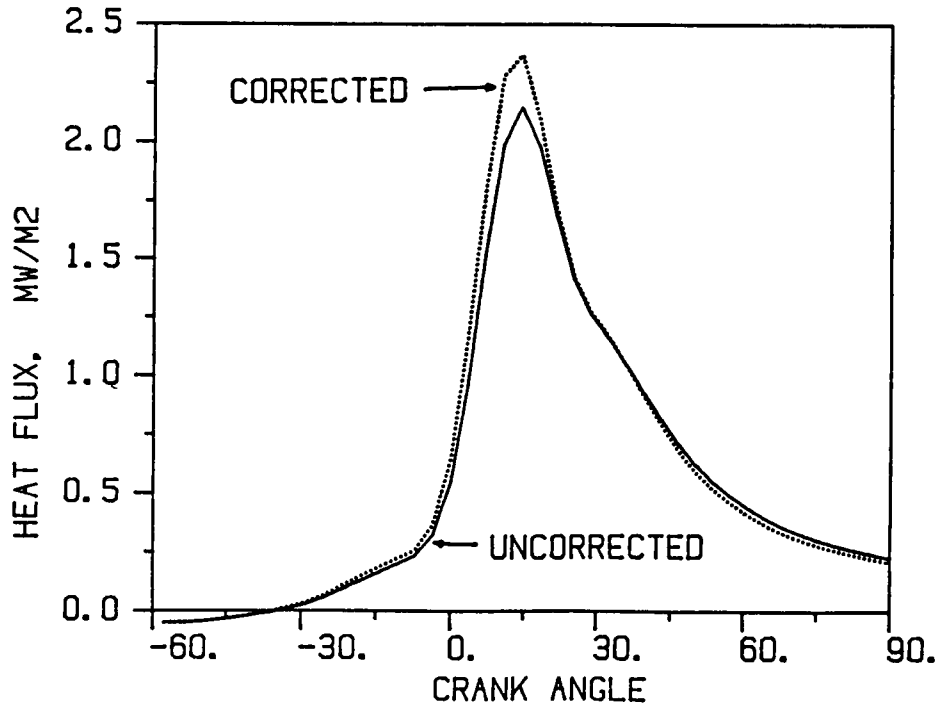

Figure 4. Heat flux in firing engine, 1300 rpm, 35% load, bowl location, probe 3. ——— uncorrected, ----- corrected.

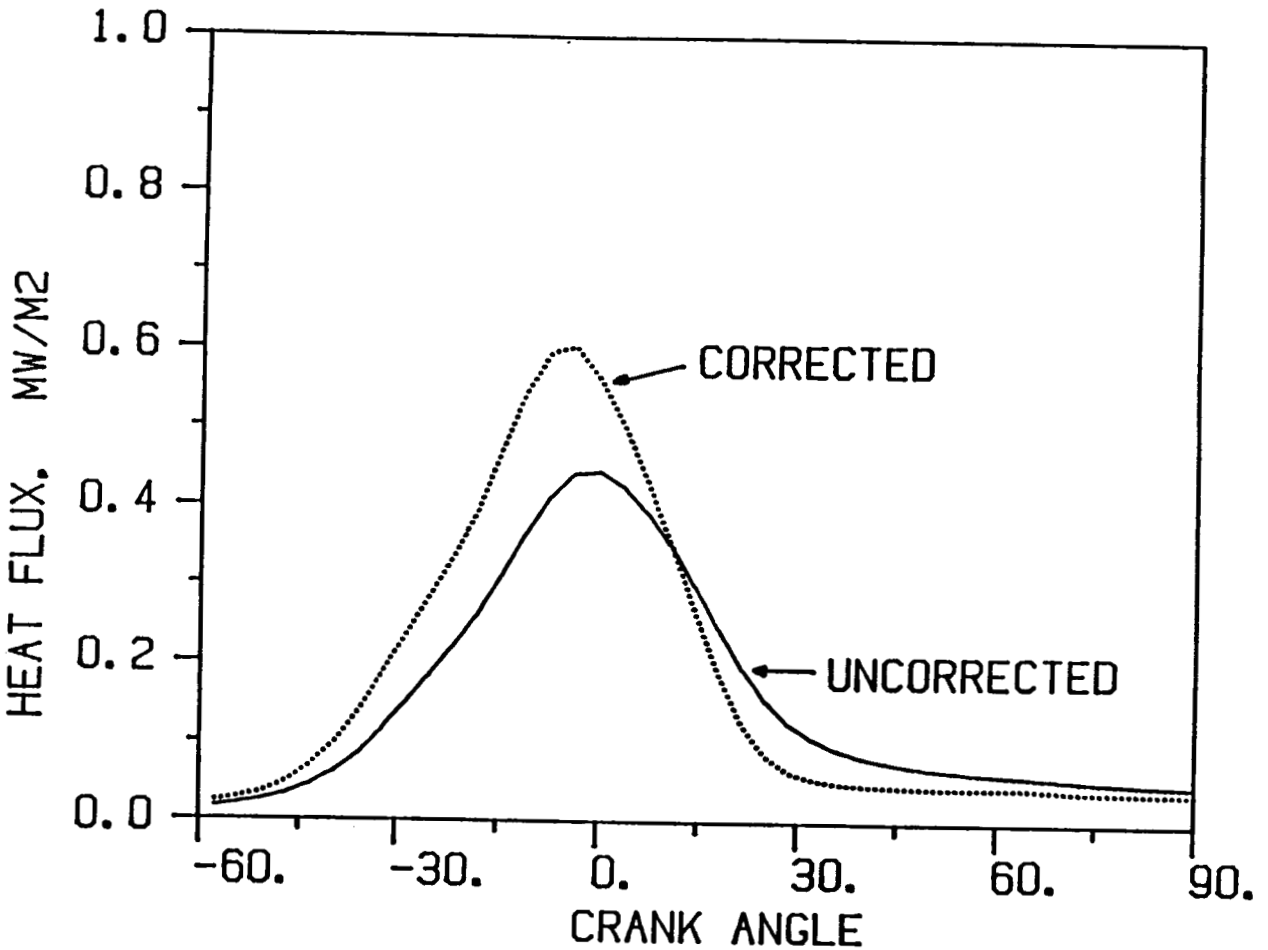

Figure 5. Heat flux in motoring engine, 1300 rpm, bowl location, probe 1. ——— uncorrected, ----- corrected.

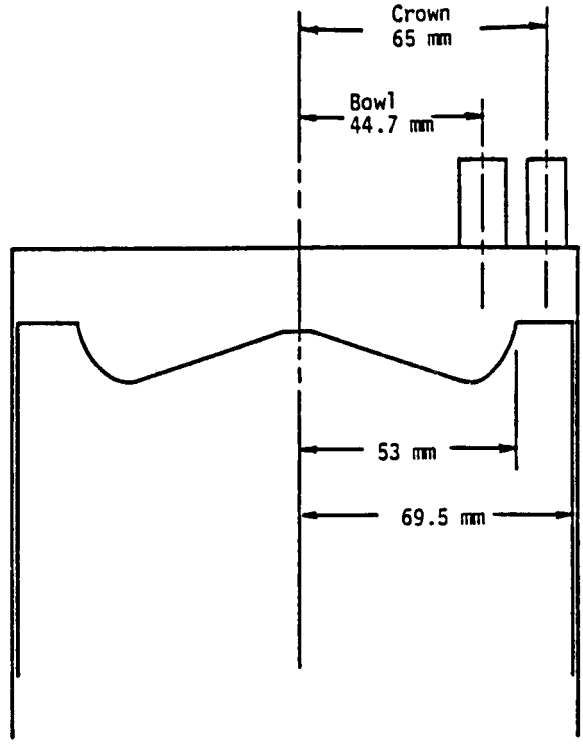

Figure 6. Piston bowl shape and probe locations.

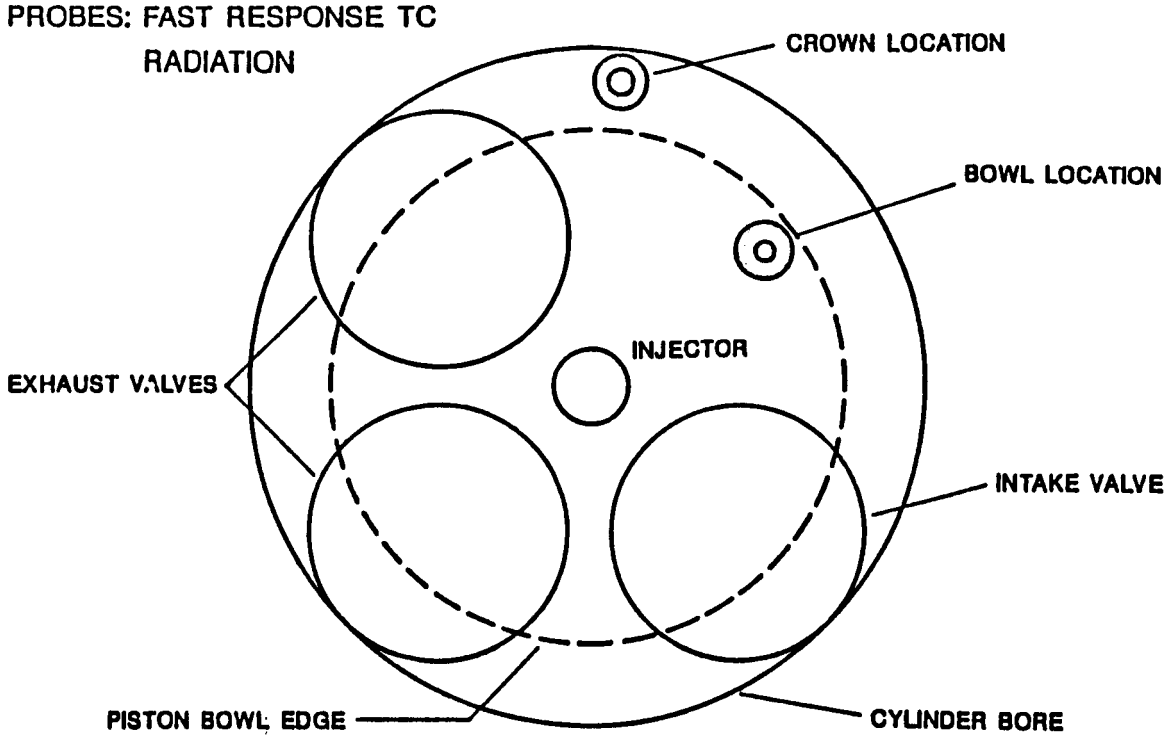

Figure 7. Section through engine head at the valve plane, showing probe locations.

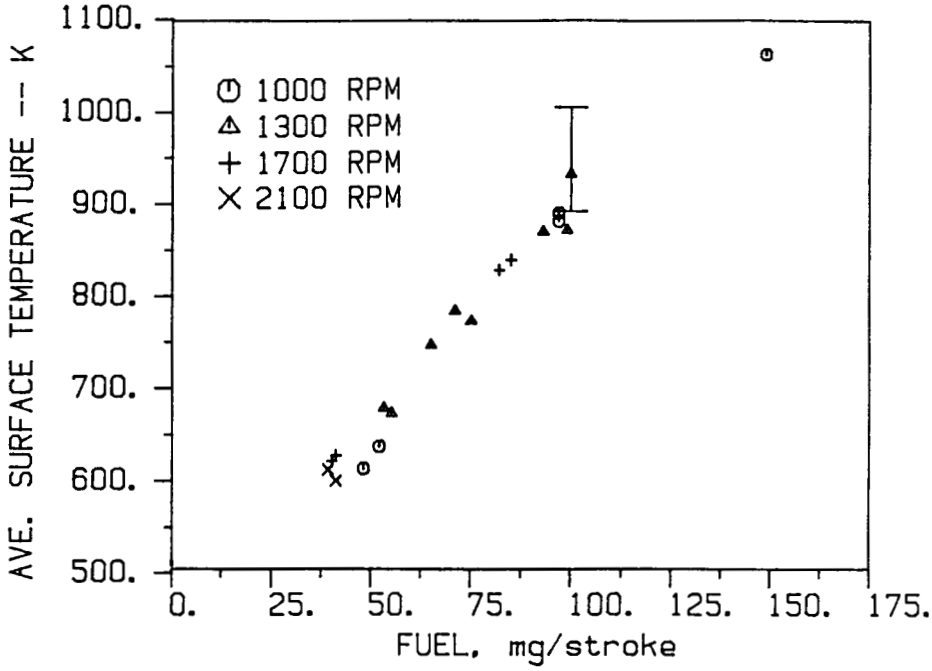

Figure 8a. Average surface temperature as a function of fueling rate (load) over speed range at bowl location. Bar indicates amplitude of cyclic temperature swings.

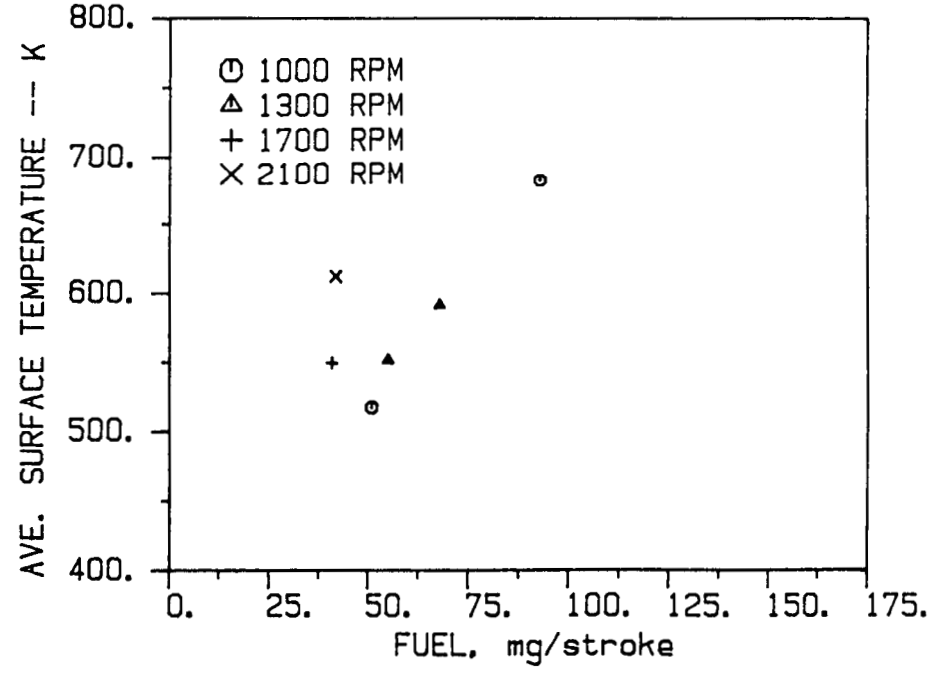

Figure 8b. Average surface temperature as a function of fueling rate (load) over speed range at crown location.

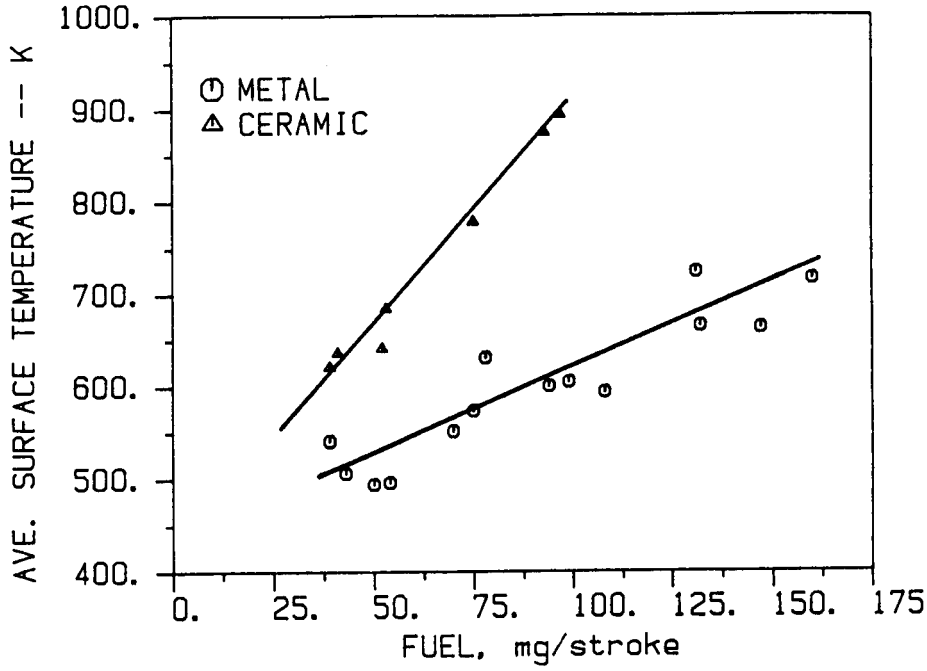

Figure 9a. Comparison of metal engine and ceramic-coated engine average surface temperature at bowl location.

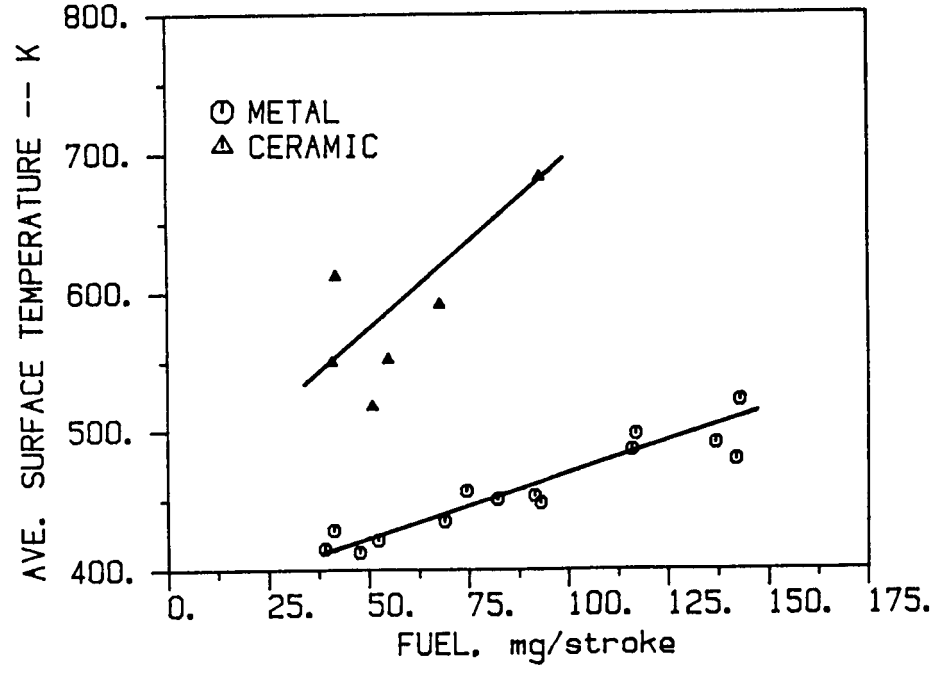

Figure 9b. Comparison of metal engine and ceramic-coated engine average surface temperature at crown location.

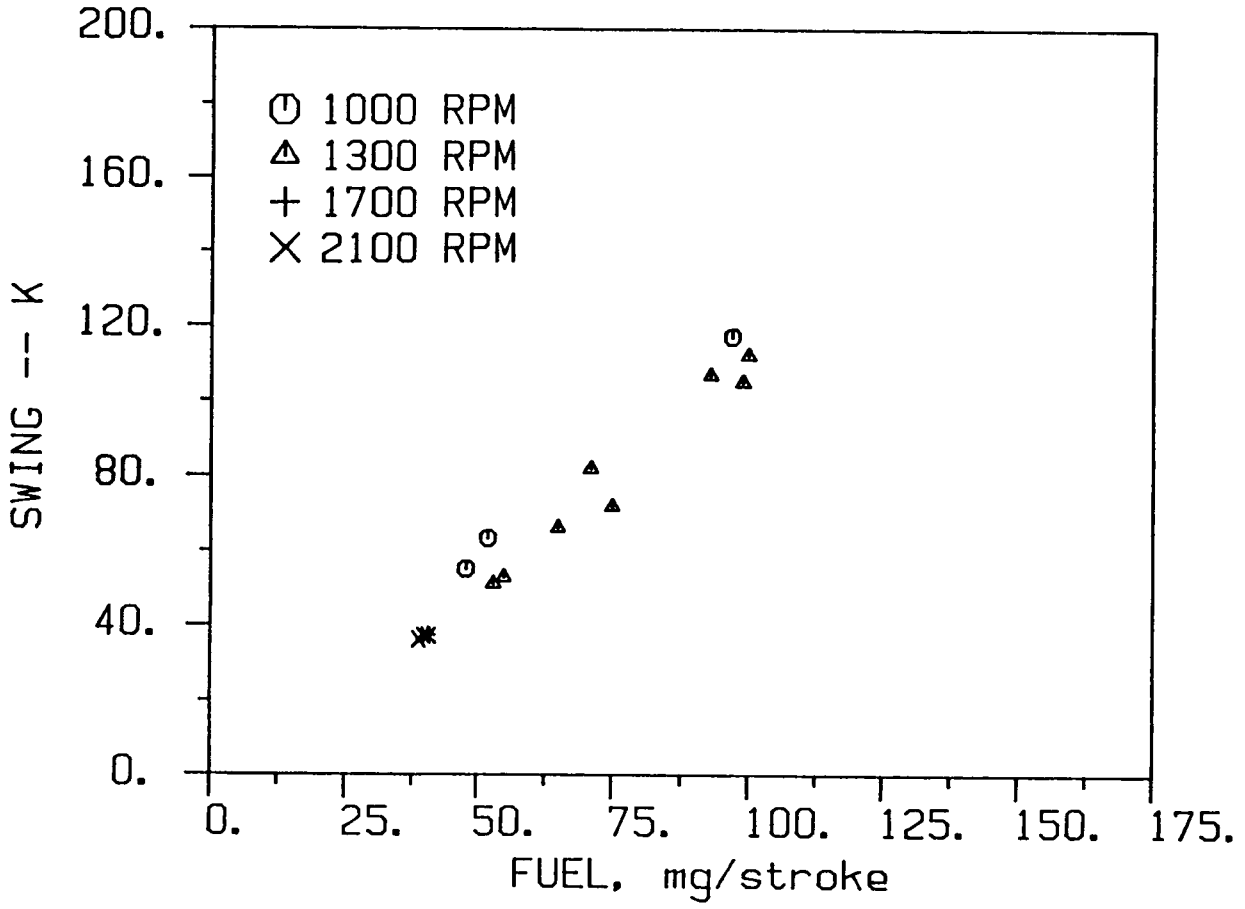

Figure 10. Surface temperature swing at bowl location obtained in the insulated engine using the NASA probes.

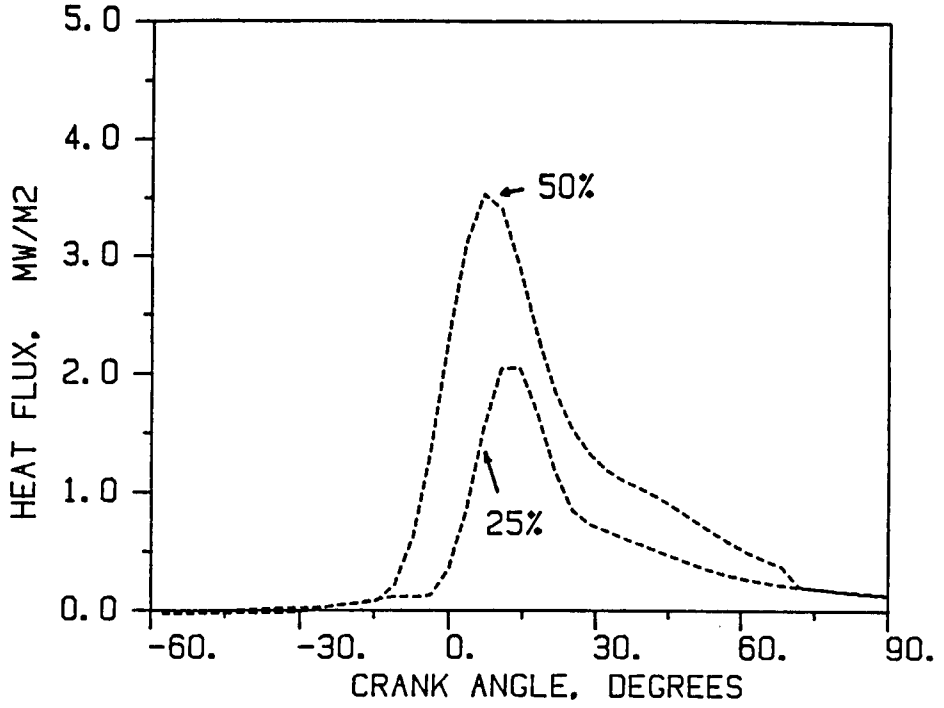

Figure 11a. Heat flux in ceramic engine measured at bowl location, 1000 rpm.

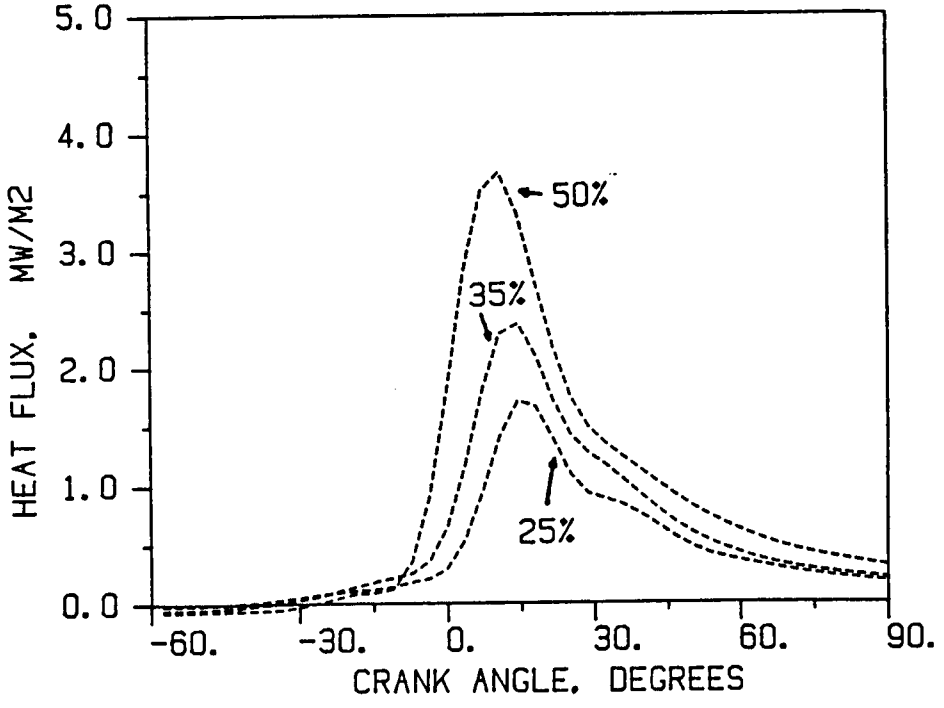

Figure 11b. Heat flux in ceramic engine measured at bowl location, 1300 rpm.

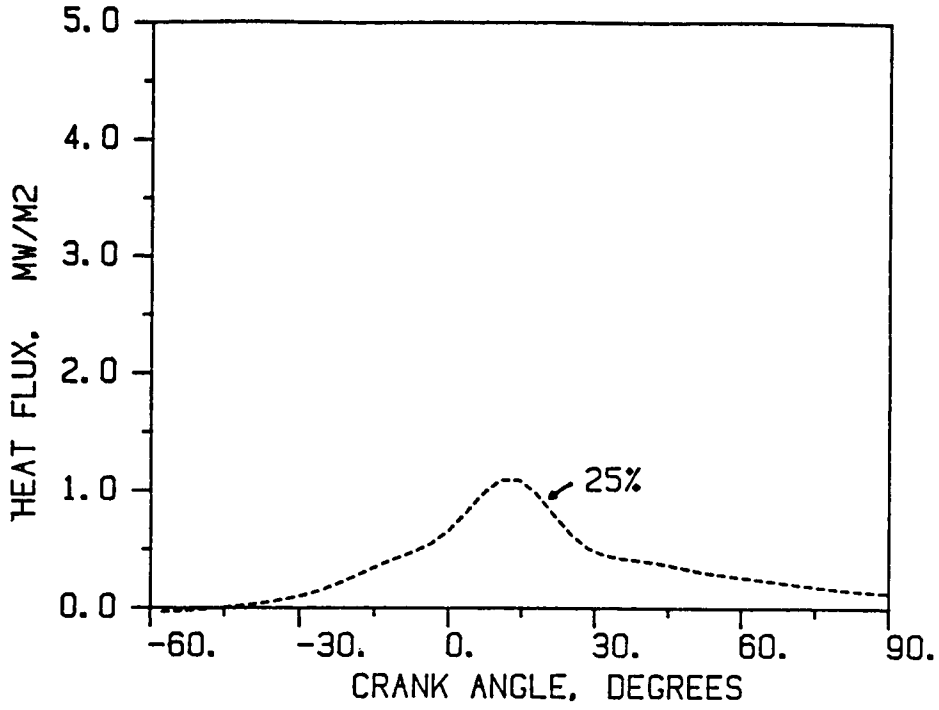

Figure 11c. Heat flux in ceramic engine measured at bowl location, 1700 rpm.

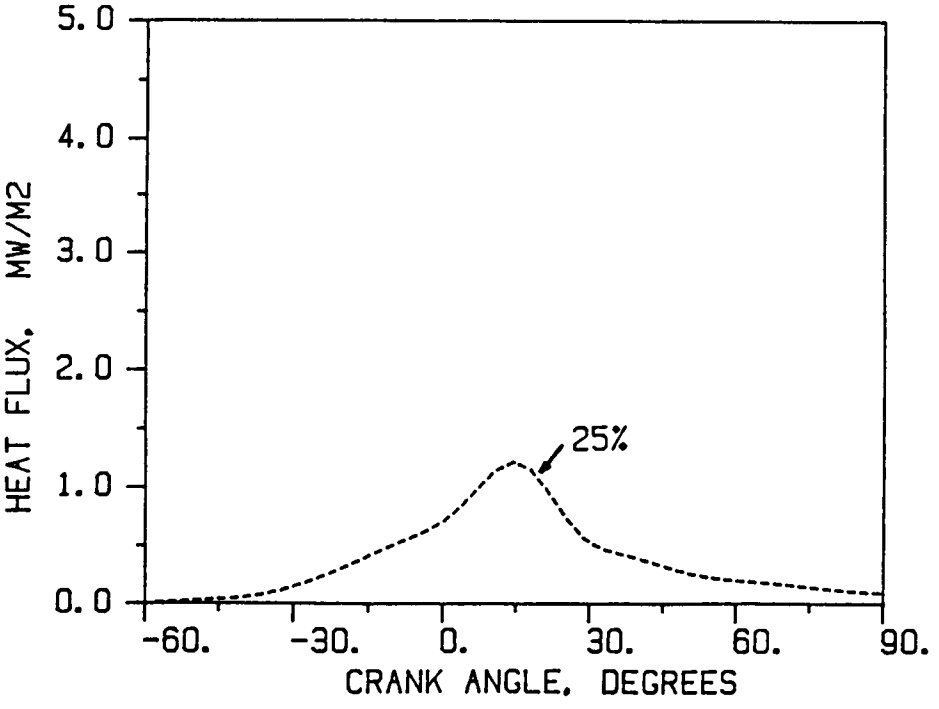

Figure 11d. Heat flux in ceramic engine measured at bowl location, 2100 rpm.

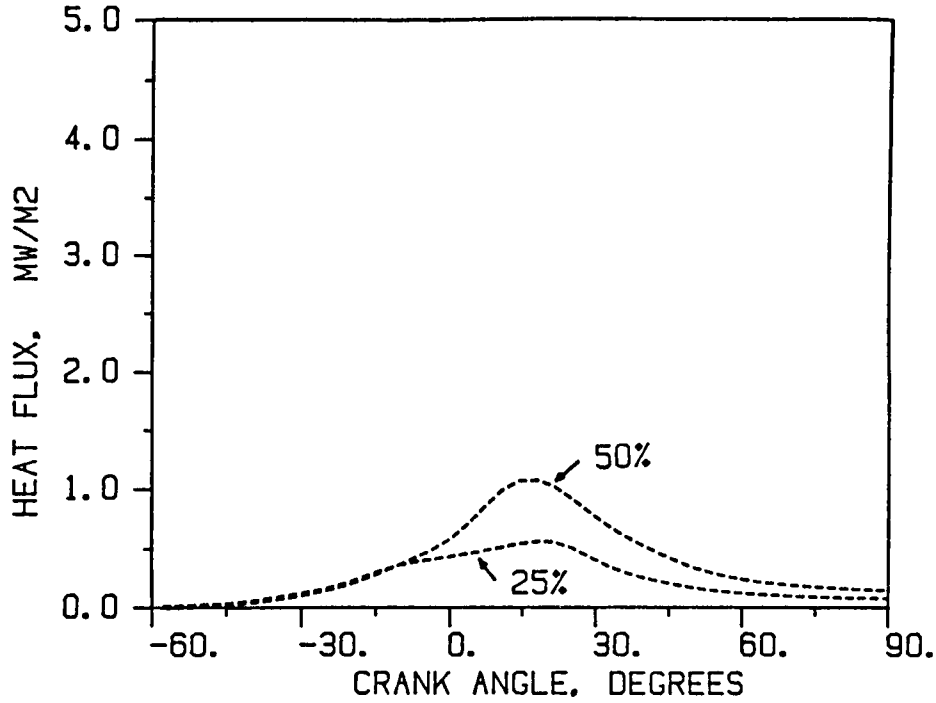

Figure 12a. Heat flux in ceramic engine measured at crown location, 1000 rpm.

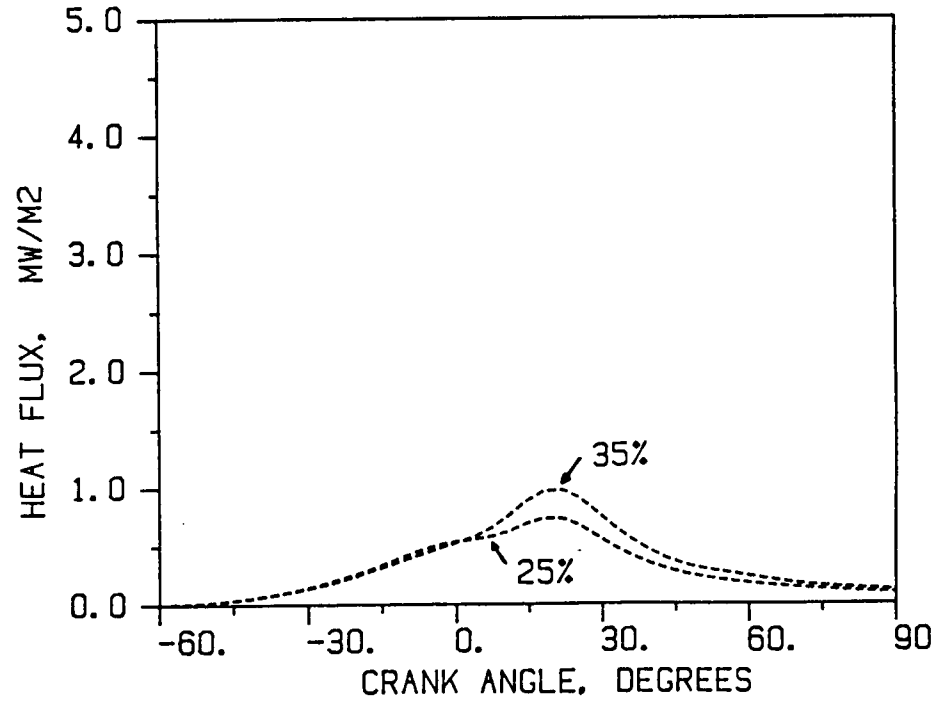

Figure 12b. Heat flux in ceramic engine measured at crown location, 1300 rpm.

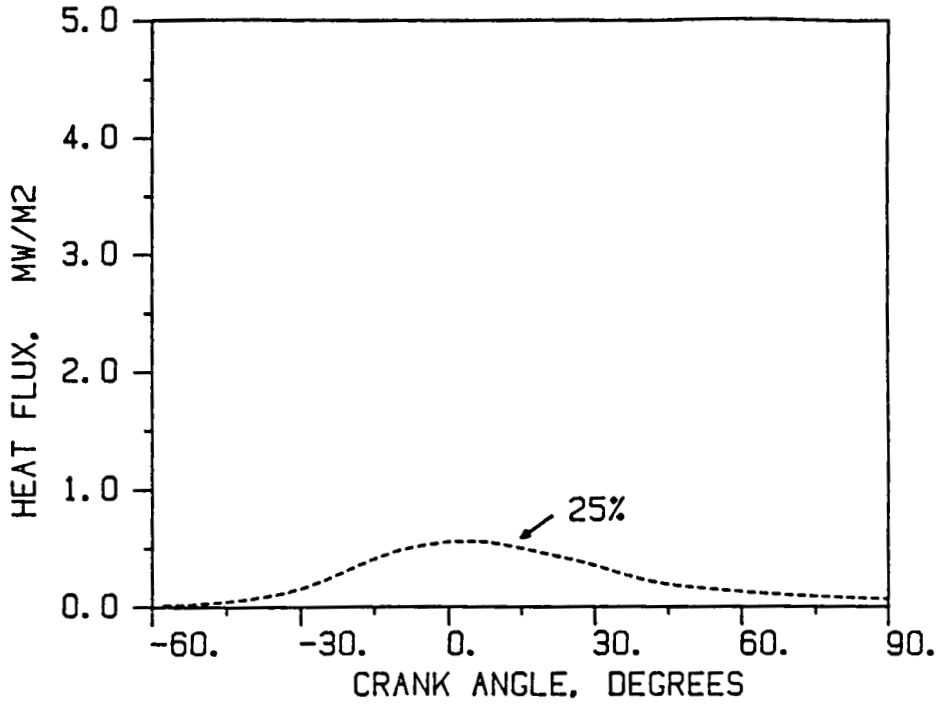

Figure 12c. Heat flux in ceramic engine measured at crown location, 1700 rpm.

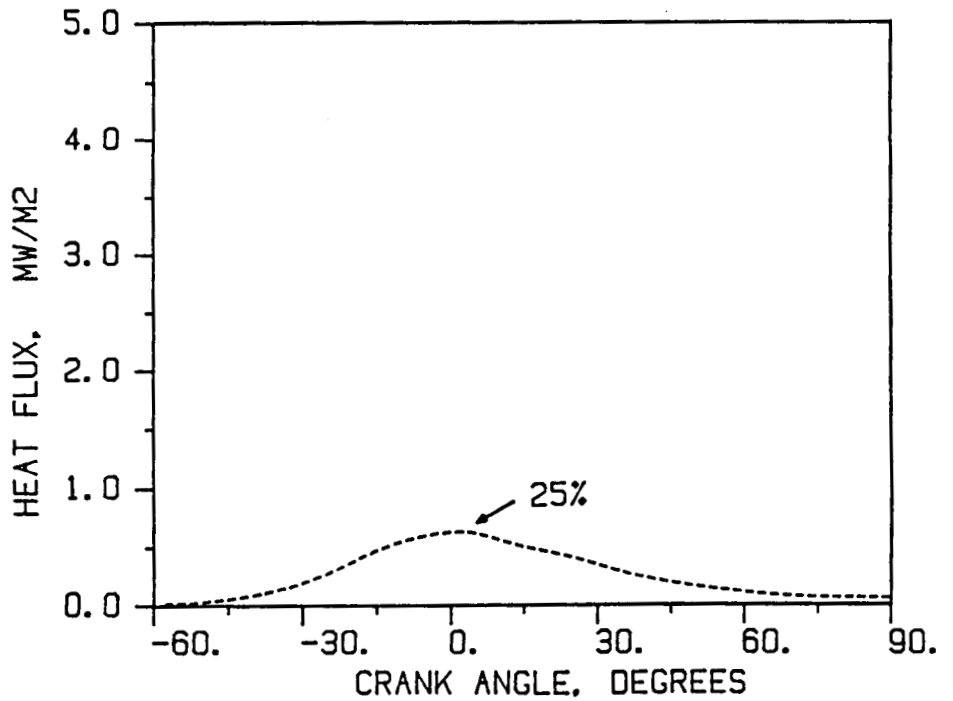

Figure 12d. Heat flux in ceramic engine measured at crown location, 2100 rpm.

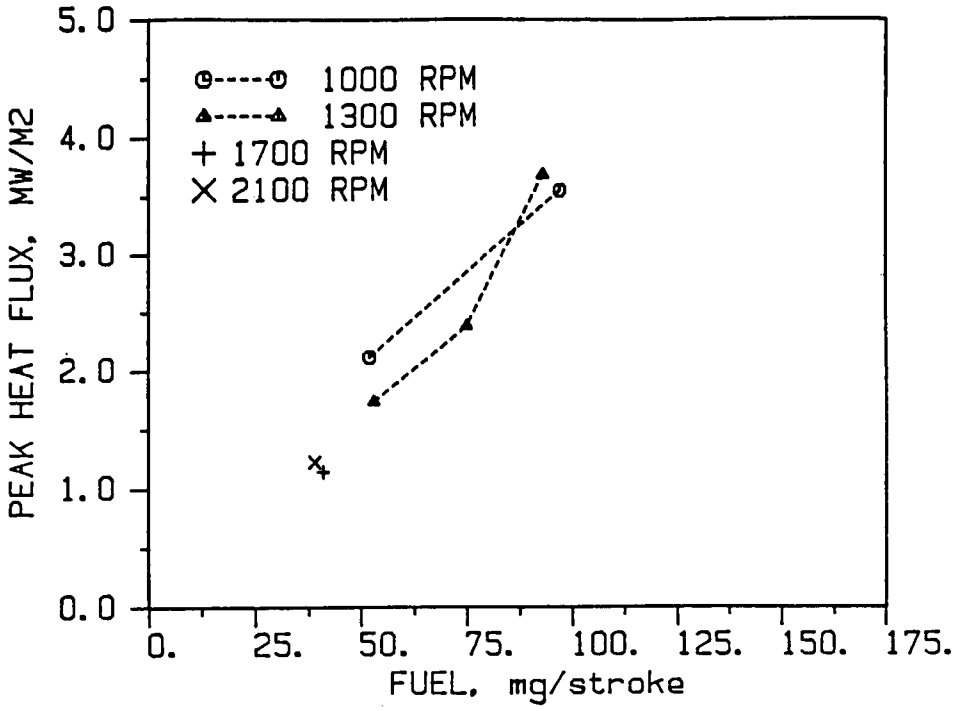

Figure 13a. Peak heat flux measured in the ceramic engine at bowl location.

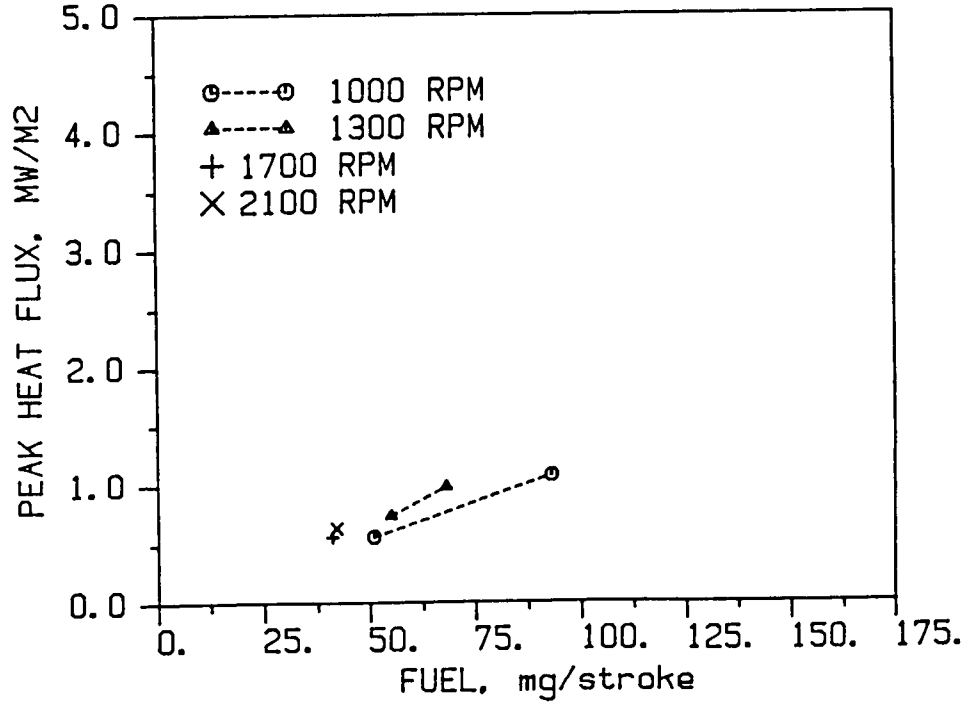

Figure 13b. Peak heat flux measured in the ceramic engine at crown location.

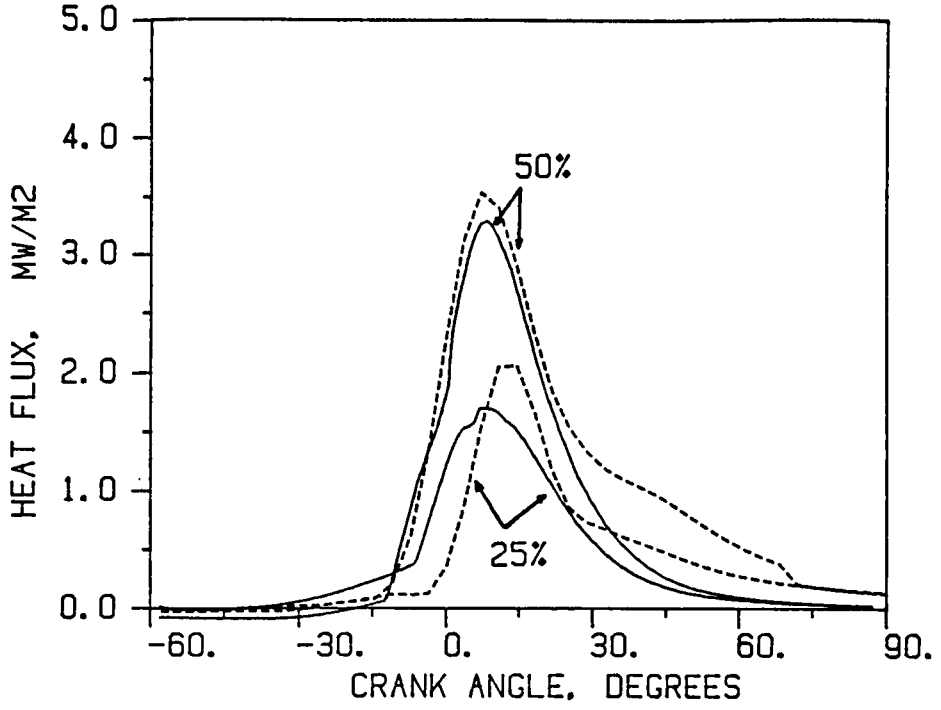

Figure 14a. Predicted and measured heat flux in ceramic engine, 1000 rpm, at bowl location. ——— predictions, ----- data.

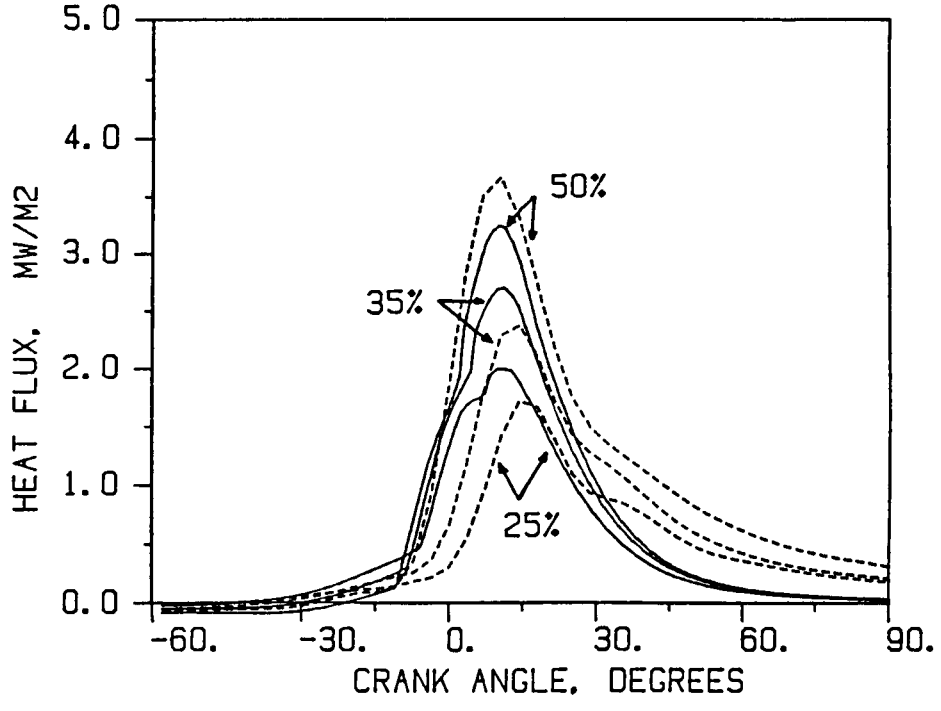

Figure 14b. Predicted and measured heat flux in ceramic engine, 1300 rpm, at bowl location. ——— predictions, ----- data.

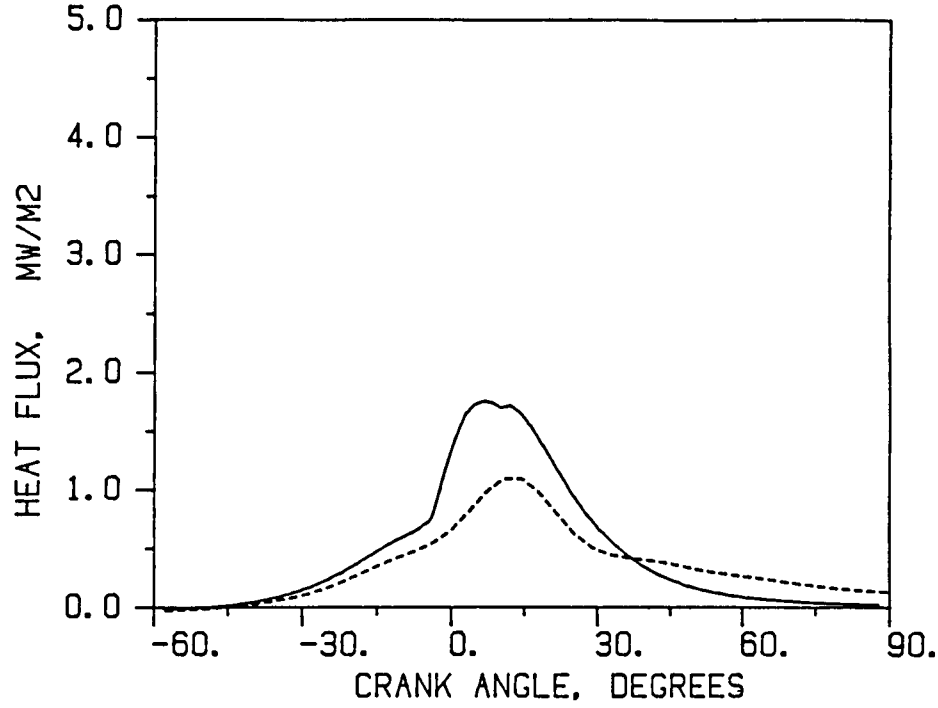

Figure 14c. Predicted and measured heat flux in ceramic engine, 1700 rpm, at bowl location. ——— predictions, ----- data.

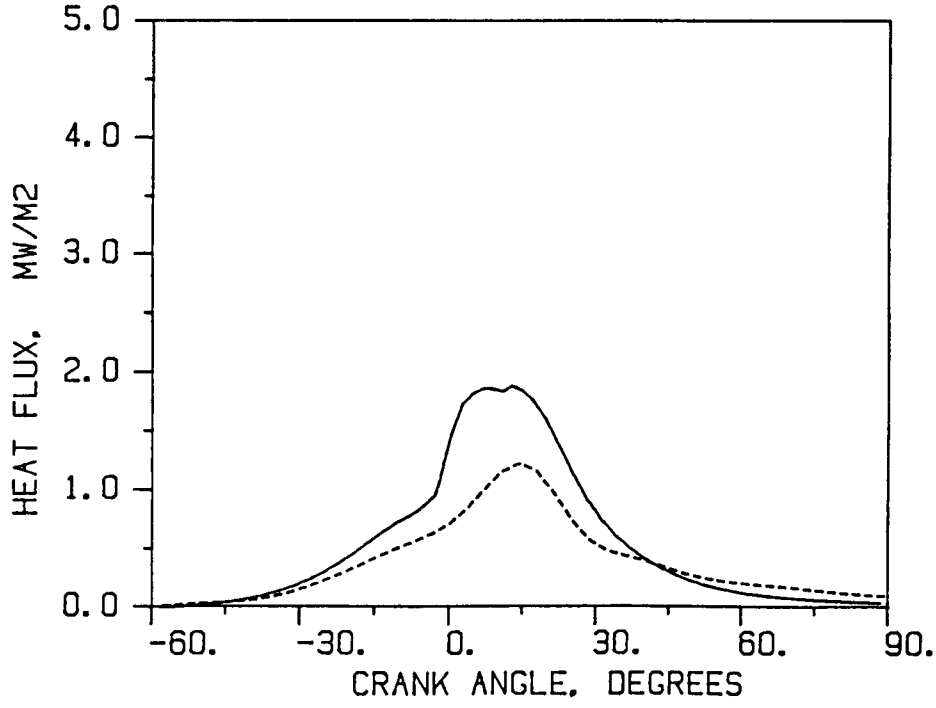

Figure 14d. Predicted and measured heat flux in ceramic engine, 2100 rpm, at bowl location. ——— predictions, ----- data.

C-2

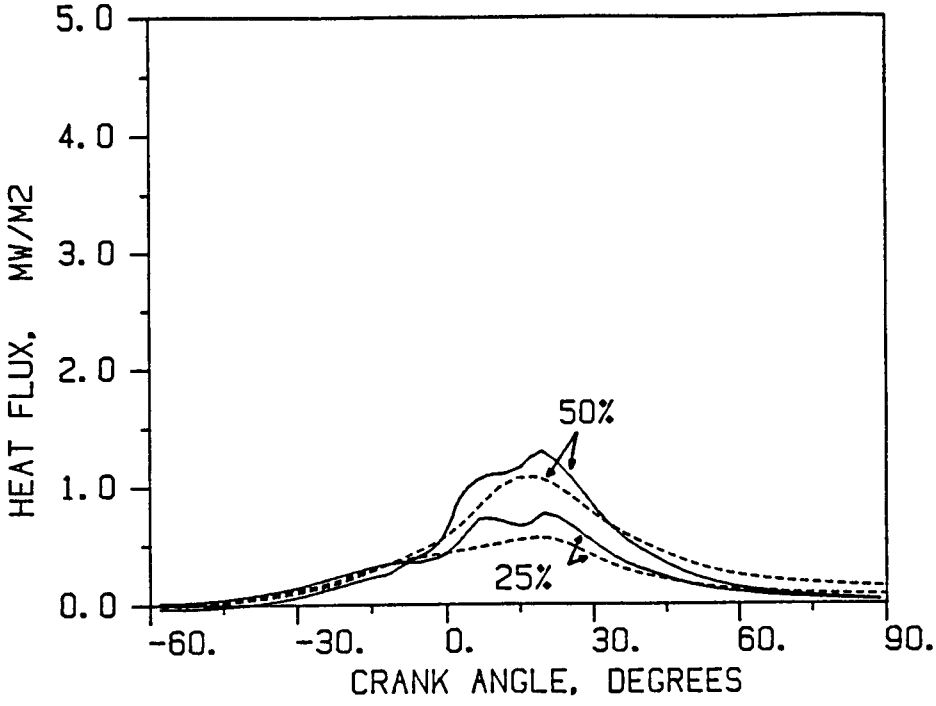

Figure 15a. Predicted and measured heat flux in ceramic engine, 1000 rpm, at crown location. ——— predictions, ----- data.

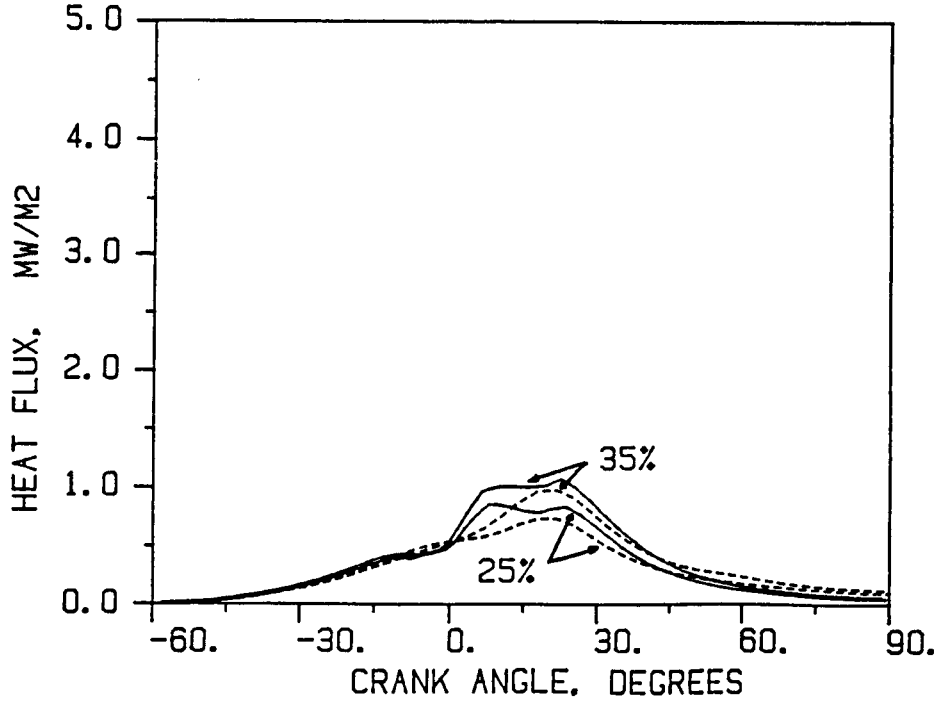

Figure 15b. Predicted and measured heat flux in ceramic engine, 1300 rpm, at crown location. ——— predictions, ----- data.

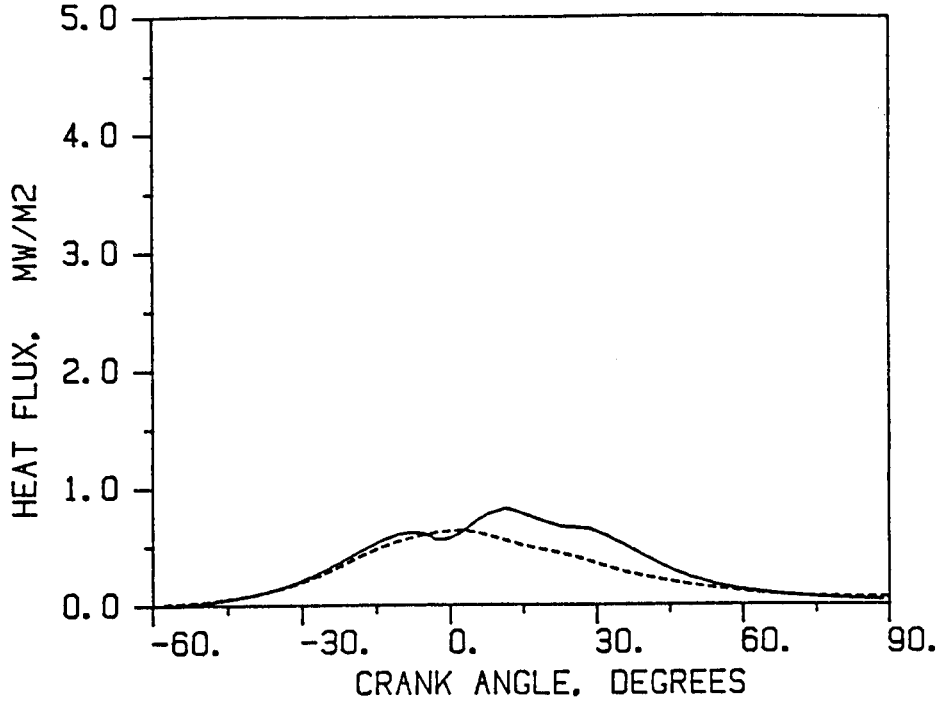

Figure 15c. Predicted and measured heat flux in ceramic engine, 1700 rpm, at crown location. ——— predictions, ----- data.

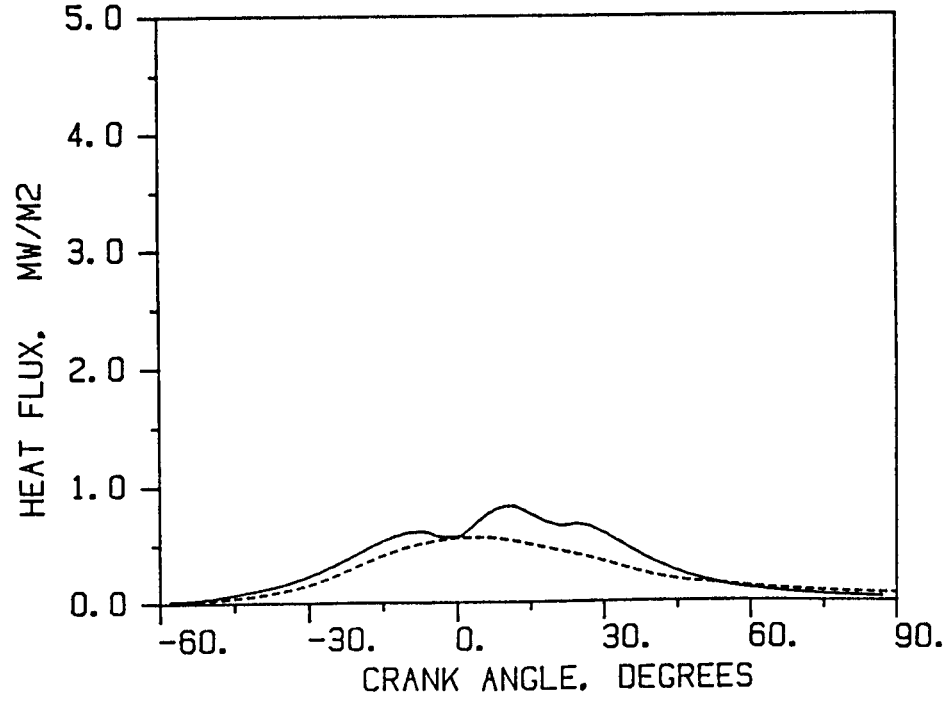

Figure 15d. Predicted and measured heat flux in ceramic engine, 2100 rpm, at crown location. ——— predictions, ----- data.

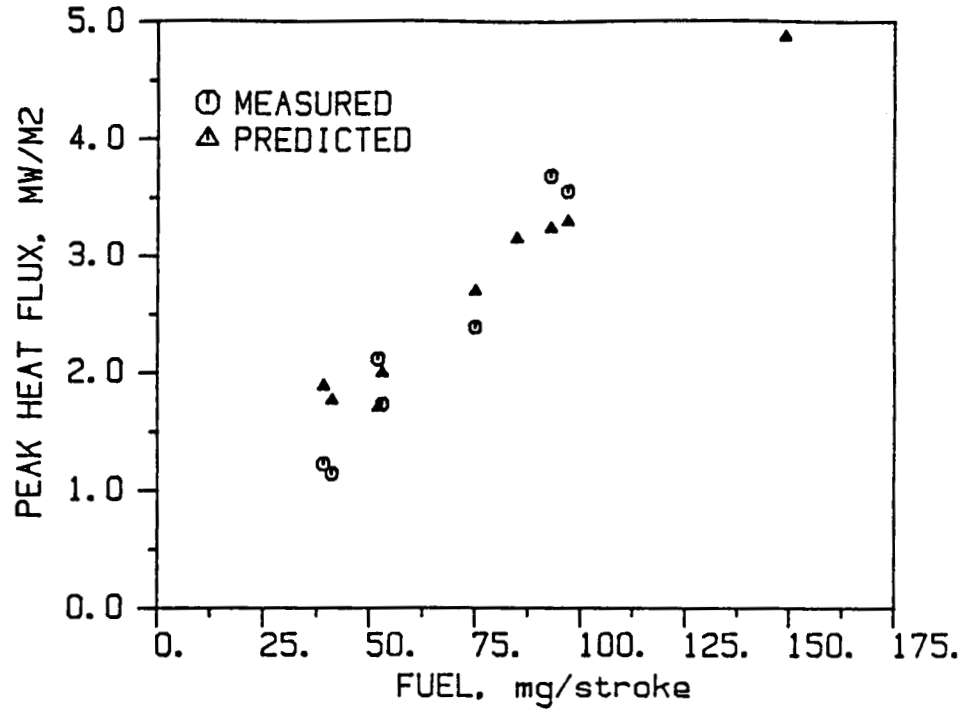

Figure 16a. Predicted and measured peak heat flux at bowl location. Δ predictions, o data.

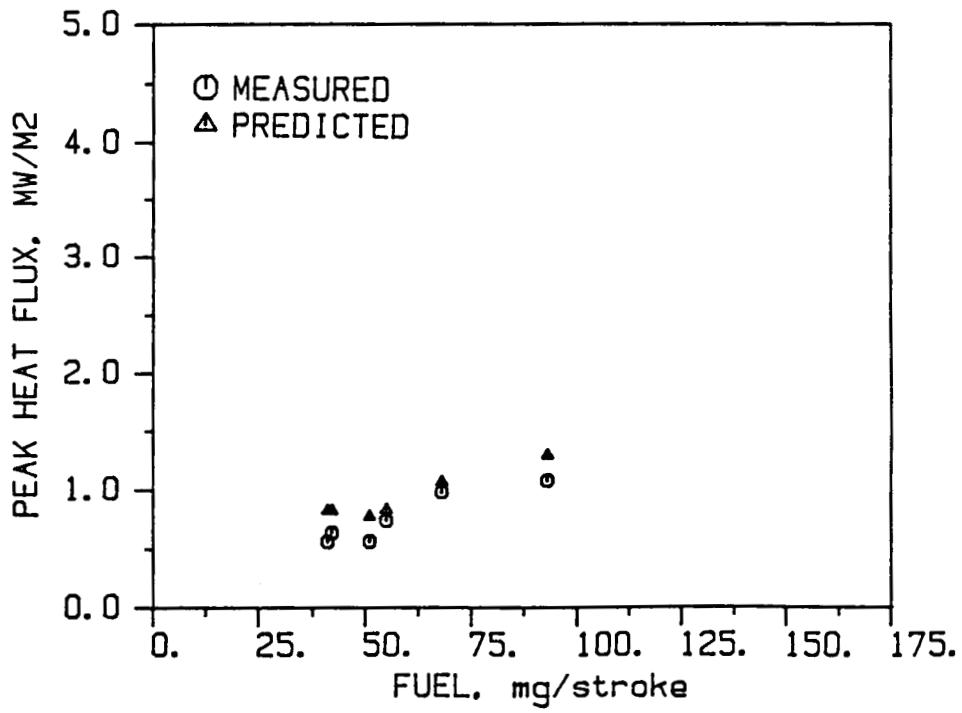

Figure 16b. Predicted and measured peak heat flux at crown location. Δ predictions, o data.

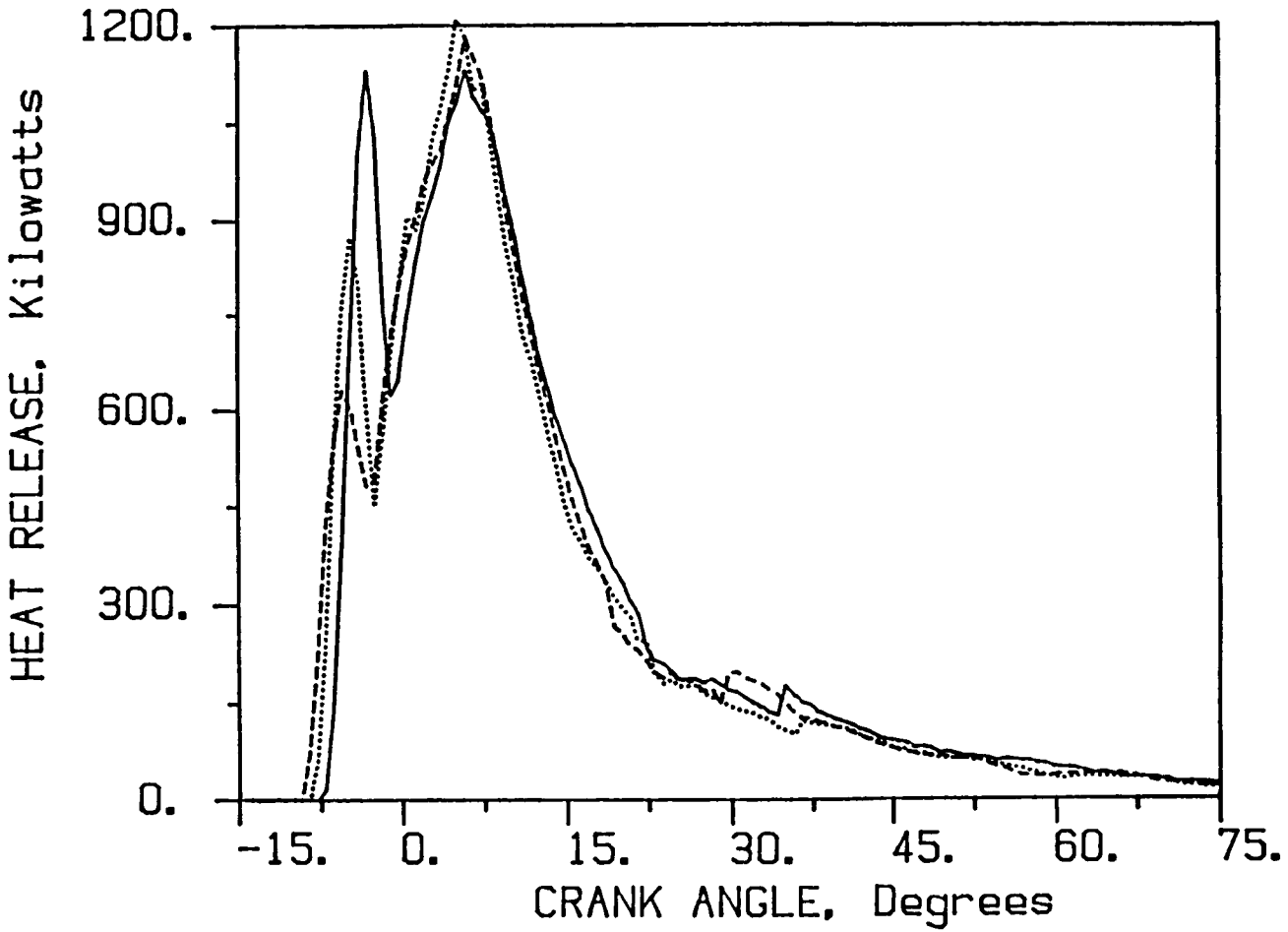

Figure 17. Heat release rate at 1300 rpm, 35% load. ——— metal engine, ----- ceramic-coated engine, ····· ceramic-coated engine with enhanced head cooling.

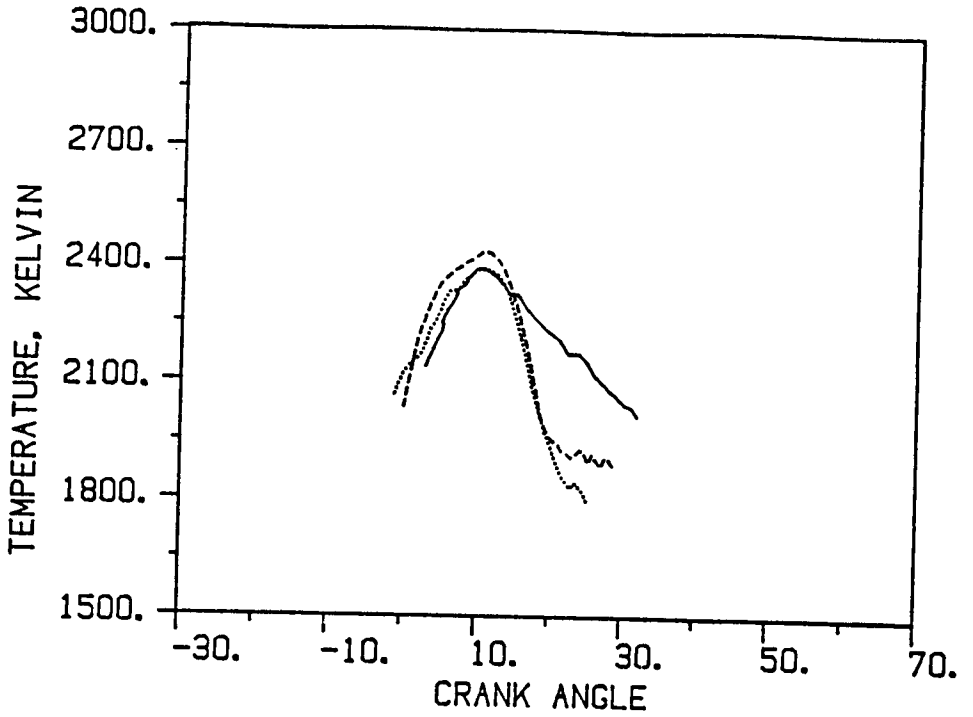

Figure 18a. Apparent radiation temperature at 1300 rpm, 25% load. ——— metal engine, - - - - - ceramic-coated engine, ····· ceramic-coated engine with enhanced head cooling.

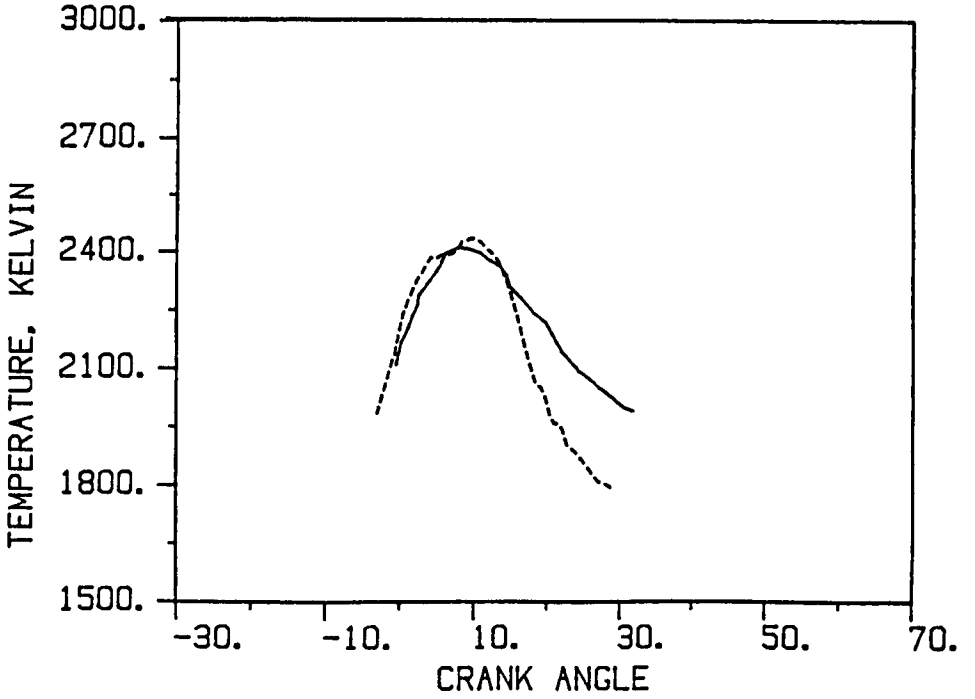

Figure 18b. Apparent radiation temperature at 1300 rpm, 35% load. ——— metal engine, - - - - - ceramic-coated engine.

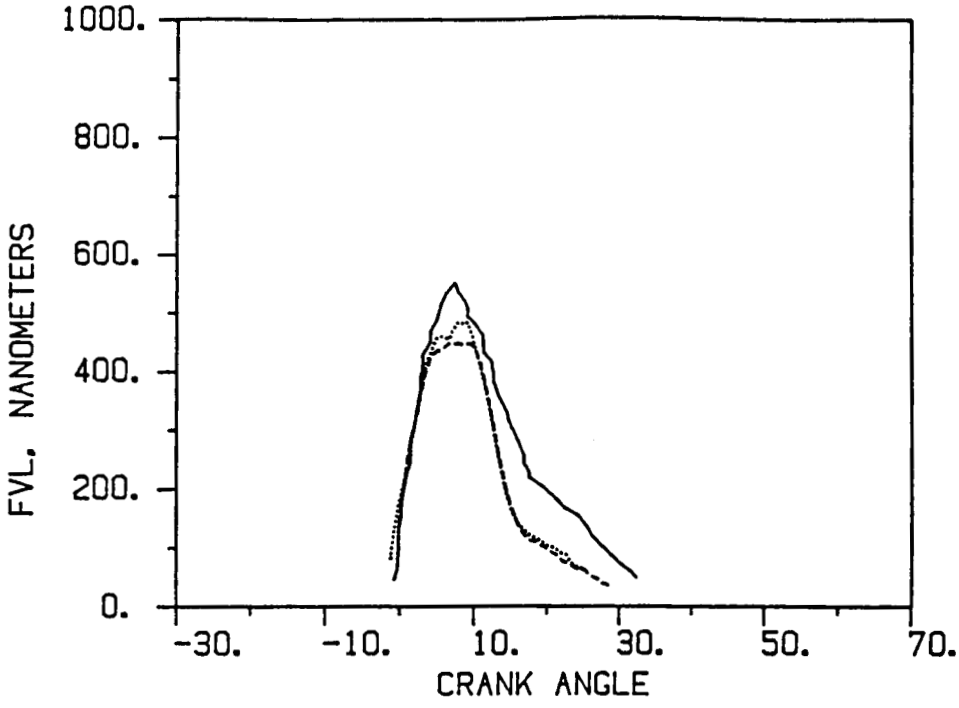

Figure 19a. Apparent product of soot volume fraction and of soot layer thickness at 1300 rpm, 25% load. ——— metal engine, ----- ceramic-coated engine, ····· ceramic-coated engine with enhanced head cooling.

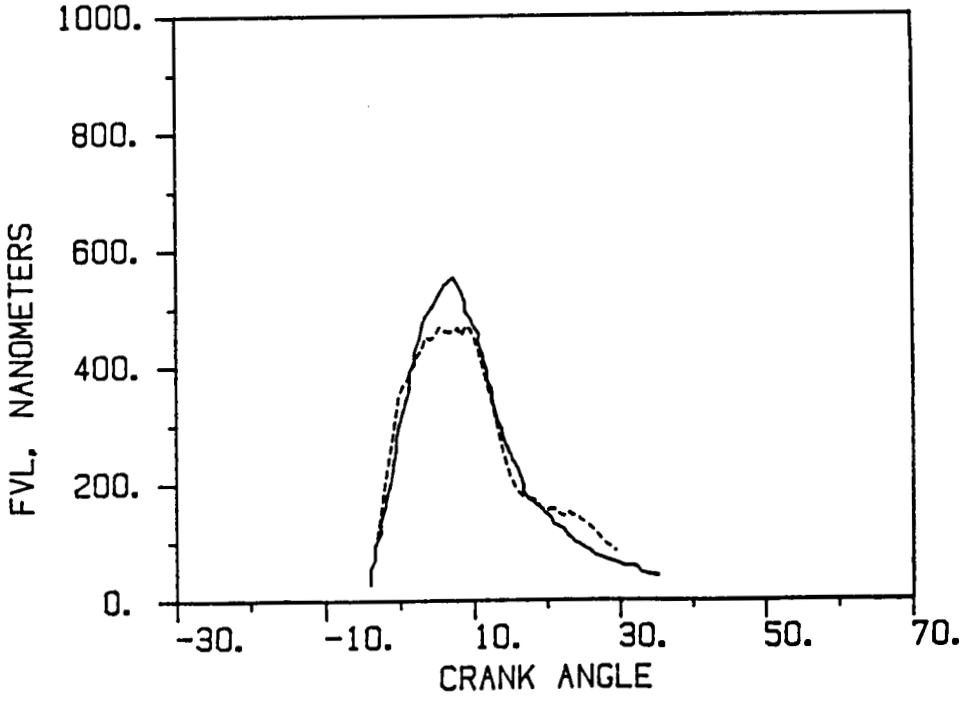

Figure 19b. Apparent product of soot volume fraction and of soot layer thickness at 1300 rpm, 35% load. ——— metal engine.

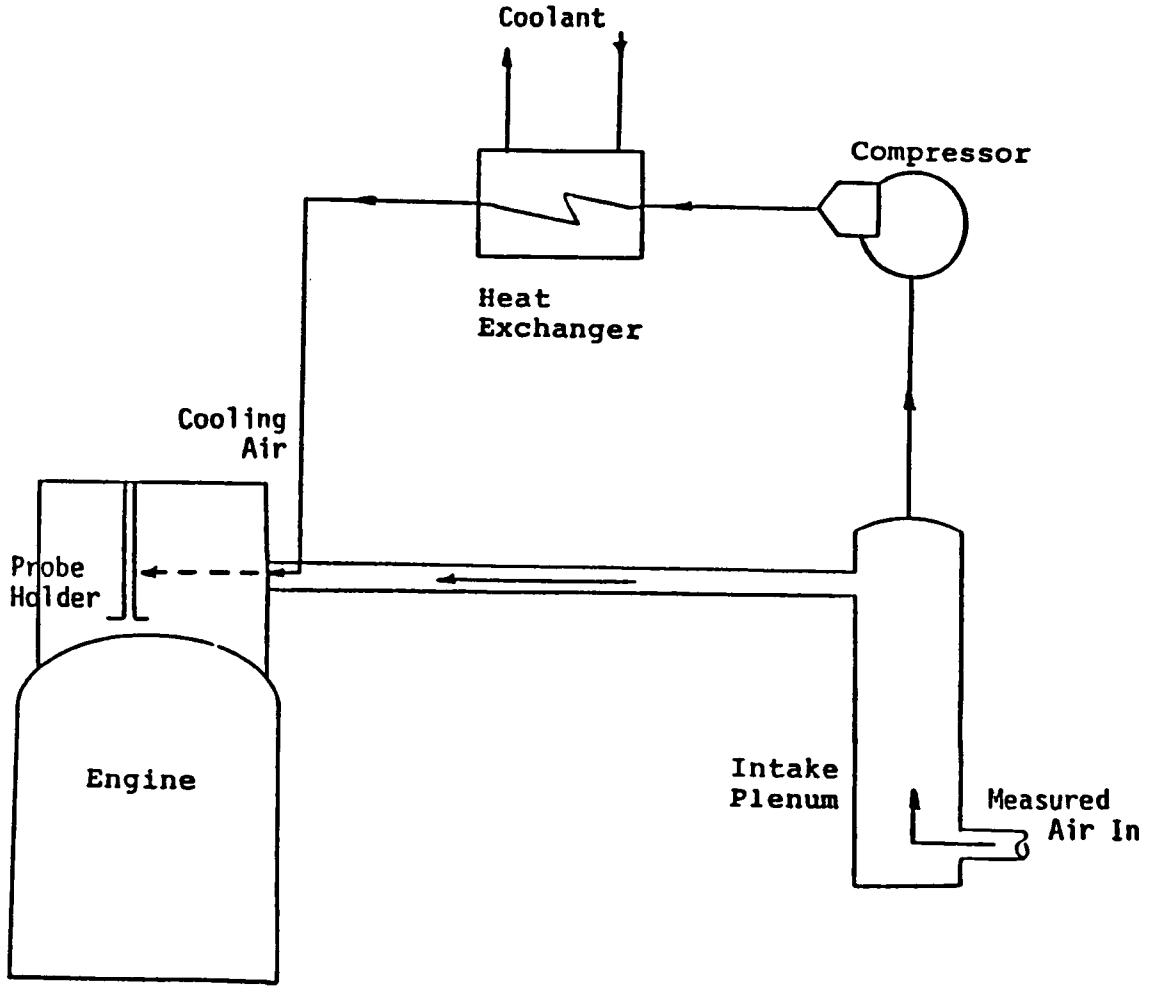

Figure 20. Schematic representation of the system used to cool the back side of the heat flux probe holder.

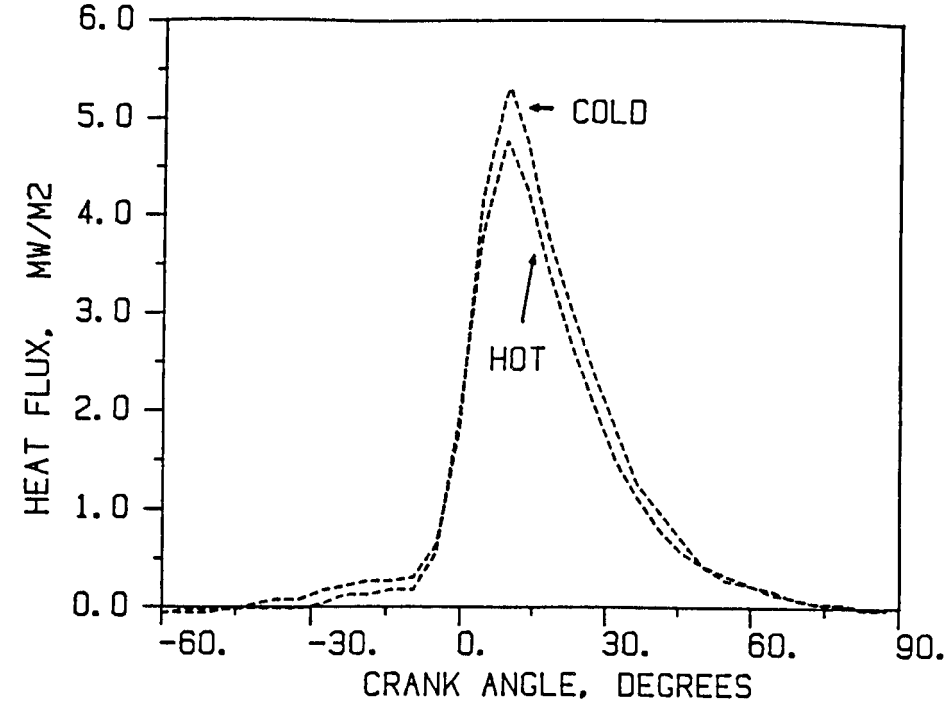

Figure 21. Heat flux measured at 1300 rpm, 50% load, with and without probe cooling.

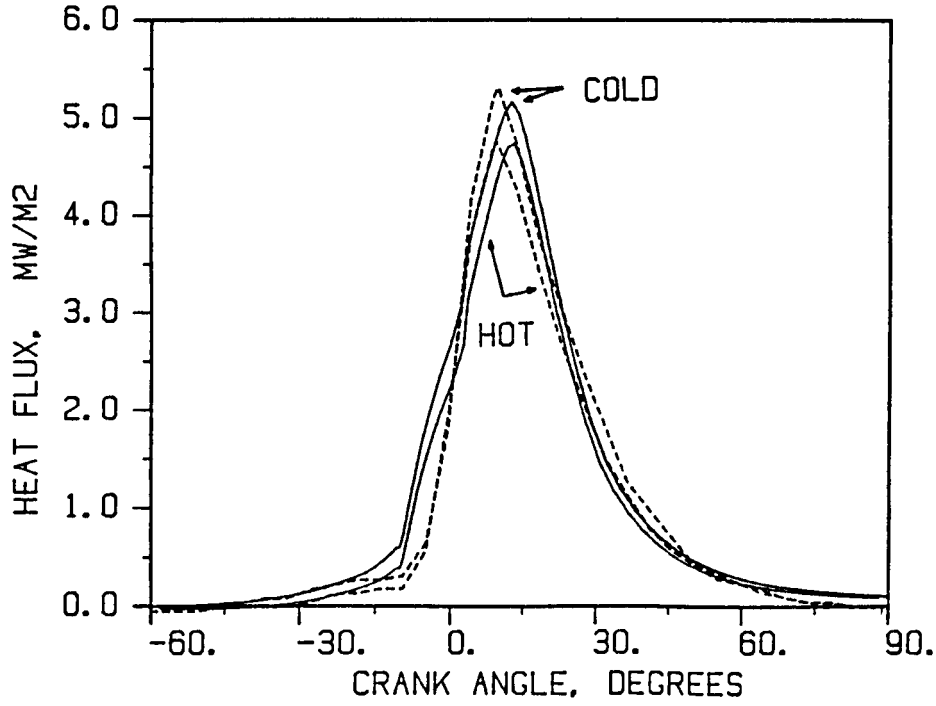

Figure 22. Predicted and measured heat flux at 1300 rpm, 50% load, with and without probe cooling.

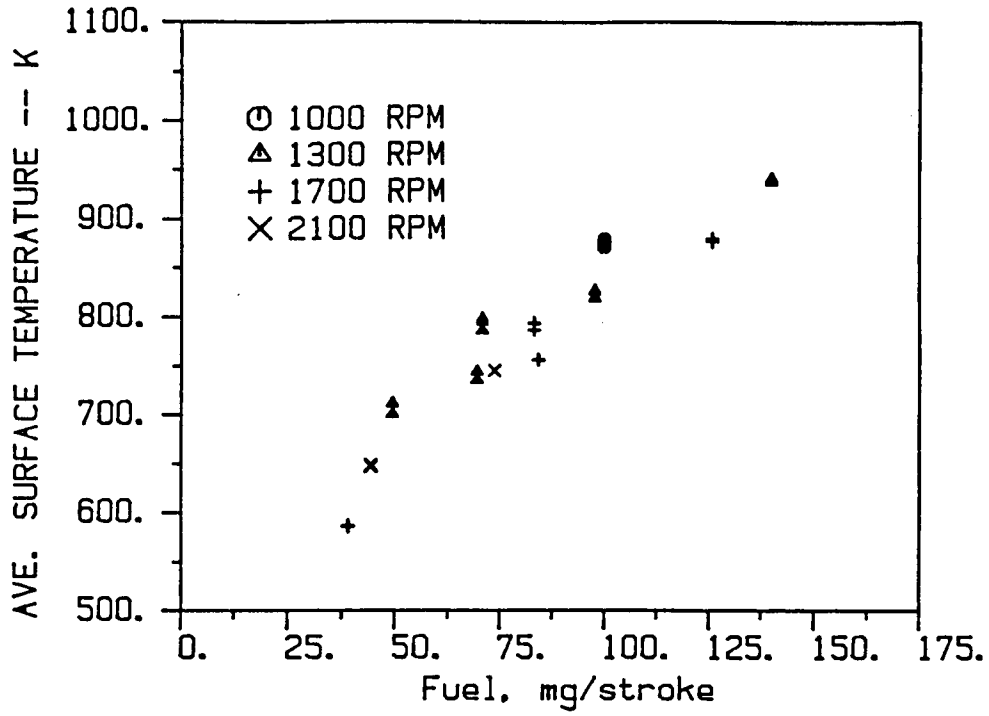

Figure 23. Average surface temperature as a function of fueling rate, NBS/Purdue probe.

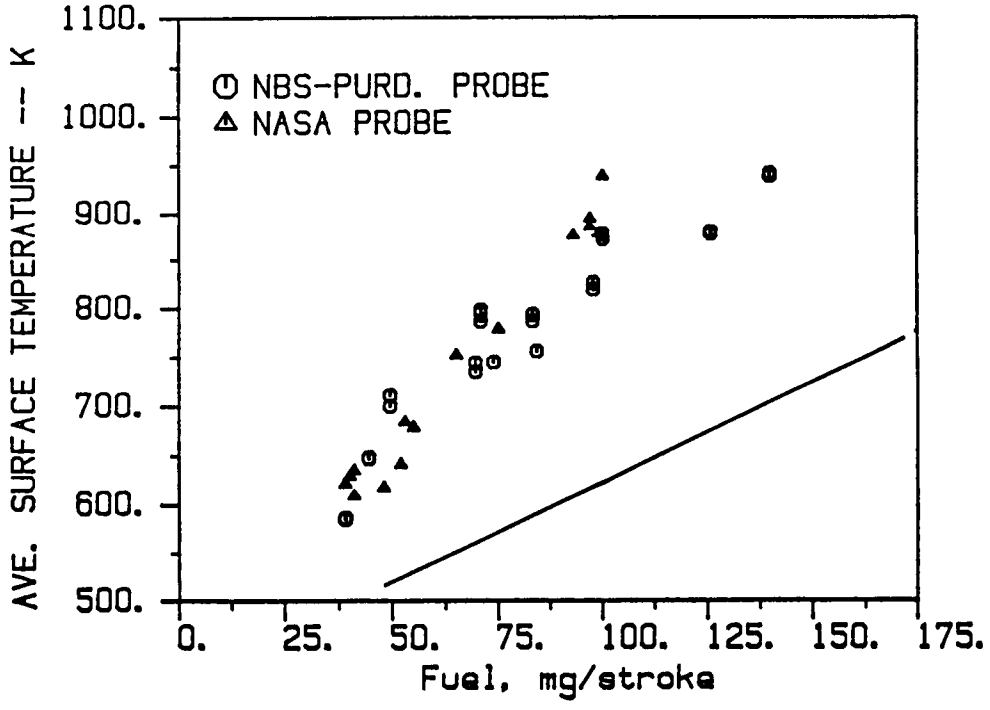

Figure 24. Average surface temperature as a function of fueling rate. Comparison of NBS/Purdue and NASA probe results. ——— cooled metal engine.

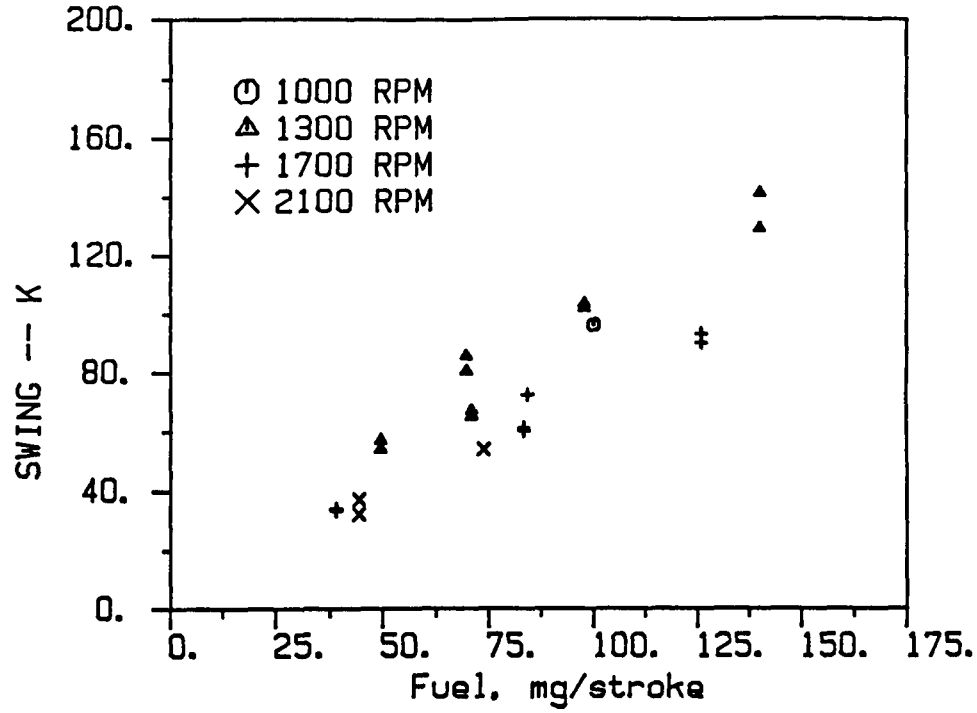

Figure 25. Surface temperature swing as a function of fueling rate, NBS/Purdue probe.

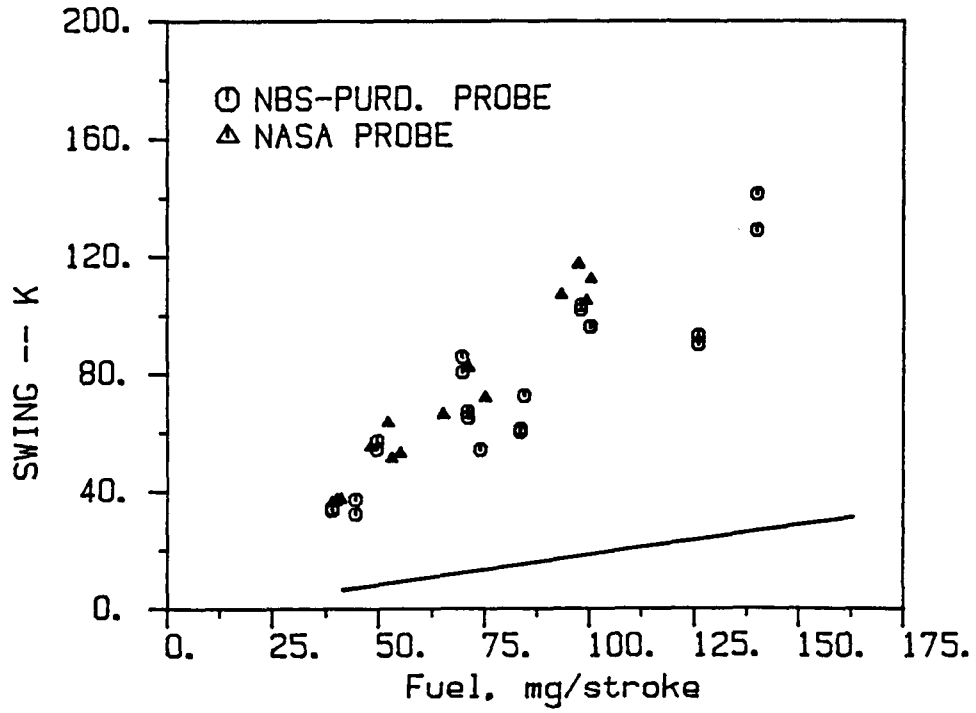

Figure 26. Surface temperature swing as a function of fueling rate. Comparison of NBS/Purdue and NASA probe results. ——— cooled metal engine.

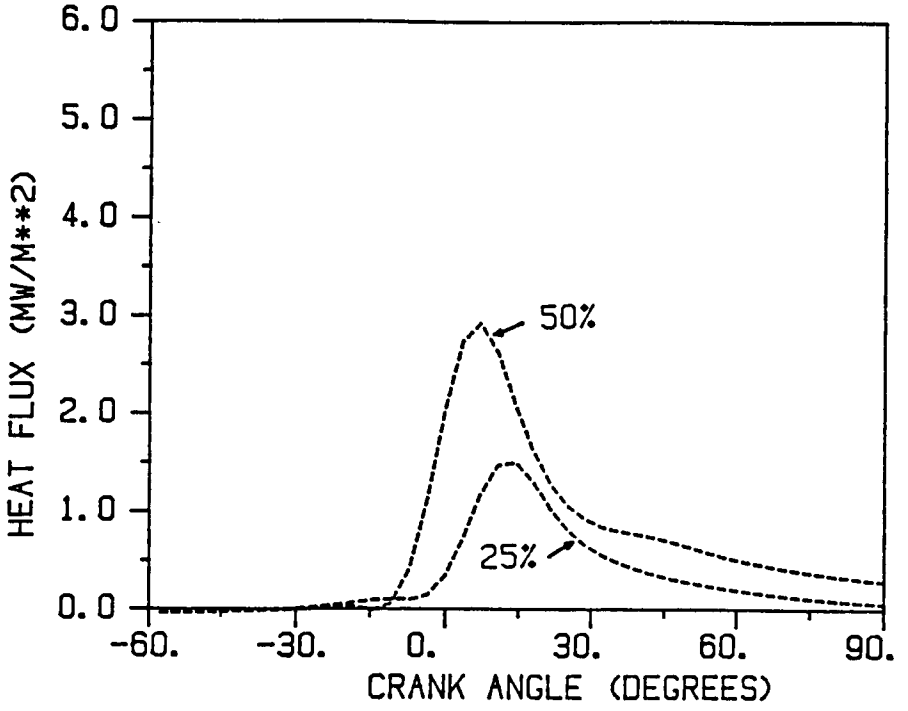

Figure 27a. Heat flux in ceramic engine measured at bowl location with NBS/Purdue probes, 1000 rpm.

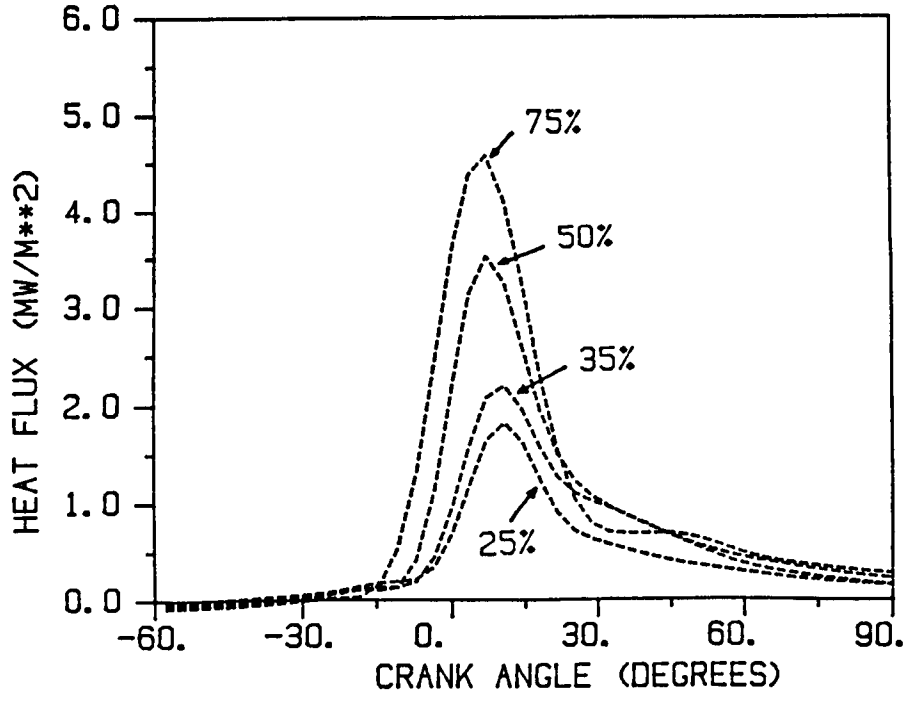

Figure 27b. Heat flux in ceramic engine measured at bowl location with NBS/Purdue probes, 1300 rpm.

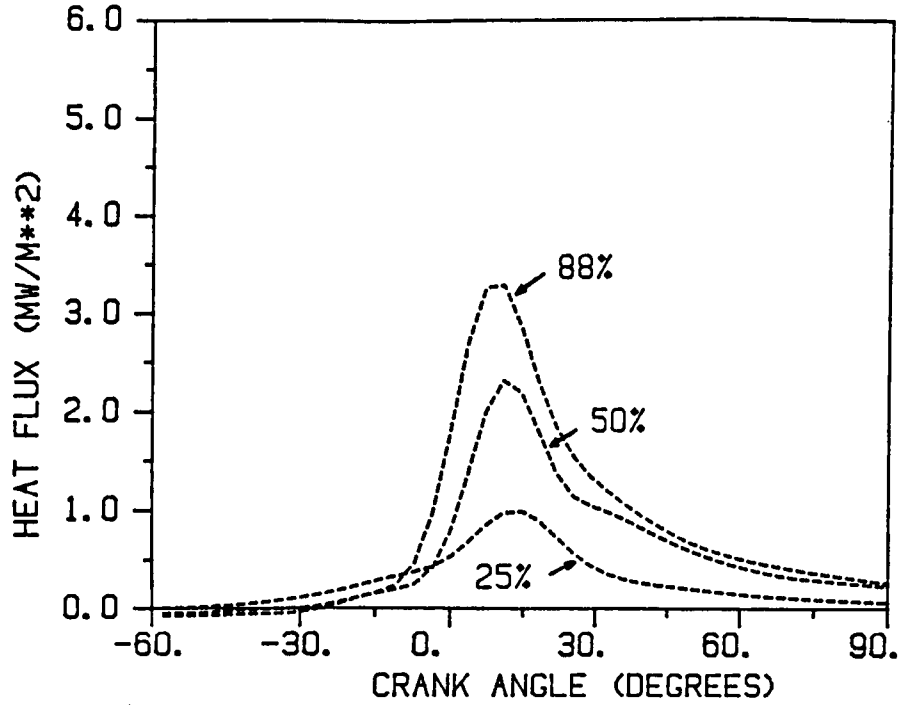

Figure 27c. Heat flux in ceramic engine measured at bowl location with NBS/Purdue probes, 1700 rpm.

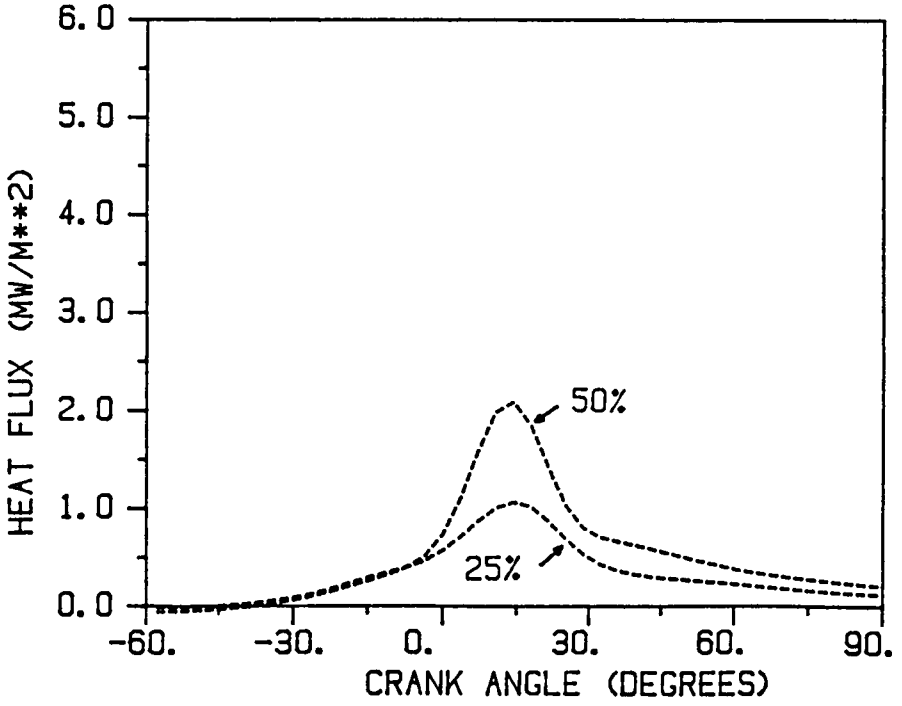

Figure 27d. Heat flux in ceramic engine measured at bowl location with NBS/Purdue probes, 2100 rpm.

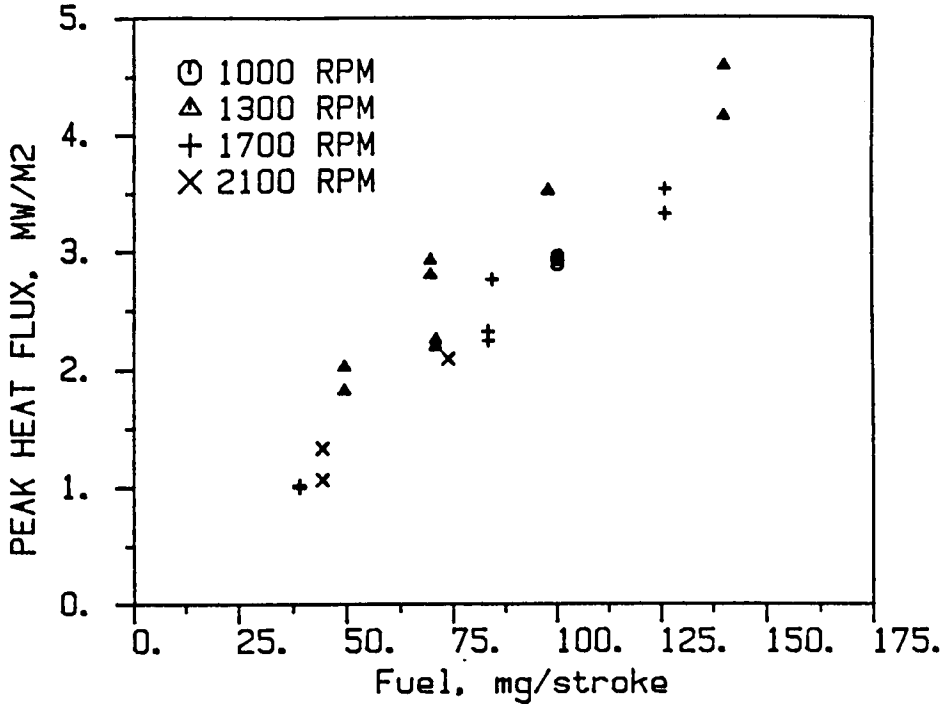

Figure 28. Peak heat flux as a function of fueling rate, NBS/Purdue probe.

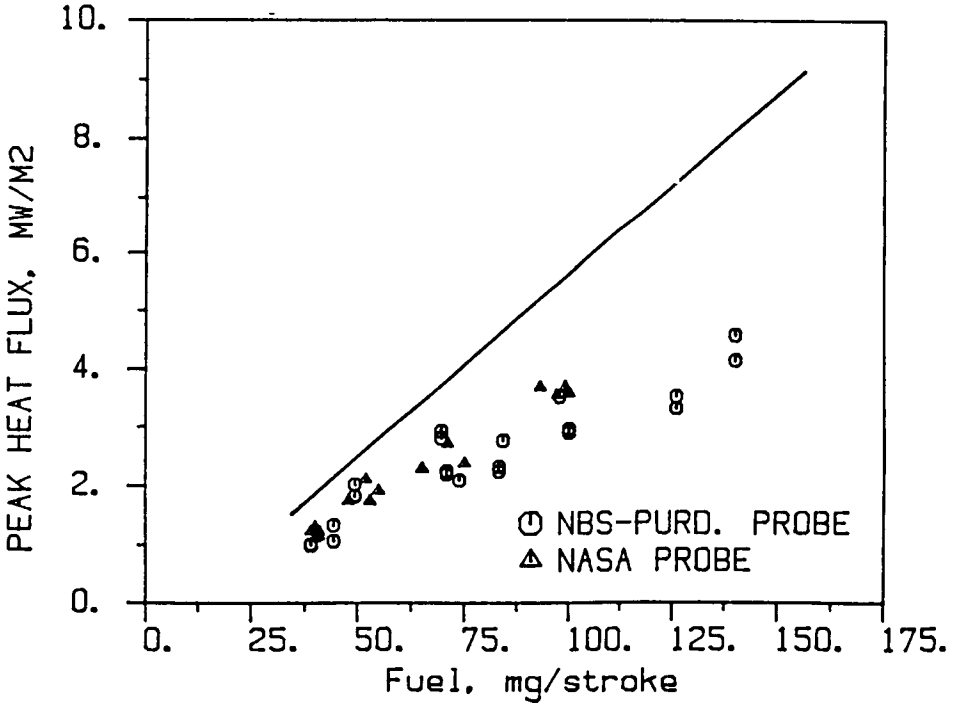

Figure 29. Peak heat flux as a function of fueling rate. Comparison of NBS/Purdue and NASA probe results. ——— cooled metal engine.

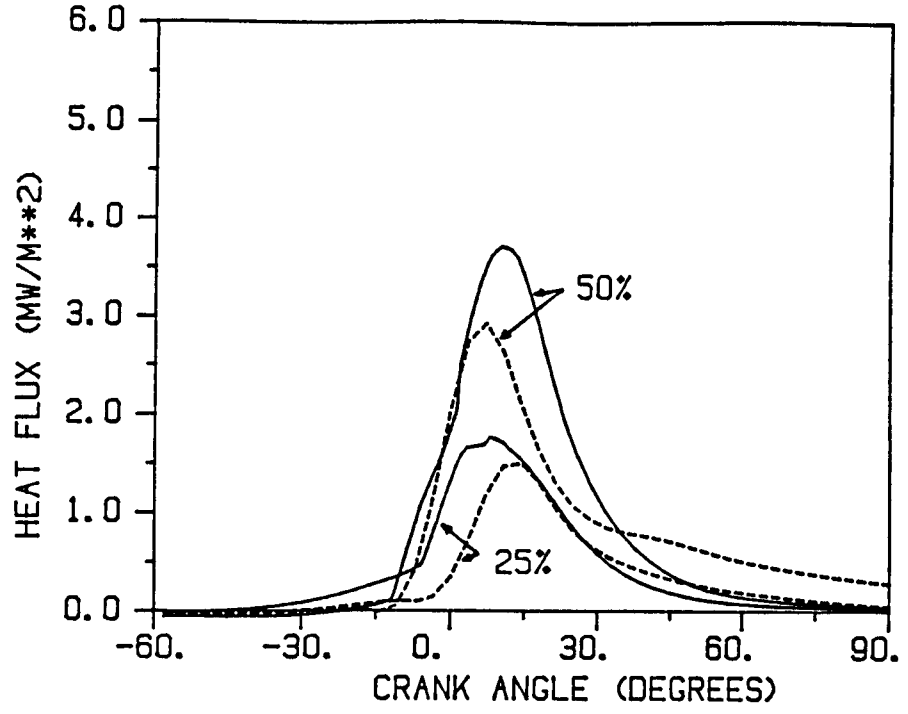

Figure 30a. Predicted and measured heat flux in ceramic engine at bowl location, NBS/Purdue probes, 1000 rpm.

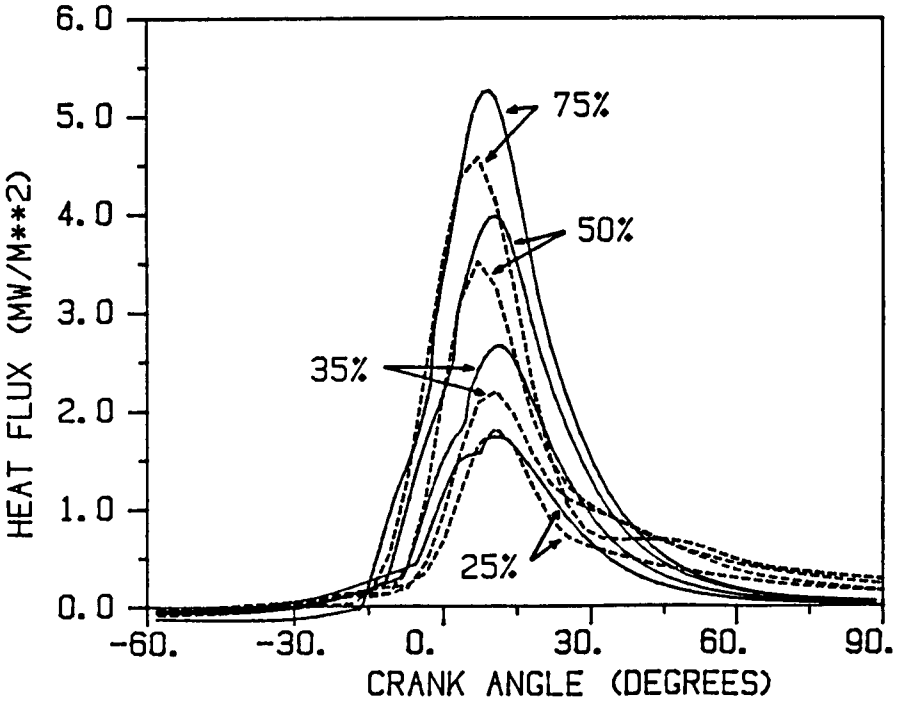

Figure 30b. Predicted and measured heat flux in ceramic engine at bowl location, NBS/Purdue probes, 1300 rpm.

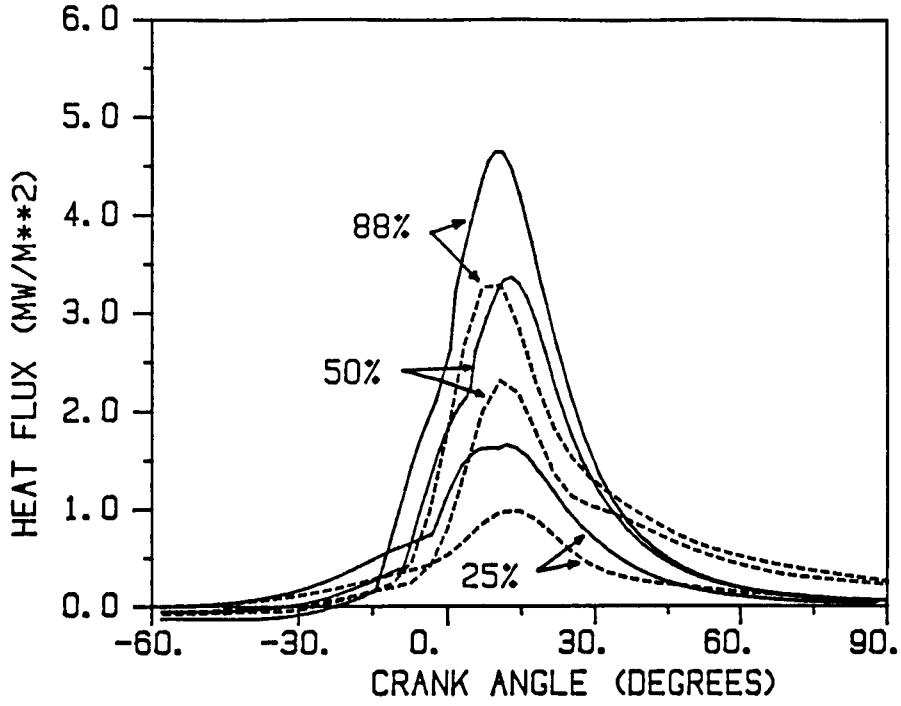

Figure 30c. Predicted and measured heat flux in ceramic engine at bowl location, NBS/Purdue probes, 1700 rpm.

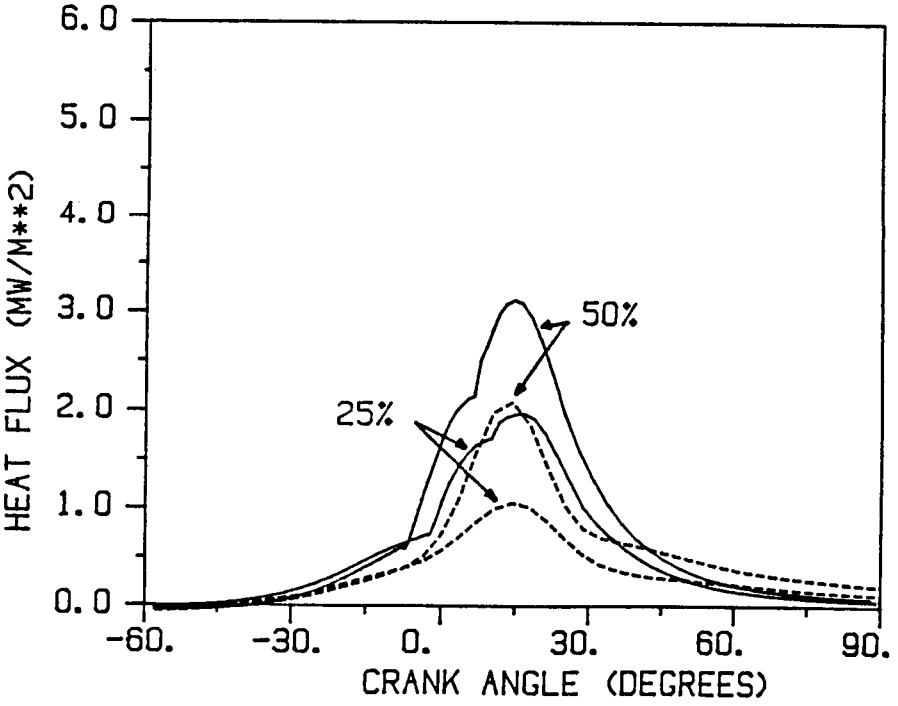

Figure 30d. Predicted and measured heat flux in ceramic engine at bowl location, NBS/Purdue probes, 2100 rpm.

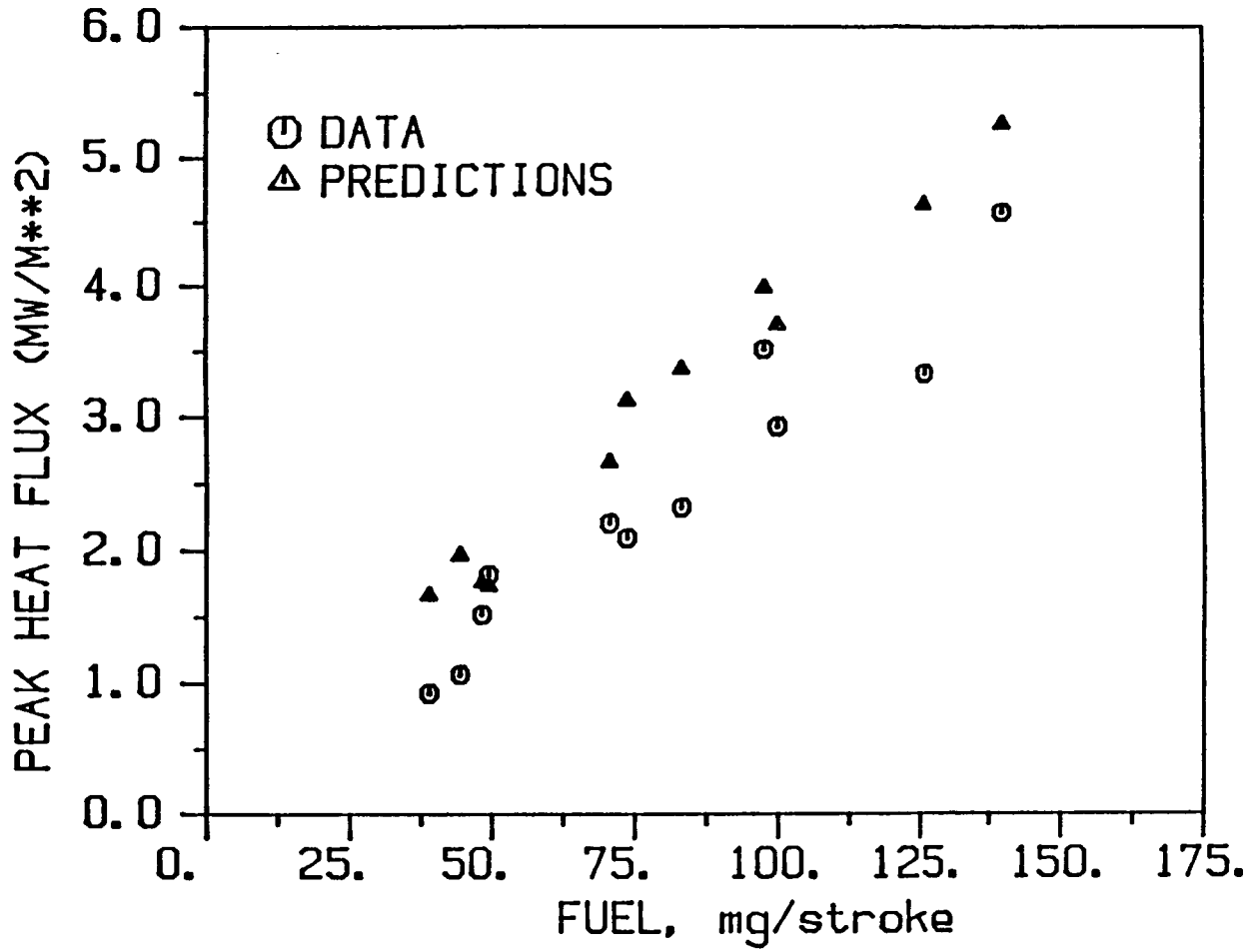

Figure 31. Predicted and measured peak heat flux at bowl location, NBS/Purdue probes.

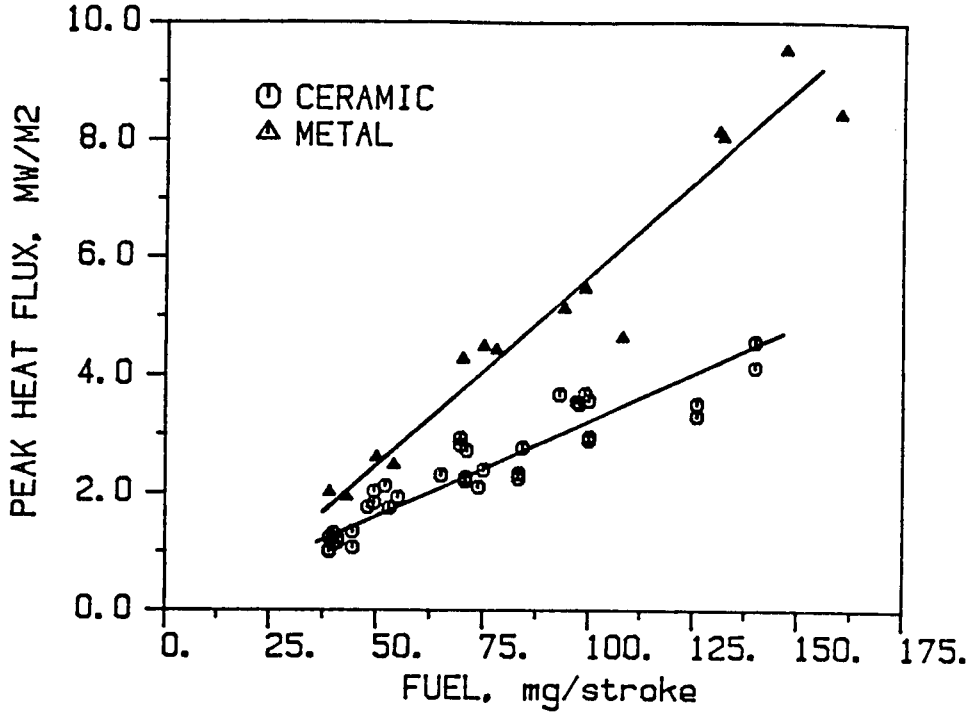

Figure 32a. Peak heat flux as a function of fueling rate in ceramic-coated and metal engines. Bowl location.

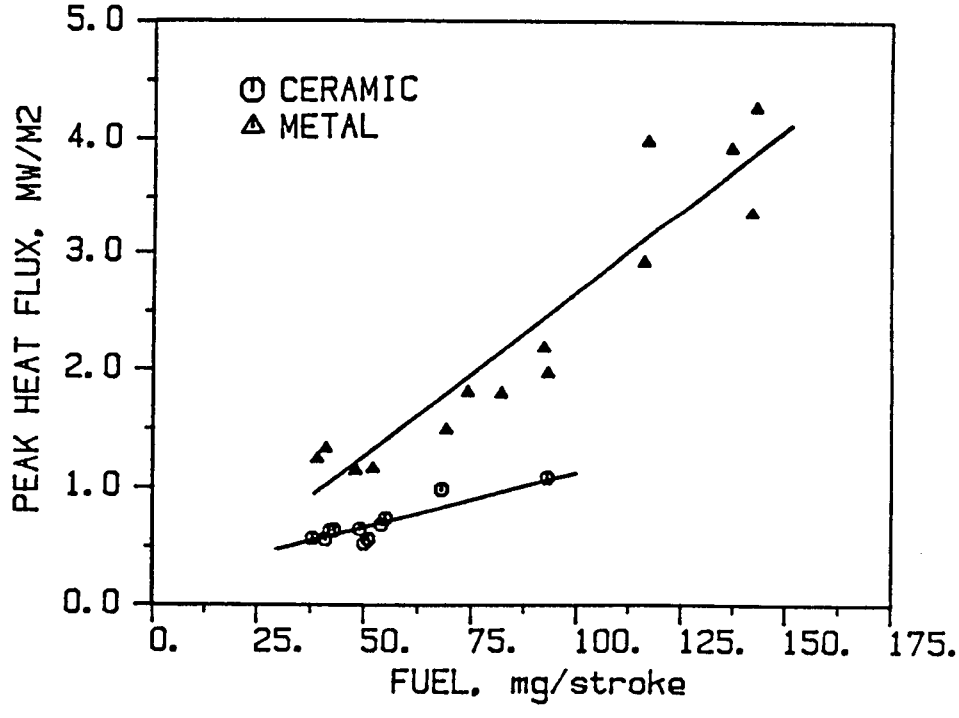

Figure 32b. Peak heat flux as a function of fueling rate in ceramic-coated and metal engines. Crown location.

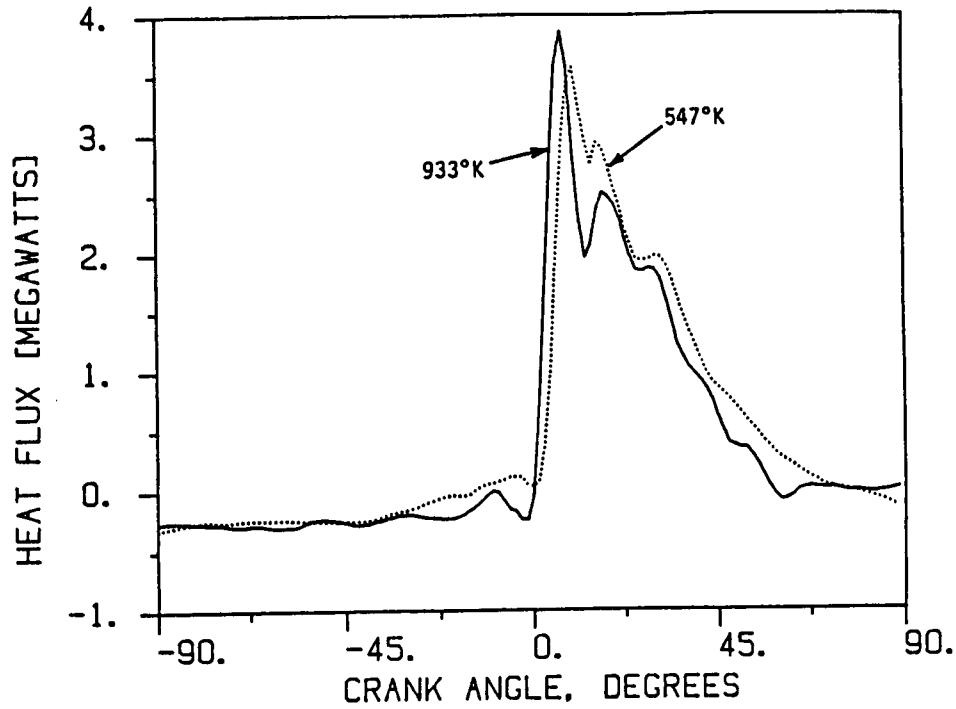

Figure 33a. Heat flux calculated from surface temperature records of Woschni and Spindler (1987) obtained at two different mean surface temperatures. IMEP = 7.3 bars.

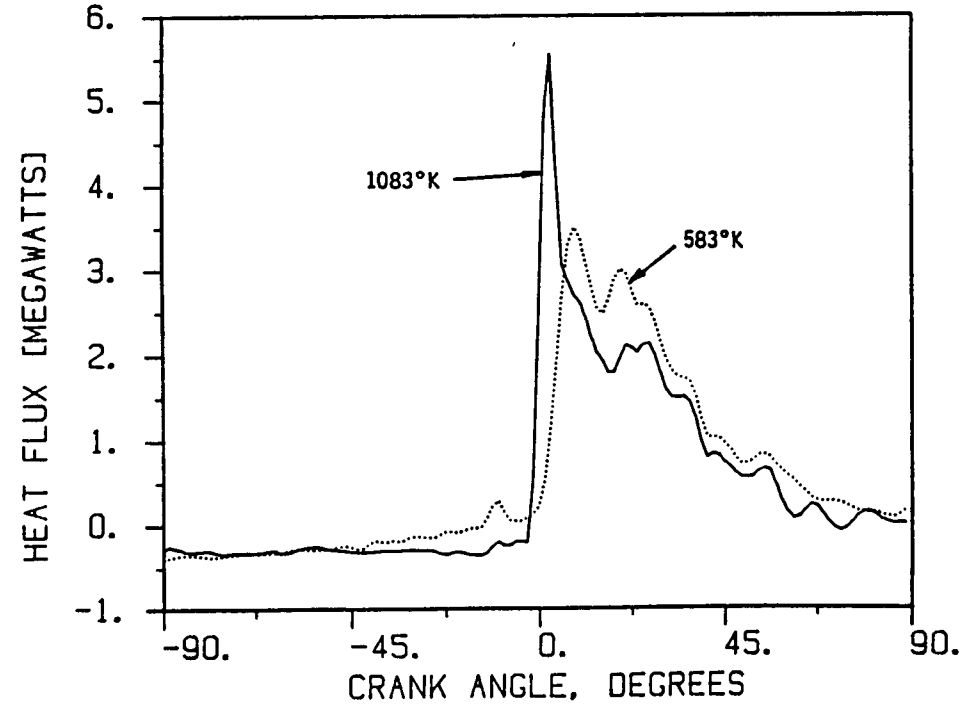

Figure 33b. Heat flux calculated from surface temperature records of Woschni and Spindler (1987) obtained at two different mean surface temperatures. IMEP = 8.2 bars.

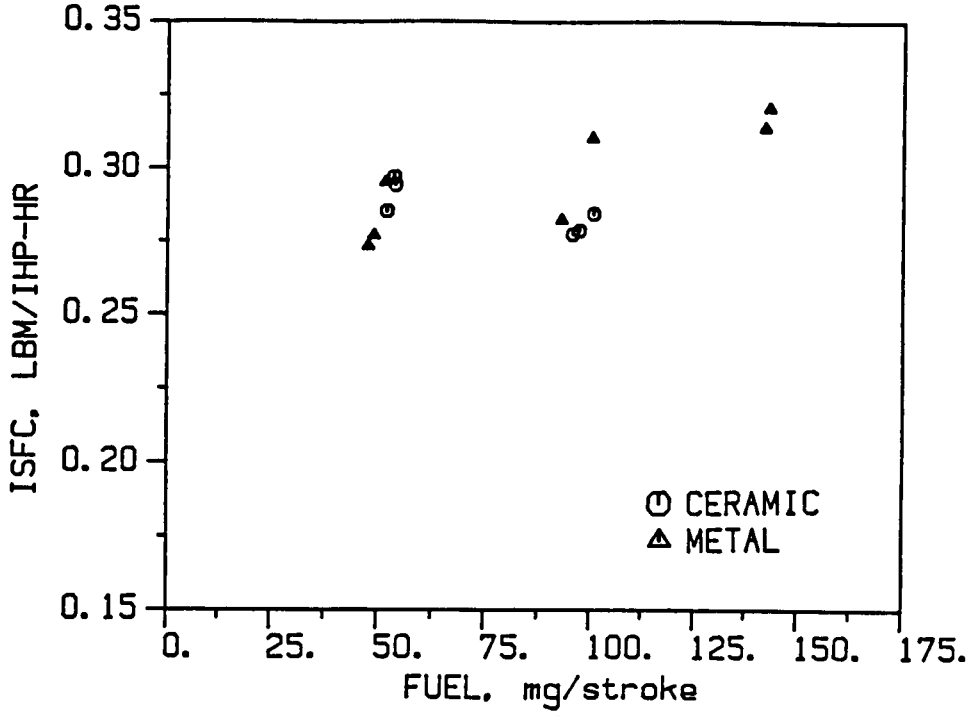

Figure 34a. ISFC obtained from measured pressure (360°CA) in the metal and ceramic engines. 1000 rpm.

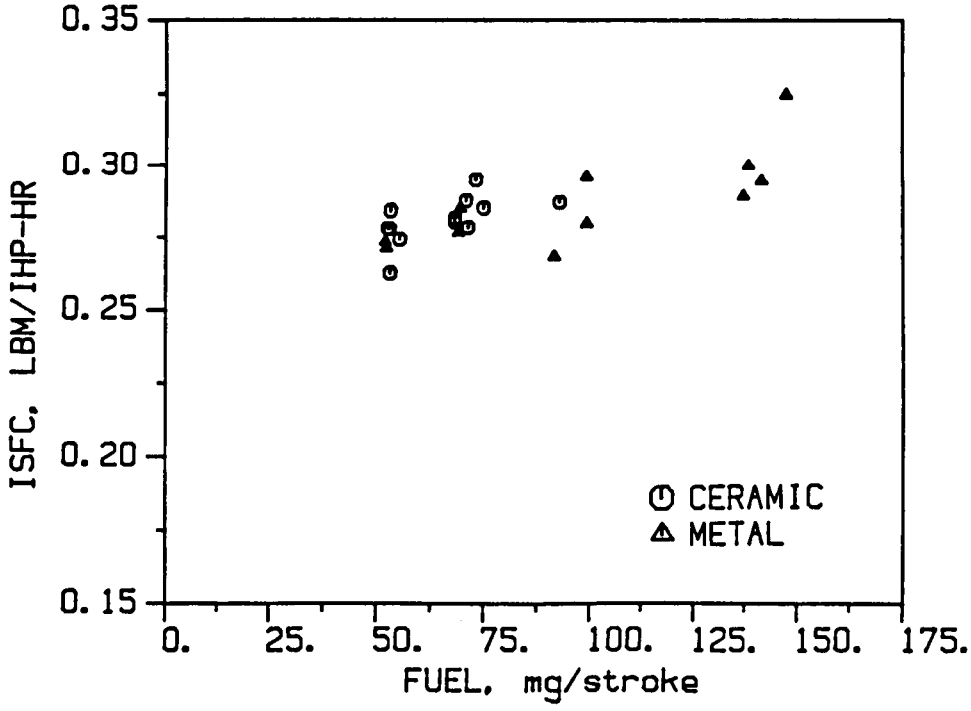

Figure 34b. ISFC obtained from measured pressure (360°CA) in the metal and ceramic engines. 1300 rpm.

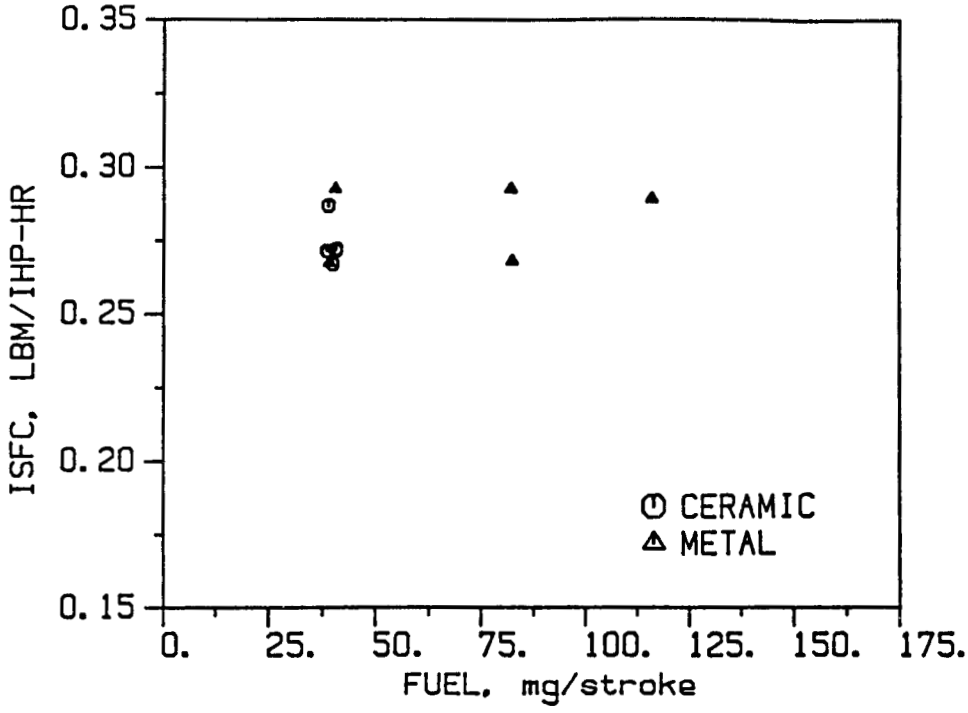

Figure 34c. ISFC obtained from measured pressure (360°CA) in the metal and ceramic engines. 1700 rpm.

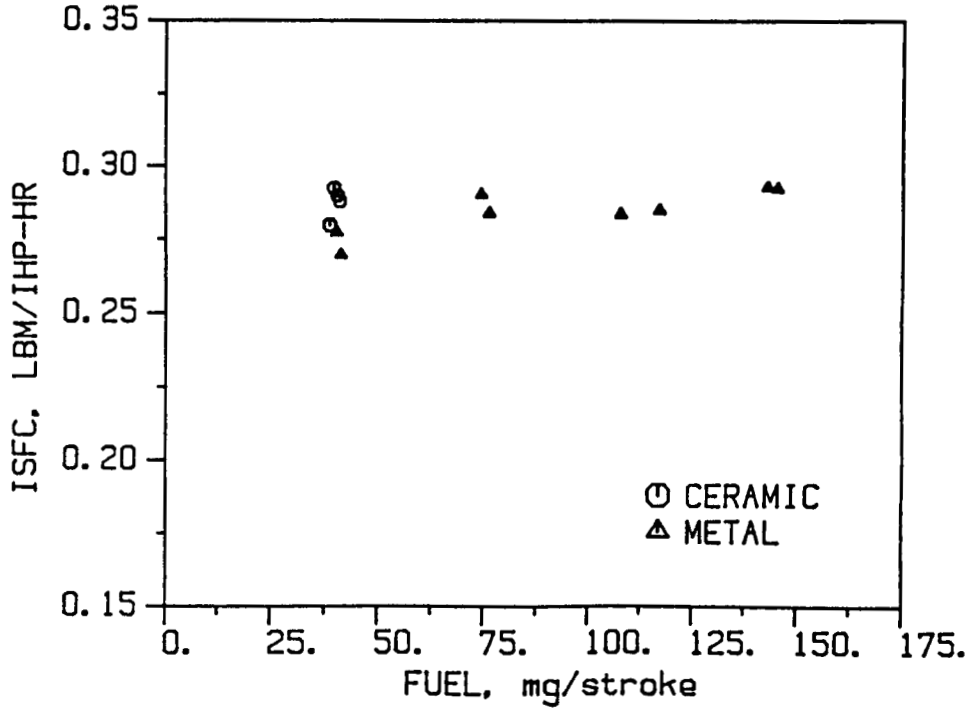

Figure 34d. ISFC obtained from measured pressure (360°CA) in the metal and ceramic engines. 2100 rpm.

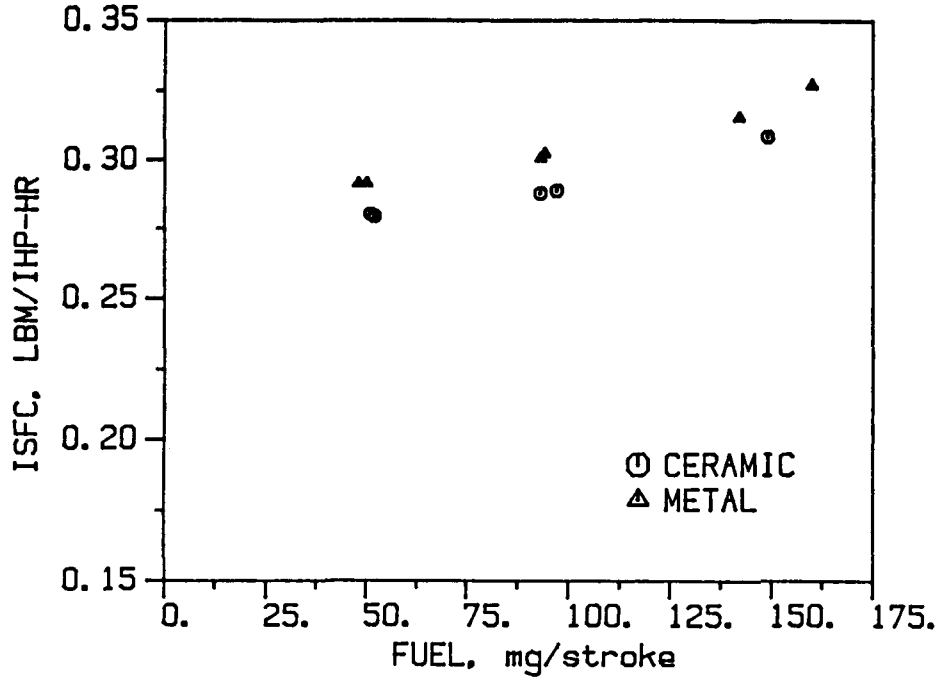

Figure 35a. Predicted ISFC (360°) in the metal and ceramic engines. 1000 rpm.

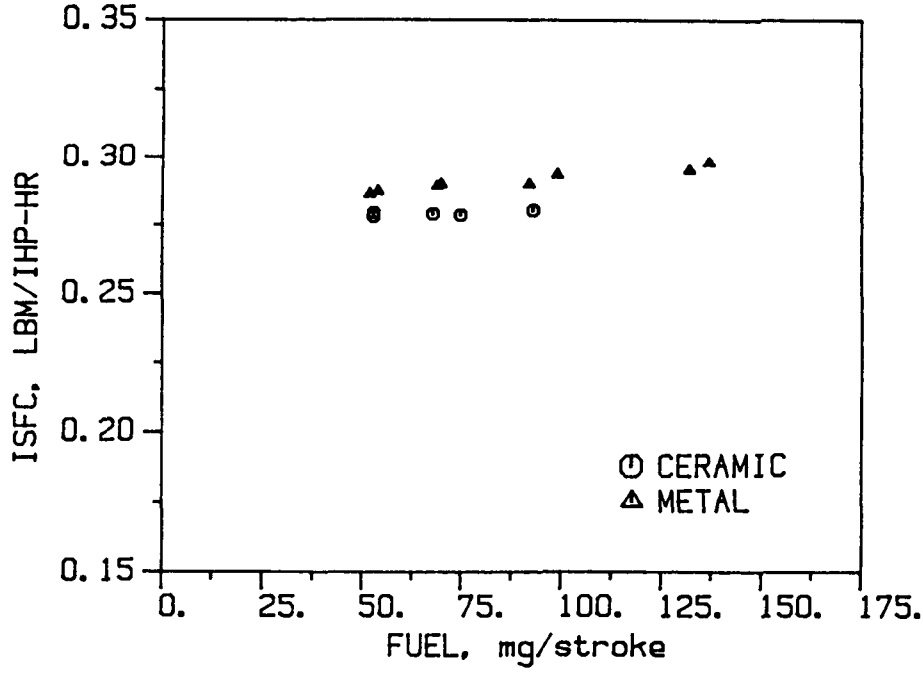

Figure 35b. Predicted ISFC (360°)in the metal and ceramic engines. 1300 rpm.

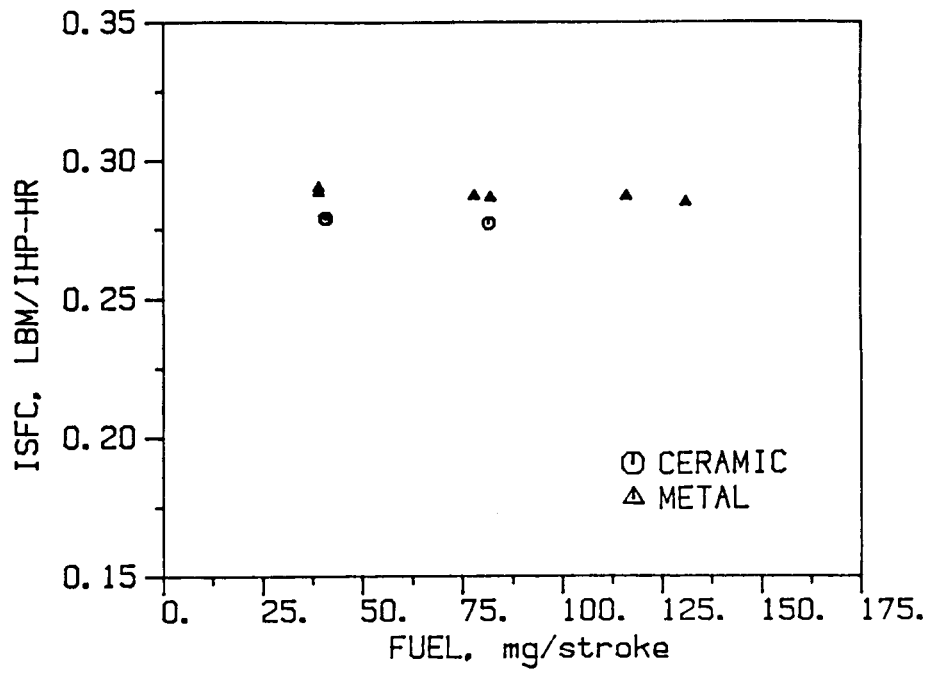

Figure 35c. Predicted ISFC (360°) in the metal and ceramic engines. 1700 rpm.

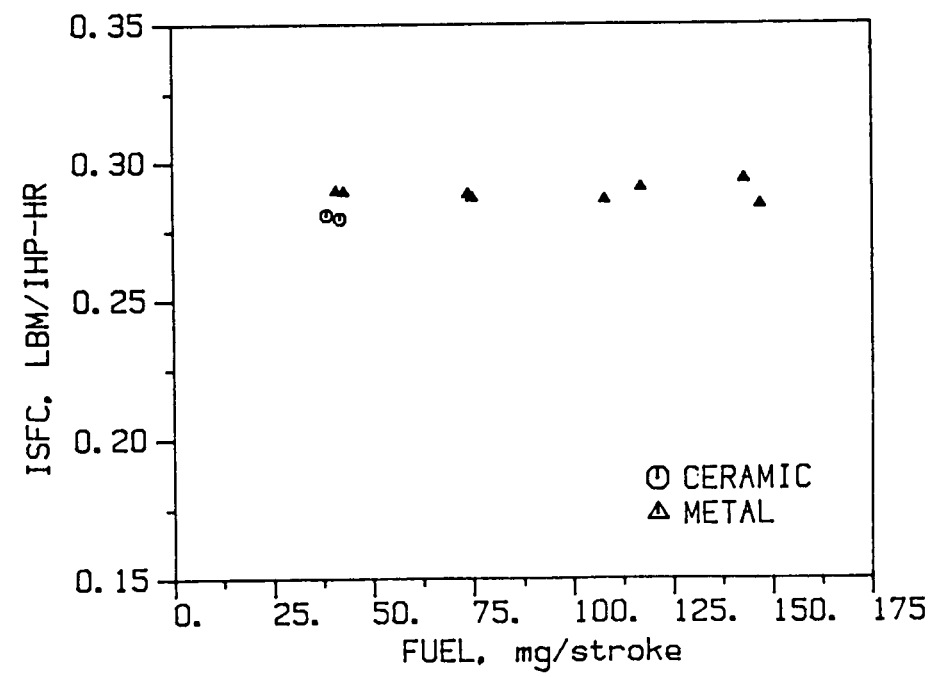

Figure 35d. Predicted ISFC (360°) in the metal and ceramic engines. 2100 rpm.

APPENDIX A

SELECTED ITI PUBLICATIONS BASED ON PHASE III RESULTS

The SAE publications are reprinted here with the permission of the Society of Automotive Engineers.

APPENDIX A-1

EFFECT OF SPEED, LOAD AND LOCATION ON HEAT TRANSFER IN A DIESEL ENGINE -- MEASUREMENTS AND PREDICTIONS

ABSTRACT

An experimental study was conducted to measure the heat transfer in a direct injection 2.3 ℓ single cylinder diesel engine. The engine was operated at speeds ranging from 1000 to 2100 RPM and at a variety of loads. The heat transfer was measured using a total heat flux probe, operating on the principle of a thin film thermocouple, sensitive to both the convective and radiative heat flux. The probe was located in the head at two locations: opposite the piston bowl and opposite the piston crown (squish region). The measurements showed about twice as large peak heat flux in the bowl location than in the crown location for fired conditions, while under motoring conditions the relationship was reversed and the peak heat flux was slightly higher in the crown position. The experimental profiles of total heat flux were compared to the predictions obtained using a detailed thermodynamic cycle code, which incorporates highly resolved models of convective and radiative heat transfer. The predictions were found to be in very good agreement with the measurements, both in magnitude and in trends with engine load and speed. The model was found to reproduce very well the observed spatial variations in peak heat flux between the two head locations.

ENGINE HEAT TRANSFER plays an important role in engine design. This is because it affects engine performance due to losses of available energy, and it also affects gas temperatures and through them combustion rate, emissions formation, knock, etc. A separate area of importance is the thermal loading of engine structural components, and the optimization of engine cooling systems.

Taking engine cooling as an example, one can note that its optimization requires the solution of the coupled problem of heat transfer from gases to walls and of heat conduction through the structure. The heat conduction portion of such a calculation can be carried out to any desired accuracy, using finite element models (FEM). By contrast, gas-to-wall heat transfer modeling is still in a developmental state. This presents a major stumbling block, since the gas-to-wall heat transfer correlations are needed to provide the necessary boundary conditions for the FEM codes. The calculated temperature field in the structure depends very critically on these boundary conditions, which must be well grounded in physics, if they are to provide an accurate description of the heat flux rates and of their spatial and temporal variation within the combustion chamber. Inadequacies in gas-to-wall heat transfer modeling also reflect themselves in inaccurate values of basic quantities such as thermal efficiency, power, and exhaust temperature and volumetric efficiency.

In an attempt to advance the state of the art in heat transfer modeling, a comprehensive research program has been carried out in order to develop better methods for evaluating the effects of heat transfer on in-cylinder processes and for establishing accurate boundary conditions for engine component FEM calculations. This program followed two parallel paths. One was analytical, involving the development of a flow-based convective heat transfer model (Morel and Keribar, 1985) and a detailed zonal heat radiation model (Morel and Keribar, 1986). The other path was experimental, in which crank-angle resolved heat transfer data were obtained in a single-cylinder direct injection diesel engine. This paper provides an overview of the models used, describes in detail the experimental part of the program, and presents comparisons between the measured and calculated heat fluxes.

MODELING OF GAS PHASE HEAT TRANSFER

Previous Convective Heat Transfer Models. The need for predictive capability to estimate engine heat transfer rates has been recognized for a long time, and first models suggested for this purpose date back over 60 years.

The models that are currently the most widely used are those due to Annand (1963) and Woschni (1967). Both of these models are based on Nusselt/ Reynolds number correlations, in which the characteristic velocities scale with mean piston speed rather than with actual in-cylinder flow velocities. These models have no spatial resolution, and they ascribe the same value of the heat transfer coefficients to all of the in-cylinder surfaces. The constants used in the model are to be adjusted from engine to engine, and Annand (1963) suggests a range from 0.35 to 0.80 according to "intensity of motion in the region considered."

It is clear that a successful convective heat transfer model must take into account all of the key in-cylinder fluid motions such as: intake flows, swirl, squish, turbulence, and injection and combustion generated motions. Also the model has to provide spatial resolution capable of differentiating between various in-cylinder surfaces. This has been recognized and there has been a gradual evolution from simple correlations towards flow-based models as reviewed eg. in Morel and Keribar (1985). However, none of the models available in the literature incorporated the effect of all of the significant in-cylinder motions, nor did they provide the needed spatial resolution.

Present Convective Heat Transfer Model. The present model attempts to account for all of the important in-cylinder motions, and introduces a differentiation between the combustion chamber surfaces. The model is global in nature, but it incorporates much more physics than previous models and thus it is expected to require much less adjustment from engine to engine or from one combustion chamber shape to another than previous models. In fact, the model has no adjustable constants. It has been used on a range of engines from small high swirl diesels to a locomotive size diesel, and the global, cycle averaged heat rejection levels it predicted have been found to be in good agreement with the heat rejection levels observed in test cell experiments.

The model is based on well established boundary layer concepts. It calculates velocities and turbulence adjoining each of a number of resolved individual in-cylinder surfaces and from these it determines the local transfer coefficients through Colburn analogy. The required skin friction coefficient is obtained directly from literature boundary layer correlations. To calculate the flow velocities, the flow model divides the combustion chamber volume into three regions (for diesel applications only; a more involved approach is taken for S.I. engines). One region is above the piston crown (squish region), one above the piston bowl and the third one is inside the bowl (Figure 1). In each of the regions the model solves an equation for conservation of angular momentum and two equations for the k-ε turbulence model. The resulting heat transfer coefficients calculated for a piston are shown in Figure 2, showing their values on the center portion of the head, the perimeter portion of the head, and on the liner. One may observe that these values vary strongly from surface to surface and in addition, the relative magnitudes of the heat transfer coefficients change

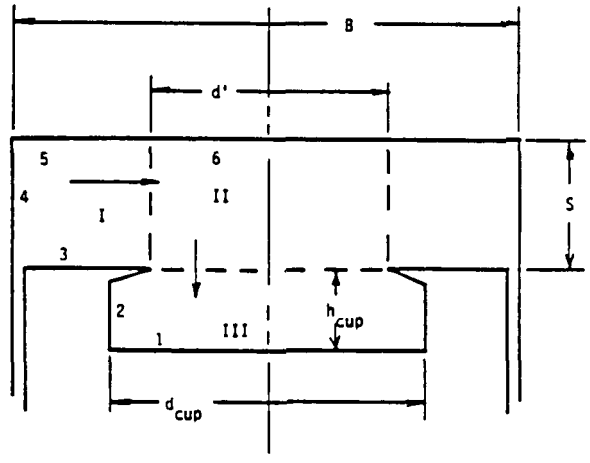

Figure 1. Flow regions appropriate for typical bowl-in-piston diesel engine geometries. Arrows indicate flow direction during compression stroke. Roman numbers refer to flow regions, arabic numbers refer to the elementary surfaces bounding those regions.

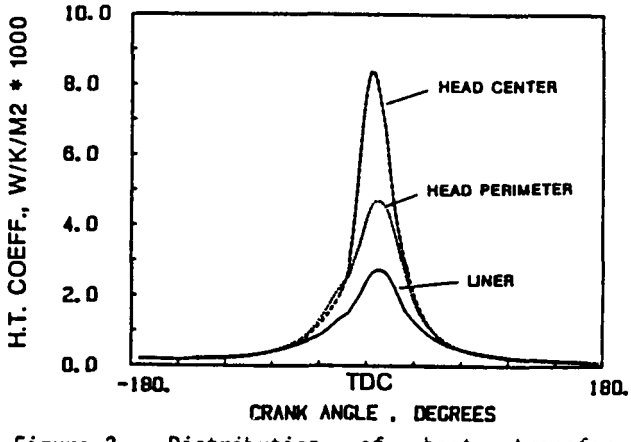

Figure 2. Distribution of heat transfer coefficients on various incylinder surfaces.

throughout the cycle. This reflects the changes in the flow velocities adjoining the individual surfaces.

When one averages the heat transfer coefficients over all of the surfaces, one can compare the resulting curve to the Annand correlation, which is meant to be applied uniformly to all surfaces. This has been done in Figure 3, where the coefficient of the Annand's correlation has been adjusted in order to give the same cycle-integrated heat rejection for the whole cylinder. It is seen that the flow-based model exhibits sensitivity to the in-cylinder flow development: it produces high values of heat transfer coefficients during intake due to the highly turbulent intake flows; it calculates high heat transfer coefficients near firing TDC due to squish, compression generated turbulence, and injection and combustion motions; finally it calculates low heat transfer coefficients during the relatively quiescent expansion and exhaust periods. By contrast, the Annand correlation shows none of these flow-related features.

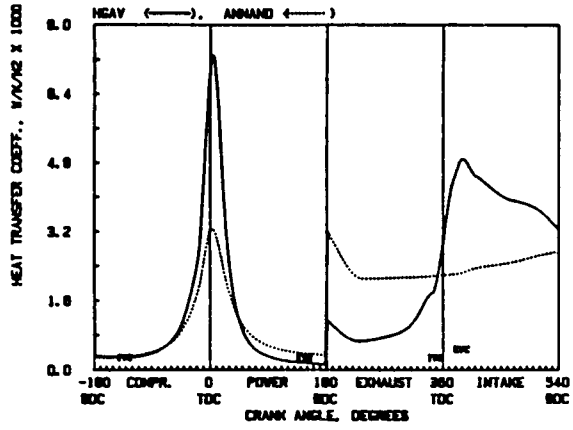

Figure 3. Area averaged heat transfer coefficient; comparison of flow-based model to Annand correlation.

Previous Radiation Heat Transfer Models. In order to calculate diesel engine radiation heat transfer, which is primarily due to soot, one must model these basic variables: soot loading (or soot volumetric fraction) in the combustion gases, radiation temperature and spatial distribution of the radiation heat transfer along combustion chamber walls. Most of the models of radiation used today provide none of the above variables, but calculate radiation heat flux as proportional to the fourth power of the mass-averaged gas temperature, make no account of soot loading, and make radiation flux uniform over all in-cylinder surfaces. The use of mass-averaged temperature is grossly incorrect, giving results that are about 10 times too low, requiring the use of large ad-hoc multipliers to compensate for it. More recently, there have been attempts to correct this situation, but none of these address all of the three basic variables simultaneously (see review in Morel and Keribar, 1986).

Present Radiation Heat Transfer Model. Due to soot formation during diesel combustion, thermal radiation from gases to surrounding combustion chamber surfaces is a significant component of heat transfer. Instantaneous and mean levels of heat radiation are functions of the volume and distribution of burning gas, amount of soot present in the burning gas, combustion chamber geometry, and also of surface emissivities and temperatures. The heat radiation model takes into account all of these dependencies (Morel and Keribar, 1986). The soot concentration levels are calculated using a kinetic model, which provides rates for soot formation and subsequent burnup as a function of engine parameters and crank angle. The spatial distribution of the heat radiation can be calculated from the volume and shape of the burned zone. The burned zone volume is calculated from the cycle thermodynamic simulation, and its shape and location are obtained from an empirically based geometric model. All soot is assumed to be contained within the burned gas. The spatial distribution also includes the effects of chamber geometry through the calculation of the actual optical thicknesses as seen from one surface when viewing another, or when viewing the burned zone. This is accomplished through the use of a zonal radiation model which divides the combustion chamber surface into seven individual subsurfaces. This model also represents the attenuation of radiation from one surface to another, as it passes through the absorbing burned zone, and accounts for multiple reflections of incident radiation from one surface to another.

Engine Simulation. All predictions presented here were generated using a comprehensive engine design analysis code, described in previous publications (see Morel et al, 1986).

EXPERIMENTAL SETUP

Engine. The experimental part of this work was performed on a Cummins single cylinder engine based on the 14-liter, NH-series heavy duty truck engine. Bore and stroke are 140 mm by 152 mm and the compression ratio is 15.7:1. The combustion chamber is quiescent and features centrally located, multi-jet direct injection into a shallow mexican hat piston cup which forms the principal part of the combustion chamber. A schematic drawing of the piston cup is shown in Figure 4. The injector is a production eight-orifice Cummins unit injector, cam/pushrod driven, operating on the Cummins P-T system. Injection timing can be adjusted by a special camshaft mechanism and is measured through a strain-gaged injector link

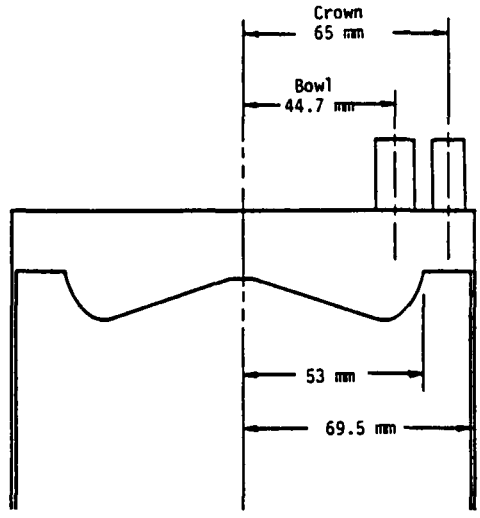

Figure 4. Piston bowl shape and probe locations.

rod. Supercharged operation is accomplished by supplying regulated high pressure air from an external compressor and accumulator to an intake plenum. This air also can be heated to reproduce typical levels of intake air temperature. Back pressure is controlled by a valve in the exhaust line. Although the engine normally has two intake and two exhaust valves, one intake valve was removed to accommodate instrumentation. Since the engine breathes very freely, this modification has very little effect on air consumption at low rpm. At higher speeds the inlet restriction resulting from using only one valve is offset by increasing inlet boost slightly until the desired air flow is attained.

The engine is supported by external circuits for fuel, lubrication oil and coolant. All fluids can be cooled or heated as required to maintain desired temperatures to the engine. Engine output is absorbed by a Westinghouse DC electric dynamometer rated at 56 kW from 2000 to 5000 rpm. The dynamometer also can supply 45 kW of motoring power over the 1800 to 5000 rpm range.

Instrumentation and Experimental Techniques.

The engine combustion chamber is accessible to the probes through two locations provided at the cylinder head. The first probe access views the squish region and the other location views the deepest section of the piston bowl. This access was created by removing an inlet valve and replacing it with a mounting insert. The locations of the two probes are shown in Figure 5 which displays a section through the head at the valve head plane. The probe accesses were designed to be compatible with both AVL pressure transducer (QP505) and Medtherm fast response thermocouple.

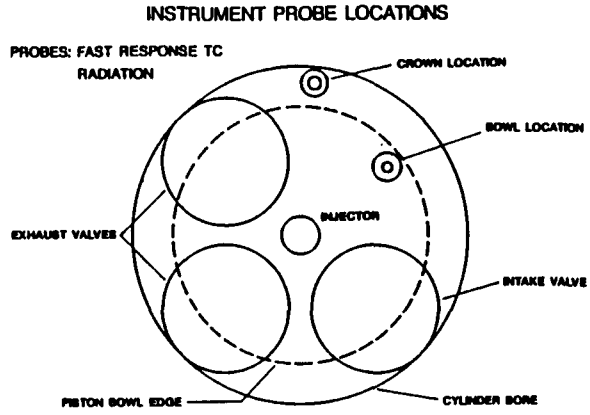

Figure 5. Section through engine head at the valve plane, showing probe locations.

The Medtherm total heat flux probe contains both a fast-response surface thermocouple and a sub-surface thermocouple located 5 mm below the surface. For fast response surface measurements the probe incorporates an electrically insulated thin nickel wire passing through a pure iron cylinder. The nickel wire and the iron cylinder are electrically connected by a thin nickel plating which forms a fast-response thermocouple junction at the probe surface. The sub-surface thermocouple is provided by welding a nickel wire onto the iron cylinder 5 mm from the plated end. The above assembly is swaged into a pure iron body whose external dimensions are compatible with the access provided for AVL pressure transducers. A common iron lead is attached to the iron body to complete the thermocouple lead wire set. The combination of the central nickel wire and the common iron lead attached to the iron body forms the surface thermocouple, whereas the in-depth nickel wire and the common iron lead forms the sub-surface thermocouple.

An experiment was devised to estimate the time constant of the Medtherm heat flux probes. A Nd:Yag laser was used as an energy source to rapidly deposit heat on the sensing face of the heat flux probe. The laser used had a nominal pulse width of 10nsec and pulse energy of 10mJ. It was operated at 20 Hz repetition rate and the thermocouple response was observed in an oscilloscope triggered by a pulse synchronous with the Q-Switch of the laser. By recording the rise time of the voltage signal, one can estimate the time constant of the heat flux gauge. It was found that the constant of the probe was between 2 and 3 μsec, which is more than an order of magnitude smaller than that required to resolve in-cylinder heat flux on a crank angle basis.

Both the indepth and the surface thermocouples are provided with differential leads to

minimize signal contamination by extraneous noises. The surface thermocouple voltage is measured in terms of the difference of the two thermocouple (surface and indepth) signals. This enables use of a higher amplifier gain (typically 5k -10k) in absence of large D.C. offset. The indepth thermocouple output is measured in absolute terms.

A dedicated data acquisition system was built around a PDP 11/23 CPU, an ADAC Corporation 1023FT-1622DMA A/D conversion system and DEC DRV11 clock. The system has 1 megabyte of solid-state memory. Since a portion of the memory is used for the I/O and data management system, about 800Kbytes is available for data storage, which corresponds to 6 to 7 runs. In practice, however, more consecutive runs are possible since data is continuously being transferred in the background to the mainframe computer, thereby freeing up memory space. The probe data was sampled at 0.6° CA resolution.

The A/D converter has a dynamic range of -10V and +10V. To enable fuller utilization of the dynamic range, the analog signals of the heat flux gage are amplified before being fed into the data acquisition system. The amplifier used is a D.C.-coupled differential amplifier (AM 502, Tektronics) having gains up to 100 k with selectable upper and lower -3 db points. The maximum upper -3 db point is 1 MHz and is operated at 10 kHz.

Heat Flux Data Reduction Scheme: In a typical operation, seventeen cycles of data were collected at 0.6 CA resolution for each of the operating conditions. The data reduction was performed on the cycle averaged surface thermocouple signal, to which was added the averaged indepth thermocouple signal to obtain the absolute voltage. This voltage was converted into temperature by interpolating a thermocouple calibration table. To eliminate high frequency noise, the temperature-crankangle record was then smoothed by a sliding least square (cubic, 20 CA interval) fit. The smoothed signal was decomposed into its harmonics by choosing 512 equally spaced points and applying Fast Fourier Transform (FFT). The first 200 harmonics were retained to calculate the cyclic heat flux rate using a 1-D heat conduction formula (Eckert and Drake, 1972):

$$Q_w = k/L\,(T_w - T_d) + k \sum_{1}^{m} \sqrt{(\omega n/\alpha)}\,[A_n \cos(n\omega t - \pi/4) - B_n \sin(n\omega t - \pi/4)]$$

where

- k = thermal conductivity of the heat flux gage
- L = distance between indepth and surface thermocouples
- T_w = average surface tempeature
- T_d^w = indepth temperature
- ω = 0.5 x angular speed of the engine
- α = thermal diffusivity of the heat flux gage
- m = number of harmonics retained

The above equation is strictly valid for cases where material properties are not functions of temperature. Although the thermal diffusivity and the conductivity of pure iron (material of the heat flux gage) vary with temperature, it is reasonable to assume that within the penetration depth the temperature, and the properties, are uniform. Hence, the above equation is still valid provided property values at the operating temperature are used. The correction factor that has to be applied to the unsteady portion of the heat flux calculated with room temperature properties is given by

$$F_c = \sqrt{(k\rho c)_o/(k\rho c)_r}$$

where ρ and c are density and specific heat, respectively, and o and r pertain to operating and room temperature, respectively. This correction factor may be deduced from a one-dimensional exact solution (see eg. Eckert and Drake, 1972).

ENGINE TEST MATRIX

The engine tests were carried out over a broad range of engine operating points representing typical conditions for a turbocharged heavy-duty diesel. To make these conditions realistic, engine simulations were made of the Cummins six-cylinder NH engine on which the single cylinder test engine is based. The specific multi-cylinder engine simulated was the NTC-350 for which Cummins Engine Company supplied detailed engine description, turbocharger maps, and test data. The simulations were carried out using the same engine design analysis code used for the predictions of radiation heat flux. After correlation with the Cummins-supplied test data, the code was used to calculate operating conditions--intake pressure and temperature, exhaust pressure--at four engine speeds and several loads at each speed to form the test matrix shown in Table I. This assured that all of the operating points were realistic steady-state points of an actual heavy-duty highway diesel engine. Due to dynamometer limitations the peak loads were limited at the lower engine speeds below the full load values. Also, the values given in Table I are those actually observed during the experiments, and differ in minor ways from the target values determined by the simulation.

RESULTS

Motored Runs. In this set of experiments, the engine was motored at four different speeds 1000, 1300, 1700 and 2100 rpm. Four sets of data were acquired at each speed: at two

Speed rpm	Nominal Load %	IMAP bar	IMAT °K	EMAP bar	A/F	BOI °BTC
2100	100	2.45	355	2.09	31.8	23
2100	75	1.86	340	1.74	33.7	18
2100	50	1.60	349	1.53	40.8	13.5
2100	25	1.25	337	1.32	56.8	9.5
1700	88	2.07	349	1.62	33.0	21
1700	50	1.53	355	1.36	40.1	14
1700	25	1.27	356	1.21	65.9	9
1300	75	1.59	331	1.42	27.0	21.5
1300	50	1.30	326	1.26	29.6	17
1300	35	1.21	340	1.19	37.6	13
1300	25	1.12	334	1.17	45.6	11
1000	75	1.36	342	1.22	18.8	24.5
1000	50	1.20	344	1.14	28.2	16
1000	25	1.09	348	1.12	47.2	10.5

Table I. Engine operating conditions for the firing runs.

different probe locations and at two different intake pressures of 1.2 and 2.0 bar respectively. The engine back pressure was always set equal to the intake pressure.

Figure 6a shows the results obtained at the bowl location (probe installed in the head in the location facing the bowl). The heat flux is seen to increase with increasing speed due to increasing intensity of in-cylinder gas motions. A simular result is obtained at the crown location (Figure 6b), except that the magnitude of the heat flux is somewhat higher. The heat flux levels obtained at the higher intake pressure were about 50% higher, but otherwise they were quite simular to those shown in Figure 3. The curves of the heat flux display asymmetry, in that they have a smaller slope during the compression stroke than during the expansion stroke. This characteristic behavior had been already observed by previous

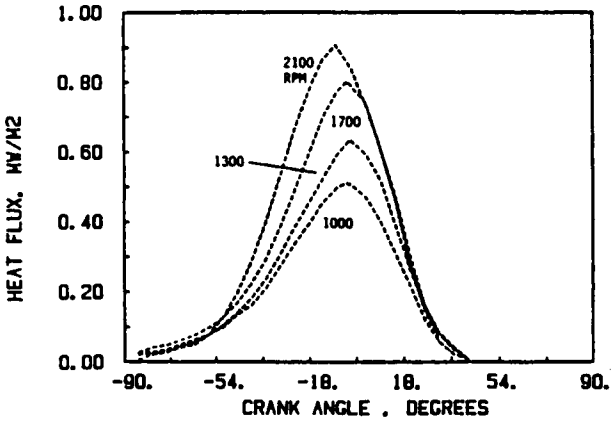

Figure 6a. Measured heat flux at bowl location, motoring operation at four engine speeds, $P_{int} = P_{exh} = 1.2$ bar.

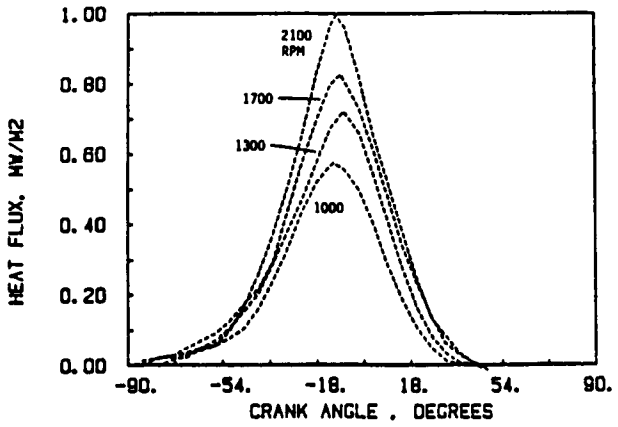

Figure 6b. Measured heat flux at crown location, motoring operation at four engine speeds, $P_{int} = P_{exh} = 1.2$ bar.

investigators, eg. by Dao et al (1973) and Annand and Pinfold (1980), and its origin lies in the gradually decreasing intensity of in-cylinder motions caused by wall friction and turbulence decay.

Fired Runs. The results obtained at the bowl position in the fired runs are presented in Figure 7 a-d. The heat flux curves are seen to have much larger maxima than for the motored runs, in fact up to 10 times larger at the highest load levels. The heat flux is seen to be relatively low during the compression stroke, increasing relatively abruptly near TDC when the combustion begins. At each speed, the rapid increase in the heat flux occurs earlier and earlier with increasing load. This is mainly a consequence of the Cummins P-T injection system, which advances the beginning of injection as the load is increased.

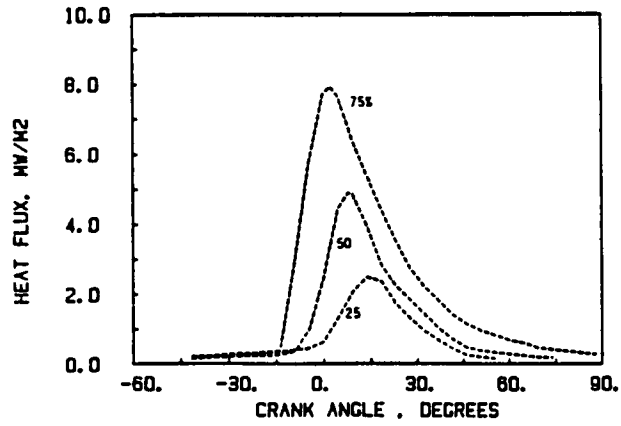

Figure 7a. Measured heat flux at bowl location, firing operation at several loads, 1000 rpm.

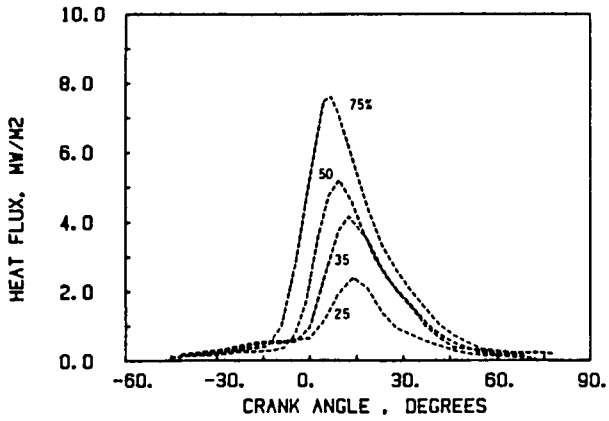

Figure 7b. Measured heat flux at bowl location, firing operation at several loads, 1300 rpm.

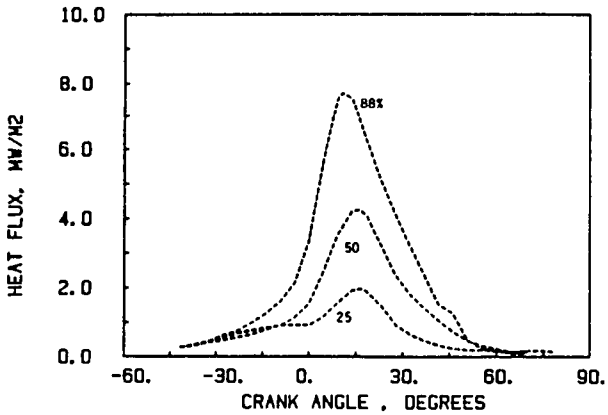

Figure 7c. Measured heat flux at bowl location, firing operation at several loads, 1700 rpm.

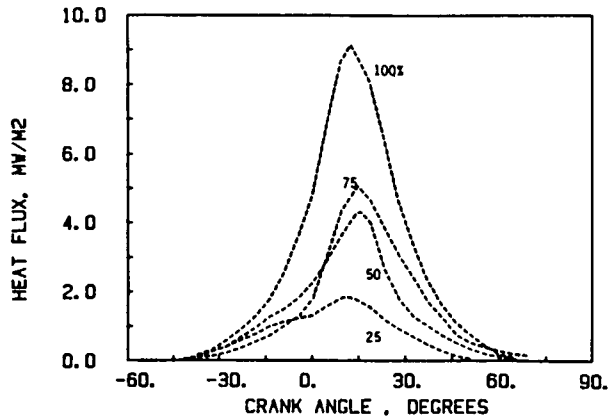

Figure 7d. Measured heat flux at bowl location, firing operation at several loads, 2100 rpm.

The heat flux measured in the crown location is shown in Figure 8 a-d. As can be seen, the heat flux in this location differs quite substantially from the bowl location. First of all, there is about a 10°CA delay in the onset of the combustion-produced heat flux increase. This is caused by the finite time it takes for the flame to propagate into the crown region. Further, the maximum heat flux levels are about two times smaller than in the bowl region, due to lower intensity of fluid flow motions in that location. This is in agreement with the observations made by Dent and Suliaman (1977) and VanGerpen et al (1985).

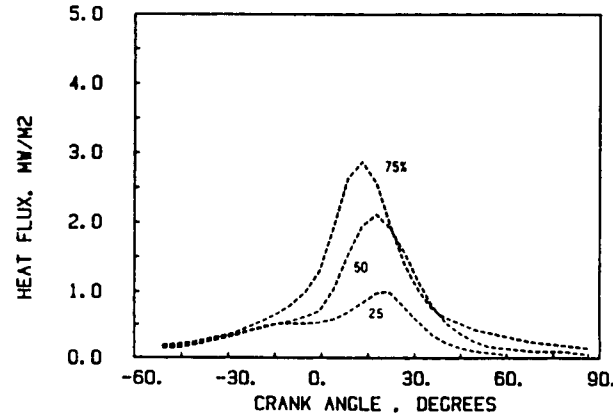

Figure 8a. Measured heat flux at crown location, firing operation at several loads, 1000 rpm.

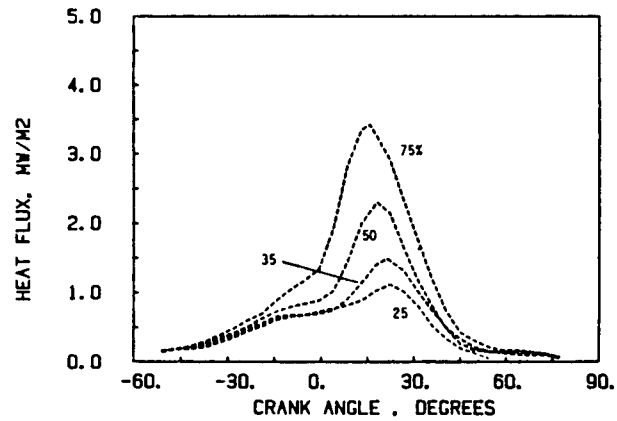

Figure 8b. Measured heat flux at crown location, firing operation at several loads, 1300 rpm.

The trends of the peak heat flux values with engine speed and load are summarized in Figure 9. It is plotted with respect to fueling rate per stroke. The fact that the data show monotonic trends over the range of speeds and loads with only a small scatter, suggests that the data set is consistent within itself and thus suitable for use in model validation.

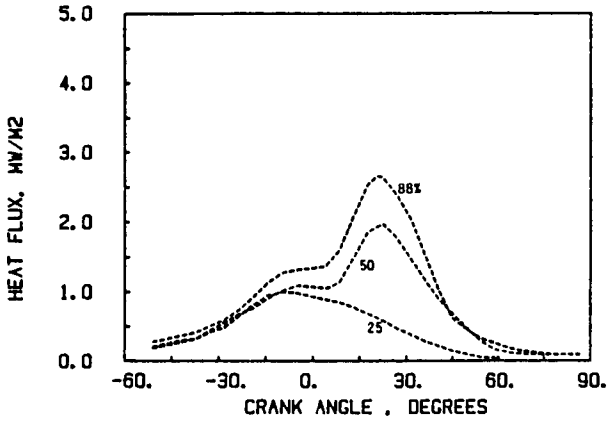

Figure 8c. Measured heat flux at crown location, firing operation at several loads, 1700 rpm.

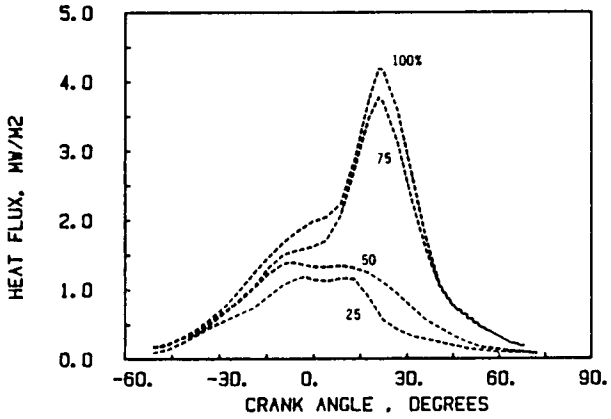

Figure 8d. Measured heat flux at crown location, firing operation at several loads, 2100 rpm.

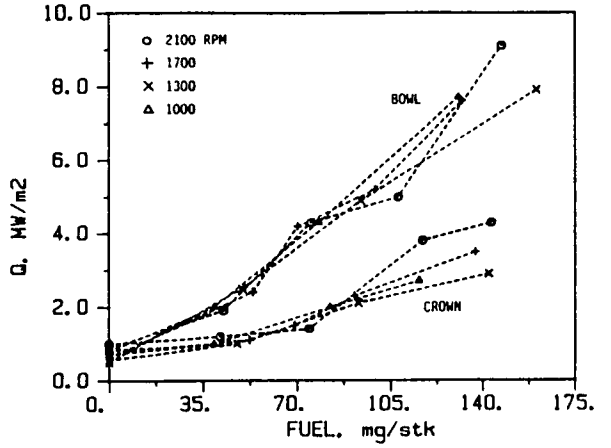

Figure 9. Measured heat flux vs. fuel/stroke at the two probe locations.

Cycle-to-cycle variations in the magnitude of the surface temperature swings were observed at both locations. A typical cycle-to-cycle variation in the crown location is shown in Figure 10. It is shown in terms of the cyclic swing ratio, defined as the cyclic thermocouple voltage swing (maximum-minimum) normalized by the average swing, averaged over 34 cycles. Although these variations can be substantial, they tend to alternate on a short time scale and thus the average over 17 or 34 cycles yielded quite repeatable results for runs performed on different days.

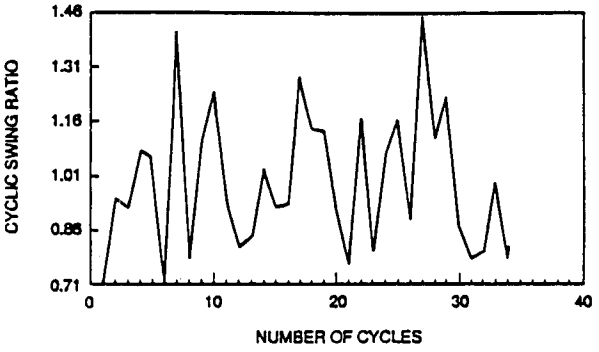

Figure 10. Typical record of cycle-to-cycle variation of peak heat flux with respect to cycle-mean peak heat flux. Crown location, 2100 rpm, 50% load.

COMPARISON OF PREDICTIONS TO DATA

Annand Correlation vs Flow-based Model. In Figure 11a are presented the data taken at the rated engine conditions (rated speed and load). The differences between the data taken at the two probe locations are seen to be quite pronounced. That was planned at the start of the experiments, and the two locations were chosen because large differences were expected between the heat fluxes there. The figure also includes a prediction obtained using Annand's correlation. It is seen that the correlation fails to show the differences between the two locations. In fact, the heat flux at the bowl location is actually lower than at the crown location, and this is due to the higher wall temperature at the uncooled valve insert location. This failure of the widely used correlations such as Annand (1963) or Woshni (1967) (Figure 11b) to represent correctly detailed features and to provide spatial resolution has been well documented in the literature, see e.g. Van Gerpen et al (1985).

By contrast, the flow-based model shows an excellent agreement with data (Figure 11c). The maximum values of the heat flux at the two locations are reproduced. Also, there is a good similarity in the shape of the heat flux at the crown location.

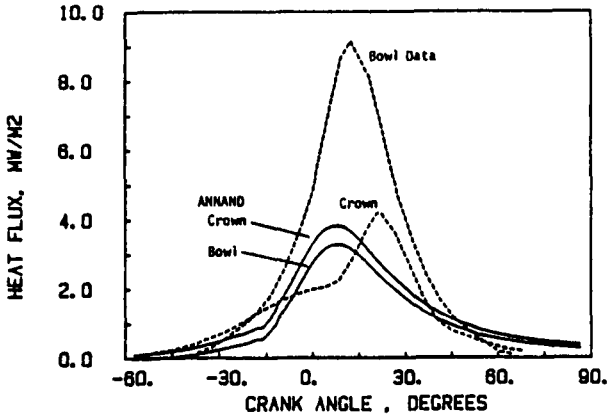

Figure 11a. Heat flux at rated conditions, comparison of Annand correlation vs. data.

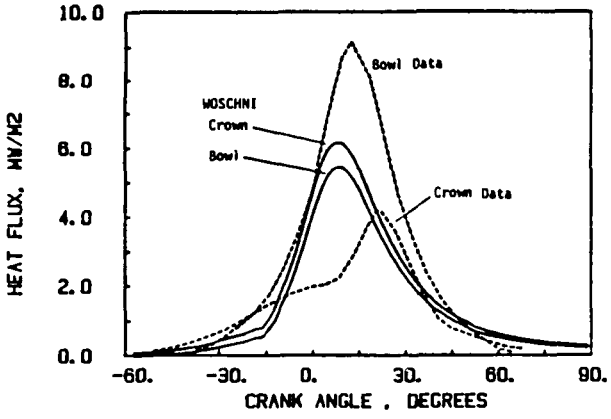

Figure 11b. Heat flux at rated conditions, comparison of Woschni correlation vs. data.

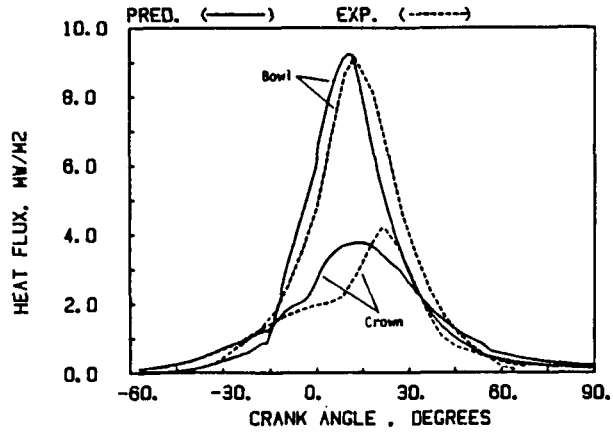

Figure 11c. Heat flux at rated conditions, comparison of flow based model vs. data.

The surface temperature swing at the bowl location at rated conditions is shown in Figure 12. Its magnitude is about 28K. The prediction shows a very good agreement with the experiment (the same material properties were used both in IRIS and in the experimental data reduction scheme), and this is not surprising in view of the agreement in the heat fluxes seen in Figure 11b.

Flow-based Model vs. Data. The agreement seen in Figure 11c extends over the entire set of data, as will be shown in the subsequent figures.

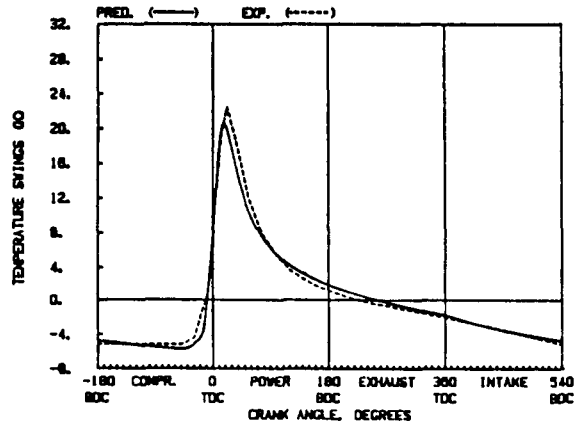

Figure 12. Wall temperature swings at the bowl location, prediction vs. data.

In motored runs, Figure 13a-b, the predictions agree with data at all speeds at both probe locations, simulating correctly the trends with speed, as well as spatial variations between the two locations. Also, the asymmetry of the heat flux curves, commented on earlier, is

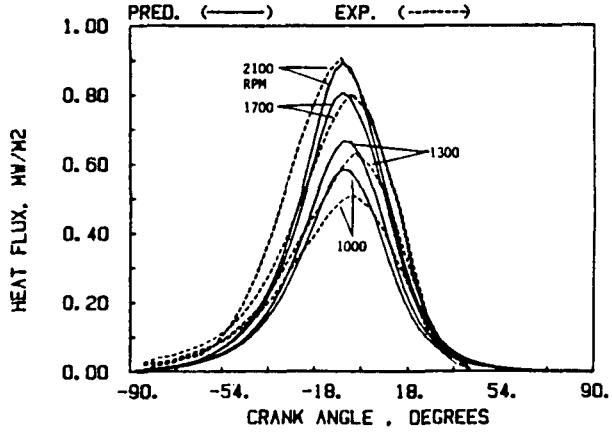

Figure 13a. Comparison of predictions and data for motoring operation, bowl location, various engine speeds, $p_{int} = p_{exh} = 1.2$ bar.

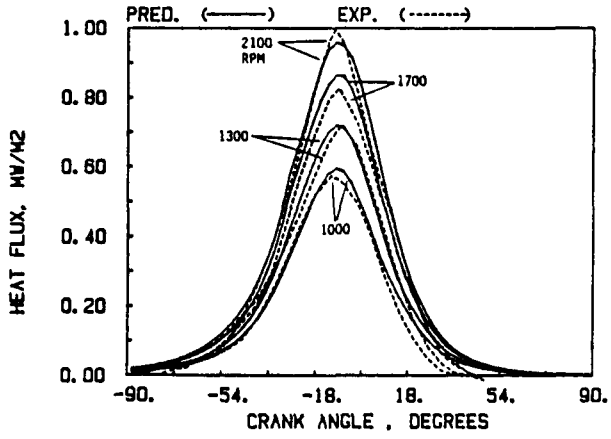

Figure 13b. Comparison of predictions and data for motoring operation, crown location, various engine speeds, $p_{int} = p_{exh} = 1.2$ bar.

predicted well as a result of a correct simulation of the rate of decay of in-cylinder flow motions.

The agreement is similarly good under firing conditions. The comparison of predictions to data is shown in Figures 14a-d for the bowl location, and in Figures 15a-d for the crown location. The model tends to show a fairly gradual and consistent change in heat flux shape and magnitude with increasing load; this is an expected behavior for a model. By comparison, the experimental curves exhibit some scatter in the trends, sometimes being somewhat below the predicted ones, sometimes above them. Overall, however, the predictions compare quite well with the data.

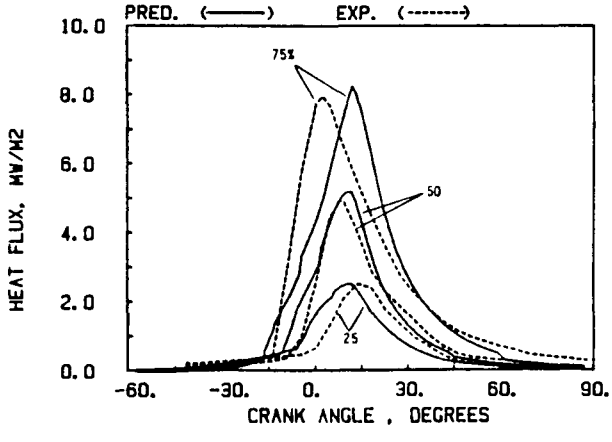

Figure 14a. Comparison of predictions and data for firing engine, bowl location, 1000 rpm. Three loads.

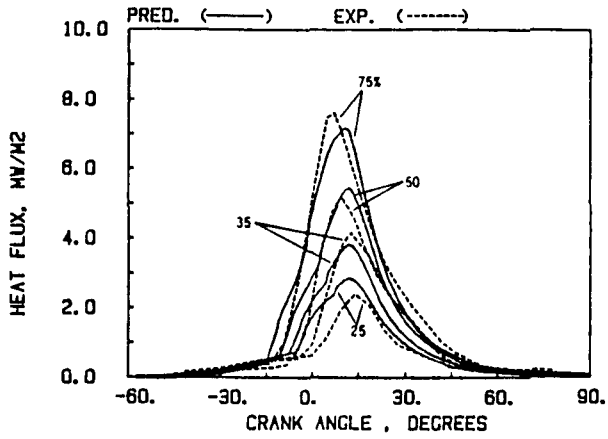

Figure 14b. Comparison of predictions and data for firing engine, bowl location, 1300 rpm. Four loads.

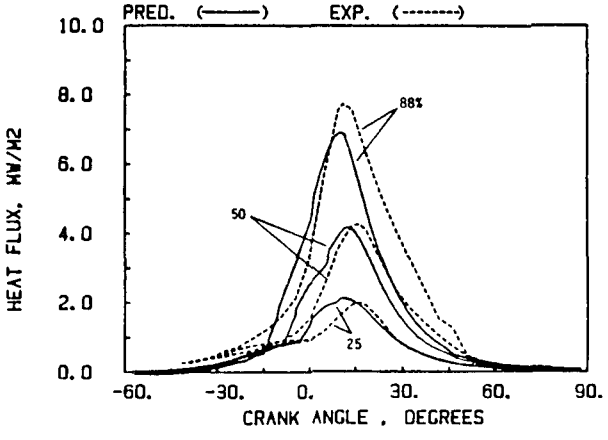

Figure 14c. Comparison of predictions and data for firing engine, bowl location, 1700 rpm. Three loads.

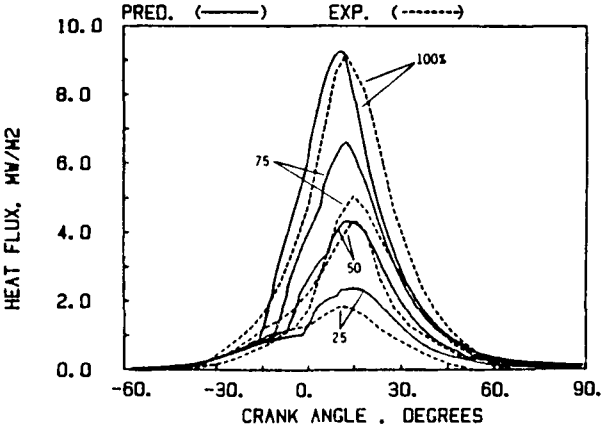

Figure 14d. Comparison of predictions and data for firing engine, bowl location, 2100 rpm. Four loads.

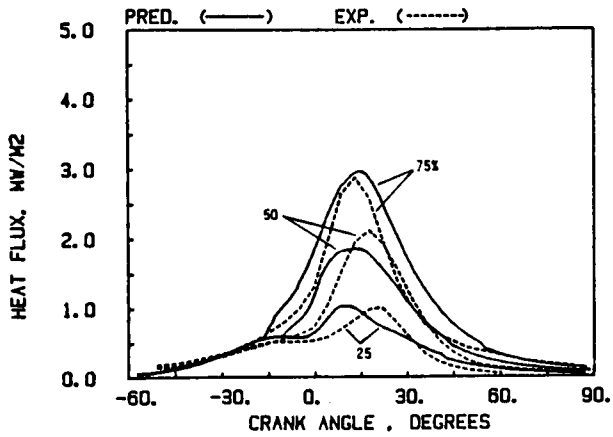

Figure 15a. Comparison of predictions and data for firing engine, crown location, 1,000 rpm. Three loads.

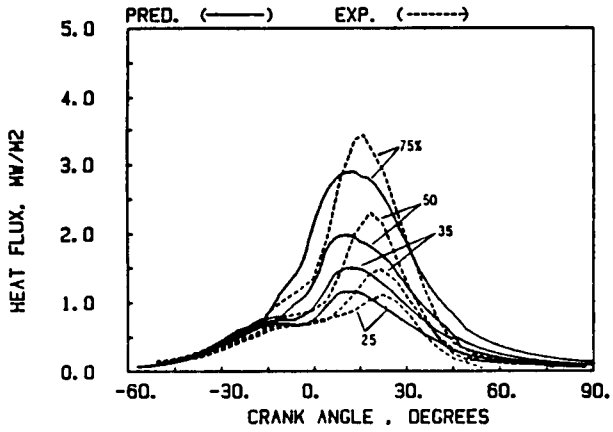

Figure 15b. Comparison of predictions and data for firing engine, crown location, 1300 rpm. Four loads.

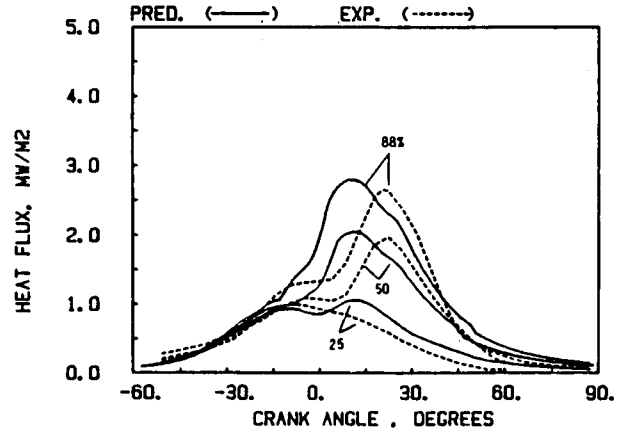

Figure 15c. Comparison of predictions and data for firing engine, crown location, 1700 rpm. Three loads.

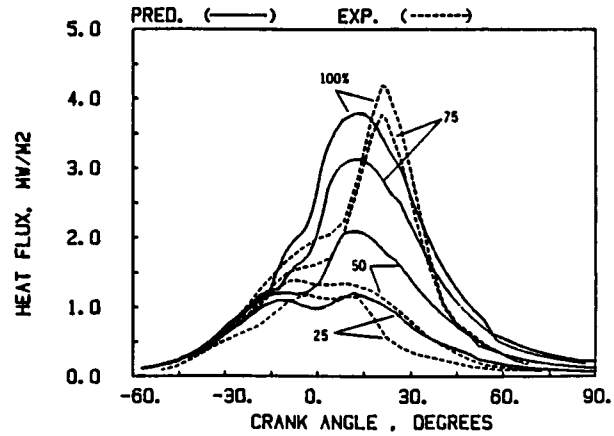

Figure 15d. Comparison of predictions and data for firing engine, crown location, 2100 rpm. Four loads.

This is also seen in Figures 16 and 17, which show the trends of peak heat flux with speed and load. The predicted curves are smooth and almost straight, while the experiments show some scatter. But again, there is a good agreement in trends and magnitude at both of the locations.

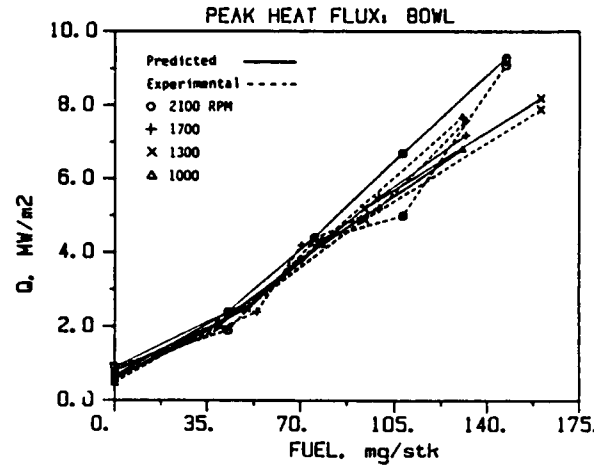

Figure 16. Comparison of predictions and data for peak heat flux, bowl location.

CONCLUSIONS

1. A comprehensive set of heat transfer data was obtained in a single cylinder D.I. diesel engine. The data is consistent and thus suitable for validation of heat transfer models.

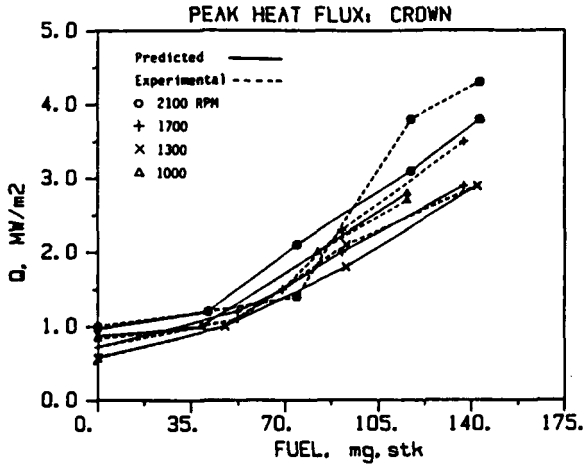

Figure 17. Comparison of predictions and data for peak heat flux, crown location.

2. The peak heat flux measured under firing conditions at head location facing the piston crown was about two times lower than that measured at a head location facing the piston crown. Also, the crown location data showed a delay in heat flux peak, caused by the piston shielding and by the finite time of flame propagation.

3. The situation was reversed under motoring conditions, and the heat flux at the crown location was slightly higher than in the bowl location.

4. Comparison of Annand's correlation to the data showed its inability to distinguish between the probe locations or to predict the correct magnitude of the heat flux. This finding was in agreement with findings made by previous investigators.

5. The present flow-based model was found to predict the magnitude and shape of the heat flux at both locations much more accurately, capturing correctly the differences between them under firing conditions. It also reproduced the behavior under motoring conditions. Overall, it gave a very good agreement over all of the operating conditions, motoring and firing, spanning a wide range of peak heat fluxes exceeding 15:1 from the lowest to the highest.

ACKNOWLEDGEMENTS

This work has been carried out under the Heavy Duty Transport Technology program, Contract DEN3-342, sponsored by the U. S. Department of Energy and administered by NASA Lewis Research Center. The authors wish to thank Mr. James C. Wood, Project Manager at NASA-Lewis for his constant interest, and for the support NASA technical personnel were providing in the development of heat transfer probe technology. Cummins Engine Company has been an active voluntary industrial participant in this project, contributing their single cylinder engine and other material resources, as well as technical advice regarding the engine installation and operation. In particular, Messrs. Kevin Hoag, Roy Primus and Gary Hunter have been very constructive in their assistance. Very significant contributions were also provided by other members of the Purdue research team, including Prof. C. Warner, Prof. C. Ferguson, Mr. G. Rodriguez, Mr. F. G. Riser and Mr. G. Urbanus.

REFERENCES

Annand, W. J. D. (1963), "Heat Transfer in the Cylinders of Reciprocating Internal Combustion Engines," Proc. Inst. Mech. Engs., Vol. 177, No. 36, p. 973

Annand, W. J. D. and Pinfold, D. (1980), "Heat Transfer in the Cylinder of a Motored Reciprocating Engine," SAE Paper 800457.

Dao, K., Uyehara, O. A. and Myers, P. S. (1973), "Heat Transfer Rates at Gas-Wall Interfaces in Motored Piston Engine," SAE 730632.

Dent, J. C. and Suliaman, S. J. (1977), "Convective and Radiative Heat Transfer in a High Swirl Direct Injection Diesel Engine," SAE Paper 770407.

Eckert and Drake (1972), "Analysis of Heat and Mass Transfer," McGraw-Hill, p. 214.

Morel, T. and Keribar, R. (1985), "A Model for Predicting Spatially and Time Resolved Convective Heat Transfer in Bowl-in-Piston Combustion Chambers," SAE Paper 850204.

Morel, T. and Keribar, R. (1986), "Heat Radiation in D.I. Diesel Engines," SAE Paper 860445.

Morel, T., Keribar, R., Blumberg, P. N. and Fort, E. F. (1986), "Examination of Key Issues in Low Heat Rejection Engines," SAE Paper 860316.

Van Gerpen, J. H., Huang, C. and Borman, G. L. (1985), "The Effects of Swirl and Injection Parameters on Diesel Combustion and Heat Transfer," SAE Paper 850265.

Woschni, G. (1967), "A Universally Applicable Equation for the Instantaneous Heat Transfer Coefficient in the Internal Combustion Engine," SAE Paper 670931.

APPENDIX A-2

EXPERIMENTAL AND ANALYTICAL STUDY OF HEAT RADIATION IN A DIESEL ENGINE

ABSTRACT

An experimental study was conducted of the heat radiation in a single-cylinder direct injection 14ℓ diesel engine. The engine was operated at speeds ranging from 1000 to 2100 RPM and a variety of loads. The radiation was measured using a specially designed fiber-optics probe operating on the two-color principle. The probe was located in the head at two different locations: in one location it faced the piston bowl and in the other it faced the piston crown. The data obtained from the probe was processed to deduce the apparent radiation temperature and soot volume concentration as a function of crank angle. The resultant profiles of radiation temperature and of the soot volume concentrations were compared with the predictions of a zonal heat radiation model imbedded in a detailed two-zone thermodynamic cycle code. The agreement between the model and the measurements was found to be good, both in trends and in magnitudes.

DURING THE COMBUSTION PROCESS in a diesel engine, soot particles are produced due to locally rich combustion. Although some unburned soot particles persist and are present in the exhaust along with other combustion products, a major portion of these soot particles is oxidized during the combustion period into carbon-dioxide and carbon monoxide. The soot particles emit radiation during the formation and oxidation periods when their temperatures are high, contributing significantly to the total in-cylinder heat transfer process. Although the importance of energy transport by radiation heat transfer in diesel engines is accepted by most engine researchers, its relative contribution to the total transfer is an issue which generates much discussion. As pointed out by Morel and Keribar (1986), the uncertainty in the relative contribution is due to the strong dependence upon the engine combustion chamber geometry and on the operating conditions. The data available in the literature are, in general, obtained by probes which are not identical in principle and, hence, do not necessarily measure the same quantities. In addition, geometry of the engines and the operating conditions used in the experiments differ widely, thereby rendering comparative study difficult. The data available in the literature tends to be incomplete in the description of the engine and of the detailed engine operating conditions, making comparison of predictions to these earlier experiments difficult.

In view of the above, there is a strong need for coupled experimental-analytical studies of heat radiation in diesel engines. In this paper we describe the acquisition of a set of well characterized measurements, which can be used to validate a previously developed detailed analytical model for in-cylinder heat radiation. Once validated, this model can be used to estimate radiant heat transfer in engines of different geometries, materials and operating conditions. The measurements were compared to predictions obtained using a previously developed heat radiation model. The description of the model and the comparisons of measurements and of predictions are also included in the paper.

MEASUREMENT METHODS FOR RADIATION HEAT TRANSFER

The direct measurement of radiation heat transfer in an internal combustion engine is a difficult experimental task. The earliest attempts to make direct measurements of local radiant heat transfer to the combustion chamber walls were only partially successful (e.g. Oguri et al., 1971) for reasons described in a later section. Later efforts relied on indirect measurements of pertinent governing

0148-7191/87/0223-0571$02.50

parameters (e.g. radiation temperature, optical depth, etc.) from which the radiant heat transfer could be calculated using a combination of first principles and realistic assumptions. The probes associated with radiation measurements can be broadly classified into four groups:

1) shielded fast response thermocouples,
2) pyroelectric detection devices,
3) discrete wavelength radiation sensing,
4) special optical diagnostic tools.

Some of the initial radiation heat transfer measurement attempts were performed with probes belonging to the first category. Ebersole et al. (1963) used the output of a fast response thermocouple shielded by a sapphire window in a two-cycle DI diesel engine to estimate radiation heat transfer. Oguri et al. (1971, 1972) and Stradomskiy et al. (1978) used similar probes to measure radiant heat flux in diesel engines. This type of probe is constructed in a way that permits only the radiant portion of the heat transfer to reach the fast response thermocouple. Associated with this probe, there are a number of design problems including keeping the window clean, avoiding contamination by the convective part of the heat transfer via conduction through the window, and minimizing occlusion of a portion of the hemispherical field-of-view by the hardware.

The probe used by Dent and Suliaman (1977) to measure heat transfer in a naturally aspirated diesel engine falls into the second group. A pyroelectric detector placed behind a Irtran-4 window responds to the rate of change of temperature caused by the radiant energy absorbed by the pyroelectric ceramic chip. The detector is calibrated by referencing to a chopped blackbody source. This detector also suffers from some of the same limitations as those of the first group.

The third method involves measurement of the line-of-sight radiant intensity at multiple wavelengths. The first such measurement was probably made by Uyehara et al. (1947) in an IDI diesel engine. Since then, the technique and the acquisition and reduction methods have undergone much improvement. Flynn et al (1972) made monochromatic intensity measurements at seven wavelengths in the infrared region of the spectrum. In this method, the measured intensities are equated to a product of the spectral emittance function and Planck's radiation distribution function. A calculation is performed to obtain the "best fit" radiation temperature and extinction coefficient. The measurements by Matsui et al. (1979, 1982) and Kamimoto et al. (1975) in DI diesel engines, employed the more common two-color version of the above method.

The fourth group includes a broad range of methods, e.g. absorption-emission measurements (Shimizu, 1973) and Coherent Anti-stokes Raman Spectroscopy (CARS) (Lucht et al., 1986). These methods, in general, require more elaborate optical systems and access and, in the case of CARS, more elaborate data reduction schemes. As a result, these methods have been restricted to a small number of laboratories and are generally used with simplified research engine geometries.

PRESENT METHOD OF MEASUREMENT

In the present study a two color method, similar to the one used by Kamimoto (1975), was employed. The technique involves measurement of the radiation intensities at two wavelengths to obtain the radiation temperature and the extinction coefficient.

Probe. The radiation detection system, developed and first used by C. Fiene employs a bifurcated fiber optics bundle (Figure 1) which provides a simple means of collecting radiation energy transmitted by the sapphire access window. The collected energy is split and directed to two detectors, each sensing a different narrow band of radiation. The sapphire window is mounted in a small holder and is recessed from the combustion chamber. The numerical aperture of the recessed window and the fiber optics assembly is 7.5°.

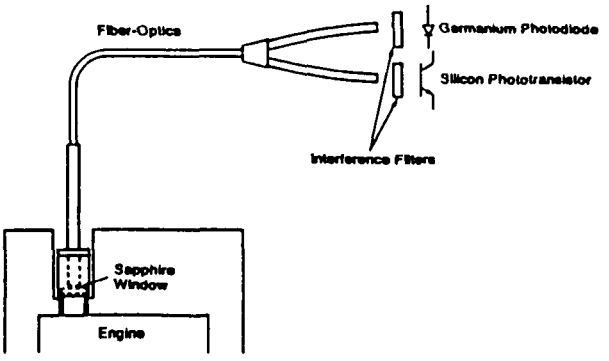

Figure 1. A schematic of the two-color radiation probe.

Method. Each of the detectors generates a voltage signal proportional to the radiation intensity at the particular wavelength and a calibration is performed to relate the voltage signal to the corresponding spectral intensity viewed by the probe. The calibration process can be illustrated by considering the expression for the signal generated by a detector:

$$V = \int S_\lambda \tau_o \tau_f I_\lambda dA_d d\Omega d\lambda \qquad (1)$$

where

Ω = solid angle viewed by the probe

A_d = sensitive area of the detector

S_λ = responsivity of the detector

τ_o = transmittance of the viewing optics

τ_f = transmittance of the narrow band pass filter

I_λ = intensity of the radiation field

λ = wavelength

Under the assumptions that (1) the radiation intensity is uniform over the solid angle viewed; (2) the interference filter has a gaussian transmittance function; (3) the detector operates in the linear region; and (4) the transmittance of the viewing optics is constant over the narrow wavelength band, equation (1) reduces to the form,

$$V = C\, I_\lambda \qquad (2)$$

The constant C lumps a number of parameters such as the band center transmittance and the half-width of the filter, the solid angle, detector responsivity, etc. The validity of the above equation was demonstrated by performing a calibration using a NBS traceable blackbody source capable of operating at up to 3000K. Figure 2 shows an example of a typical calibration. The small non-zero y-axis intercept is probably due to experimental errors.

Several steps were taken to ensure that quality of the data would be maintained throughout the entire test matrix (to be described subsequently). Early in our work it was observed that the signal could be affected by bending of the fiber optics bundle. To minimize this effect, the geometry of the fiber optics bundle and of the entire assembly was kept invariant during both running time and calibration by enclosing the entire probe assembly in a rigid tube. The optical probe was calibrated both before and after the collection of a data set for a single engine operating condition. The calibration used for reduction of data from that single operating condition was the bisector of the two calibrations bracketing that operating point. This practice minimized the effect of decreased window transmittance due to sooting. The recessed location of the window from the combustion chamber, as described previously, also helped prevent excessive soot buildup, and thus the change in probe sensitivity due to soot deposition during data taking at a single operating point was quite modest, and the associated error was small.

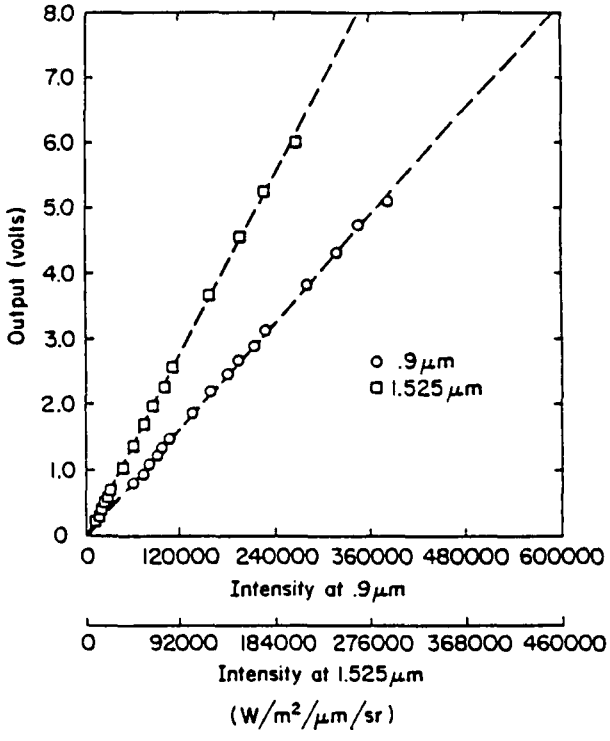

Figure 2. A typical set of calibration curves for the radiation probe.

The choice of the two wavelengths was based on several considerations. The upper limit of the wavelength is dictated by the transmittance of the fiber optics bundle and was determined to be 2.0 μm. At certain wavelength bands, continuum soot radiation is supplemented by gaseous radiations (CO_2, H_2O). Hence, wavelengths 0.9 μm and 1.525 μm, which are free from such contamination, were chosen. In addition, at these wavelengths blackbody radiation modulation (dI_b/dT) rate is higher than at wavelengths farther into the visible region (e.g. 0.528 μm used by Matsui et al., 1982). As a consequence, the computed $f_v L$ (the product of soot volume fraction and a characteristics length) is much less sensitive to voltage measurement error for the current choice of wavelengths than other wavelength pairs used by some previous investigators. The above fact was also demonstrated by a sensitivity analysis, whose details are omitted here.

The filters used for detection of monochromatic radiation have a bandwidth of 0.034 μm. At the shorter wavelength, the spectral intensity is detected by a silicon detector (TIED460 or TIED461, Texas Instruments) and at the longer wavelength, by a germanium detector (G-010, Electro-Optical Systems).

The calibration curves for the two spectral conditions are of the form

$$V_1 = a_1 + b_1 \, Ib_1 \quad (3a)$$

$$V_2 = a_2 + b_2 \, Ib_2 \quad (3b)$$

where V is the detector voltage, Ib is the blackbody intensity and subscripts 1 and 2 denote the two spectral conditions.

Two nonlinear equations can now be constructed whose solutions will give the apparent radiation temperature and a quantity related to the spectral emittance of the soot cloud.

$$F_1 = V_1 - (a_1 + b_1 \, \varepsilon_1 \, Ib_1) = 0 \quad (4a)$$

$$F_2 = V_2 - (a_2 + b_2 \, \varepsilon_2 \, Ib_2) = 0 \quad (4b)$$

where ε is the spectral emittance, defined by the following equation:

$$\varepsilon_1 = 1 - \exp(-g \, f_v L/\lambda_1{}^n) \quad (5a)$$

$$\varepsilon_2 = 1 - \exp(-g \, f_v L/\lambda_2{}^n) \quad (5b)$$

where λ_1 and λ_2 are the two wavelengths.

The value of 'g' is taken as 6.3, based on Gray and Muller (1974). The selection of a value for 'n' warrants some discussion here. Hottel et al. (1932), based partly on some previously published data (on stearin soot, acetylene soot, amyle acetate soot, Cambridge city gas soot etc.), concluded that the exponent 'n' equals 1.39 for wavelengths shorter than 0.8 μm, and 0.95 for all longer wavelengths. A later study by Siddal et al. (1962) demonstrated wide variations of 'n' for soot of different origin and in many instances exhibited strong dependence on wavelength. However, their data did not show any abrupt change in 'n' at the visible-infrared boundary. Liebert et al. (1970) while studying candle soot observed mild variation in 'n' with the thickness of the soot layer (deposited on a flat surface), but little wavelength dependence. Their measured value of 'n' (0.95 $\pm$ 0.1) was invariant from 0.35 μm to far into the infrared. This observation is in contradiction with Hottel's (1932) findings.

It can be seen from equation (5) that the sensitivity of the emittance function to 'n' is small in the visible region (where λ is near unity), and it is only for the longer wavelengths that the variation in emittance with 'n' becomes a factor. Hence, for the emittance function at 1.525 μm a proper choice of 'n' is necessary. Upon review of the available data it was felt that for hydrocarbon soot the value of 'n' is closer to 1.0 than 1.39. This led us to choose a value of 'n' equal to 0.95. An uncertainty analysis was carried out for an uncertainty band of $\pm$ 0.1 suggested by Liebert et al (1970). It was found that the uncertainties in the deduced radiation temperature and $f_v L$ for the wavelengths used by the present sensor are on the order of 1% and 10%, respectively due to this uncertainty in 'n'.

It can be seen, that by substitution of equations 5a and 5b, equations 4a and 4b are functions of $f_v L$ and radiation temperature only. The dependence of the temperature is through Planck's radiation distribution function. Equations 4 can now be solved by the following iteration process,

$$J(X^k) \, Y^k = -F(X^k) \quad (6a)$$

$$X^{k+1} = X^k + Y^k \quad (6b)$$

where J is the jacobian matrix and is given by

$$J = \begin{vmatrix} \delta F_1/\delta T & \delta F_1/\delta f_v L \\ \delta F_1/\delta T & \delta F_1/\delta f_v L \end{vmatrix} \quad (7)$$

and X is the solution matrix,

$$X = \begin{vmatrix} T \\ f_v L \end{vmatrix} \quad (8)$$

The array X is updated at each iteration step k according to equation 6b until a convergence criterion is met. This data reduction procedure is also applicable for nonlinear calibration curves (equation 3).

RADIATION MODEL FORMULATION

The heat radiation model to which the data is compared in this work is imbedded in a general I.C. engine simulation code (Morel et al, 1986). The model has been described previously by Morel and Keribar (1986).

The radiation model has been constructed on a level consistent with that used to represent the combustion process. The combustion chamber is divided into two zones, burned and unburned, and the carbon particles (soot) produced by the combustion are assumed to remain confined within the burned zone whose equivalence ratio varies with time. The radiation produced by the gas species is small and is neglected, although its inclusion would not be a major complication. The conditions within the burned zone are assumed to be spatially uniform, specifically the soot concentration, absorption coefficient and temperature. Further, the soot-laden gas is assumed to be gray, although, in calculation of the total effective absorption coefficient, the actual spectral variation of the absorption coefficient is taken into account. The surrounding surfaces are assumed to be diffuse.

There are six separate complementary elements of the radiation model:

1. combustion model;
2. geometrical description of the burned zone as a function of crankangle;
3. radiation temperature;
4. absorption coefficient;
5. soot concentration model; and
6. spatial distribution of radiation heat flux.

The modeling approaches employed in these areas are reviewed briefly in the subsections which follow (see Morel and Keribar, 1986 for a more detailed description).

Combustion Model. During the combustion period the contents of the combustion chamber are divided into two parts: unburned and burned. The burned products of air and fuel are thermodynamically treated as a mixture of 11 species representing the key combustion products and dissociated species.

During each time step, a portion of mass in the unburned zone is transferred to the burned zone according to the combustion rate. This rate is calculated from a combustion correlation which accounts for premixed combustion, diffusion burning, and a slow mixing "tail" burning region which becomes increasingly important at rich overall equivalence ratios.

Geometrical Description. The burned zone is assumed to be located in the central portion of the combustion chamber, surrounded by the unburned zone. The volume of the burned zone is calculated from its mass and density, available from a two-zone thermodynamic model. Its shape is obtained from a geometrical model which calculates the thickness of the surrounding unburned zone. As shown in Figure 3, near TDC all of the burned volume lies inside the piston bowl and, as the piston descends, this volume expands into the squish region and eventually fills the whole combustion chamber.

Radiation Temperature. The radiation temperature is linked to the average temperature of the burned zone (T_b). After the start of combustion, T_b at first gradually increases from its initial value, reaching a maximum shortly after TDC, and then decreases rather rapidly towards the end of combustion due to rapid entrainment of air from the unburned zone and volume expansion. Up to the point of the temperature maximum, the model sets $T_{rad}=0.9\ T_b$. This is done to account for the preferential radiant heat transfer from the soot particles which are thus cooler than the surrounding burned gases. This effect has been observed and reported by Cashdollar and Hertzberg (1982). After the burned zone temperature maximum has been reached, the soot radiation temperature is obtained from

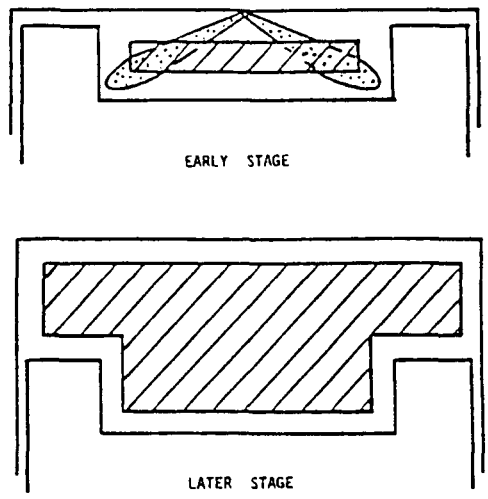

Figure 3. A geometric description of the burned (shaded) and unburned (clear) zones early in the combustion process.

$$T_{rad} = 0.9\ [r_b\ T_b + (1-r_b)]\ T_{b,max} \quad (9)$$

where r_b is proportional to the square of the ratio of burned mass to total mass and it increases from zero to unity during the tail end of the combustion period. This particular form of the radiation temperature was adopted in order to reflect the fact that due to the fourth power temperature dependence the effective soot radiating temperature is dominated by the actively burning flame front, whose temperature is higher than the average of the burned zone (which includes actively burning species as well as burned-out products and which is being diluted by entrained air). Also, since the soot is produced in the flame itself, its concentration is the highest in these hottest parts of the burned zone.

Absorption Coefficient. As already mentioned, the soot is considered to be uniformly distributed over the burned zone. The absorption coefficient produced by this soot concentration can be calculated using the results of experimental and analytical studies of radiation from soot laden gases available in the literature. From these one can deduce the relationship of soot emittance or soot absorption coefficient to the soot volumetric fraction (f_v):

$$\varepsilon_s = 1 - \exp(-1575\ f_v\ TL) \quad (10)$$

where L is the radiation path length and T is the radiation temperature. Therefore, to calculate the soot absorption coefficient it is necessary to have the value of soot concentration. This concentration can be obtained from a soot model which tracks the instantaneous rates of soot production and oxidation and integrates them in time.

Soot Concentration Model. In the model, the time development of soot mass is described as a process taking place in two regions: 1) an actively burning region, and 2) a fully burned region. The amount of fuel burned in any finite time increment is assumed to produce soot, which immediately begins to burn up. Since the mass from the actively burning zone is continuously being entrained into the fully burned zone, the soot formed in the actively burning zone is entrained as well. The actively burning zone is assumed to be a very thin layer separating the burned and unburned zones and as such does not require a separate thermodynamic zone.

The amount of soot entering the burned zone is described in the model by a net formation term

$$ds/dt = A_1 \dot{m}_d \exp(-A_2/T_b) \quad (11)$$

$\dot{m}_d$ is the rate of fuel burned in the diffusion burning mode and T_b is the temperature of the burned zone. The fuel burned in premixed mode is assumed to produce no soot. The values of the constants are $A_1 = 0.30$ and $A_2 = 3000$. The subsequent burn up in the burned zone is described by

$$ds/dt = -B_1 s/(\rho_s d_s) \exp(-B_2/T_{rad}) \times PO_2^{1/2} \quad (12)$$

where ρ_s is soot density, d_s diameter of an elementary soot particle (a single soot particle consists of strings of many such elementary particles), and PO_2 is the partial pressure of oxygen in the burned zone and T_{rad} is the radiation temperature. The values of the constants are B_1=0.4 and B_2=10000. The soot density is taken to be ρ_s=900 kg/m^3, which is the mean of values quoted in the literature (400-1500 kg/m^3). The diameter of elementary soot particles entering the burned zone is taken to be $d_s = 0.16\ \phi_{total}$ (μm).

Spatial Distribution of Radiation Heat Flux. The spatial distribution of radiant heat flux is calculated using the zonal method. This method is very powerful and it includes the representation of all key heat radiation mechanisms i.e.:

1. soot radiation to walls;
2. surface radiation from one wall to other walls, including absorption in the gaseous medium;
3. reflection of incident radiation from one surface to other surfaces.

It may be described by the following equation representing heat flux at the k-th surface:

$$q_k[A_k - \overline{s_k s_k}\,(1-\varepsilon_k)] = \varepsilon_k [\Sigma\, \overline{s_j s_k}\,((1-\varepsilon_j)/\varepsilon_j q_j + \sigma T_j^4) + \Sigma\, \overline{g_n s_k}\,\sigma T_n^4 - \sigma A_k T_k^4] \quad (13)$$

where $s_j s_k$ and $g_n s_k$ are the surface-surface and gas-surface direct exchange areas, respectively. This equation describes heat absorbed by a surface in terms of incoming radiation from reflections from other surfaces, heat radiated by other surfaces, heat radiated by the gas, less the heat loss by outgoing radiation from the surface itself. In mathematical terms, this is a set of coupled algebraic equations, one for each subsurface of the combustion chamber.

It should be noted that the method treats the burned zone as transparent when the absorption coefficient is small, and it automatically progresses to an opaque (surface) model as the absorption coefficient increases.

EXPERIMENTAL SETUP

Engine. The experimental part of this work was performed on a Cummins single cylinder engine based on the 14-liter, NH-series heavy duty truck engine. Bore and stroke are 140 mm by 152 mm and the compression ratio is 15.7:1.

The combustion chamber is quiescent and features centrally located, multi-jet direct injection into a shallow mexican hat piston cup which forms the principal part of the combustion chamber. A schematic drawing of the piston cup is shown in Figure 4. The injector is a production eight-orifice Cummins unit injector, cam/pushrod driven, operating on the Cummins P-T system. Injection timing can be adjusted by a special camshaft mechanism and is measured through a strain-gaged injector link rod. Supercharged operation is accomplished by supplying regulated high pressure air from an external compressor and accumulator to an intake plenum. This air also can be heated to reproduce typical levels of intake air tempera-

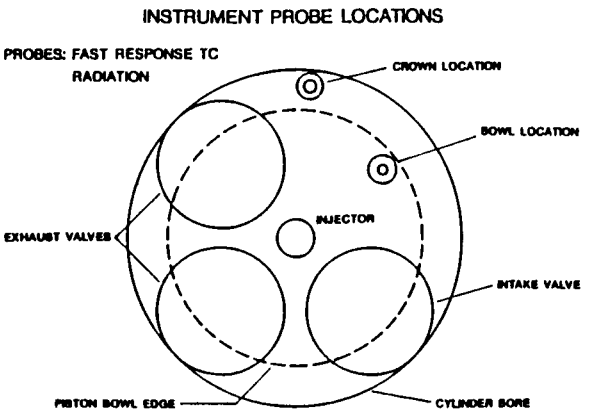

Figure 4. A section through the valve head plane showing the probe access locations.

ture. Back pressure is controlled by a value in the exhaust line. Although the engine normally has two intake and two exhaust valves, one intake valve was removed to accommodate instrumentation. A check was made whether the removal of one valve changed the swirl characteristics of the head. A test was made on a steady-state flow stand and it was found that practically no swirl is generated with either one or two intake valves. Since the engine breathes very freely, this modification has very little effect on air consumption at low rpm. At higher speeds the inlet restriction resulting from using only one valve is offset by increasing inlet boost slightly until the desired air flow is attained.

The engine is supported by external circuits for fuel, lubrication oil and coolant. All fluids can be cooled or heated as required to maintain desired temperatures at the engine. Engine output is absorbed by a Westinghouse DC electric dynamometer rated at 56 kW from 2000 to 5000 rpm. The dynamometer also can supply 45 kW of motoring power over the 1800 to 5000 rpm range.

Probe Access and Data Acquisition. The engine combustion chamber is accessible to the probes through two locations provided at the cylinder head. The first probe access views the squish region and the other location views the deepest section of the piston bowl. This access was created by removing an inlet valve and replacing it with a mounting insert. The locations of the two probes are shown in Figure 4 which displays a section through the head at the valve head plane. The probe accesses were designed to be compatible with both AVL pressure transducer (QP505) and the radiation probe.

The access ports of the radiation probe are located in the engine head. One of them (location #1) viewed the deepest portion of the piston bowl (Figure 5). For some of the measurements, the probe was located in the second access port located in the head near the cylinder wall and it was facing the piston crown (location #2).

A dedicated data acquisition system was built around a PDP 11/23 CPU, a ADAC Corporation 1023FT-1622DMA A/D conversion system and DEC DRV11 clock. The system has 1 megabyte of solid-state memory. Since a portion of the memory is used for the I/O and data management system, about 800KBytes are available for data storage which corresponds to 6 or 7 runs. In practice, however, more consecutive runs are possible since data was continuously being transferred in the background to the mainframe computer, thereby freeing up memory space.

The A/D converter has a dynamic range of -10V and +10V. To enable fuller utilization of the

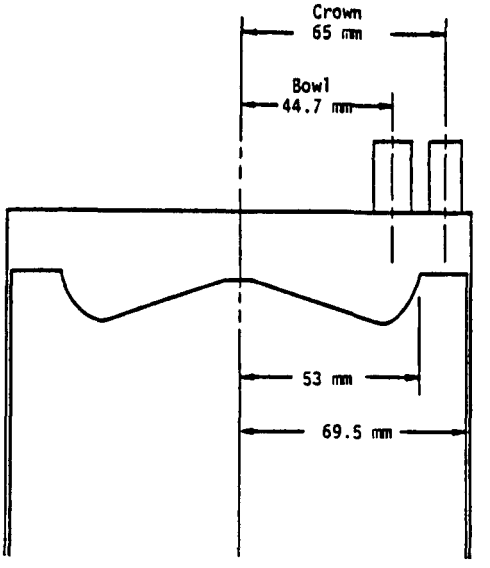

Figure 5. Schematic drawing showing probe locations with respect to the piston geometry.

dynamic range the analog signals of the radiation probe are amplified before being fed into the data acquisition system. The amplifier used is a D.C.-coupled differential amplifier (AM 502, Tecktronics) having gains up to 100 k with selectable upper and lower -3 db points. The maximum upper -3 db point is 1 MHz and is operated at 10 kHz.

The engine data was sampled at 0.2° CA resolution. The data reduction calculations were carried out at each crank angle for every cycle (17 or 34 cycles) of acquired data. The cycle resolved radiation temperature and fvL was then statistically averaged to obtain the mean value and the standard deviation. This method is relatively more time consuming and requires larger online data storage. Some previous investigators (e.g. Flynn et al. (1962), Matsui et al. (1982)) cycle averaged their radiation data before processing was performed. Since the radiation temperature is not a linear function of the voltage, such signal averaging may introduce error if large cycle-to-cycle variations are present.

ENGINE TEST MATRIX

The engine tests were carried out over a broad range of engine operating points representing typical conditions for a turbocharged heavy-duty diesel. To make these conditions realistic, engine simulations were made of the Cummins six-cylinder NH engine, on which the single cylinder test engine is based. The specific multi-cylinder engine simulated was the NTC-350 for which Cummins Engine Company supplied detailed engine description, turbocharger maps, and test data extending from 800

to 2100 rpm, in 100 rpm increments, at full load at each speed. The simulations were carried out using a comprehensive simulation code, IRIS (Morel et al, 1986). This code was used to calculate operating conditions--intake pressure and temperature, exhaust pressure--at four engine speeds and several loads at each speed, to form the test matrix shown in Table I. This assured that all of the operating points were realistic steady-state points of an actual heavy-duty highway diesel engine. Due to dynamometer limitations, the peak loads were limited at the lower engine speeds below the full load values. Also, the values given in Table I are those actually observed during the experiments, and differ in minor ways from the target values determined by the IRIS simulation.

Speed rpm	Nominal Load %	IMAP bar	IMAT °K	EMAP bar	A/F	BOI °BTC
2100	100	2.17	334	2.02	29.5	23
2100	75	1.74	341	1.70	31.4	18
2100	50	1.57	339	1.56	40.1	14
2100	25	1.22	339	1.27	58.7	9
1700	88	2.08	357	1.62	30.3	22.5
1700	50	1.44	338	1.38	36.8	15
1700	25	1.22	342	1.22	59.8	9.5
1300	75	1.70	347	1.43	26.2	22.5
1300	50	1.35	333	1.28	29.9	17
1300	35	1.22	329	1.23	39.0	13
1300	25	1.13	330	1.18	49.3	10.5
1000	75	1.38	334	1.30	21.6	23
1000	50	1.14	336	1.18	24.8	17
1000	25	1.07	332	1.13	46.1	10.5

Table I. Matrix of Engine Operating Conditions

EXPERIMENTAL RESULTS

A typical result produced by the data reduction program is shown in Figure 6a-c for a 50% load at 1300 rpm. The figure shows the apparent radiation temperature, the product $f_v L$ (product of the soot volume fraction and of the path length along the narrow cone extending from the probe to the piston), and the apparent emittance of the radiating soot defined for the purposes of this figure by equation (10). All three figures display a mean curve averaged over 17 engine cycles, plus two curves representing one standard deviation from the mean values. The cycle-to-cycle variations of the voltage signal swing (maximum-minimum) normalized by the cycle-averaged swing are shown in Figure 7, they are found to be of the order of 5%, i.e. quite small. This is in contrast to the data taken in the crown location, to be discussed later.

Certain common features are observed in all operating conditions of the test matrix. The

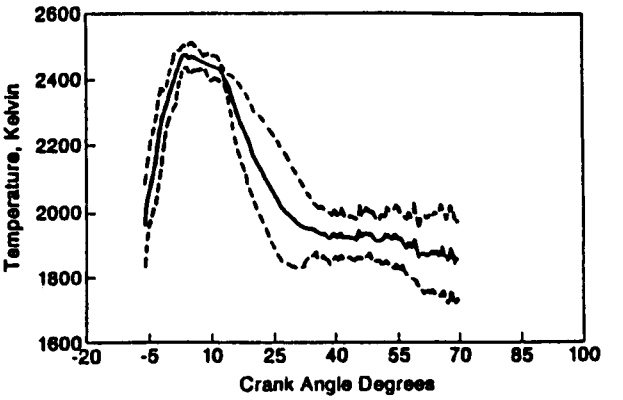

Figure 6a. Typical temperature-crank angle variation showing one standard deviation dispersion band (17 engine cycles), at 1300 rpm, 50% load.

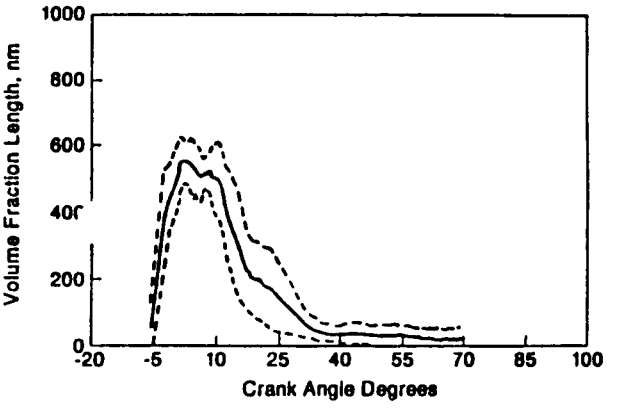

Figure 6b. Typical $f_v L$-crank angle variation showing one standard deviation dispersion band, at 1300 rpm, 50% load.

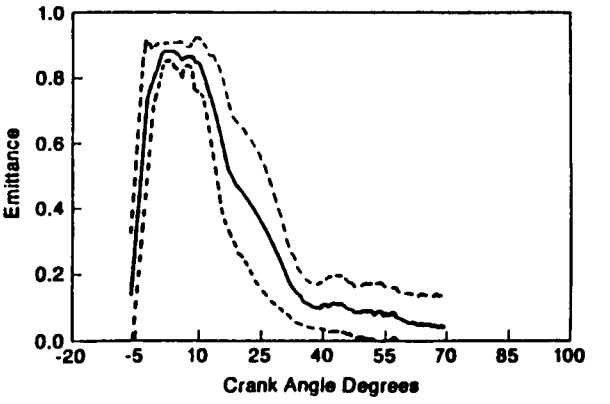

Figure 6c. Typical emittance-crank angle variation showing one standard deviation dispersion band, at 1300 rpm, 50% load.

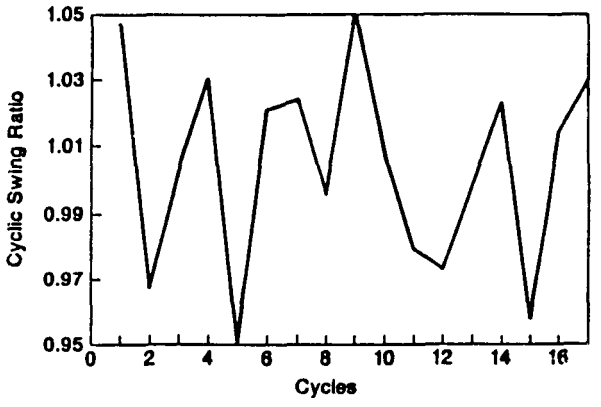

Figure 7. Cycle-to-cycle signal variation in terms of the ratio of individual amplitude to average amplitude for a typical run (silicon detector output).

standard deviation, which is a measure of uncertainty of the measurements, is smaller around the peak regions and increases in the trailing and the leading periods of the combustion duration. The standard deviation of temperature is much smaller than the standard deviation of the $f_v L$. Although the temperature histories exhibit the same qualitative trend, the magnitudes of the peaks are 200K to 300K higher than those measured in DI diesel engines by Flynn et al. (1972) and Matsui (1979, 1980, 1982). On the other hand, the peak temperatures (~2500K) observed by Peterson et al. (1986) in the prechamber of a IDI diesel engine agree quite well with the present results. Also, data of Heinrich et al (1978) show radiation temperatures of that magnitude. The temperature peaks observed on some occasions at the very start of combustion by Peterson et al. (1986) were not seen. It is possible that these peaks were merely artifacts of poor signal-to-noise ratio that always exists at the beginning of the combustion.

The peak values of $f_v L$ observed in the present study are somewhat lower than that observed by Flynn et al. (1972). A direct comparison with their data is difficult since their combustion chamber dimensions were different, but more importantly, in their work the flame was viewed from the side through a cutout in the piston cup and, consequently, the optical thickness would tend to be higher than when viewed from the top.

In the present study the $f_v L$ record exhibits a flat peak region. This trend is also observed by Matsui et al. (1982) at a similar probe location (location x = 29mm in Matsui's work, 1980) in a shallow bowl DI engine without swirl. Matsui et al (1982) observed a more peaked $f_v L$ record in probe locations closer to the piston axis. They attribute the flatness of the optical depth profile in the outside locations to a presence of cooler soot layer near the cylinder head. The observed temperature profiles do not tend to support this postulation. One possible explanation is the retardation of soot oxidation process near the boundary of the combustion chamber and production of soot from the burning fuel trapped in the crevices of the combustion chamber. The magnitude of the peak $f_v L$ measured in the present study is consistent with that measured by Matsui et al. (1982) when scaled by the ratio of the depths of the two piston bowls.

Another noticeable feature is the rather slow rise of the apparent radiation temperature in the early stages of the process. This is contrary to intuition which would suggest that the radiation temperature is close to the flame temperature right from the start. The rather slow rise seen in the reduced data may be explained by two factors. There is cycle-to-cycle variation of the start of detectable radiation at the probe location and, consequently, the averaging of the cycle resolved radiation temperatures results in a somewhat smeared profile which includes the slow initial temperature ramp.

The second factor is that in the initial periods of signal detection, the field-of-view of the probe may not be completely filled by the radiating flame. An attempt can be made to deduce the occlusion factor (the fraction of the probe field of view filled with the assumed uniform radiating medium) during the initial period of signal detection. To do so one has to make some assumptions about the nature of the process. For illustration purposes, let us reanalyze the experimental data under the assumption that during the early period the product $f_v L$ is in fact constant and equal to the maximum value reached during the combustion, and that the radiation seen by the probe during that period is intermittent. The data can then be reduced to produce the radiation temperature and the apparent radiation intermittency (or occlusion factor). The result obtained is shown in Figures 8a-c. Figure 8a shows the profile of $f_v L$ obtained by the standard procedure and the assumed profile, which is constant during the early stages. The deduced temperature is presented in Figure 8b, showing a much more gradual initial temperature rise. The apparent occlusion factor is shown in Figure 8c, indicating a period of about 10 crank angle degrees at the start of combustion where intermittency plays a significant role. The calculated profiles are quite plausible, giving credence to the theory that the relatively slow rise in the radiation temperature during the initial portion of the process is an unavoidable result of the measurement method (finite volume viewed by the probe) and of the data reduction/averaging procedures, and that in reality the radiation temperature is close to the flame temperature.

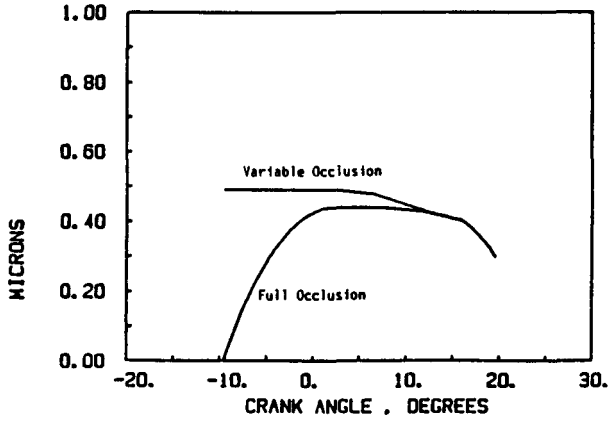

Figure 8a. Profiles of $f_v L$ corresponding to two types of analysis. Lower curve refers to $f_v L$ obtained by the standard procedure which assumes full occlusion at all times. Upper curve refers to analysis which assumes that $f_v L$ is constant during the early stages of combustion, while occlusion may be less than 100 percent.

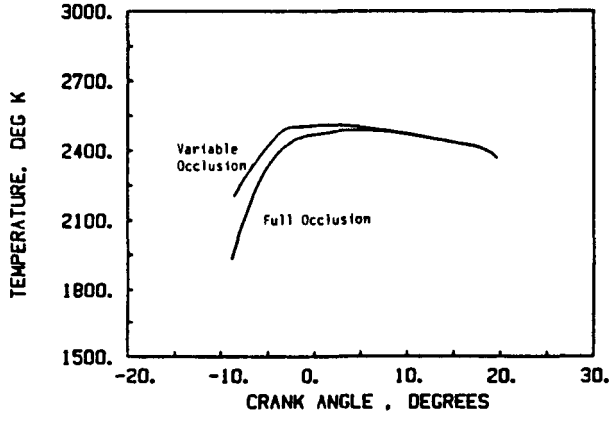

Figure 8b. Profiles of radiation temperature corresponding to the $f_v L$ profiles in Figure 8a.

Figures 9a-d show radiation temperature records for all the operating points of the test matrix. Figures 10a-d show corresponding $f_v L$ records. For each engine speed, the radiation temperatures at the later portion of the combustion process have similar values for all engine loads. On the other hand, the peak temperatures exhibit modest increase with load. The start of the temperature rise is also advanced with load. The trends in $f_v L$ are not as clear as in radiation temperature, although increase in load is reflected by broadening of the $f_v L$ record showing earlier start of combustion and delayed end of combustion. The peak $f_v L$ does not increase with engine load as strongly as the radiation temperature and seem to saturate around 0.5 μm at higher loads.

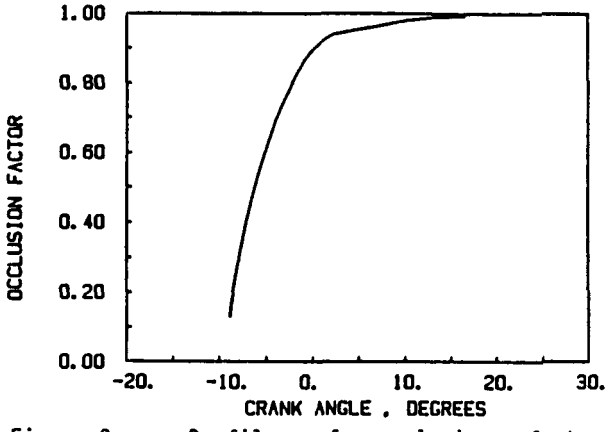

Figure 8c. Profile of occlusion factor corresponding to the adjusted $f_v L$ profile (upper curve) in Figure 8a.

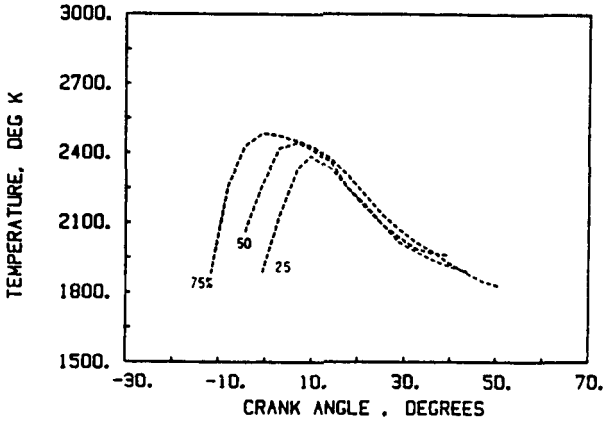

Figure 9a. Radiation temperature variation with crank angle for all loads at 1000 rpm.

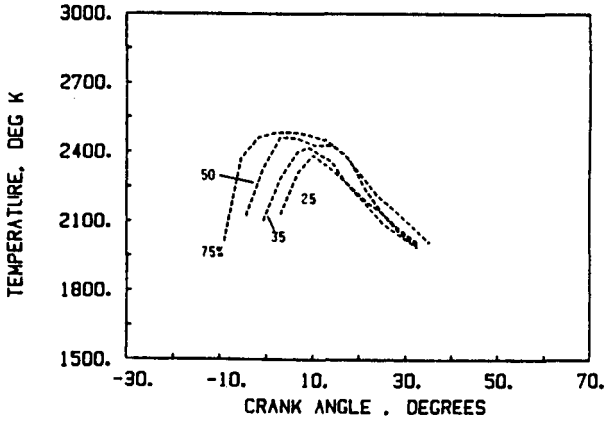

Figure 9b. Radiation temperature variation with crank angle for all loads at 1300 rpm.

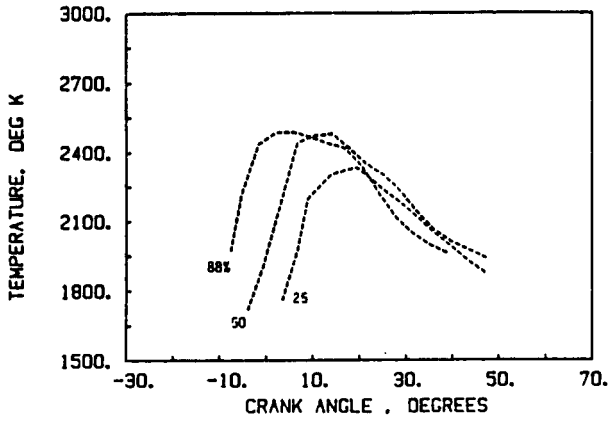

Figure 9c. Radiation temperature variation with crank angle for all loads at 1700 rpm.

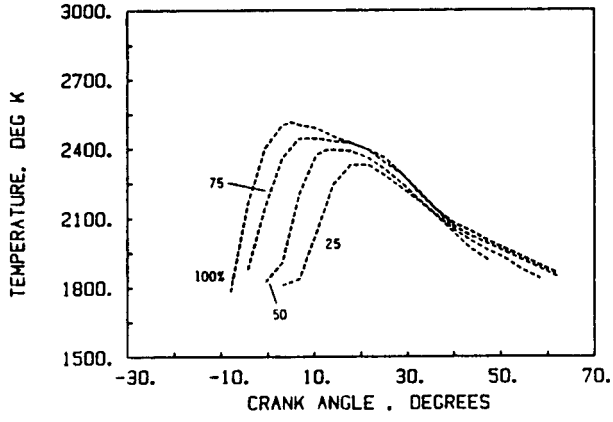

Figure 9d. Radiation temperature variation with crank angle for all loads at 2100 rpm.

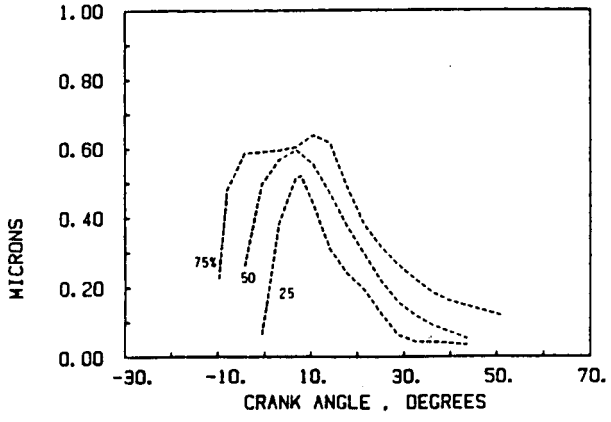

Figure 10a. Variation of $f_v L$ with crank angle for all loads at 1000 rpm.

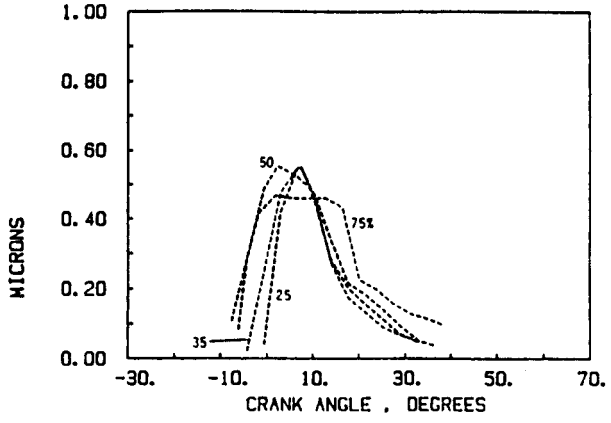

Figure 10b. Variation of $f_v L$ with crank angle for all loads at 1300 rpm.

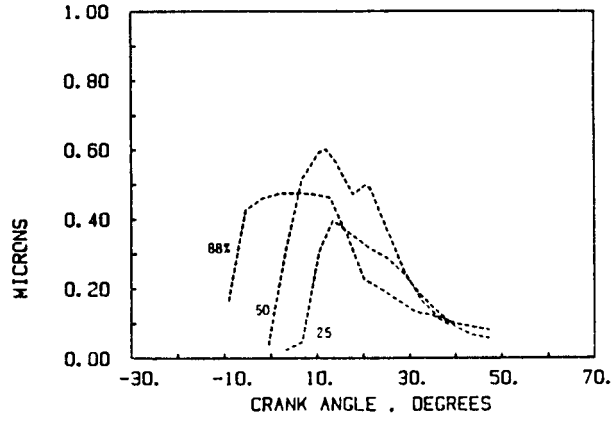

Figure 10c. Variation of $f_v L$ with crank angle for all loads at 1700 rpm.

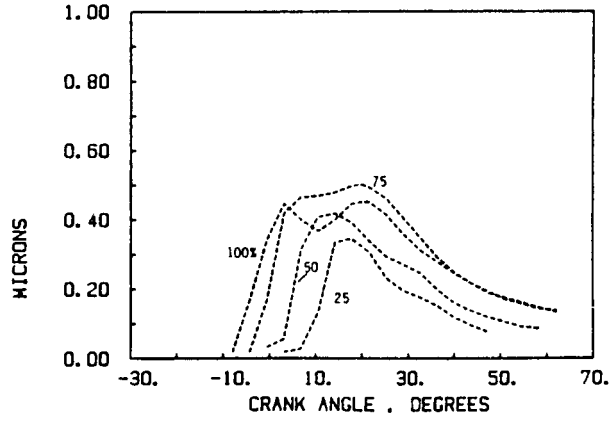

Figure 10d. Variation of $f_v L$ with crank angle for all loads at 2100 rpm.

Figures 11a-b show radiation temperature and f_vL peaks plotted against fuel per stroke. When plotted in this manner, the peaks of radiation temperature exhibit excellent correlation with fuel per stroke and collapse into a single curve irrespective of the engine speed. The correlation of the peak f_vL is not so simple but this may be at least partly due to the increased uncertainty of the measurement discussed earlier.

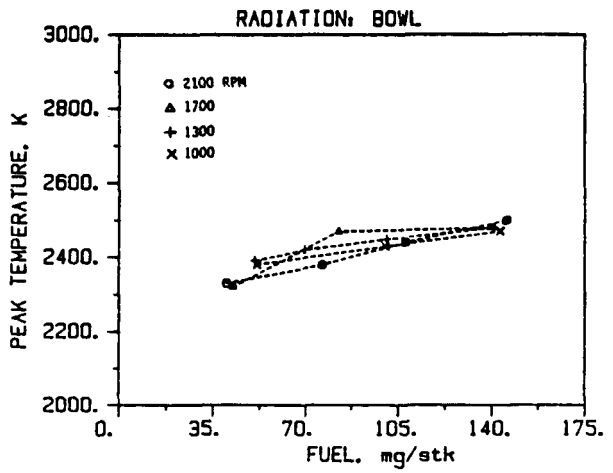

Figure 11a. Peak measured radiation temperature as a function of fuel/stroke at all engine speeds.

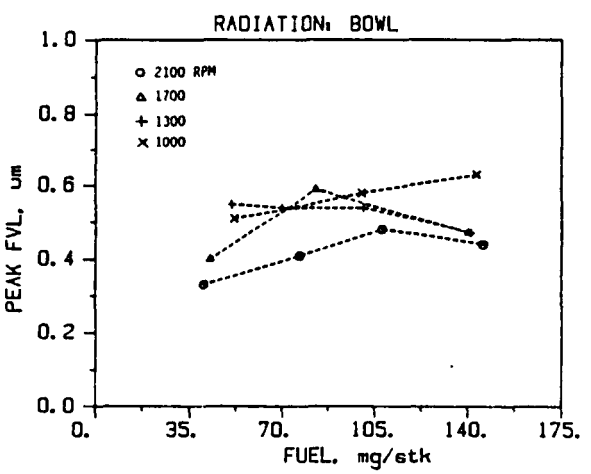

Figure 11b. Peak measured f_vL as a function of fuel/stroke at all engine speeds.

In addition to measurements taken at the bowl location, some data were taken also at the crown location. These were taken at all speeds only at the highest loads. The peak f_vL observed at the crown location was found to be an order of magnitude lower than the values at the bowl location. It also exhibited very large cycle-to-cycle variations, and in fact, for 60-80% of cycles, the collected data showed no or very small soot radiation. This observation indicated a strong radial non-uniformity in soot distribution, with only a small amount extending to the region near the cylinder wall. Another possibility was a circumferential non-uniformity due to the finite number (8) of injection holes. To study this aspect, a series of experiments was performed at one operating point (1300 rpm, 50% load). In this series of experiments the injector was rotated incrementally by 11.25° from its original position and measurements were made at both probe locations. Two increments brought the injector orientation half of the angular separation between the plumes of the injector. But again, the data obtained in the crown location showed that only few cycles (typically 7-8 out of 34) exhibited significant radiation level, and in some cycles no detectable radiation was observed at all. This means that the main reason for the absence of radiation at the outboard location is the radial stratification of the soot.

In the bowl location, for the first two angular positions of the injector, the measured temperature and f_vL were about the same. However, at the third angular position corresponding to 22.5° rotation from the original position, the start of detectable radiation was delayed by about 4 CA degrees. The duration of high values of f_vL was also shortened (Figure 12a-b). This suggests that for this injector orientation the bowl probe access views the combustion zone between two plumes and it takes some time before the plumes merge and come into the field of view of the probe.

It was observed that, at the crown location, the duration of significant radiation in the

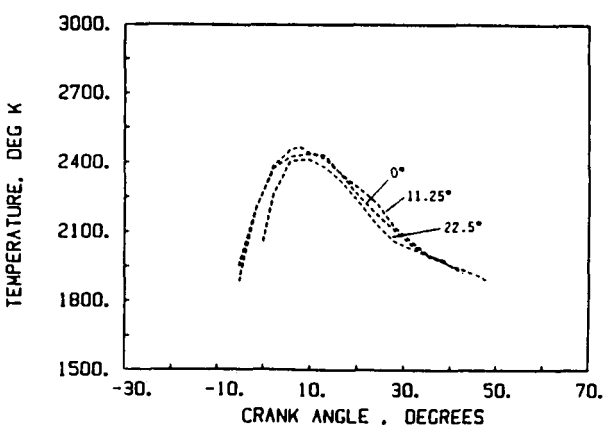

Figure 12a. Effects of injector orientation on radiation temperature at the bowl location.

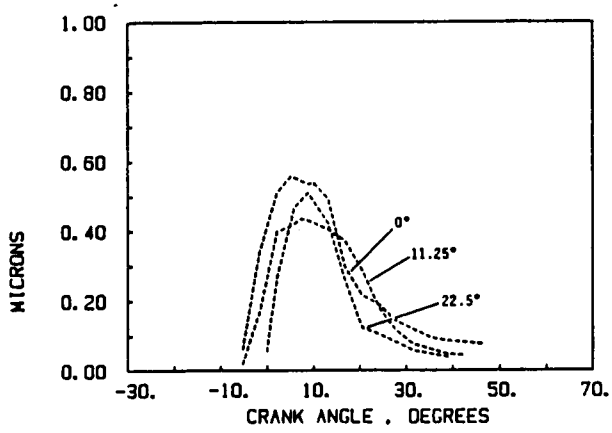

Figure 12b. Effect of injector orientation on $f_v L$ at the bowl location.

active cycles was only about half as long (~25° CA) as in the bowl location. In addition, the start of the detectable radiation was delayed by about 10° CA, presumably due to the time delay in flame propagation into the squish volume. This delay increased somewhat as the injector was rotated from the original position, indicating some degree of azimuthal stratification of soot (and burned zones) even in the crown area.

COMPARISON OF PREDICTIONS TO DATA

Figures 13a-d show the predicted and the measured values of the radiation temperatures. There is a reasonably good agreement between the curves except at the beginning of the combustion. In both the experiments and the predictions, the start of radiant emission and peak temperature occur earlier and earlier as the load is increased. This is consistent with the fact that as the load increases, the Cummins PT fuel injector begins injection earlier, while keeping the end of combustion fixed. The onset of emission in the predictions occurs earlier than in the experiments. This is at least partly, if not entirely, due to the reasons discussed earlier, i.e. the gradual growth of the burned zone. The measured temperature represents a quantity measured along a vertical line of sight at the edge bowl, while the predicted is that existing in the whole burned zone, which is initially quite small and does not extend to the edge of the bowl. Thus the model predicts the onset of high radiation temperature the moment combustion starts, whereas the optical probe does not sense radiative energy until later, when the burned zone passes underneath the probe. Therefore, the two quantities compared here are not identical until later in the combustion event.

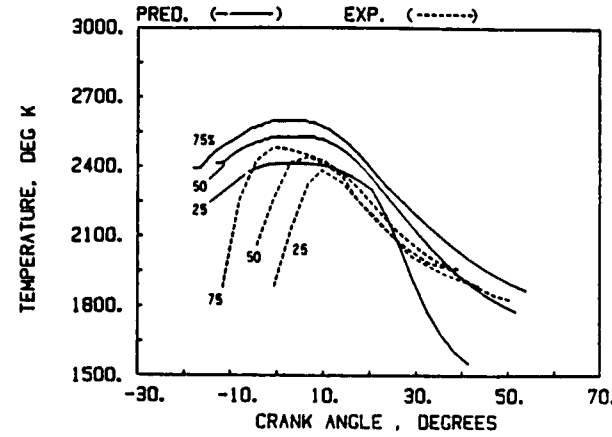

Figure 13a. Predicted and measured radiation temperature for 1000 rpm. Three loads.

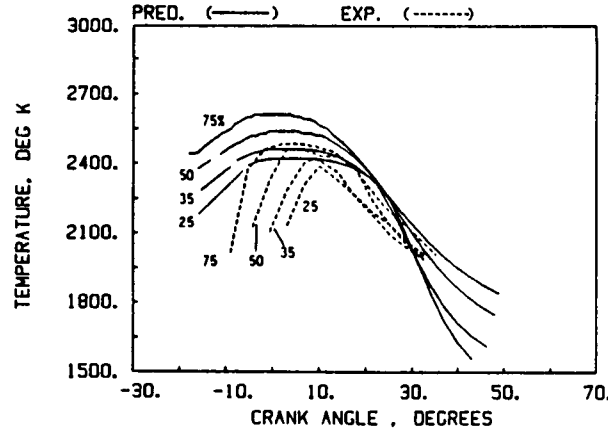

Figure 13b. Predicted and measured radiation temperature for 1300 rpm. Four loads.

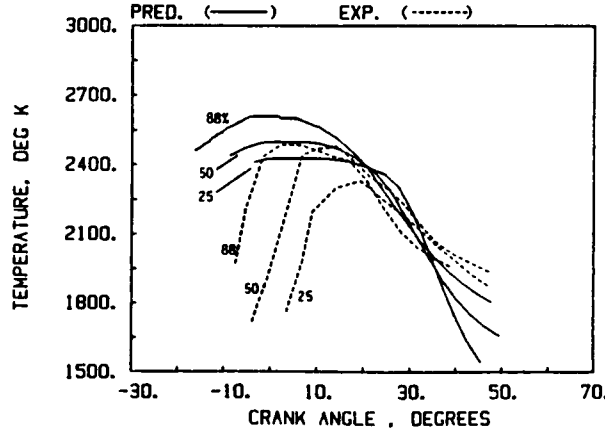

Figure 13c. Predicted and measured radiation temperature for 1700 rpm. Three loads.

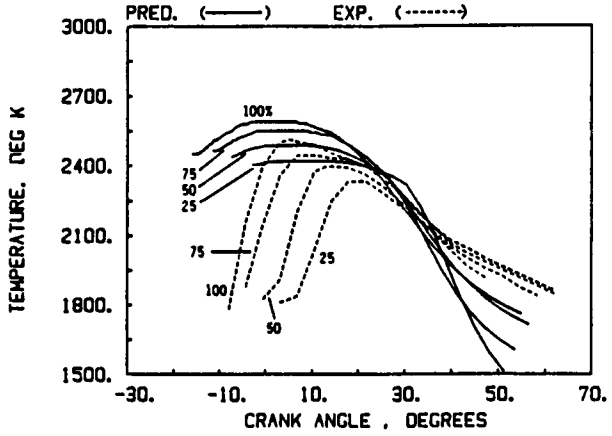

Figure 13d. Predicted and measured radiation temperature for 2100 rpm. Four loads.

The predicted peak temperatures for the fourteen operating conditions are plotted in Figure 14 together with the measured data. The trends of the predicted peak temperatures show good quantitative and qualitative agreement with the experiment.

Figures 15a-d show the predicted and the measured values of $f_v L$. Here it should be emphasized again that in the initial stages of the process the predicted quantity is not identical in concept with the measured quantity. The soot volume fraction (f_v) used in the prediction is an average quantity for the entire burned zone. The characteristic length (L) is the thickness of the burned zone which is assumed in the model to be of uniform thickness in the bowl, being sandwiched between

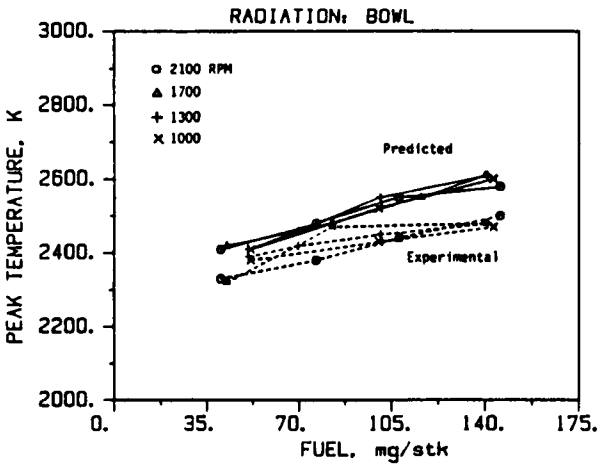

Figure 14. Predicted and measured peak radiation temperatures as a function of fuel/stroke.

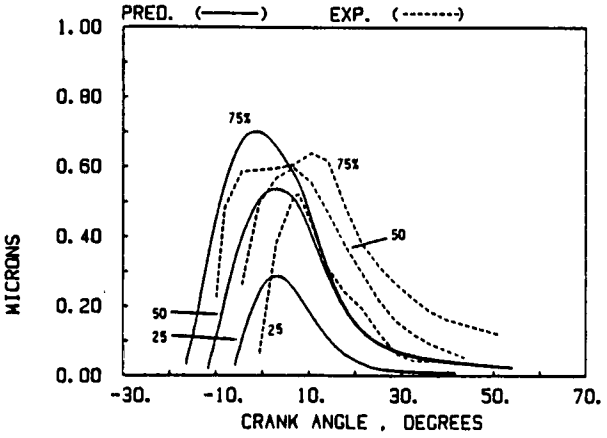

Figure 15a. Predicted and measured values of $f_v L$ for 1000 rpm. Three loads.

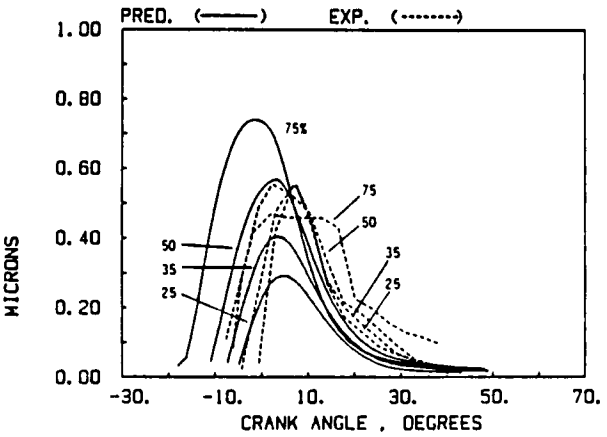

Figure 15b. Predicted and measured values of $f_v L$ for 1300 rpm. Four loads.

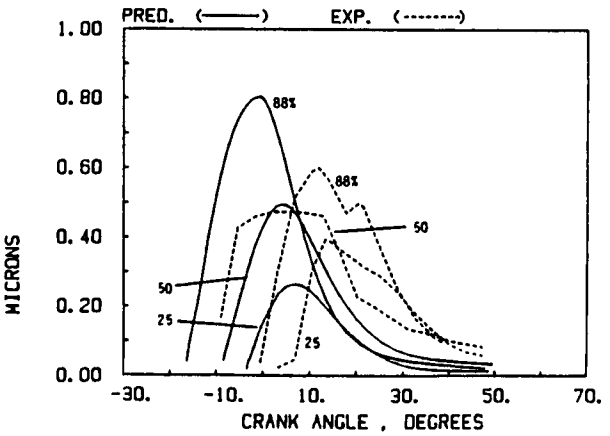

Figure 15c. Predicted and measured values of $f_v L$ for 1700 rpm. Three loads.

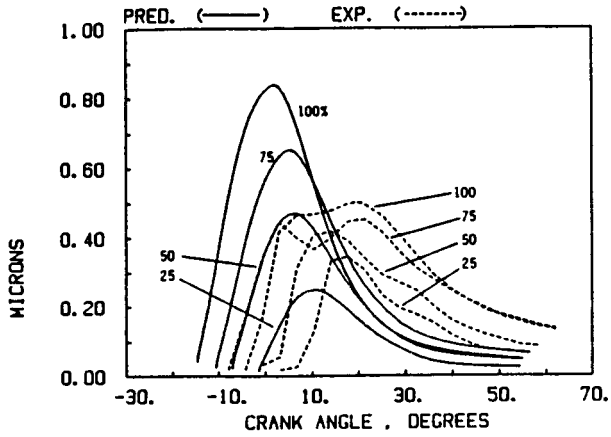

Figure 15d. Predicted and measured values of $f_v L$ for 2100 rpm. Four loads.

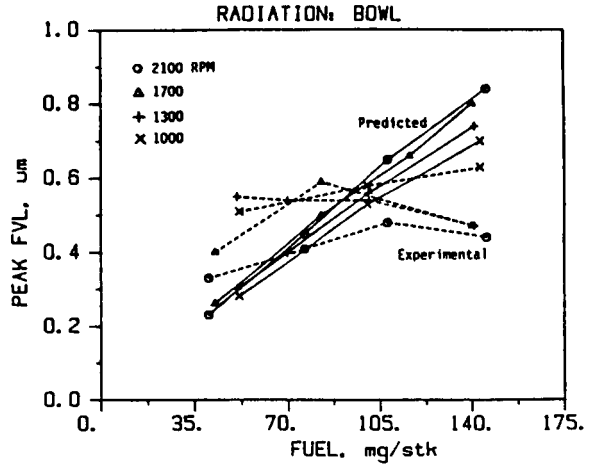

Figure 16. Predicted and measured peak values of $f_v L$ as a function of fuel/stroke.

the two unburned gas layers: one below the cylinder head and the other above the piston. This layer is assumed to grow not only in axial direction, but also in the radial direction as the burned zone expands towards the bowl edge. The predicted $f_v L$ shown in Figures 15a-d is one that could be seen by a probe located on the cylinder centerline where the combustion is assumed to originate and grow from. This explains why the onset of predicted $f_v L$ occurs earlier than in the experiment.

As for the overall level of $f_v L$, there is a good quantitative agreement between the predictions and the data. Both experiment and prediction show gradual lengthening of the crank angle extent of high $f_v L$ values with increasing load, both early on due to earlier injection, and at the tail end due to longer combustion duration. However, the peak value of $f_v L$ grows much less strongly in the experiment than in the prediction, tending to saturate at a level of about 0.5-0.6 microns (Figure 16). It is not immediately obvious why this should be so, since one may expect that increasing the fuel/air ratio (decreasing oxygen availability) will tend to increase the soot loading monotonically. However, the data was quite consistent in showing this trend.

In addition to the test matrix shown in Table I, which represents actual operating points of the engine, several other runs were made, in which the intake pressure and temperature were perturbed around one of the test matrix points. The point chosen was 1300 rpm and 50% load fueling rate. In the first perturbation, the intake pressure was increased from the baseline value of 1.37 bar to 2.11 bar, and then decreased to 1.18 bar. This produced a change in the overall air/fuel ratio from 30.6 to 45.3 and 24.9, respectively. The results of the experiments and of the predictions are shown in Figures 17a and b. They show that the higher boost produced higher peak temperatures and a shorter, lower temperature tail, consistent with the expected shorter combustion duration and higher air/fuel ratio; similar effects were seen in the plot of the soot volume fractions. The lower boost produced just the opposite effects. The simulation predicted correctly the trends and the magnitude of these effects.

The effects of intake temperature were studied by first raising the intake temperature from the baseline value of 335K to 364K and then reducing it to 293K. This changed the overall air/fuel ratio from 30.6 to 28.8 and 37.2, respectively. The results are shown in Figures 18a and b. The peak radiation temperature increased with increasing intake temperature by

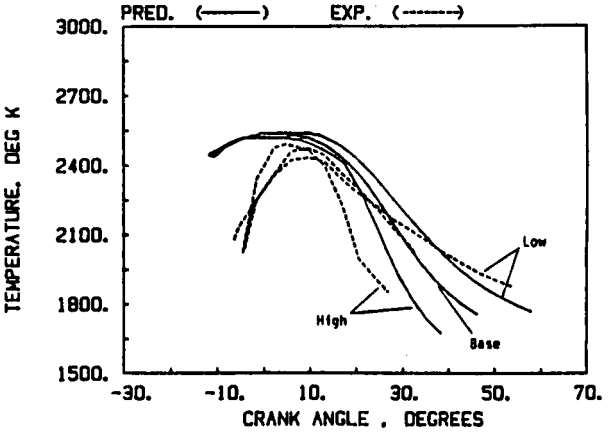

Figure 17a. Predicted and measured effects of intake pressure on radiation temperature at 1300 rpm, 50% load.

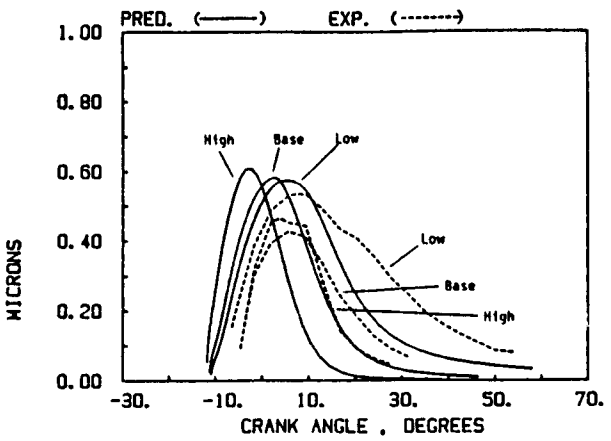

Figure 17b. Predicted and measured effects of intake pressure on soot volumetric formation at 1300 rpm, 50% load.

an amount that was about 50% greater than the increase in intake temperature. It is likely that most of this additional increase was linked to the concurrent decrease in air/fuel ratio. The soot volume fraction increased with increased intake temperature, and its tail lengthened. The simulation quite well predicted all of these trends as well as their magnitude.

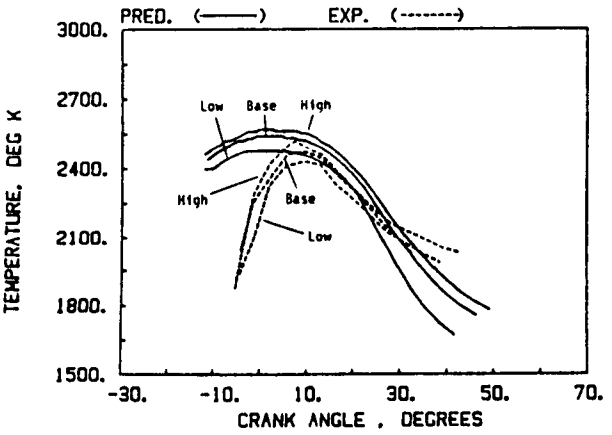

Figure 18a. Predicted and measured effects of intake temperature on radiation temperature at 1300 rpm, 50% load.

CONCLUSIONS

1. A set of experiments was conducted on heat radiation in a single cylinder diesel engine using a novel fiber optics based probe and a rigorous calibration procedure.

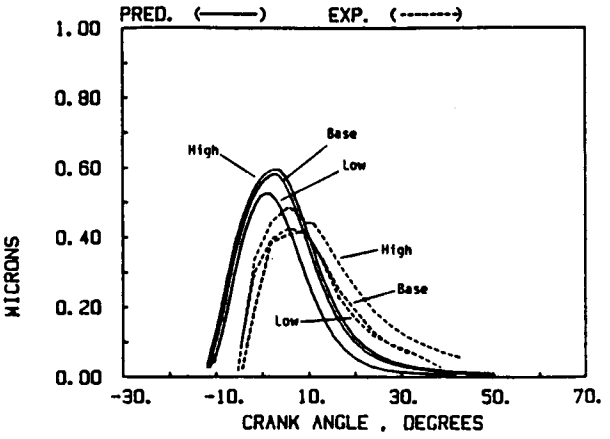

Figure 18b. Predicted and measured effects of intake temperature on soot volumetric fraction at 1300 rpm, 50% load.

2. The measured radiation temperatures are 200-300 K higher than some of the previous measurements (e.g. Flynn et al., 1972), although it compares well with more recent experiments (e.g. Peterson et al., 1986).

3. At high loads the peak values $f_v L$ tend to saturate at around 0.5-0.6 μm. The reason for this is not yet apparent.

4. There is evidence of radial and azimuthal stratification of soot, and the integrity of this stratification appears to be maintained long after the beginning of the combustion period.

5. The apparent radiation temperature and $f_v L$ calculated from these measurements compare favorably with predictions of a heat radiation model in the region where model parameters are a valid representation of the experiment.

6. The spatially resolved zonal model of radiation, complemented by the two-zone combustion/thermodynamics formulation and by a kinetics-based soot submodel, provides a good representation of the radiation process in diesel engines.

ACKNOWLEDGEMENTS

This work has been carried out under the Heavy Duty Transport Technology program, Contract DEN3-342, sponsored by the U.S. Department of Energy and administered by NASA Lewis Research Center. The authors wish to thank Mr. James C. Wood, Project Manager at NASA-Lewis for his constant interest and suggestions. Cummins Engine Company has been an active voluntary industrial participant in this project, con-

tributing their single cylinder engine and other material resources, as well as technical advice regarding the engine installation and operation. In particular, Messrs. Kevin Hoag and Gary Hunter have been very constructive in their assistance. The two-color radiation probe was developed by Mr. Curtis Fiene as a part of his graduate research at Purdue. Very significant contributions were also provided by other members of the Purdue research team, including Prof. C. Warner, Prof. C. Ferguson, Mr. F. G. Riser and Mr. G. Urbanus.

REFERENCES

Cashdollar, K. L. and Hertzberg, M. (1982), "Infrared Temperature Measurements of Gas and Dust Explosions," in Temperature, Its Measurement and Control in Science and Industry, APS, Vol. 5, pp. 453-463.

Dent, J., and Suliaman, S. (1977), "Convective and Radiative Heat Transfer in a High Swirl Direct Injection Diesel Engine," SAE Paper 770407.

Ebersole, G., Myers, P., and Uyehara, O. (1963), "The Radiant and Convective Components of Diesel Engine Heat Transfer," SAE paper 701c.

Flynn, P., Mizusawa, M., Uyehara, O. A., and Myers, P. S. (1972), "An Experimental Determination of the Instantaneous Potential Radiant Heat Transfer Within an Operating Diesel Engine," SAE Transactions, Vol. 81, pp. 95-126.

Gray, W. A. and Muller, R. (1974), Engineering Calculations in Radiative Heat Transfer, Pergamon Press, p. 69.

Heinrich, G., Prescher, K., and Finsterwalder, G. (1978), "Spectrometrisches Messverfahren zur Untersuchung der Verbrennung im Dieselmotor," Motortechnische Zeitschrift, Vol. 39, No. 9, pp. 385-390.

Hottel, H., and Broughton, F. (1932), "Determination of True Temperature and Total Radiation from Luminous Gas Flames," Industrial and Engineering Chemistry, Vol. 4, No. 2, pp. 166-175.

Kamimoto, T., Matsuoka, D., Matsui, T., and Aoyagi, A. (1975), "The Measurement of Flame Temperature and the Thermodynamic Analysis of Combustion Processes in a Direct Injection Diesel Engine," Inst. Mech. Eng., London, Paper no. C96/75, pp. 139-145.

Liebert, C., and Hibbard, R. (1970), "Spectral Emittance of Soot," NASA TN D-5647.

Lucht, R., Green, R., Palmer, R., Teets, R., and Ferguson, C. (1986), "Unburned Gas Temperature in an Internal Combustion Engine: I. CARS Temperature Measurement," Western States Section of Combustion Institute, Banff, Canada, Paper no. WSS/CI 86-48.

Matsui, Y., Kamimoto, T., and Matsuoka, S. (1979), "A Study on the Time and Space Resolved Measurement of Flame Temperature and Soot Concentration in a D.I. Diesel Engine by the Two-Color Method," SAE Paper 790491.

Matsui, Y., Kamimoto, T., and Matsuoka, S. (1980), "A Study on the Application of the Two-Color Method to the Measurement of Flame Temperature and Soot Concentration in Diesel Engines," SAE Paper 800970.

Matsui, Y., Kamimoto, T., and Matsuoka, S. (1982), "Formation and Oxidation Process of Soot Particulates in a D.I. Diesel Engine - An Experimental Study Via Two-Color Method," SAE Paper 820464.

Morel, T., and Keribar, R. (1986), "Heat Radiation in D.I. Diesel Engines," SAE Paper 860445.

Morel, T., Keribar, R., Blumberg, P. N. and Fort, E. F. (1986), "Examination of Key Issues in Low Heat Rejection Engines," SAE Paper 860316.

Oguri, T., Inaba, S., and Hsiue, H. (1971), "Radiant Heat Transfer in a Diesel Engine Cylinder," Transactions of Society of Automotive Engineers of Japan, No. 2, pp. 18-28.

Oguri, T., and Inaba, S. (1972), "Radiant Heat Transfer in Diesel Engines," SAE Paper 720023.

Peterson, R., and Wu, K. (1986), "The Effect of Operating Conditions on Flame Temperature in a Diesel Engine," SAE Paper 861565.

Shimizu, S. (1973), "Temperature Measurement of Premixed Fuel-Air Mixture by an Infrared Radiation Pyrometer," Bulletin of JSME, Vol. 16, No. 92, pp. 333-344.

Siddall, R., and McGrath, I. (1962), "The Emissivity of Luminous Flames," Ninth Symposium (International) on Combustion, pp. 102-110.

Stradomskiy, M., Maksimov, Y., Asmalovskiy, V., and Malyarov, V. (1978), "Radiative Heat Transfer in the Cylinder of a Large Diesel Engine," Heat Transfer-Soviet Research, Vol. 10, No. 3, pp. 51-54.

Uyehara, O. A., Myers, P. S., Watson, K. M., and Wilson, L. A. (1947), "Diesel Combustion Temperatures--The Influence of Operating Variables," ASME Transactions, Vol. 69, pp. 465-477.

APPENDIX A-3

THERMAL SHOCK CALCULATIONS IN I.C. ENGINES

ABSTRACT

An integrated transient engine simulation methodology has been developed to allow the calculation of a thermal shock as it propagates in time through the engine structure. It links, in a fully consistent way, a very comprehensive thermodynamic model of in-cylinder processes, including a detailed gas-phase heat transfer representation, with a turbocharger/air flow/plenum model and a finite element model of the structure. The methodology tracks the turbocharger boost increase and the cycle-by-cycle build-up of in-cylinder heat transfer during engine load and speed changes, producing a transient thermal response in the structure, until new steady-state is reached. The presented results highlight the calculated transient engine performance response and the thermal and stress response of various metal and ceramic components during sudden speed and load changes in heavy duty diesel engines.

1. INTRODUCTION

A sudden change in engine speed and load produces a change in the rate of heat flux from in-cylinder gases to the adjacent structural components. As a result, a thermal transient is produced in the components, which is sometimes referred to as thermal shock. This thermal transient generates a moving front of sharp temperature gradients which propagates through the structure and produces high local stresses. An associated effect is the creation of a moving distortion pattern. As a consequence of these effects, severe load/speed transients are considered to be highly adverse engine operating conditions, which can lead to early material failures. This is particularly true in highly rated engines, with thinner-wall (lighter) components, and in low heat rejection engines employing insulating materials. Methodologies for analyzing the effects of thermal shock must be developed if durability, maintenance and life-cycle cost targets are to be met in these kinds of engine systems.

2. ANALYTICAL METHODS FOR ENGINE HEAT TRANSFER

The issues discussed above can be analyzed effectively through computer simulations which correctly represent the key processes, i.e.:

a. engine thermodynamics and combustion;

b. engine transient operation during load/speed changes, including the turbocharger and air flow system;

c. fluid motion based convective heat transfer;

d. radiation heat transfer and frictional heat generation; and

e. steady-state and transient structural heat transfer.

Accurate representation of thermal processes enumerated above is also important in addressing other design issues such as component temperatures and stresses, performance, optimum insulation strategy etc., arising in the design of advanced conventionally cooled engines and low heat rejection engines.

Numerous steady-state thermodynamic cycle simulation codes have been developed over the years, e.g., the pioneering work of McAuley et al [1]. A more complex problem is the representation of load or speed transients with the complexity of turbocharger inertia, as exemplified by the work of Watson [2].

A long list could also be cited of publications dealing with representation of engine heat transfer. There have been many which have discussed gas-to-wall heat transfer via convection and radiation. No attempt will be made to refer to them here, but comprehensive lists of references

have been presented in References 5 and 6. A number of other publications have dealt with the heat conduction within the structure, using the finite element method.

Although the individual processes of the heat transfer problem have been previously addressed, a complete system simulation has not yet been accomplished. In fact, a review of the state-of-the-art with respect to convective and radiative heat transfer, and structural heat transfer, shows that the modeling efforts in these areas have not been adequate for studies of key thermal issues such as component temperatures, effects of insulation and thermal shock.

- convective heat transfer models have not included the representation of all of the key fluid motions such as swirl, squish, and turbulence, and have provided no spatial resolution within the combustion chamber;
- radiation heat transfer models have lacked one or all of the important submodels for: radiation temperature, soot concentration and spatial distribution through direct transmission and reflections; and
- transient (cyclic or speed/load) structural heat transfer was not represented at all.

The area which is the most advanced is that of steady-state structural heat transfer, generally addressed by finite element codes, but this has been traditionally done in a decoupled manner, with only approximate boundary conditions, which has degraded the utility of the calculated results.

In view of these deficiencies in the state-of-the-art, a comprehensive research program was initiated by ITI to 1) develop new methods that would represent the key engine physical processes with a greater precision, and 2) integrate these methods into a computational methodology in a fully coupled and consistent manner.

3. PRESENT METHODOLOGY

The above tasks were accomplished within the context of a comprehensive computer code, IRIS, which has recently been developed for steady-state as well as transient simulation of internal combustion engine processes and performance (Figure 1). In IRIS, a series of physically-based models of engine processes have been appropriately coupled in a way that allows multi-purpose, integrated simulations. The methodology has been extensively used to address issues such as effects of insulation on performance of low heat rejection engine [3], and effects of variable and electronically controlled valve timing [4].

Among unique features of IRIS are detailed heat transfer models representing convective and radiative gas phase heat transfer, heat conduction in the engine structure, and cyclic heat transfer thermal transients in the surfaces surrounding the

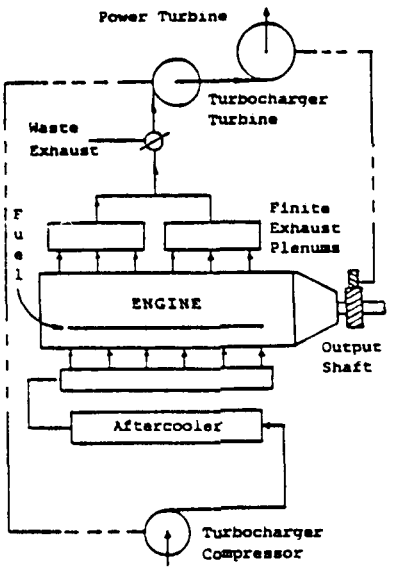

Figure 1 Schematic of the IRIS code engine system representation

combustion chamber. These models and their coupled use have been described in individual publications dealing with convective heat transfer [5], heat radiation [6], cyclic transients [7] and coupled use [8], and they are briefly summarized below.

3.1 Convective Heat Transfer Model. The convective heat transfer model is based on an in-cylinder flow model which computes swirl, squish and turbulence as a function of crank angle. It has a degree of spatial dependence, in that it divides a bowl-in-piston geometry into three flow regions (squish region above piston crown, cup volume, and region above the cup), and solves differential equations in each for swirl and turbulence. Its main features are: (1) the inherent dependence of the convective heat transfer on the actual flow velocities, and (2) the spatial resolution, which this allows, including the capability to treat re-entrant piston bowl shapes. A total of eleven distinct in-cylinder surfaces are accounted for, with a separate heat transfer coefficient calculated for each. An additional convective heat transfer model calculates heat transfer between port gases and port surfaces.

3.2 Radiation Heat Transfer Model. Due to soot formation during diesel combustion, thermal radiation from gases to surrounding combustion chamber surfaces is a significant component of heat transfer. Instantaneous and mean levels of heat radiation are functions of the volume and distribution of burning gas, concentration of soot present in the burning gas, combustion chamber geometry, and also of surface emissivities and temperatures. The heat radiation model incorporated in IRIS takes into account all of these dependencies. The

soot concentration levels are calculated versus crankangle using a kinetic model, which provides rates for soot formation and subsequent burnup as a function of engine parameters and operating conditions. The spatial distribution, accomplished through a zonal representation, includes the effects of chamber geometry by calculation of the actual optical thicknesses as seen from one surface by another, or when viewing the burned zone.

3.3 Structural Heat Conduction. The calculation of structural heat conduction in the context of an engine cycle simulation can be viewed as having a dual purpose: 1) it provides wall temperatures needed for gas-phase heat transfer boundary conditions; 2) it supplies detailed structural temperature distributions, which can be used as the basis of thermostructural design analyses, materials selection and tribological studies.

Steady-state or transient conduction through the engine structure is calculated in IRIS via the finite element method which is suitable for representation of geometrical detail as well as differentiating materials through property specification. Any finite element code (such as NASTRAN, which was utilized for studies presented here) can be used to generate a geometrical representation of part of the engine structure or component of interest. There are no limitations on the FEM model; large 3-D models with many thousands of nodes can be accommodated. An internal pre-processor generates a coarser, quasi-dimensional scalar finite element model (thermal resistance and lumped capacitance network) of the remainder of the engine structure. Such generic networks can be constructed by the pre-processor for Diesel as well as SI engine geometries using a library of component sub-networks. The network model can also be selected for representing the entire engine structure when details of temperature distribution are of no interest. The FEM-Network approach results in CPU time economies allowing detailed multi-dimensional design-stage thermal analyses of components to be carried out simultaneously and coupled with performance analysis of the parent engine.

Structure geometry information is input and stored in IRIS in the form of global conductance and capacitance matrices of the combined FEM-Network system, together with data mapping boundary elements of the model onto different surfaces for which IRIS computes gas convection/radiation and friction thermal loads or prescribes coolant convective boundary conditions.

In the context of a distributed computational model and for the general, transient problem, the heat conduction equation is expressed as

$$[C]\,\dot{T} + [K]\,T = Q \qquad (1)$$

where [C] and [K] are thermal capacitance and resistance matrices, respectively, T is the vector of nodal temperatures, and Q is the thermal load (boundary condition) vector.

For the transient problem equation (1) is integrated in time using backward differencing:

$$[C](\{T\}_{n+1}-\{T\}_n)/\Delta t+[K]\{T\}_{n+1}= \{Q\} \qquad (2)$$

or

$$[C/\Delta t+K+H]\{T\}_{n+1} = [C]\{T\}_n/\Delta t+\{F\}_{n+1}+\{N\}_{n+1} \qquad (3)$$

where the thermal load has been divided into its (structure) temperature independent and dependent components {F} and -[H]T. The left hand matrix is reduced (by a rapid "skyline" algorithm) only when the non-linear load N (caused by changes in convective load H, time step Δt or C and K due to temperature dependent properties) becomes large. Solution is otherwise obtained by iteration on the non-linear load. This allows economical transient simulations involving complex transient events and large FEM models. Approximately a dozen reductions are required during a typical transient spanning several minutes. The time step dynamically varies and is related to the engine simulation time step. Its minimum is one engine cycle. Criteria for convergence on N and coolant-side boundary conditions are specified as input.

3.4 Cyclic Temperature Transients. The heat flux from the gas to the wall is highly transient during each cycle, with high flux levels occurring during combustion followed by low heat flux periods. Even under steady-state conditions, this pattern produces temperature transients in thin layers adjacent to the gas-side surfaces. The surface temperature swings are on the order of 20K for iron or aluminum surfaces, but for low conductivity coatings it can reach several hundred degrees Kelvin. IRIS analyzes the surface temperature dynamics by a transient one-dimensional model which interacts, in a spatially resolved way, directly with the finite element heat conduction model through an appropriate second order correction of gas-side boundary conditions [7].

3.5 Mechanical Friction. The mechanical friction model is used to calculate the brake performance quantities and also to provide the frictional heat loads at the piston/liner interface. The model simulates the piston-connecting rod dynamics, which together with gas forces provides the total piston-liner contact force. Solving for ring hydrodynamic film lubrication, the instantaneous friction at the ring-liner interface is calculated for hydrodynamic, boundary and mixed conditions, depending on film thickness friction thermal loads are appropriately deposited onto surfaces in frictional contact.

3.6 Thermodynamic Analysis. Engine heat transfer is driven by the air flow and combustion phenomena. Because of that, the heat transfer methodology is implemented in an advanced detailed

thermodynamic simulation of the engine operation. This model provides time resolved information about combustion chamber pressure, temperature and thermodynamic properties (separately for burned and unburned gases), flow velocities and mass flow through valves, intake angular momentum flux, details of the injection process, as well the instantaneous piston location and chamber geometry. The structural heat transfer calculations, which are coupled to IRIS, feed back into the thermodynamic analysis through the heat transfer term in the energy equation. Therefore, they have an effect on the instantaneous energy balance, which ultimately determines the piston work done and exhaust temperatures, as well as component temperatures.

In the diesel combustion mode of IRIS (which is a general I.C. engine code), a correlative combustion submodel, which is an extension of the work of Watson et al [9], tracks separately the burned and unburned zones, and accounts for premixed combustion, diffusion burning and a slow mixing "tail" burning region for rich overall equivalence ratios. The extent of premixed combustion is calculated from the extent of fuel vaporization in the ignition delay period, which itself is based on the injection schedule, injection pressure and mean droplet size. The ignition delay is calculated from an empirical expression as a function of cylinder gas temperature, pressure and fuel cetane number.

3.7 Engine System Description. In addition to the capability to describe the in-cylinder processes, IRIS also treats the engine as a system, including the turbocharger, aftercooler, power turbine or other bottoming systems. This allows studies of turbocharger/engine matching and of proper sizing of the turbine and of the compressor using scaled dimensionless maps. The effects of pressure pulsations produced in finite exhaust plenums are also included.

3.8 Transient Engine/Turbocharger/Air System Simulation. To simulate correctly the variation of gas-to-wall heat transfer during an engine transient, one has to track from a cycle-to-cycle, and on a crankangle resolved basis within a cycle, key charge parameters such as:

- mass trapped
- mean flow velocities
- turbulence level
- air/fuel ratio
- gas temperatures

All of these are required for the calculation of heat loads to the individual surfaces and components in the combustion chamber. These heat loads (their mean values as well as their time-variation) are the inputs, or boundary conditions, to the structure temperature calculations.

The parameters enumerated above depend on engine and turbocharger dynamics which need to be simulated so that the time-dependent evolution of engine speed, turbocharger speed, intake plenum pressure and temperature, and exhaust plenum pressure can be calculated.

Engine speed dynamics is the result of the balance between brake torque, load torque imposed on the engine, and engine inertia.

$$I_E d\omega_E/dt = T_{Brake} - T_{Load} \qquad (3)$$

A sophisticated model of the load system can be constructed to provide dynamic values of T_{load} for particular applications under a variety of operating conditions. For studies of thermal shock, however, these dynamics may be more simply represented by an imposed ramp of engine load and speed, typical of the severe conditions brought about by sudden changes in engine fueling and/or load torque.

Turbocharger dynamics is the result of the balance between the turbine and compressor torques on one hand, and turbocharger inertia and friction on the other:

$$I_{TC} d\omega_{TC}/dt = T_{Turbine} - T_{Compressor} - T_{Friction} \qquad (4)$$

The turbine and compressor torques are calculated using the usual quasi-steady approach, i.e., relying on the steady-state turbine and compressor maps at each instant of time. The friction torque is lumped into the turbine torque through an overall turbine efficiency. On decelerations during rapid load reductions, the compressor operating point may travel beyond the surge line for a brief period of time. The procedure used allows such excursions. A careful treatment of the compressor work during that period is required to obtain a smooth and consistent solution.

The air system consists of turbine, intercooler, intake and exhaust manifolds and compressor. The intercooler and intake plenum are treated in a quasi-steady fashion, but the exhaust manifold dynamics is treated by a filling and emptying dynamic model.

3.9 Integration Technique and Synchronization of Models. The main time step used in the overall calculation is a single engine cycle (720°CA) or a multiple of cycles. Inputs to each new cycle, such as rpm and fueling rate, can change according to a given schedule, but they are fixed within the cycle.

Events (history in time or engine cycles) in fuel rate and rpm are prescribed as inputs to the simulation. Injection timing and duration and coolant temperature events are also optionally input. In the absence of a user specified history of injection timing and duration, these quantities are dynamically varied with fuel rate and rpm according to empirical relationships. The strategy for controlling air-fuel ratio (at the smoke limit) during transients is also input.

Through continuous monitoring of variations in key engine quantities (intake pressure, air-fuel ratio and exhaust temperature) as well as progression of the transient event, the time step is dynamically changed and can be several hundred engine cycles. This makes extended simulations that track a slow approach to steady-state (after a relatively rapid event) economically feasible.

THERMAL SHOCK STUDIES

In this paper, results will be reported from three studies of component thermomechanical behavior carried out with the integrated methodology described above. The studies involve 1) monolithic metal and ceramic pistons; 2) coated intake and exhaust valves; and 3) an iron piston with press-fit silicon nitride cap.

It should be noted that IRIS transient simulations produce dynamic response results for all simulated components and processes, e.g. turbocharger, combustion, thermodynamics, flow and heat transfer, friction, blowby, emissions, etc. For the present work discussion of simulation results will be limited to key quantities describing engine and turbocharger state (engine mass flow, exhaust temperature, turbocharger rpm and intake pressure) and it will mainly concentrate on the thermal and stress response of the structure. For each study, description will be given of the engine, component material composition, finite element geometry representation and of the transient engine conditions. The response of the engine and component temperatures and stresses are then presented and discussed.

4. MONOLITHIC ALUMINUM AND ZIRCONIA PISTONS

In this study, the effects of severe engine transients on conventional aluminum and monolithic zirconia diesel pistons were considered.

4.1 Engine. The engine modeled is a typical U.S. heavy-duty highway diesel six-cylinder truck engine. Its displacement is 14 liters, and at rated conditions (1900 RPM, A/F = 29) it delivers approximately 400 HP. The engine has a quiescent combustion system with a shallow piston cup, the shape of which will be shown below in connection with its finite-element representation.

4.2 Piston/Liner FEM Model and Engine Structure Representation. A total of 663 node points were employed to describe the piston and rings. An axisymmetric approximation was used excluding the pin boss area, as it is mainly the top axisymmetric portion of the piston which is of interest in a thermal shock study. To better display the resolution of the nodal distribution, only the important top part of the piston is shown in Figure 2. The liner was represented by 198 nodes, while the head and valves, which are not in direct contact with the piston, were represented by a quasi-three dimensional network model using 80

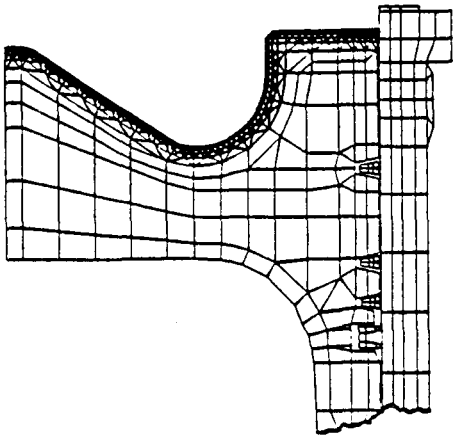

Figure 2 Finite element representation of top portion of diesel piston-ring-liner assembly.

nodes. Careful attention was given to the piston/ring/liner interface through which passes a large quantity of heat. This included accounting for the fraction of time that each individual pair of surface elements (for example on a ring and liner) are in contact during the cyclic piston motion. Several hundred "scalar" elements whose thermal resistances were computed in this manner, establish the thermal connectivity between piston (side), liner and ring FEM nodes.

4.3 Piston Material Compositions. Two different material compositions were used for the piston. One was a standard aluminum piston with thermal conductivity $k = 190$ W/mK and heat capacity $\rho c = 2.3$ MJ/m^{3}K. The second piston was entirely made of monolithic partially stablilized zirconia with $k = 2.5$ W/mK and $\rho c = 2.3$ MJ/m^{3}K. The aluminum and zirconia pistons were coupled with the rest of the engine structure which was made of iron and steel, as appropriate. The boundary conditions on the coolant side were kept the same for both pistons.

4.4 Engine Transients. Two different engine transient conditions were considered:

1. speed linearly increasing from 1100 to 1900 RPM over a period of 50 cycles (4 secs); fueling rate increasing from 15% to 100% of rated value, while being controlled to maintain an air-fuel ratio above 20; (Transient #1) and

2. constant speed at 1900 RPM, fueling rate decreasing linearly from 100% to 15% of rated value over a period of 20 engine cycles or about 1.2 sec (Transient #2).

The first of the above transients represents an engine test under a severe increase in heat load, while the second approximates a drop in load, e.g, due to sudden change from uphill to downhill grade.

Results will be reported here for three specific combinations of transient event and piston material composition: Transient #1 with aluminum piston (1A), transient #1 with zirconia piston (1Z), and transient #2 with zirconia piston (2Z).

4.5 Short Term Engine/Turbocharger Response. The transient engine events for cases 1Z and 2Z are shown in Figures 3(a,b) for the first 100 cycles (approximately 6 sec) of the simulation, where each cycle equals 720 crank angle degrees. In case 1Z, as a result of turbocharger inertia, the air-fuel ratio decreases rapidly and undershoots the new steady-state value during that period, while the compressor mass flow is increasing to its new steady-state. During this period of rich combustion, exhaust temperature is seen to overshoot, before settling down to the final value. Conversely, for case 2Z, where fuel rate suddenly decreases, turbocharger lag causes a temporary oversupply of air, and an undershoot in exhaust temperature due to lean combustion. Air-fuel ratio and exhaust temperature responses for case 1A are not shown. They are similar to those for 1Z, but exhibit a lower exhaust temperature due to higher heat transfer.

The short-term responses of the turbocharger for cases 1Z and 2Z are illustrated in Figures 4(a,b). In both cases the initial responses of compressor mass flow, turbocharger rpm and intake plenum pressure are seen to lag the end of the transient event by about 40 cycles. The variation of the local convective heat transfer coefficient (h_g) on the bottom surface of the piston cup (one of the surfaces for which h_g is calculated by the convective heat transfer model) is also plotted in Figures 4(a,b). It is represented by the cycle-mean-effective coefficient, defined as $h_{g,eff} = \int h_g A_g / \int A_g$. Being strongly dependent on fluid density, its response is seen to parallel that of intake pressure after the end of the transient event.

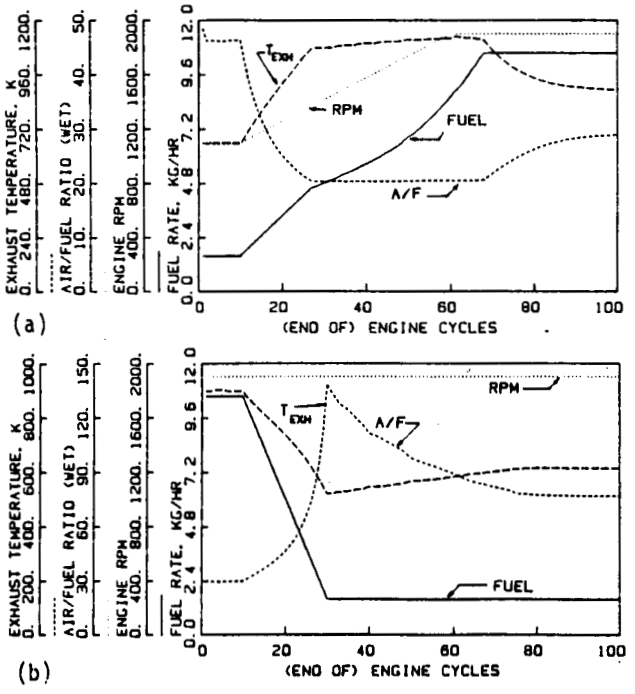

Figure 3 Transient event in fueling rate and RPM and initial response of air fuel ratio and exhaust temperature: a) case 1Z (fuel and rpm up, zirconia piston) b) case 2Z (full down, zirconia piston).

4.6 Long-term Engine and Turbocharger Response. While the occurrence of turbocharger lag discussed above is common to both cases 1Z and 2Z, there is a marked difference: for case 2Z (fuel down), a near-steady-state in turbocharger performance is achieved as soon as the initial turbocharger response (lag) is complete; for the 1Z (fuel, rpm up) case, turbocharger quantities and intake pressure are about 10% below their final steady-state after the first 100 engine cycles. These differences arise from the slowly changing exhaust temperature caused by the long time scale associated with the heat conduction in the engine structure. For case 1Z, where the final state is highly boosted, the gradual warm-up of the structure causes an upward drift, i.e., a "tail", in boost and turbocharger rpm response. By contrast, in case 2Z there is almost no boost in the final state because of the generally low exhaust temperature levels and pressures, and so the slow decrease in the exhaust temperature has almost no effect on the turbocharger quantities.

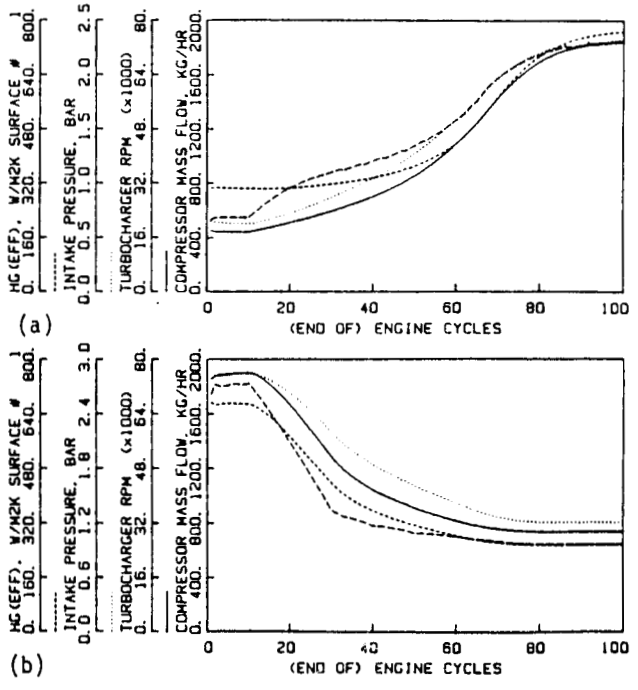

Figure 4 Initial transient response of turbocharger RPM, compressor mass flow, intake pressure and cycle-averaged heat transfer coefficient for piston cup bottom: a) case 1Z, b) case 2Z.

While the more severe thermal shock effects (stresses and deformations) occur early on, the duration and shape of the long term structure thermal transients are also of interest due to their effects on engine warm up, turbocharger response and on heat transfer during engine transients. To study the long term thermal transients, cases 1Z, 2Z and 1A were simulated for 5,000 engine cycles, which corresponds to approximately 5 minutes of real time. Plots of wall temperature, exhaust temperature and intake pressure responses for each case are given in Figures 5(a,b,c). Wall temperatures shown are local temperatures for the point on the axis of the piston at the tip of the conical protrusion, and for a point on the liner surface located at a distance from the head equal to TDC clearance.

Even though full steady-state, including structure temperatures, was achieved for the acceleration

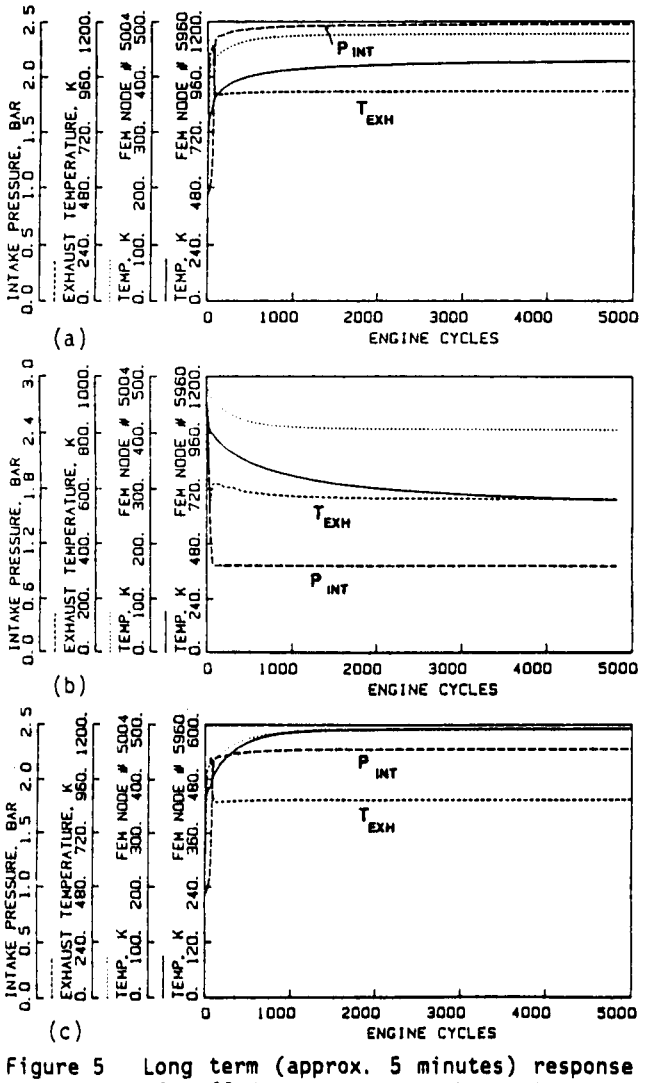

Figure 5 Long term (approx. 5 minutes) response of wall temperatures, exhaust temperature and intake pressure: a) case 1Z; b) case 2Z; c) case 1A.

event with aluminum piston (1A) in about 2000 cycles, both zirconia piston cases studied (1Z, 2Z) took longer. For these two cases, the structural thermal response of the piston is slower due to the low conductivity of the piston material. Equilibration of structural temperatures come after about 3000 cycles for case 1Z and took the longest for case 2Z (5000 cycles), where only fuel (load) is decreased. Exhaust temperature response parallels that of structural temperatures.

4.7 Structure Thermal Response (Thermal Shock). Among the outputs of the coupled methodology are instantaneous temperature distributions for the engine structure and, thus, the complete history of the structure thermal response. Instantaneous temperature contours in the top portion of the piston and for selected times during the simulation, are shown in Figure 6 (case 1Z) and 7 (case 2Z). The times were selected so as to follow and characterize each stage of the thermal response.

The temperature contours document the effects of geometry on the steady-state, as well as on the transient history. For both cases, protruding corners and tips have the peak temperatures for the initial and final steady-states. These areas receive a larger portion of the thermal load (due to larger, irregular area in contact with gas) and are furthest from coolant. During transients, these "hot spots" take the longest to warm-up or cool-down due to their large thermal inertia in proximity to the surface. For case 1Z, this results in lower gradients of the temperature and a milder thermal shock for these areas compared to piston crown or base of bowl. For case 2Z, Figure 7 (30-1500 cycles) shows that the central cores of the protrusions (tip and cup rim) remain warmer than their surfaces through part of the simulation.

More revealing from the standpoint of thermal shock phenomena are 1-dimensional plots of temperature versus depth at various instants of time. Such plots, tracking the history of the thermal response along the axis of the piston for cases 1Z, 2Z and 1A, are shown in Figures 8(a,b,c). The dashed lines represent the initial and final steady-states.

The overall structural thermal response of the zirconia piston in cases 1Z and 2Z (Figures 8a and b) is slow and displays typical characteristics of transient heat conduction in low diffusivity solids. The surface temperature rises rapidly, and the slow penetration of the thermal wave into the structure results in large temperature gradients at and near the surface relative to either the initial or the final steady-state. The temperature change on the oil side is small.

By contrast, Figure 8c indicates the absence of any significant thermal shock for the aluminum piston. The thermal wave travels rapidly through the piston, raising surface temprature gradients only marginally above those for the final steady state. The transient response of structure tem-

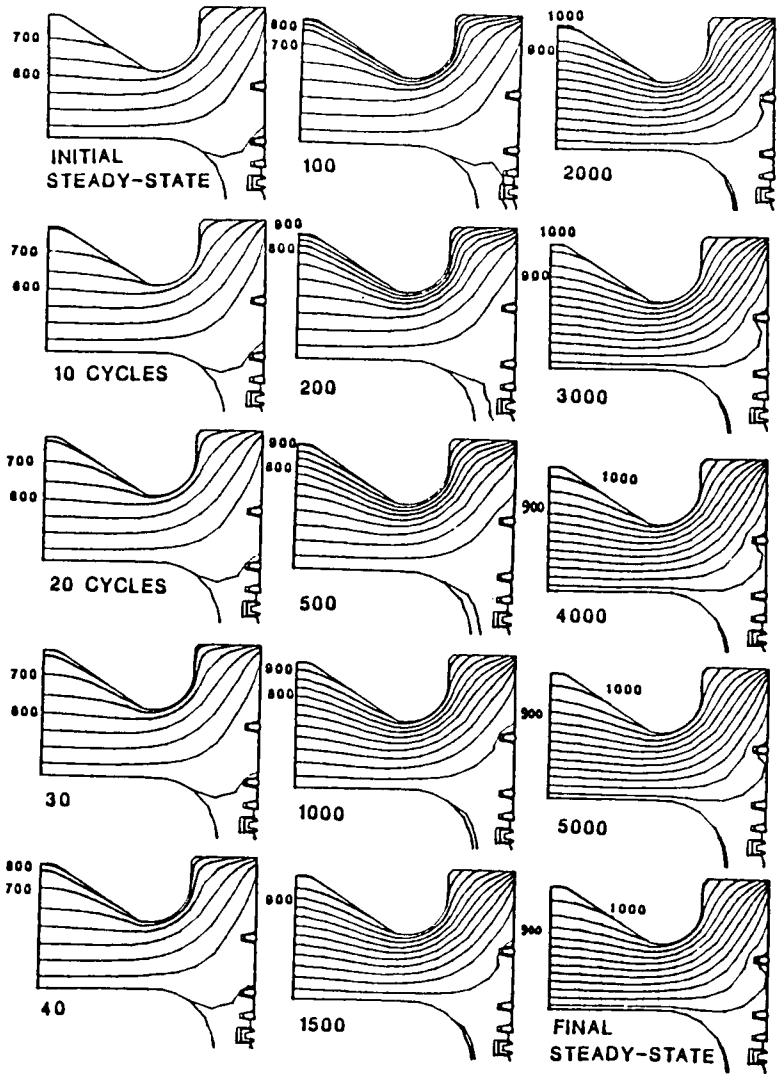

Figure 6 Transient temperature history in top of piston structure for case 1Z; equally spaced contour levels in increments of 50K: (numbers below figures denote nominal number of engine cycles from beginning of event).

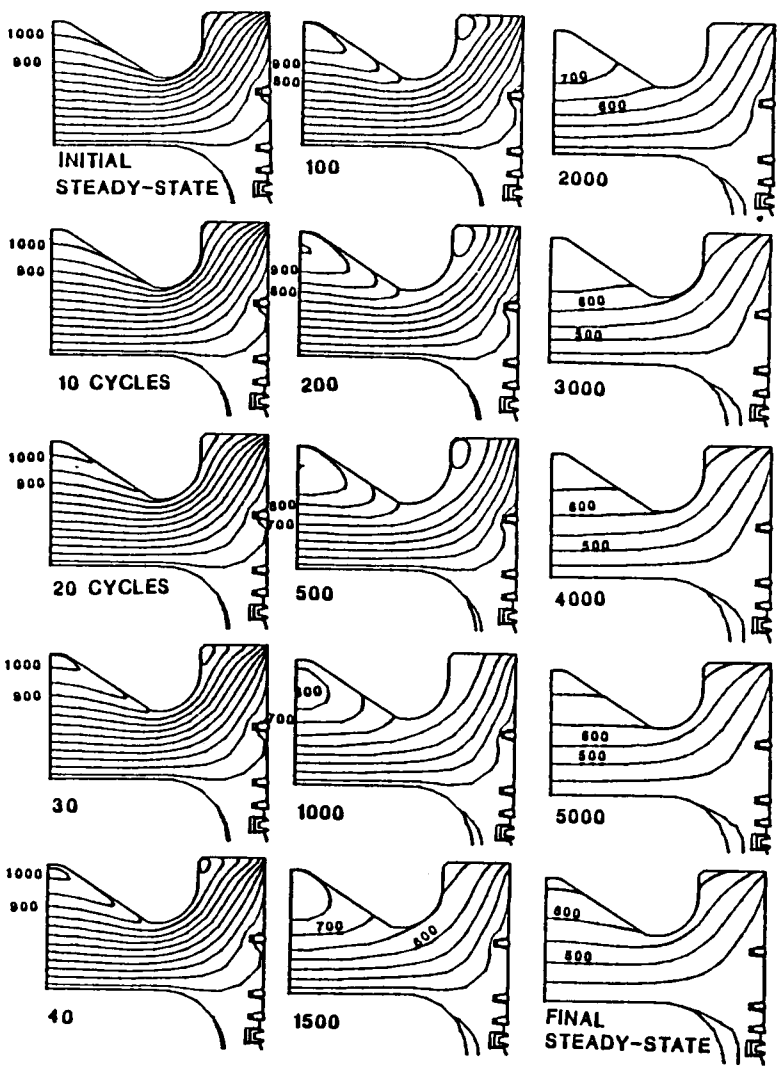

Figure 7 Transient temperature history in top of piston structure for case 2Z; equally spaced contour levels in increments of 50K: (numbers below figures denote nominal number of engine cycles from beginning of event).

peratures is complete after about 2000 cycles. The temperature on the oil side of the piston begins to rise about 100 cycles (6 sec) after the start of the event and the total rise is of the same order as that on the gas side (100 K vs 150 K).

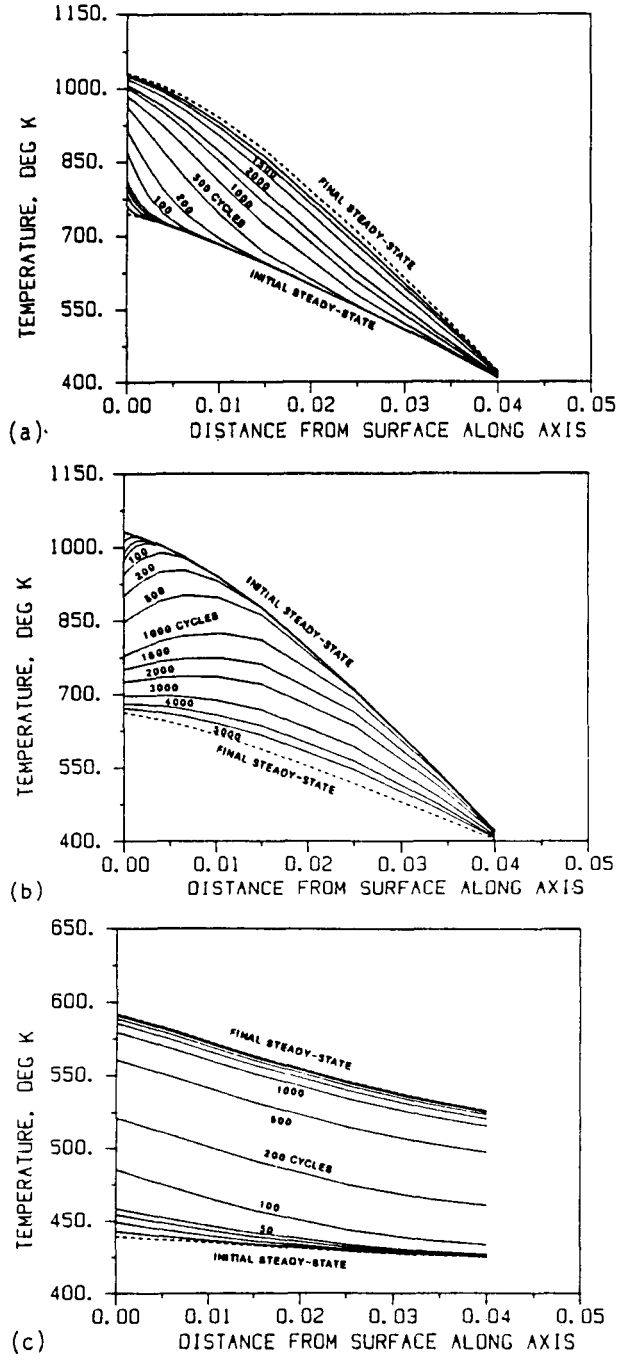

Figure 8 Transient thermal response of piston structure along axis of piston: 1) case 1Z; b) case 2Z; c) case 1A.

4.8 Structure Stress Response. In order to determine the thermal stresses and deformations during engine transients, finite element structural analysis of components were carried out with NASTRAN, using the predicted transient temperature profiles as input. The analysis was conducted in a decoupled manner and on a quasi-steady basis, since structural response is almost instantaneous compared to the thermal dynamics. Results presented here will be limited to the zirconia piston cases 1Z and 2Z. Elastic properties used for zirconia were as follows: Young's modulus = 2×10^5 MPa (N/mm^2); Poisson ratio = 0.32; linear thermal expansion coefficient = $9.8 \times 10^{-6} °K^{-1}$ Flexural and compressive strength of monolithic partially stabilized zirconia are given as 300 and 1800 MPa respectively. Results obtained at selected times shown in Figures 6 and 7, are presented in Figures 9 and 10.

For case 1Z (Figure 9), the gas side surface of the piston (which warms up rapidly) undergoes increased compression (shaded area), and peak compressive thermal stresses are seen to overshoot their final steady state. The peak appears to be midway through the transient, i.e. not at the outset where the temperature gradient is the steepest. Maximum tensile stress is on the piston rim which is being forced outward by the expanding interior. It increases gradually with the warmup of the piston, and it eventually exceeds the flexural strength of zirconia. Based on this result it appears that the high tensile hoop stresses will prevent the use of zirconia for a full top of the piston without restraining metal outer support. Figure 9 also shows the associated distortions produced by the high temperatures, displaying the deformed piston shape. Maximum deformations, occurring at the outer edge of piston crown are also given on each plot. As the piston warms, differential expansion causes a "bending" of its structure and the side surface of the piston takes a more arched appearance. A detailed examination shows that early on (100 cycles) the curvature of the surface is more accentuated and concentrated near the top (above top compression ring groove). The curvature progressively diffuses downward, and for the final steady-state is more uniform along this surface as a result of the deformation wave moving through the structure.

History of hoop stresses and distortion for case 2Z is shown in Figure 10. Here the cooling, which begins at the surface, progressively relieves the high surface compressive stresses. This trend leads to an overshoot in the stresses and after 1000 cycles part of the piston surface, including the central conical protrusion, is under tension, an undesirable condition for zirconia. The hot center of the piston constrained by the cooler outside is under compression. The final steady-state resembles the initial one, but with lower stress levels. The distortion pattern parallels that of case 1Z, but in reverse.

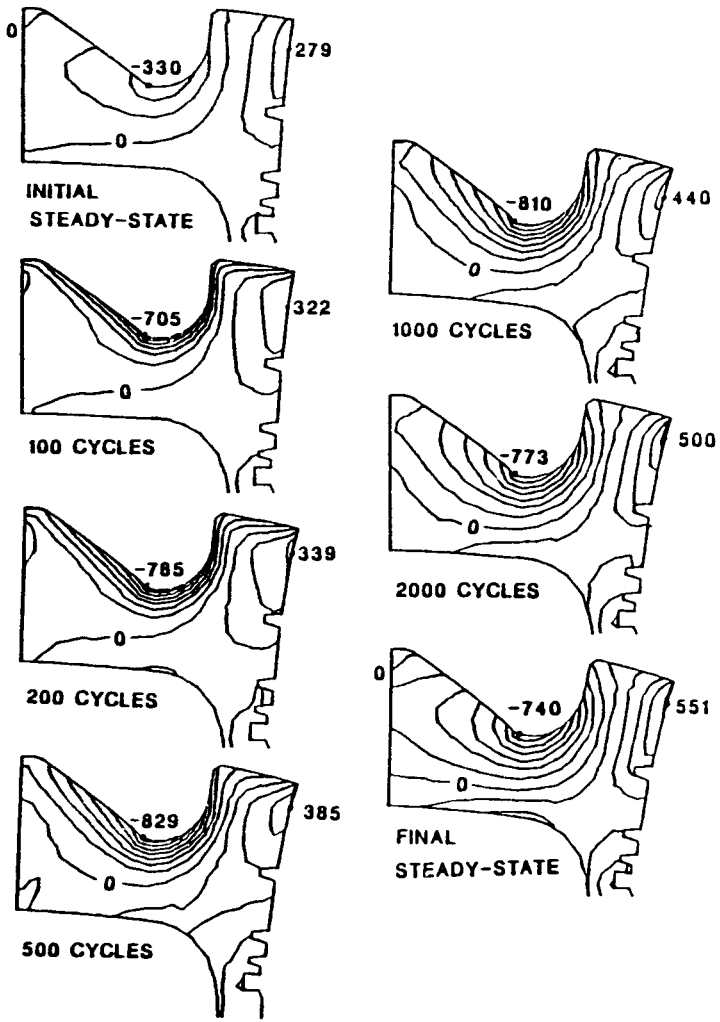

Figure 9 History of piston distortions and circumferential (hoop) thermal stress distribution (Mpa) for case 1Z; stress contours are in 100 Mpa increments. Zero hoop stress and maximum tensile (+) and compressive (-) stresses are labeled in each plot. Selected lines are among those in Figure 7.

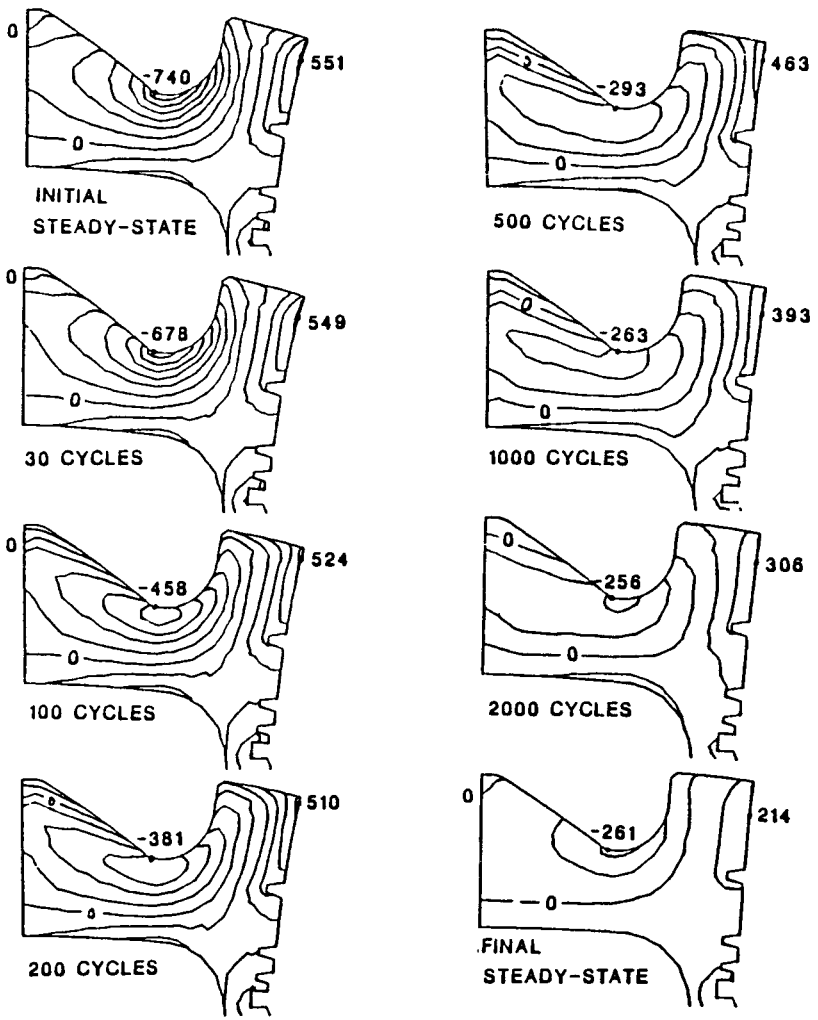

Figure 10 History of piston distortions and circumferential (hoop) thermal stress distribution (Mpa) for case 2Z; stress contours are in 100 Mpa increments. Zero hoop stress and maximum tensile (+) and compressive (-) stresses are labeled in each plot. Selected lines are among those in Figure 8.

Radial stress histories for both events (not shown here) were also obtained; they are quite small except for very locally concentrated high compressive stress at the same location and with peaks of the same magnitude as the peak compressive hoop stresses. These stresses are the largest at the highest engine load condition.

It should be reiterated that the above results are for purely thermal loading. For design purposes, one would need to superimpose the thermal load onto the instantaneous gas pressure and connecting rod pin forces in order to carry out piston structural analysis for key instants within the cycle, such as peak pressure. For pistons with solid crowns such as the one selected for this study, thermal stresses are likely to be dominant in the crown; however for thin-walled pistons the interplay of mechanical and thermal loads may be important and needs to be fully accounted for.

5. PSZ-COATED INTAKE AND EXHAUST VALVES

Results will be presented in this section for transient thermomechanical behavior of diesel engine valves with plasma-sprayed zirconia coated faces. The components of thermal and mechanical loading on an exhaust valve and its coating are schematically shown in Figure 11. They are similar for the intake valve, with the exception of the presence of the intake gas behind the valve, which cools the valve during the intake period.

5.1 Engine and Valve Description. The engine studied here is the one considered in the previous section. The modeled valves are uncooled, high alloy steel poppet valves with 48 mm face diameters. The coating is 1.5 mm thick and covers the face of the valve. In this design, the coating has been sprayed directly onto the metal surface with no bondcoat or strain isolator. The piston and head are also PSZ-coated.

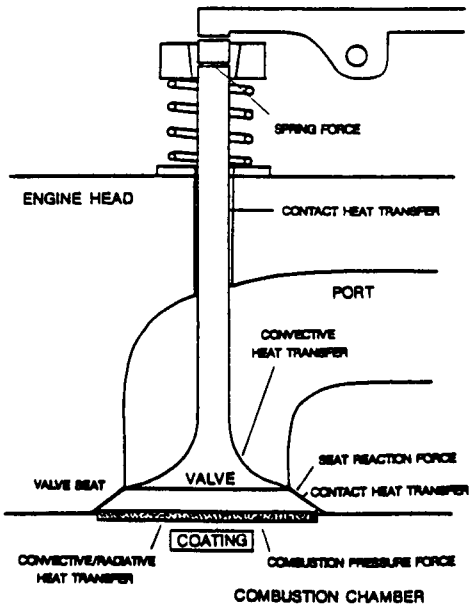

Figure 11 Thermal and mechanical loads on a diesel engine valve.

5.2 Finite Element Representation. The valve and coating were represented by the finite element mesh shown in Figure 12, consisting of 433 nodal points and axisymmetric solid elements. The same mesh was used for thermal and structural analysis. The plasma-sprayed zirconia coating was modeled using a higher resulution than the rest of the valve, with 8 non-uniformly distributed grid points spanning its thickness. Heat conduction in the rest of the engine structure and components was modeled by a quasi-3-dimensional network model, not shown here. In this model proper heat paths between valve and the remaining structure (through seats and guides) are established. While surfaces of finite elements on valve face are mapped onto the appropriate IRIS combustion chamber surfaces, the rear face elements are exposed onto port gases whose flow and thermodynamics are also simulated by IRIS to compute appropriate convective boundary conditions.

5.3 Thermomechanical Material Properties. Properties used for intake and exhaust valve and coating materials were as follows:

Property	Valve	Coating
k, thermal conductivity, W/mK	22	0.79
ρc, heat capacity, MJ/m^3K	2.3	4.18
E, Young's modulus, MPa	205,000	89,600
N, Poisson ratio	0.30	0.28
α, thermal expansion coefficient K^{-1}	19.6×10^{-6}	13×10^{-6}

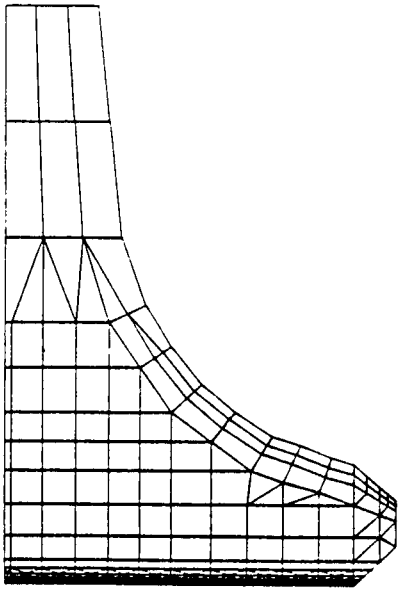

Figure 12 Portion of 2-dimensional axisymmetric finite element model of valve and coating geometry (excluding valve stem).

5.4 Transient Events Studied. Two transient load conditions (referred to as transients #3 and 4) involving an increase and a decrease in load at an approximately constant engine speed of 1300 RPM were simulated. Histories of fuel rate, rpm and other engine parameters input to the transient simulation were guided by transient dynamometer test data, obtained from Mr. Kevin Hoag of Cummins Engine Company. This assured that the transients used were realistic.

5.5 Steady-State Temperatures. The steady-state temperature distributions for the region of interest in exhaust and intake valves shown in Figures 13(a,b) (for rated engine conditions) are instructive and help interpretation of transient results. For both valves the profiles within the coatings are characterized by a nearly one-dimensional distribution and large gradients, a direct result of the low thermal conductivity of plasma-sprayed zirconia. The exhaust valve coating surface temperature is higher at its center by about 90K than the intake valve coating. This is due to gas heating on both sides of the exhaust valve, which causes higher metal substrate temperatures. For the same reason, the temperature drop through the exhaust valve coating at the center location is lower (114K vs 233K) than for the same coating on the intake valve. Although strongly one-dimensional, the coating temperature distribution has some degree of radial variation, which is caused by edge effects as well as the extent of non-uniformity of metal temperatures. The framed numbers in Figure 13 indicate coating surface and metal/coating interface temperatures at the center and edge of exhaust and intake valve faces. For the exhaust valve, which is cooled by contact to the engine structure, the coating surface temperature does not change from center to edge, but the temperature differential across the coating increases towards the edge of the valve due to seat cooling. In the intake valve, cooling at the seat is not as significant and edge effects cause a rise in surface coating temperature. The drop across the coating is uniform in the radial direction.

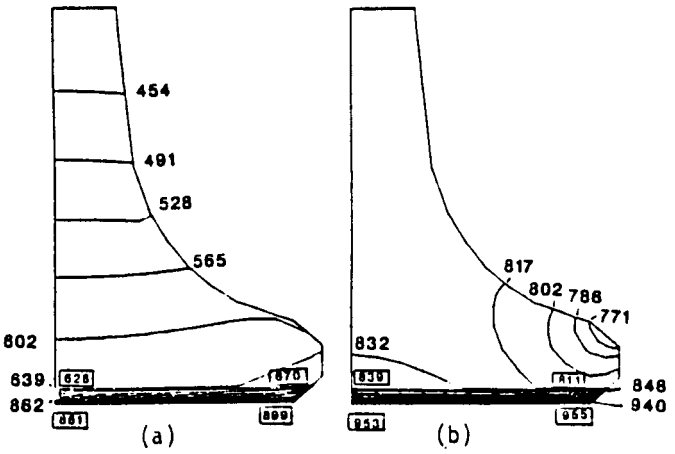

Figure 13 Steady-state temperature distribution in valve and plasma-sprayed zirconia coating at the rated engine condition: a) intake valve; b) exhaust valve; temperatures in degrees K.

5.6 Transient Thermal Response. The two engine transient events (transients #3 and #4) at which the thermomechanical behavior of the intake valve and coating were studied are shown in Figure 14(a,b). The events consist of an increase and a decrease in fuel rate at an essentially unchanged engine rpm of 1300 rpm. In the event where fuel is increased, the rate of increase has been controlled so as to keep the air/fuel ratio above 20. The high fuel condition at this speed is the engine peak torque condition, at which the highest steady-state thermal loads on engine components generally prevail. While the engine event lasts only seconds, component (including valve and coating) temperatures take minutes to achieve steady-state. Temperature histories for the intake and exhaust valve coatings during transient #4 are given in Figures 15(a,b). The initial and final steady states are qualitatively similar but at differing temperature levels, and much lower temperature gradients in the final state. Contour levels and temperature increments between them are decreased with each successive contour plot in order to better illustrate the behavior of local temperatures in the coating. Coating surface temperatures rapidly cool, temporarily reversing surface gradients. During this period the hot

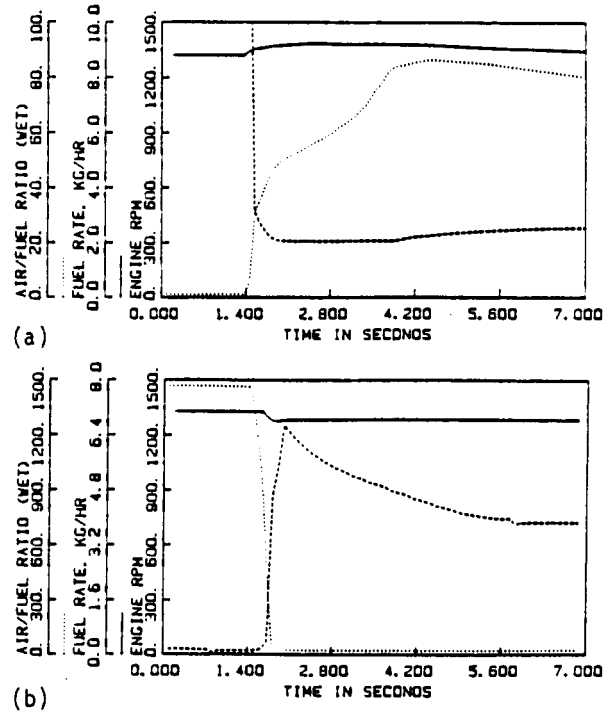

Figure 14 Event in fuel rate and rpm and short term response of air-fuel ratio: ZPS-coated engine. a) transient #3 (fuel up); b) transient #4 (fuel down).

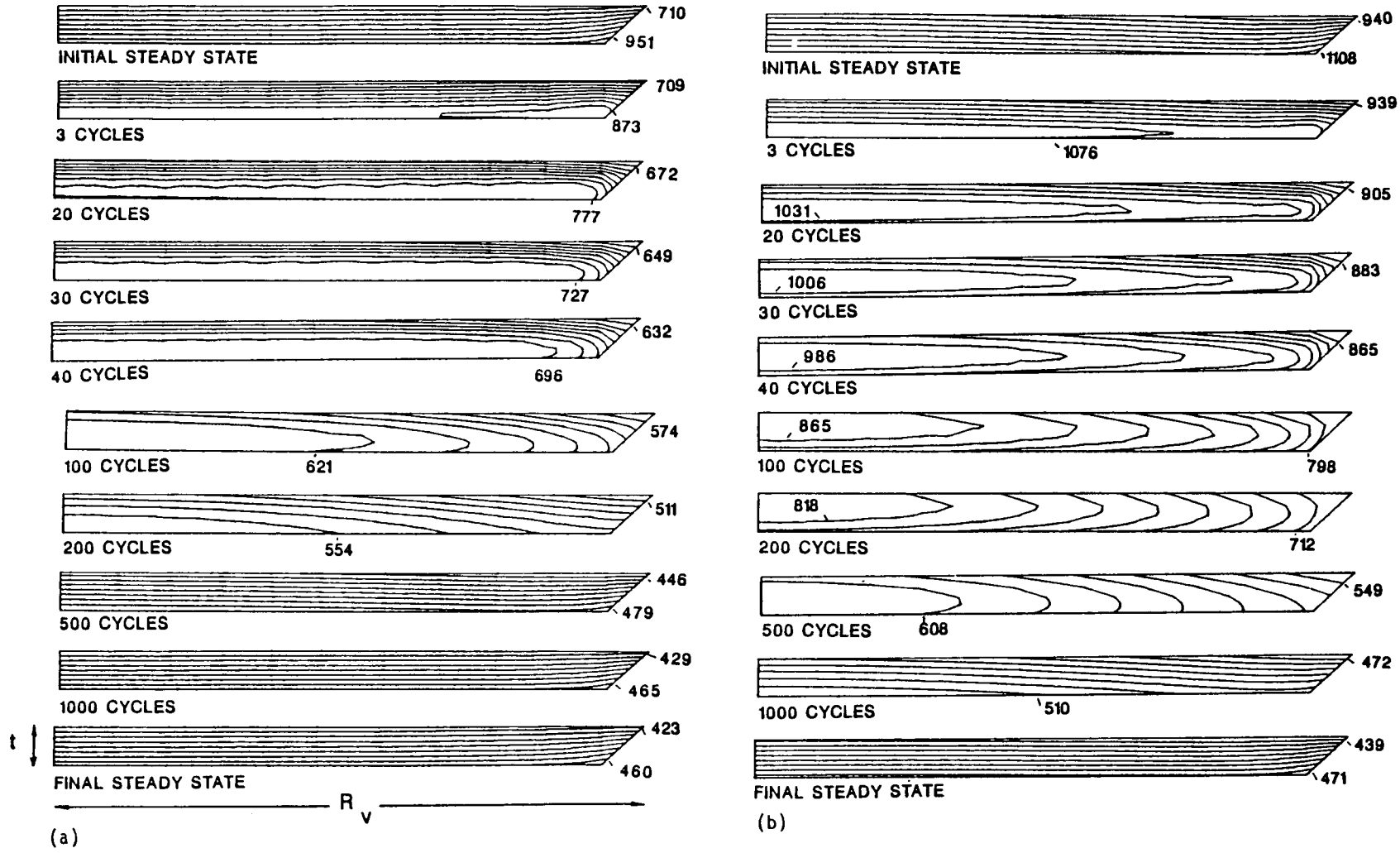

Figure 15 Transient temperature history in valve coating during transient #4. a) intake valve coating; b) exhaust valve coating. (Rv = valve radius; t = coating thickness).

core of the coating is cooled by the metal substrate as well as cooler combustion chamber gases. This is also seen in Figure 16a where the coating temperature history is tracked along the axis of the intake valve. Because of relatively fast cooling of the metal portion of the valve the effect is not as accentuated as it would be for a component with larger thermal inertia or with temperature less affected by engine transients (eg piston). The thermal response along valve axis during transient #3 is shown in Figure 16b, which indicates that coating temperature gradients during a (fuel up) transient will exceed gradients for both initial and final steady-states. Figure 16 also shows that for the intake valve equilibration of structural temperatures occurs within about 1000 cycles (1.5 min) after beginning of the transient event, for both transients #3 and 4. Figure 17(a,b) shows similar behavior for the exhaust valve and coating, but with a slightly slower approach to steady state, due to the longer response in exhaust temperatures.

5.7 Transient Structural Response. Finite element structural analysis of the intake valve and coating was carried out subject to thermal loads prevailing at selected instants during the two transients. Circumferential stress history within the coating thickness (at a radius of 4mm) for transient #3 is shown in Figure 18a. In the beginning of the event the coating is under some tension due to the larger expansion coefficient of the substrate. As the surface begins to warm up, a large portion of the coating adjoining the surface rapidly becomes subjected to increasing compressive stresses; as heat diffuses to the interior of the coating and eventually to the substrate (after about 100 cycles), the substrate begins to expand, increasing tensile stresses in the coating near the interface and relieving surface compressive stresses. The latter are further decreased by the leveling of surface temperature gradients after they overshoot. Surface compressive stress level during the transient peaks after about 50 cycles, at more than 3 times the final steady-state level. Circumferential stresses at selected instants during transient #4 are shown in Figure 18b. For this transient the rapid cooldown of the surface causes tensile stresses. The coating remains under

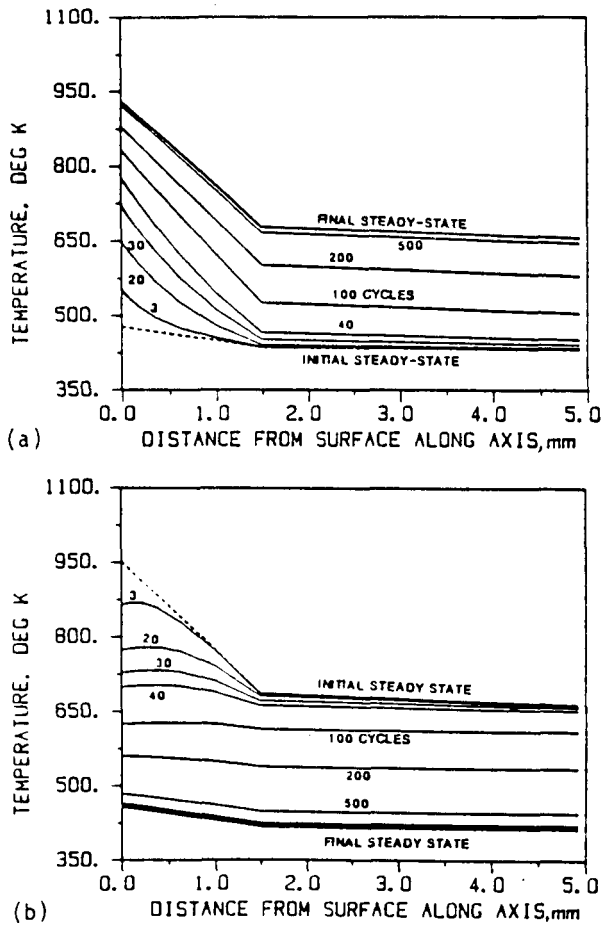

Figure 16 History of temperature response through intake valve and coating along valve axis. a) transient #3; b) transient #4.

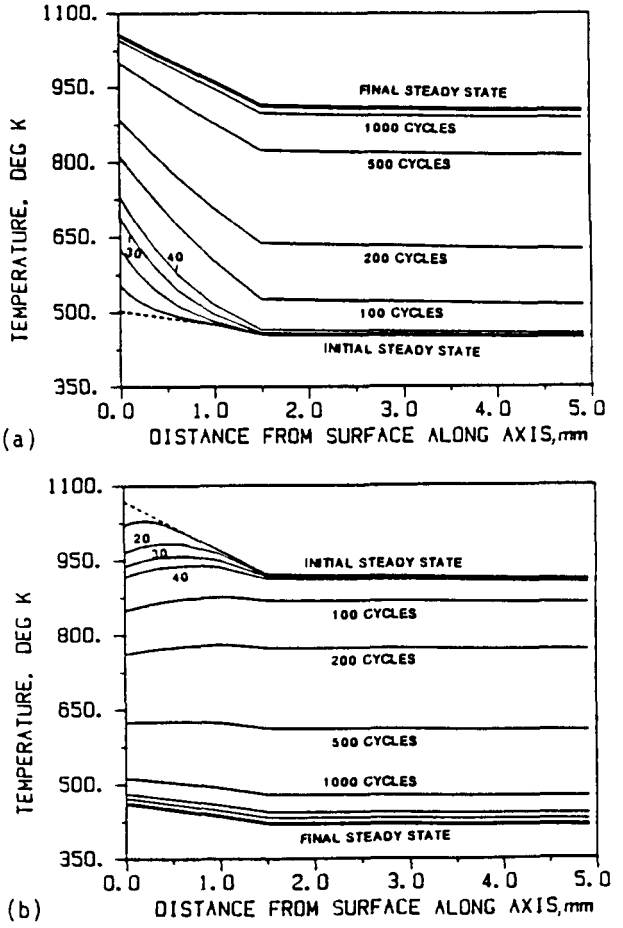

Figure 17 History of temperature response through exhaust valve and coating along valve axis. a) transient #3; b) transient #4.

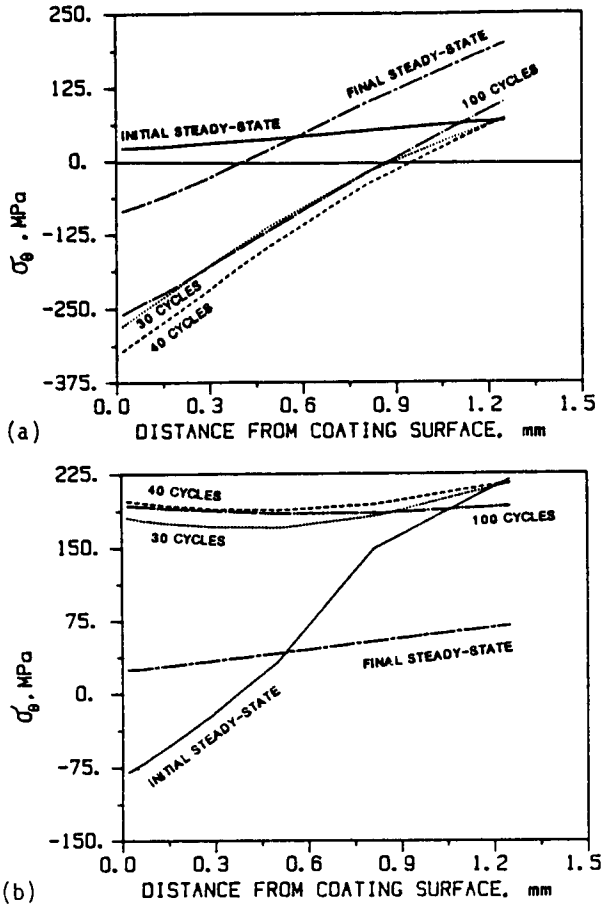

Figure 18 Transient behavior of circumferential stresses within the PSZ coating of intake valve during a) transient #3; b) transient #4.

tension (but at a lower stress level) at the final steady thermal stresses. For a cooldown transient, compressive stresses are relieved and high tensile stresses are temporarily observed throughout the coating.

6. SILICON NITRIDE CAP PISTON WITH AIR GAPS

The third study reported here is related to the design analysis of a low heat rejection, uncooled engine piston of a joined ceramic-metal construction. The piston was designed by Detroit Diesel Allison as a part of DOE-sponsored program and its finite element model was provided to ITI to carry out the analysis described below.

6.1 Piston Assembly Design, Materials and Joining Method. The piston assembly considered utilizes a silicon nitride ceramic piston crown press-fit into the piston body on a cylindrical surface with a radial mismatch of 0.15 mm, with additional contact on horizontal surfaces (Figure 19). Air gaps between the ceramic crown and body are important inhibitors of heat flow through the

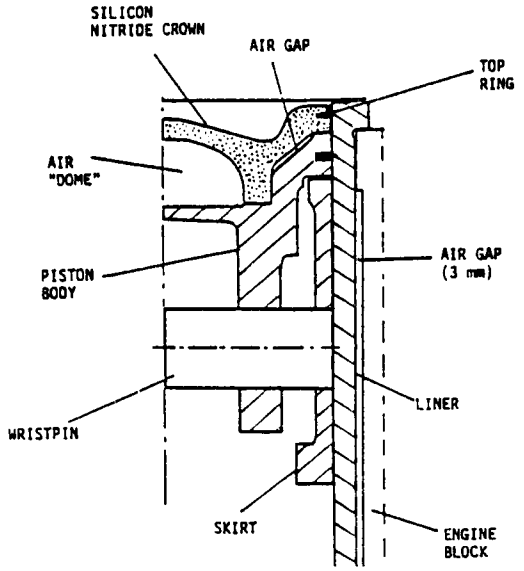

Figure 19 Cross-section of joined ceramic-metal piston assembly with air gaps for low-heat rejection engine.

structure, since conductivity of silicon nitride, an excellent temperature resistant ceramic, is 16-21 W/m°K (in the 400-900°C range), i.e. not much less than, for example, that of high alloy steels, although advanced silicon composites can have conductivity values on the order of 50 percent of the currently quoted values. Calculations were carried out both for the current technology silicon nitride as well as the projected advanced material. However, only the results for the latter are presented here. Cast iron is used for the piston body, skirt and liner. The entire piston-liner assembly has axisymmetric geometry, except bores in the lower part of the piston body and skirt for the wristpin. The wristpin is rigidly attached to the piston body, but the skirt is allowed to rotate around it. There are two rings: an L-ring positioned flush with the ceramic crown surface and a rectangular cross-section ring in a groove in the metal body. The design is completely uncooled. Since crankshaft, connecting rod and wristpin bearings are grease-lubricated, cooling by crankcase oil splashing is not present. Solid lubrication is contemplated for a liner and skirt-liner contacts. Thus the structure rejects heat only to the vented crankcase air, to the air gap surrounding the liner, and to the ambient air directly or through the engine block.

6.2 Finite Element Model of Engine Components. The main objective of the study was the analysis of the piston and liner thermal distributions. The axisymmetric finite element representation of the piston assembly (piston crown, body and rings) and the liner are shown in Figure 20. A network model of the head and ports/valves connects to the upper end of the liner. Piston crown and body

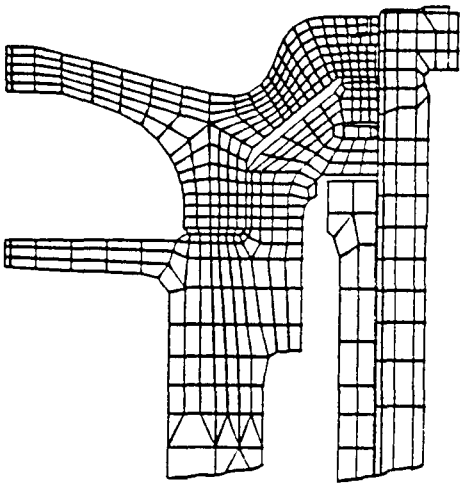

Figure 20 Portion of two-dimensional axisymmetric finite element model of piston-liner assembly (piston design of Figure 19).

were assumed to be in perfect thermal contact at the joining surfaces with no additional thermal contact resistance. The wristpin dimensions and thermal properties (low alloy steel) were used to compute the total thermal resistance between piston skirt and body. Since the model is axisymmetric, the connectivity based on this resistance was uniformly distributed in the azimuthal direction. Conductivity and heat capacity (ρc) of sintered silicon nitride were set to 10 W/mK and 3.35×10^6 J/m^{3}K, respectively.

6.3 Air Gap Models and Other Boundary Conditions. The two air gaps incorporated in the piston design are treated by a special transient heat convection submodel, input to which includes a heat transfer coefficient and the thermal inertia (mc_p) of the gap gases. A heat transfer coefficient of 100 W/m^{2}K was chosen for use in both gaps of the piston design, with values of mc_p, based on gap volumes and specific heat of air, of 0.055 and 0.008 J/°K for the large and small gap, respectively.

Surfaces of the form model exposed to the combustion chamber gases and those in frictional contact are subject to IRIS convection radiation and friction boundary conditions. The remaining surfaces, which are coolant or oil cooled in conventional engines, are uncooled in this application. Cooling due to crankcase oil splashing, which is the major heat sink in uncooled but oil-lubricated engines, is also absent from this design, which uses grease-packed bearings. Instead, these surfaces are exposed to vented crankcase air, other air gaps and to ambient air, directly or through the skin of the engine block. There is no dominant heat sink and some heat is transferred to air from large surfaces for which one needs to specify the appropriate air temperatures and heat transfer coefficients. These metal-to-air boundary conditions were estimated based on previous experience, literature on measured temperatures and free or forced convection calculations.

6.4 Simulated Engine Transient Event. The simulated event (transient #5) is a segment in the federal smoke cycle. During the transient, the engine speed is linearly increased from 700 RPM to near-rated speed (1575 RPM) within 5 seconds. Steady-state idling at 700 RPM with no load is taken to be the operating condition before and up to the event. At the point when engine RPM starts increasing, a step increase in the requested fuel rate is also applied, which increases up to the full load fuel rate at 1575 RPM. Simultaneously, a control algorithm is activated that limits actual fuel rate in order to maintain an air-fuel ratio at or above 22 to maintain smoke-free operation. The event lasts until the actual fuel rate reaches the full load rate at the final RPM level. Injection timing is advanced during the event linearly with the fuel rate from 4 degrees BTDC to 10 degrees BTDC. Also, the duration of injection increases depending on instantaneous fuel rate and engine RPM.

6.5 Engine Transient Response. The simulated event in rpm and fuel as well as engine air-fuel ratio and exhaust temperature responses are illustrated in Figure 21a. The event begins at 3 sec. The smoke limitation on air fuel ratio, active between 3.4 and 13 seconds in this case, causes a rather protracted (10 sec) fuel rate increase extending beyond the nominal end of the transient. The exhaust temperature is shown to overshoot during this period, and this is caused by the turbocharger lag. The long-term response of the same quantities (Figure 21b) shows that the air-fuel ratio response ends soon after the end of the fuel event, but exhaust temperature gradually rises by about 25°K to its final steady-state level within the next 4 minutes.

As in the previous two studies, results for engine performance response indicate the presence of two time scales, associated with turbocharger lag and structure thermal response.

6.6 Gas-to-Wall Heat Transfer and Structure Thermal Response. During transient simulation, engine quantities affecting gas-to-wall heat transfer are tracked by gas-to-wall heat transfer models, on a crankangle by crankangle basis. Figure 22 shows the transient history of cycle-mean convection heat transfer coefficients on the three piston surfaces (cup base, cup side and crown). During the early response, heat transfer coefficient histories reflect fuel rate variation. In this period when RPM and engine pressure are increasing but are still low, the dominant effect on heat transfer coefficients is fuel injection-related turbulence in this low-swirl engine. The long term history of heat transfer coefficients indicates a decay after an early overshoot; the decay is related to the effect of the increasing wall tempeatures on the thermal boundary layer properties.

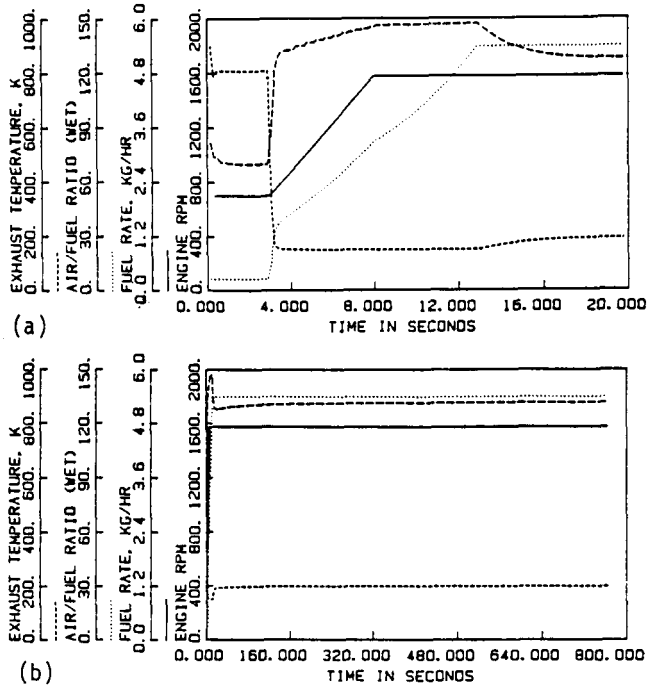

Figure 21 Transient #5: transient event in RPM/fuel and air-fuel ratio and the exhaust temperature response: a) short term; b) long term.

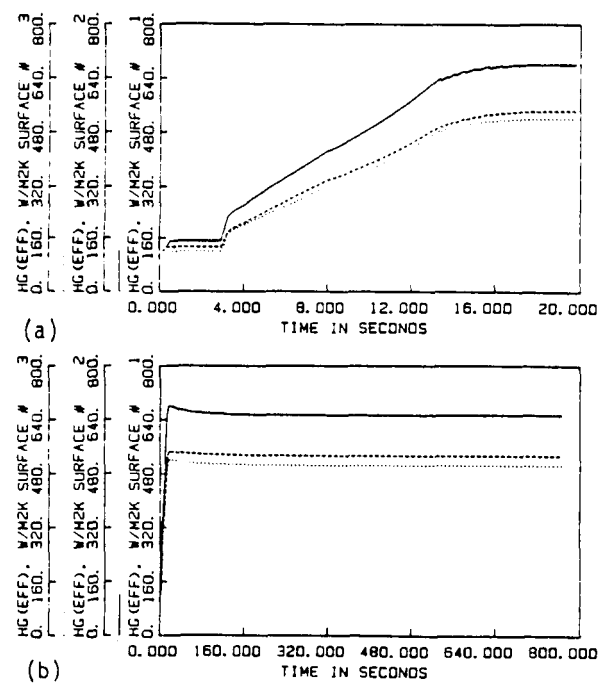

Figure 22 Predicted history of convective heat transfer coefficients on silicon nitride piston cap surfaces (cup base, cup side, crown) during transient #5. a) short term; b) long term.

Radiant heat fluxes and friction heat generation rates are also tracked during the transient, so that correct instantaneous boundary conditions for transient heat conduction calculations can be computed. Similarly the special submodels for air gap heat transfer are integrated in the transient mode. The history of air temperature in the two air gaps is illustrated in Figure 23, which shows the temperature of air in the "dome" remains consistently above that of the air inside the thin gap.

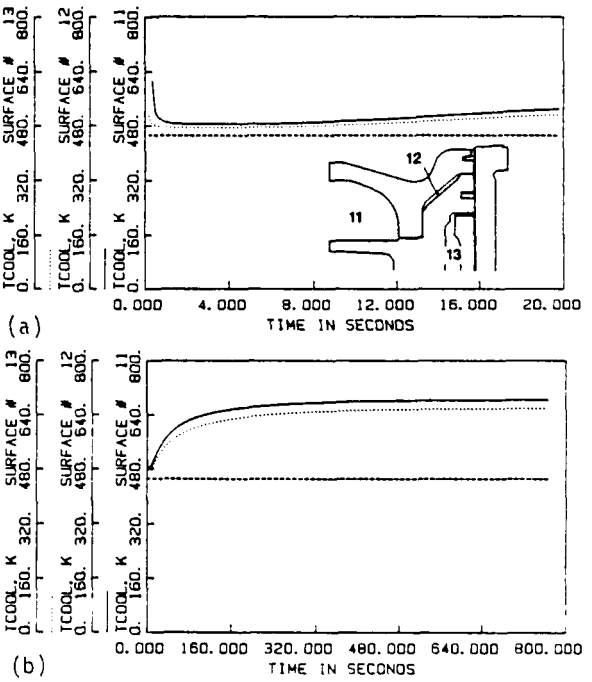

Figure 23 Predicted transient response of air gap temperatures in silicon nitride air gap piston during transient #5 a) short term; b) long term.

The transient thermal response of the combustion chamber surfaces of the engine may be observed through the histories of temperature on four selected finite element nodes on the piston-liner assembly given in Figure 24.

The predicted history of the entire temperature field for the FEM model is also stored at selected time steps. Contour plots in Figure 25 show temperature distribution in the silicon nitride cap of the piston at several instants during the transient simulation. Results indicate the presence of a relatively mild thermal shock (concentration of isotherms in contour plots) compared to that produced in monolithic zirconia pistons, with conductivity up to 10 times lower than silicon nitride. The thermal shock is also somewhat dampened by the relatively long (20 sec) turbocharger lag. However, there is still a discernible increase in surface temperature gradients between cycles 40 and 500, which may be expected to cause compressive thermal stresses exceeding those at the final steady-state.

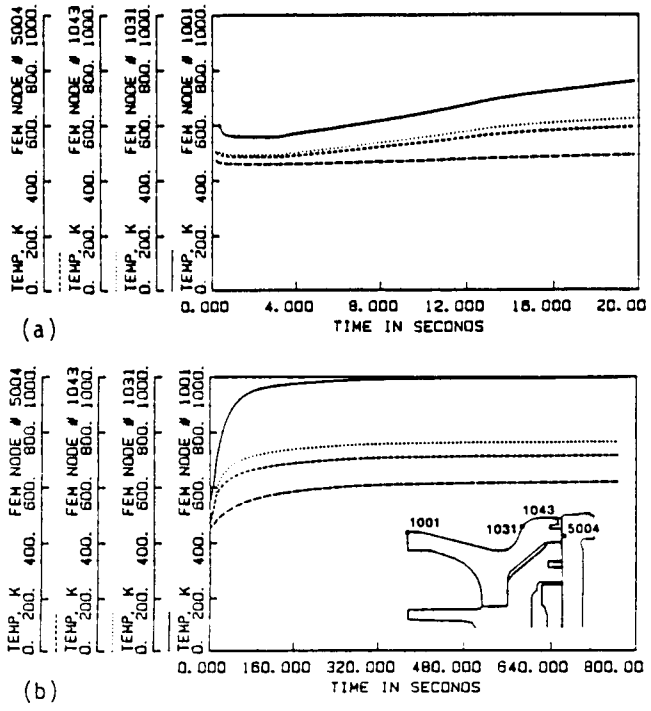

Figure 24 Predicted transient thermal response of the silicon intake/air gap piston/liner assembly at selected finite element nodes during transient #5. a) short term; b) long term.

7. CONCLUSIONS

1. An integrated methodology for the coupled transient simulation of engine and turbocharger performance, gas phase heat transfer and heat conduction in engine structure was developed. Using this methodology, effects of typical rapid engine speed and load transients on thermostructural behavior of various low heat rejection components was effectively and economically calculated. Engine and turbocharger responses as well as transient structural temperature and stress histories were documented.

2. For all studies carried out the engine response exhibits distinctly separate near-term and long-term behaviors. During the near term (approximately 20-100 cycles), the turbocharger responds with a lag and most engine quantities approach the final steady-state levels within 10 percent of those values. The subsequent long term response reflects gradually changing structure temperatures, which affect exhaust temperature and with it the turbocharger. Steady-state is reached within minutes, the exact duration of the response depending on equilibration time for structure temperatures.

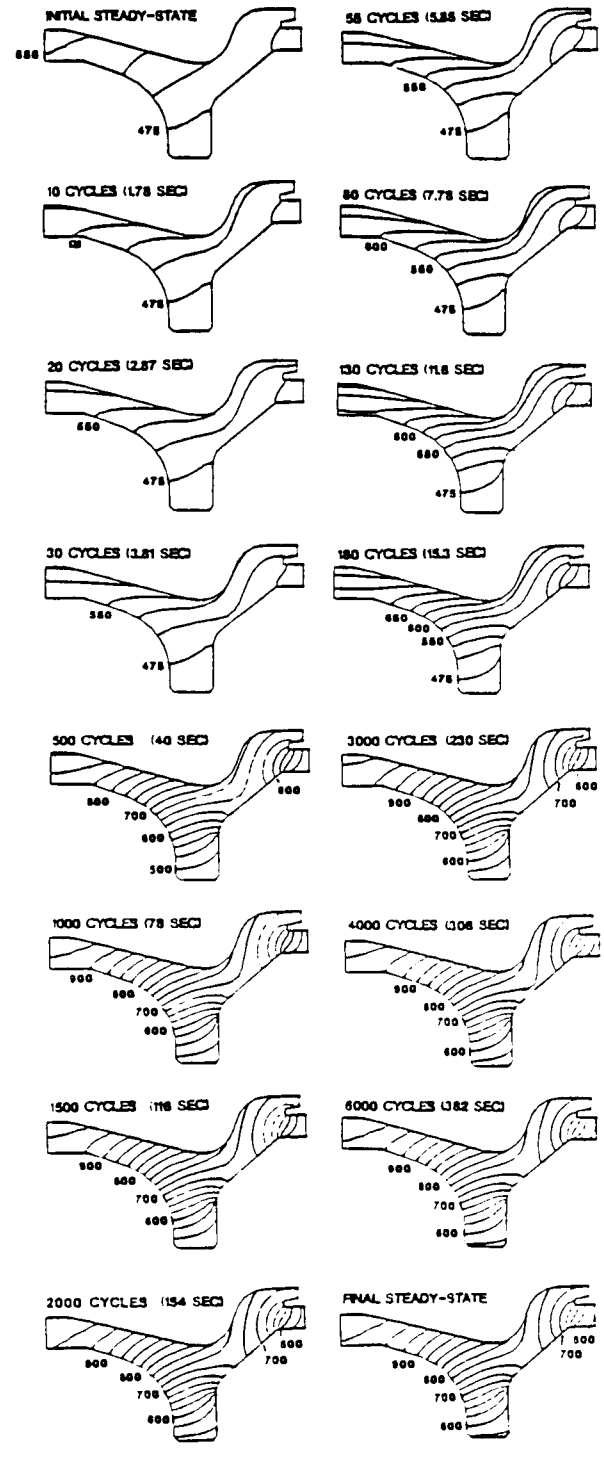

Figure 25 Predicted temperature distributions in silicon nitride piston cap at selected instants during transient #5 (nominal cycles from beginning of event; contour levels in degrees K and 25K increments.

3. A thermal wave is shown to propagate through engine component structures during engine speed and load transients. The steepness of the front in the wave depends on component thermal properties and on the turbocharger response to the transient. In low conductivity ceramics such as monolithic zirconia and PSZ this behavior reaches "thermal shock" proportions. A steep wave is formed early on with maximum gradients between 30 and 100 cycles after the start of the transient. The severity of the thermal shock is not as pronounced in higher conductivity materials. It is also attenuated by turbocharger lag and differs from component to component.

4. Results of stress analysis of ceramic components under thermal loads prevailing during engine transients indicate that: a) a severe thermal load increase causes surface compressive stresses to increase and overshoot their final steady-state level; b) a thermal load decrease causes relief of surface compressive stress, which temporarily subjects the surface to tension; c) this is especially pronounced in coatings when there is mismatch between coating and substrate thermal expansion coefficients; d) under the transient conditions of thermal shocks, the structure is briefly exposed to stresses that exceed those encountered under maximum steady state loads.

ACKNOWLEDGEMENTS

This work has been carried out under the Heavy Duty Transport Technology program contract DEN3-342 sponsored by the U.S. Department of Energy and administered by NASA Lewis Research Center under program manager J. C. Wood and Detroit Diesel Allison subcontract DE-078386 (under DOE contract DEN3-329) managed by Mr. N. Hakim. Mr. Kevin Hoag and Ms. Sharon Frisch of Cummins Engine company provided valuable assistance with definition of engine transients. Messrs. M. Sawliwala and L. Lee of Detroit Diesel Allison have supplied engine performance data, component descriptions and structure finite element models for the prototype ADRE (Adiabatic Diesel Reference Engine) being developed under DOE contract DEN3-329.

REFERENCES

1. McAulay, K. J., Wu, T., Chen, S. K., Borman, G. L. Myers, P. S., and Uyehara, O. A. Development and Evaluation of the Simulation of the Compression-Ignition Engine. SAE Transactions, Vol. 74 (1966), paper 650451.

2. Watson, N. Transient Performance Simulation and Analysis of Turbocharged Diesel Engines. SAE Paper 810338.

3. Morel, T., Keribar, R., Blumberg P. N. and Fort, E. F. "Examination of Key Issues in Low Heat Rejection Engine Concepts." SAE Paper 860316, SAE Congress, Detroit, 1986.

4. Morel, T., Keribar, R., Sawlivala, M. and Hakim, N. "Application of Several Variable-Valve-Timing Concepts to an LHR Engine." ASME Symposium on Automotive Engine Technology, Dallas, Texas, February 1987.

5. Morel, T. and Keribar, R. A Model for Predicting Spatially and Time-Resolved Convective Heat Transfer in Bowl-in-Piston Combustion Chambers. SAE Paper 850204.

6. Morel, T. and Keribar, R. Heat Radiation in D.I. Diesel Engines. SAE Congress, Paper 860445.

7. Morel, T., Keribar, R. and Blumberg, P. N. Cyclical Thermal Phenomena in Engine Combustion Chamber Surfaces. SAE Paper 850360.

8. Morel, T., Fort, E. F. and Blumberg, P. N. Effect of Insulation Strategy and Design Parameters on Diesel Engine Heat Rejection and Performance. SAE Paper 850506.

9. Watson, N., Marzouk, M. and Pilley, A. D. A Combustion Correlation for Diesel Engine Simulation. SAE Paper 800029.

☆U.S. GOVERNMENT PRINTING OFFICE:1989-648-162/81029

NASA
National Aeronautics and Space Administration

Report Documentation Page

1. Report No.	2. Government Accession No.	3. Recipient's Catalog No.
NASA CR-182237 DOE/NASA/0342-3		

4. Title and Subtitle

Methods for Heat Transfer and Temperature Field Analysis of the Insulated Diesel

Phase III—Final Report

5. Report Date

December 1988

6. Performing Organization Code

7. Author(s)

Thomas Morel, Syed Wahiduzzaman, Edward F. Fort, Rifat Keribar, and Paul N. Blumberg

8. Performing Organization Report No.

10. Work Unit No.

778-34-22

9. Performing Organization Name and Address

Ricardo-ITI
645 Blackhawk Drive
Westmont, Illinois 60559

11. Contract or Grant No.

DEN3-342

13. Type of Report and Period Covered

Contractor Report
Final

12. Sponsoring Agency Name and Address

U.S. Department of Energy
Office of Vehicle and Engine R&D
Washington, D.C. 20585

14. Sponsoring Agency Code

15. Supplementary Notes

Prepared under Interagency Agreement DE-AI01-86CE50162. Project Manager, James C. Wood, Propulsion Systems Division, NASA Lewis Research Center. Cleveland, Ohio 44135.

16. Abstract

This report describes work done during Phase III of a program aimed at developing a comprehensive heat transfer and thermal analysis methodology for design analysis of insulated diesel engines. The overall program addresses all the key heat transfer issues: (1) spatially and time-resolved convective and radiative in-cylinder heat transfer, (2) steady-state conduction in the overall structure, and (3) cyclical and load/speed temperature transients in the engine structure. These are all accounted for in a coupled way together with cycle thermodynamics. This methodology was developed during Phases I and II. During Phase III, an experimental program was carried out to obtain data on heat transfer under cooled and insulated engine conditions and also to generate a database to validate the developed methodology. A single cylinder Cummins diesel engine was instrumented for instantaneous total heat flux and heat radiation measurements. Data were acquired over a wide range of operating conditions in two engine configurations. One was a cooled baseline. The other included ceramic coated components (0.050″ plasma sprayed zirconia)—piston, head and valves. The experiments showed that the insulated engine has a smaller heat flux than the cooled one. The model predictions were found to be in very good agreement with the data.

17. Key Words (Suggested by Author(s))	18. Distribution Statement
Diesel engine; Heat transfer; Transportation; Insulated engine; Fuel consumption; Adiabatic engine	Unclassified – Unlimited Subject Category 85 DOE Category UC-96

19. Security Classif. (of this report)	20. Security Classif. (of this page)	21. No of pages	22. Price*
Unclassified	Unclassified	171	A08

*For sale by the National Technical Information Service, Springfield, Virginia 22161